MATHEMATICAL INVESTIGATIONS OF WAVE-STRUCTURE INTERACTION PROBLEMS

Ph.D. Thesis

By

AMAN KUMAR KUSHWAHA

DEPARTMENT OF MATHEMATICS
INDIAN INSTITUTE OF TECHNOLOGY INDORE

NOVEMBER 2025

MATHEMATICAL INVESTIGATIONS OF WAVE-STRUCTURE INTERACTION PROBLEMS

A THESIS

Submitted in partial fulfillment of the
requirements for the award of the degree
of
DOCTOR OF PHILOSOPHY

by

AMAN KUMAR KUSHWAHA

DEPARTMENT OF MATHEMATICS
INDIAN INSTITUTE OF TECHNOLOGY INDORE
NOVEMBER 2025

INDIAN INSTITUTE OF TECHNOLOGY INDORE

I hereby certify that the work which is being presented in the thesis entitled **MATHEMATICAL INVESTIGATIONS OF WAVE-STRUCTURE INTERACTION PROBLEMS** in the partial fulfillment of the requirements for the award of the degree of **DOCTOR OF PHILOSOPHY** and submitted in the **DEPARTMENT OF MATHEMATICS, Indian Institute of Technology Indore,** is an authentic record of my own work carried out during the time period from August 2021 to August 2025 under the supervision of Dr. Vinay Kumar Gupta, Associate Professor, Department of Mathematics, Indian Institute of Technology Indore.

The matter presented in this thesis has not been submitted by me for the award of any other degree of this or any other institute.

Signature of the student with date

(Aman Kumar Kushwaha)

This is to certify that the above statement made by the candidate is correct to the best of my knowledge.

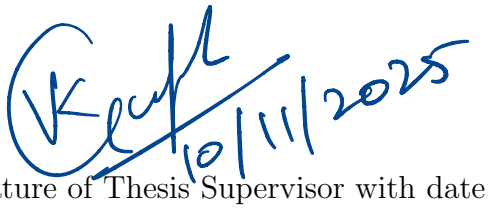

Signature of Thesis Supervisor with date

(Dr. Vinay Kumar Gupta)

Aman Kumar Kushwaha has successfully given his Ph.D. Oral Examination held on **November 6, 2025**.

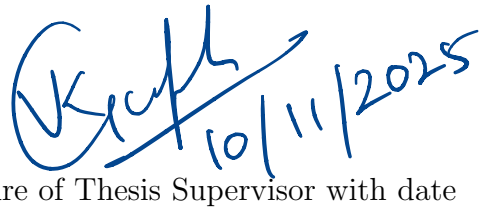

Signature of Thesis Supervisor with date

(Dr. Vinay Kumar Gupta)

ACKNOWLEDGEMENTS

The successful completion of this study would not have been possible without the support, guidance, and goodwill of many individuals. Their contributions were invaluable in helping me achieve the objectives of this research. I am deeply grateful to the following individuals for their encouragement and assistance. First and foremost, I express my heartfelt gratitude to God Almighty, our Lord and Savior, for granting me the wisdom, strength, knowledge, and perseverance needed to overcome challenges and pursue this study. Furthermore, I would like to express my heartfelt gratitude to my Master's supervisor, Prof. Jugal Mohapatra, and my advisor, Dr. Durgesh Kushwaha, for inspiring and encouraging me to embark on a journey in research. His guidance and blessings provided me with the determination to complete this work successfully.

This dissertation owes its realization to the help and patience of several people, without whom this journey would have been incomplete. I extend my sincere gratitude to my thesis supervisor, Dr. Vinay Kumar Gupta, for his unwavering mentorship and support throughout my tenure as a research scholar. His guidance during challenging times, both during the analysis and the dissertation writing process, was instrumental, and I am profoundly thankful for his confidence in my abilities. I could not have asked for a better mentor and advisor for my doctoral studies.

Beside my supervisor, I would also like to express my heartfelt gratitude to my collaborator, Prof. Hareksurhna Behera, whose constant support, insightful guidance, and unwavering availability for discussions—whether academic or friendly—have been invaluable to this research. His expertise and innovative ideas significantly enriched the quality of this study, providing clarity and direction whenever I encountered challenges. This study would not have been possible without his tireless efforts and profound contributions, for which I am deeply grateful.

I am also deeply thankful to the Department of Mathematics at the Indian Institute of Technology Indore, India, for granting me the opportunity to pursue my doctoral studies as a research scholar. I am also grateful to the technical and non-technical staff of the department, who provided invaluable assistance with administrative tasks and ensured the availability of a well-equipped laboratory that greatly supported my research endeavors.

I would like to express my heartfelt appreciation to my close friends, hostel-mates, and research scholar roommates, who have been by my side over the past five years. They

have shared in my moments of joy, celebrating happy times, and have lifted my spirits during challenging days. I am especially thankful to Aditya, Prabhu, Navneet, Sahil, Himanshi, Shreyas and Neha for their unwavering support and companionship throughout this journey. I am also deeply grateful to Akshay, Mahendra, Kapil and Pooja who, despite being miles away, always made time to connect with me and offer encouragement. While it is impossible to list everyone who has been part of this incredible chapter of my life, the cherished memories and meaningful moments I shared with them remain etched in my heart, and I will treasure them for a lifetime.

I am deeply thankful to the Council of Scientific & Industrial Research (CSIR), India, for their generous financial support, which made this research possible. I am sincerely grateful for the continued fellowship provided throughout the duration of my Ph.D., enabling me to focus on and successfully complete my studies.

Finally, I wish to express my heartfelt and deepest gratitude to my parents, my elder brother Dhananjay Kushwaha, and my elder sister Manisha Kushwaha. Their unwavering love, guidance, and encouragement have been the cornerstone of my journey throughout this doctoral program. They stood by me in every moment of joy and hardship, offering me strength, motivation, and an endless reservoir of patience and understanding. Words fall short in expressing the profound love, respect, and appreciation I hold for them, as their presence and influence have shaped not only my academic accomplishments but also the person I am today. For this, I will forever remain indebted and grateful.

DEDICATION

To my family

and

to every student whose dreams of higher studies were dimmed—not by a lack of talent, but by the weight of family responsibilities.

ABSTRACT

This thesis presents a comprehensive mathematical framework for analyzing wave scattering by single and multiple structures under the assumption of small-amplitude water wave theory. The primary goal of the thesis is to deepen the understanding of wave-structure interactions near the shore, particularly the behavior of strong waves and the role of different structural configurations in mitigating wave energy. The study considers various breakwater geometries, including cylindrical, rectangular, and inverse T-shaped structures. In this thesis, the fluid is assumed to be inviscid, incompressible, and irrotational flow, with negligible surface tension on the free surface. This assumption allows the use of a velocity potential governed by the Laplace equation. To find this velocity potential, the method of separation of variables is used to derive explicit expressions, where the unknown coefficients are determined by applying boundary conditions—namely, dynamic, kinematic, and seabed conditions.

To further explore the seabed effect, a flat porous seabed is added to the physical problem, as it represents a realistic condition. This setup is first used to study wave scattering by a surface-piercing single circular cylinder. In this case, Sommerfeld radiation and boundary conditions are applied to calculate the velocity potentials in both the open-water region and the region covered by the structure. The incident and scattered wave potentials are expressed using the Fourier–Bessel series, and the eigenfunction expansion method is used to solve the resulting boundary value problem analytically. Once the unknown coefficients are evaluated, wave forces, flow distributions, and temporal simulations of fluid flow for various wave and structural characteristics are calculated.

The physical problem is then extended to multiple circular cylinders floating over a porous seabed. Graf's addition theorem is used to relate Bessel functions for scattered waves in the open-water region, simplifying the analysis. Again, the eigenfunction expansion method is applied to solve the problem analytically. Various cylinder arrangements, including array, triangular and rectangular configurations, are considered in the analysis. The results are validated against existing studies to ensure accuracy of the code.

The same framework is then adapted to study the impact of a porous seabed on multiple circular elastic plates floating on the water surface. Three types of edge conditions—clamped, moored, and free— on the plates are considered. Using the same analytical approach as in the case of multiple cylinders case, the velocity potentials are derived in

each region, and heave forces exerted on the plates are calculated for various wave and structural parameters.

In addition to the effect of a porous seabed, this thesis also studies the influence of ocean currents on wave scattering by structures. This includes surface-piercing single and dual docks, as well as compound inverse T-shaped breakwaters. To address these physical problems, analytical through the eigenfunction expansion method and numerical through the boundary element method are employed. The results are validated against existing studies in the absence of ocean currents to ensure accuracy of the code. Reflection and transmission coefficients are computed across a range of current velocities, wave conditions, and structural parameters, offering valuable insights into the influence of ocean currents on wave scattering and their effectiveness in mitigating wave energy in the leeside zone.

Overall, this thesis helps understand the behavior of strong waves when pounding to different structures, and provides an idea for reducing their impact.

LIST OF PUBLICATIONS

List of Published/Communicated Research Papers from the Thesis

Journal publications:

1. **Kushwaha, A.K.**, Behera, H. and Gupta, V.K., 2024. Wave scattering by a circular cylinder over a porous bed. *Archive of Applied Mechanics* (Springer), **94**, 555–570. DOI: 10.1007/s00419-023-02536-8
2. **Kushwaha, A.K.**, Behera, H. and Gupta, V.K., 2025. A temporal study of wave scattering by multiple circular cylinders over a porous bed. *Physics of Fluids* (American Institute of Physics), **37**, 037117. DOI: 10.1063/5.0258203
3. **Kushwaha, A.K.**, Gupta, V.K., Behera, H. and Hsu, T.W., 2024. Wave scattering by multiple floating flexible circular plates over a porous bed. *Ocean Engineering* (Elsevier), **314**, 119663. DOI: 10.1016/j.oceaneng.2024.119663
4. **Kushwaha, A.K.**, T. Gokulakrishnan and Behera, H., 2025. Impact of wave-current interaction on wave scattering by single and dual surface-piercing docks. *Engineering Analysis with Boundary Elements* (Elsevier), **179**, 106334. DOI: 10.1016/j.enganabound.2025.106334
5. **Kushwaha, A.K.**, Behera, H. and Gupta, V.K., 2025. Wave scattering by inverse T-type compound breakwater with ocean currents: An analytical and numerical study. (Under review)

List of Published/Communicated Research Papers apart from the Thesis

1. Naik, N., **Kushwaha, A.K.**, Behera, H. and Tsai, C.C., 2024. Wave energy extraction by an OWC device in the presence of a porous bottom. *Energy Reports* (Elsevier), 11, 5602-5618. DOI: 10.1016/j.egyr.2024.05.017
2. Singh, P., Maurya, P., Gupta, S. and **Kushwaha, A.K.**, 2025. Mean estimation in time-scaled surveys: A dual auxiliary information approach with applications to agricultural data. (Under review)

Publications in conference proceedings:

1. **Kushwaha, A.K.**, Behera, H. and Gupta, V.K., 2023. Wave scattering by a circular cylinder: A time-marching perspective. In the proceedings of *International Conference on Applied Mathematics and Mechanics (ICAMM 2023)* (Accepted).

TABLE OF CONTENTS

LIST OF FIGURES

LIST OF TABLES

Chapter 1

Introduction

1.1 Preamble

Waves are disturbances that travel through space and time, conveying energy without the transfer of matter. They are generally classified into two main types—mechanical waves such as sound and water waves and electromagnetic waves such as light. This thesis focuses solely on mechanical waves, specifically water waves, which are ubiquitous in nature and have significant engineering implications. Water waves occur at the interface between two fluids, such as air and water, and are primarily generated by gravity, wind, or seismic activity.

A common illustration of water waves is the ripples formed when a stone is dropped into a pond, spreading energy outward. In oceanic contexts, wave generation results from wind action, vessel movement, or water flowing over irregular seabeds. Although many such waves have small amplitudes, some—such as tsunamis, tidal waves, and rogue waves—carry vast amounts of energy, demonstrating their destructive power and their impact on coastlines. Understanding the generation, propagation, and impact of such waves is vital for coastal protection and the design of marine infrastructure. The study of wave-structure interaction is a cornerstone of fluid mechanics, playing a key role in the development of coastal protection solutions. Among these, breakwaters are the most widely used structures to dissipate wave energy, shield shorelines, ports, and infrastructure, providing safe zones for economic and recreational activities. Their relevance has amplified as coastal regions have become economic and population centers, now increasingly threatened by climate change, rising sea levels, and severe weather.

Breakwaters are commonly classified into three main types: floating, submerged (positioned between the seabed and the free surface), and bottom-mounted (fixed directly at the seabed). Each type is designed to meet specific environmental conditions and functional needs. A key aspect of breakwater design is a thorough understanding of wave-structure interactions—that is, the behavior of water waves when they encounter a structure. In such interactions, the incoming wave energy is partially reflected, partially transmitted, and partially absorbed by the structure. The distribution of energy among

these three components depends on several factors, including the geometry, size, material composition, and placement of the breakwater. A clear understanding of these energy transfer processes—reflection, transmission, and absorption—enables engineers to better predict wave behavior and enhance the effectiveness of breakwater designs. This supports the development of resilient and sustainable coastal defenses, ensuring long-term protection of infrastructure and ecosystems against threats like sea-level rise, storm surges, and coastal degradation.

This thesis builds on the concepts of wave-structure interaction, wave energy distribution (reflection and transmission), and the influence of structural geometry to investigate wave forces, flow distribution, and the velocity field around structures. To provide a realistic perspective on how waves approach and interact with these structures, temporal simulations of fluid flow are also presented. A deeper understanding of wave-induced forces, flow dynamics around structures, and energy redistribution is expected to support the design of effective breakwaters near the harbor area, which can significantly reduce wave energy and protect the shoreline. The next section delves into the foundation of water wave theory, exploring the evolution of early discoveries into a comprehensive understanding of wave dynamics.

1.2 Foundation of water wave theory

The exploration of water waves dates back several centuries, as comprehensively documented by Craik [34], who traced the development of water wave theory. Drawing inspiration from his insights, we provide a brief overview of this historical progression. The journey began in 1687 when *Sir Isaac Newton* accurately deduced that the frequency of deep-water waves is inversely proportional to the square root of their wavelength. He arrived at this conclusion by drawing an intriguing analogy with oscillations of water in a U-tube, as detailed in Book II, Proposition XLV of the *Principia Mathematica*. Newton's findings were later supported by researchers such as *Wilhelm-Jacobs Gravesande* in 1721 and *Charles Bossut* in 1786. Building on these early insights, during the period between 1757 and 1761, *Leonhard Euler* made a significant leap by formulating the fundamental equations of hydrodynamics, providing a mathematical framework to describe fluid motion. This development marked a key turning point in the theoretical study of waves. Shortly thereafter in 1776, *Pierre-Simon Laplace* attempted to develop a complete

description of wave motion. While his approach was unsuccessful for the general case, his solution accurately described small-amplitude plane waves propagating in channels of finite depth, thus refining our understanding of wave behavior. Around the same time, *Joseph-Louis Lagrange*, possibly working independently, advanced the theory further by deriving linearized equations for small-amplitude waves. He successfully obtained solutions for long plane waves in shallow water, publishing these results in 1781 and 1786. However, Lagrange mistakenly believed that these shallow-water approximations could equally apply to deep-water waves, reasoning that most of the wave motion occurs near the surface, an idea proven inaccurate later.

Before the 19th century, there were limited references to wave motion in literature. However, notable works by Flaugergues [49] and Coudraye [33] stood out, and their findings were later summarized by Weber [151]. In 1802, the field took a bold step forward as *Franz Joseph von Gerstner* gave the first exact nonlinear solution for waves of finite amplitude on deep water. The Gerstner wave solution was long overlooked; even today it is usually regarded more as a curiosity than a result of practical importance because the wave is not irrotational. Recognizing the importance of advancing wave theory, the *Académie des Sciences* in France launched a prize competition in late 1813 focused on the mathematical description of surface wave propagation in liquids of infinite depth. This competition attracted bright minds, including *Augustin-Louis Cauchy*, who was 25 years old when he submitted his research in July 1815. Almost simultaneously, one of the judges, *Simeon D. Poisson*, contributed his own independent work. Cauchy was awarded the prize in 1816, Poisson's memoir was published in 1818, and Cauchy's complete findings appeared in 1827, richly supplemented with extensive notes. The combined efforts of Cauchy and Poisson represent a significant milestone in the mathematical treatment of initial-value problems for waves. Notably, before tackling the full initial-value problem, Cauchy provided a concise and precise derivation of the frequency of linear sinusoidal standing waves in water of finite depth [113], greatly enhancing the theoretical foundation.

As the 19th century progressed, the fostering of hydrodynamics theory gained momentum at Cambridge, thanks to the encouragement of *Challis*, *Whewell*, and the eminent *William Hopkins*. Simultaneously, in 1837, the British Association established a "Committee on Waves" comprising distinguished members like *John Scott Russell* and *Sir John Robison*, to direct attention toward experimental observations and systematic

study of wave phenomena. Although *John Robison* passed away in 1843, marking the close of his contributions, Russell Subsequently took it upon himself to continue the work and wrote a brief supplementary report, which was published in 1842 [120]. Building on this foundation, Russell later published his seminal work, "Reports on Waves", in 1844 [121]. Russell's experiments are now well-known for discovering the nonlinear solitary wave. Subsequent years saw important contributions from notable figures such as *George Green*, *Philip Kelland*, *George Gabriel Stokes*, *George Biddell Airy*, and *Samuel Earnshaw*, who collectively pushed the boundaries of wave theory. In particular, *George Biddell Airy* made a significant contribution through his article 'Tides and Waves' published in the Encyclopaedia Metropolitana (1841). By that time, Airy was already well recognized for his expertise in mathematics and astronomy, and his work on wave motion marked a major advancement in the development of water wave theory.

In summary, the early development of water wave theory was shaped by the curiosity and ideas of many pioneering scientists. Their combined efforts established a strong foundation for understanding the complex behavior of water waves and encouraged continued research and innovation in this area. The following section provides a detailed literature review focusing on the interaction between waves and structures.

1.3 Wave-structure interaction: A historical survey

The study of wave-structure interaction has advanced considerably, aiming to enhance the protection of the leeside zone from intense wave activity. To achieve this, a wide range of breakwater types has been developed, each varying in shape and structural configuration. Breakwaters can be either floating or fixed, submerged or surface-piercing, rigid or flexible, and porous or solid. Some structures span the full depth from seabed to surface, while others cover only a portion of this range. Owing to this diversity, the literature review is systematically organized into distinct categories, as presented in the following subsections.

1.3.1 Wave interaction with rigid structure

This subsection examines wave interactions with rigid structures of representative geometries. Rather than attempting an exhaustive review of all possible shapes, it focuses on structural forms that have been widely studied and hold practical significance. For each configuration, a historical perspective is presented, tracing the evolution of research and

highlighting key milestones in the understanding of wave-structure interactions. A brief overview of the historical context and major findings for each category is presented.

Category I: Thin barrier

The first investigation of wave reflection on a water surface due to a thin, vertically submerged plane barrier was carried out in 1945 by a British applied mathematician and fluid dynamicist, William Reginald Dean [41]. His research involved calculating the reflection and transmission of waves in relation to the parameter $m = an^2/g$, where a represents the gap between the free-surface wave and the top endpoint of the barrier; n is the angular frequency and g is the gravitational acceleration. A key finding was that as m increases significantly, the amplitude of the disturbance diminishes rapidly with the depth. Consequently, when m approaches infinity, the reflection coefficient becomes zero, and the transmission coefficient becomes unity. Later, from the inspiration of Dean's work, Ursell [146] also studied the reflection of surface waves by a vertical barrier. His study revealed that as the barrier's edge approaches the surface, the wave motion near the top of the barrier loses its oscillatory nature. Instead, a rapid flow occurs over the barrier when a wave crest arrives. Following the framework established by Dean [41] and Ursell [146], Wiegel [152] also developed a theoretical model for the partial transmission and reflection of uniform long-crested water waves by thin vertical barriers. This work included the derivation of a mathematical formula to compute the transmission coefficient. Although vertical barriers are more effective at reflecting wave energy, inclined barriers were studied to address practical issues like high wave impact forces and construction challenges on uneven seabeds. To include such cases, Liu & Abbaspour [74] extended earlier models by considering both vertical and inclined barriers at arbitrary angles using the BEM. Their study revealed that, unlike vertical barriers, inclined barriers do not exhibit monotonicity in reflection coefficient. Later, Kriebel *et al.* [66] examined the wave load on a vertical wave barrier, a problem that had already been explored by previous researchers. In their study, they employed the EEM to determine the unknown coefficients in the velocity potentials, which were then used to compute the horizontal force acting on the barrier. Building on these foundational works, numerous researchers have explored wave transmission and wave scattering caused by a vertical thin barrier; see, e.g., Refs. [18, 43, 51, 75, 116] and references therein.

The above mentioned studies primarily focus on wave interactions with a single vertical thin rigid barrier. In contrast, employing dual or multiple barriers is significantly more effective in controlling wave transmission and scattering. Physically, when an incident wave strikes the first barrier, a portion of the wave energy is reflected, while the remaining part is transmitted through the barrier. The transmitted wave, now with reduced energy, subsequently interacts with the second barrier. At this stage, the wave undergoes additional reflection and transmission, with even less energy propagating beyond the second barrier. This sequential reduction in energy continues with each additional barrier, resulting in enhanced attenuation of wave energy. This phenomenon is attributed to the cumulative effects of reflection and energy dissipation across multiple barriers. Many researchers have extensively investigated wave interactions in the presence of dual or multiple rigid barriers; see, e.g., Refs. [52, 78, 83, 114, 119] and references therein.

Category II: Rectangular structure

In wave scattering problems, thin barriers are often vulnerable to failure under strong wave action due to their limited structural strength. High-energy waves can bend, displace, or eventually damage these barriers. In such situations, rectangular breakwaters offer a more robust alternative. Their greater mass and surface area provide enhanced resistance against wave forces, allowing them to withstand more severe conditions.

The study of wave propagation through different types of breakwaters, including bottom-standing/submerged, and surface-piercing structures, has been a focal point of research for many decades. A pioneering work based on rectangular structure was made by Jeffreys [57], who conducted a theoretical analysis of wave transmission over a bottom-standing rectangular barrier. Building on Jeffreys' theoretical framework, Johnson *et al.* [59] performed laboratory experiments to measure the transmission coefficient, which demonstrated strong agreement with Jeffreys' predictions. Their experimental findings further highlighted that, for a given barrier dimension and water depth, the transmission coefficient is higher—indicating reduced wave damping—for relatively flat waves compared to steeper waves. Later, Dick & Brebner [44] also conducted laboratory experiments to investigate the reflection and transmission of waves by a submerged rectangular rigid structure. During these experiments, it was observed that wave behavior was influenced by energy losses due to wave interaction with the breakwater. Furthermore, Mei & Black

[91] employed a numerical approach to study both wave reflection and transmission in the presence of bottom-standing and surface-piercing rectangular obstacles. Their theoretical findings were specifically validated against the experimental results of Dick & Brebner [44]. Since these early studies primarily focused on wave propagation under normal incidence, further research was needed to understand the impact of oblique incident wave angles on structures. To address this, Abul-Azm [2] conducted a detailed investigation of wave scattering by a bottom-mounted rectangular breakwater under oblique incident wave. This study employed an exact analytical method based on the eigenfunction expansion technique to evaluate the effectiveness of a wide, submerged, and impermeable breakwater in reflecting oblique waves. Additionally, two approximate solutions—the plane-wave approximation and the long-wave solution—were developed. These were shown to closely estimate the exact solution in deep and shallow water conditions, respectively. Later, Abul-Azm & Gesraha [3] further examined the problem by investigating wave interactions with surface-piercing rigid floating structures under oblique wave incidence, addressing both scattering and radiation phenomena. In their study, it was observed that as the angle of wave incidence increased, the wave forces exerted on the structures gradually decreased. However, there is a limitation in their work: they used the Laplace equation (instead of the modified Helmholtz equation) for radiated waves, leading to inconsistency in the governing equations. As a result, the wave forces on the structure could not be calculated correctly. Zheng *et al.* [173] resolved this issue by applying the modified Helmholtz equation to both scattering and radiation problems under oblique incident waves. Their study also examined the influence of incidence angle, structural draft, and width on hydrodynamic coefficients. Continuing from prior investigations on rectangular breakwaters, researchers have extensively explored a variety of rigid rectangular breakwater configurations—including submerged, surface-piercing, and floating types—for coastal protection and wave energy dissipation; see, e.g., Refs. [72, 88, 154, 172] and references therein. Furthermore, dual or multiple breakwaters are often more effective than a single rectangular breakwater in dissipating wave energy. Numerous studies have investigated the performance of dual or multiple rigid rectangular structures for wave attenuation; see, e.g., Refs. [45, 77, 89, 128, 140, 169].

Category III: Cylindrical/circular structure

While rectangular and thin-plate breakwaters have long been studied for their practical applications in coastal protection, increasing attention has been directed toward circular structures owing to both their geometric simplicity and hydrodynamic characteristics. Over the past few decades, forms such as cylindrical columns, circular disks, and plates have become prominent in the mathematical modeling of wave scattering. Their axisymmetric geometry also allows for more efficient implementation of analytical and numerical techniques. The work by Miles & Gilbert [99] is regarded as a pioneering theoretical study on gravity wave scattering by a circular dock, wherein, the authors employed a variational approximation method to calculate wave forces exerted on the dock. However, subsequent analysis by W. H. Munk revealed errors in their numerical computation of the horizontal force, particularly regarding incorrect asymptotic behavior for small wavenumbers. Beyond these computational issues, Garrett [50] identified a more fundamental flaw in their formulation—one that, although it did not affect the far-field approximation, significantly impacted the accuracy of the vertical force calculation. He also questioned the reliability of their near-field approximation method. To address these concerns, Garrett [50] revisited the problem and applied Galerkin's method for his numerical analysis, providing more accurate results for the horizontal force, vertical force, and torque exerted on the dock. Following the foundational work of Garrett [50], many subsequent studies have focused on wave interaction with right circular cylinders. These studies have significantly advanced both analytical and numerical approaches, contributing to a deeper understanding of wave-structure interactions; see, e.g., Refs. [16, 67, 115, 123, 165] and the references therein.

It is well established that using multiple structures as breakwaters is more effective in dissipating wave energy than relying on a single structure as discussed in Categories I and II. This understanding has led to extensive research on wave interactions with multiple cylindrical structures. Theoretical studies on this topic have predominantly focused on rigid right circular cylinders, which can be classified into two main subcategories: fully-extended cylinders that span from the seabed to the water surface; see, e.g., Refs. [27, 28, 73, 96, 117] and surface-piercing cylinders that are partially submerged; see, e.g., Refs. [105, 135, 157]. Although fully-extended cylinders provide a continuous barrier against wave forces, they are also more susceptible to structural damage due to

the direct and concentrated impact of pounding waves. This makes them vulnerable to fatigue and potential failure under extreme conditions. To mitigate these risks, surface-piercing cylinders have been explored as an alternative. These structures, being partially submerged, experience less concentrated wave impact, thereby reducing structural stress and extending durability. Additionally, they offer a cost-effective solution compared to fully-extended cylinders, making them a preferred choice for many coastal and offshore engineering applications. Consequently, significant research has been dedicated to understanding wave interactions with multiple surface-piercing circular cylinders; see, e.g., Refs. [105, 135, 157].

On the other hand, circular plates have gained increasing attention in recent decades due to their numerous applications in offshore oil platforms, floating bridges, military operations, floating runways, and other marine structures. To analyze the stresses and deformations in such thin plates under external forces, the foundational Kirchhoff–Love plate theory was introduced by Love [79] in 1888. Love later formalized and extended this theory in his 1892 treatise "*A Treatise on the Mathematical Theory of Elasticity*", in which he established a rigorous theoretical foundation for the analysis and modeling of thin elastic plates. This theoretical foundation was further provided by Timoshenko & Woinowsky Krieger [143] in their book "*Theory of plates and shells*". Leveraging these advancements, Dorfmann [47] applied the integral transform technique to study wave diffraction by a circular plate, aiming to extend the dual integral equation method to handle the problem of circular structure. Building on this, Zilman & Miloh [174] developed a hydroelastic model for a circular buoyant elastic plate with uniform stiffness floating in shallow water. Their work provided important insights into the use of such structures for large-scale applications, such as floating airports. Later, Pete *et al.* [111] extended the method of Zilman & Miloh [174] to the case where the water depth is finite. Following these studies, Pham *et al.* [112], Watanabe *et al.* [150] also investigated the hydroelastic responses of a very large floating circular structure, which is crucial in the construction of large offshore floating oil storage facilities. Over the past decade, circular plates have been widely studied through mathematical models, motivated by their importance in marine and offshore engineering; see, e.g., Refs. [93, 97, 98, 168].

Category IV: T-type structure

Among the various coastal protection systems, T-shaped structures have emerged as effective solutions for mitigating wave impact. A pioneering contribution to the study of T-shaped breakwaters was made by Neelamani & Rajendran [104], who conducted experimental investigations to evaluate the wave transmission, reflection, and energy dissipation characteristics of this type of breakwater. This study laid the groundwork for future theoretical and numerical analyses. In this context, Wang *et al.* [148] and Deng *et al.* [42] employed the eigenfunction expansion mehtod (EEM) within the framework of linear water wave theory to gain a deeper understanding of the wave attenuation characteristics of T-shaped breakwaters. Their analytical results demonstrated that increasing the vertical screen length significantly enhances the reduction of transmitted wave energy, particularly in the long-wave region. While T-shaped breakwaters have proven effective, inverse T-type breakwaters have gained wider application in recent years due to their enhanced structural efficiency and adaptability. As a result, numerous studies have been conducted using both numerical simulations and laboratory experiments to evaluate their hydrodynamic performance; see, e.g., Refs. [53, 87, 158, 161]. Building on this foundation, Sharma *et al.* [134] recently explored wave scattering by bottom-mounted dual inverse T-type breakwaters using Havelock's expansion and the Galerkin method. Their study highlighted the importance of structural geometry—specifically, the width of the head and tail—in influencing the breakwater's wave attenuation performance. Apart from the structures discussed in Categories (I–IV), several innovative breakwater designs also exist, such as pi-type, triangular-type, trapezoidal-type, and semi-circular-type, among others.

1.3.2 Wave interaction with porous structure

The previous subsection focused primarily on rigid structures but they do not offer the real-world functionality and environmental advantages as porous structures. Porous breakwaters are considered more effective in many cases because they allow partial wave transmission, which dissipates wave energy more efficiently. Additionally, their permeability enables water to pass through, reducing wave force while minimizing reflection. From an ecological perspective, porous structures are less disruptive, as they allow the free movement of marine organisms such as fish and aquatic plants. This helps preserve natural habitats and supports biodiversity. In contrast, rigid breakwaters fully obstruct both

water flow and marine life, potentially causing ecological disturbances. Owing to their combined benefits in wave attenuation and environmental compatibility, porous structures are often preferred for sustainable coastal protection.

The study of wave reflection and transmission by porous structures began with the experimental work of Iwasaki & Numata [56], which provided early insights into wave behavior around such barriers. Building on this, Sollitt & Cross [137] developed a theoretical model aimed at practical use, especially for predicting the height of reflected and transmitted waves. Their approach was one of the first to analyze wave motion through a permeable breakwater with a rectangular cross-section. Following this foundational work, Madsen [81] and Massel & Mei [90] investigated the performance of porous structures as breakwaters for coastal protection. While the early work by Sollitt & Cross [137] was limited to simple rectangular geometries—restricting its applicability to more complex structural configurations—this limitation was later addressed by Sulisz [138], who investigated wave interactions with permeable breakwaters featuring a variety of cross-sectional shapes. Their analysis showed that porous structures significantly reduce the energy reaching the leeside zone, demonstrating their effectiveness in dissipating wave energy. However, Sulisz's study focused only on normal incident wave propagation to the porous structure, which limited whose scope. To extend this analysis, Dalrymple *et al.* [35] investigated wave interaction with porous structures under oblique wave incidence. Their study revealed that when the angle of wave approach exceeds 80°, the reflection coefficient increases sharply to nearly 1, indicating that most of the wave energy is reflected at such high angles. Further advancing this research, Isaacson *et al.* [55] adopted the same physical problem proposed by Dalrymple *et al.* [35] but introduced an impermeable wall behind the permeable structure to analyze its impact on wave reflection. Their study found that as the porosity parameter increases, the reflection coefficient also increases, highlighting the influence of structural porosity on wave reflection characteristics. In Ref. [55], they examined porous breakwaters that extended from the seabed to the free surface, analyzing their effect on wave reflection. Chen *et al.* [26] further extended the work of Isaacson *et al.* [55] by considering a vertical impermeable wall placed in front of a bottom-mounted rectangular porous breakwater. Their results showed that increasing the width of the porous section led to reduced wave reflection.

Building on earlier studies that focused mainly on bottom-mounted porous structures under normal or oblique wave incidence, more recent research has explored alternative designs that offer additional functional benefits. One such design is the surface-piercing porous structure, which provides several advantages over bottom-mounted configurations. A key benefit of these structures is their ability to respond dynamically to wave motion. Unlike fixed bottom-mounted structures, surface-piercing porous structures can move with incoming waves and naturally return to their original position. This flexibility improves their overall stability and enhances wave energy dissipation. In this context, Liu & Li [76] examined wave reflection by a surface-piercing porous rectangular structure and evaluated the reflection and transmission coefficients using both analytical and numerical techniques. Later, this work was extended by Behera *et al.* [12] to include a two-layer fluid system. Their study also applied both analytical and numerical methods, with the numerical approach offering an advantage by avoiding the need to solve the complex dispersion relation that arises within the porous region in a two-layer system. Recently, Barman *et al.* [8] investigated wave interaction in a two-layer fluid in the presence of a floating rectangular porous breakwater placed in front of a very large floating structure. Later, Kaligatla *et al.* [62] also analyzed the combined effect of a two-layer fluid system and a wavy seabed on the performance of a surface-piercing rectangular porous structure. In addition to rectangular porous structures, various other geometries have been studied to enhance performance under different marine conditions. These include thin porous barriers [13, 22, 24, 70, 103, 155, 162], circular porous cylinders [68, 80, 108, 133, 136, 153], porous plates [15, 70, 94, 101], and porous trapezoidal breakwaters [30, 58, 64, 147]. These diverse configurations reflect the growing interest in optimizing porous structures for improved wave attenuation and environmental compatibility across a range of marine engineering applications.

1.3.3 Wave-structure interaction over a porous seabed

It is worthwhile mentioning that the bottom bed of the sea/ocean, in all the references mentioned above, has been considered as rigid. However, in reality, the physical characteristics of the seabed are quite different. The seabed is not a flat, rigid, immovable surface; instead, it is porous, sloping and slippery. There have been laboratory experiments with porous bed to study the effect of the porosity of the bed on wave damping;

see, e.g., [32]. Torres Freyermuth *et al.* [145] utilized the laboratory data obtained by Corvaro *et al.* [32] to develop a numerical model aimed at predicting wave attenuation and the velocity field near a porous bed under various regular wave conditions. Nevertheless, in theoretical studies, owing to the unavailability of boundary condition at a porous bottom, it was customary to assume the seabed as a rigid surface until Martha *et al.* [86] proposed a boundary condition for the porous seabed and utilized it to study the problem of an oblique wave scattering by an undulated porous bed (in the absence of any structure). To the best of the author's knowledge, the seabed—for wave-structure interaction problems—was taken as porous for the first time by Maiti & Mandal [82]. In this work, Maiti & Mandal [82] used the boundary condition for the porous bottom proposed by Martha *et al.* [86] and computed the scattering coefficients in the problem of wave scattering by a floating elastic plate over a porous seabed by exploiting the EEM. Their study revealed that the reflection coefficient increases as the porosity parameter increases, which shows that the porosity of the seabed is an important factor to be considered in mitigating the wave energy. Since the work by Maiti & Mandal [82] was limited to a homogeneous (single-layer) fluid, Behera *et al.* [14] extended their study to a more realistic two-layer fluid system. Their findings revealed that wave transmission decreases significantly with an increase in the length of the floating plate, primarily due to enhanced energy dissipation caused by the porous seabed. After these works, several researchers extended the study of wave interaction over a porous seabed by investigating a wide range of structural configurations; see, e.g., Refs. [9, 21, 25, 63, 130].

1.3.4 Wave-structure interaction in the presence of ocean currents

Besides using different types of breakwater structures and considering seabed characteristics, ocean currents also act like a natural breakwater by helping to reduce wave impact in the leeside zone. Ocean currents are continuous movements of seawater that flow through the oceans. These currents can move at the surface or deep below and may travel short distances along the coast or stretch across entire ocean. ocean currents are caused by several natural forces, including wind, gravity, tides, variations in water temperature and salt content.

The idea of using ocean currents as natural wave barriers was first introduced by Taylor [141], who showed that outward-flowing surface currents can reduce the impact

of incoming waves. This early study laid the foundation for understanding interactions between waves and currents. Building on this, Peregrine [110] proposed a classification system for wave–current interactions, including effects caused by large-scale currents and turbulence. This framework helped researchers analyze many important coastal and oceanic phenomena, such as wave behavior near shores. Further progress was made by Jonsson & Wang [61], who studied wave propagation over sloping seabed in the presence of ocean currents. Later, Jonsson [60] consolidated decades of research in his seminal book "*Wave-Current Interactions*", systematically exploring the mutual influence between waves and currents, including mechanisms of energy transfer. Further advancements came from Ardhuin & Magne [7], who investigated surface gravity wave-current interactions over variable bottom topography, refining predictions of wave scattering and energy redistribution in shelf seas to improve modeling accuracy for coastal engineering and climate studies. Motivated by these foundational studies, a wide range of physical problems has been investigated in the presence of ocean currents, incorporating diverse structural configurations and environmental conditions to evaluate their effectiveness in attenuating wave energy; see, e.g., Refs. [36, 39, 100, 102, 126, 149].

1.3.5 Time-domain analysis of wave scattering problems

In recent years, there has been a growing interest in studying wave behaviour using the time-domain technique, which allows for a more comprehensive understanding of wave dynamics as wave-structure interactions evolve over time. The time-domain approach enables researchers to visualize fluid motion in wave-structure interactions more effectively, offering detailed insights into transient phenomena that are often difficult to capture using traditional steady-state or frequency-domain methods. The time-domain approach to wave scattering problems involves analyzing how waves interact with objects or obstacles during their propagation, emphasizing the time-dependent behavior of phenomena such as reflection, transmission, and wave dissipation. The paper by Meylan & Sturova [95] can be regarded as the pioneering work that introduced time-dependent simulations of wave interactions with floating elastic plates in two dimensions. Building upon this foundational work, Das *et al.* [38] conducted time-marching simulations to investigate wave motion with a positive phase velocity. These simulations provided a detailed visualization of the wave propagation. Subsequently, the study presented in [38] was further extended

by Das *et al.* [37], who explored time-marching simulations of wave motion in the presence of a shear current. For many years, time-marching simulations remained confined to two dimensions. This changed in 2019 when Meylan [92] introduced the concept of time-marching simulations in three dimensions. Their work demonstrated the interaction of waves with elastic circular plates, revealing how the waves decay after interacting with the plates. Furthermore, the three-dimensional simulations introduced by Meylan [92] provided a more realistic representation of wave behavior compared to the two-dimensional case. Later, following [92], several studies; see, e.g., Refs. [19, 125, 133], investigated various wave-structure interaction problems using the time-marching approach. These works collectively contributed to a deeper understanding of fluid dynamics by offering clear and detailed visualizations of fluid motion in various complex scenarios.

1.4 Motivation of the thesis

As discussed earlier, previous studies were restricted by the assumption of a rigid seabed, which limited the realistic representation of wave behaviour in marine environments. Alongside these considerations, the time-domain approach proposed by Meylan [92] emphasized the importance of temporal analysis in capturing the dynamic evolution of wave-induced motions, offering valuable insights into transient flow behaviour. However, the combined consideration of porous seabed effects and time-domain simulations of fluid motion has remained largely unexplored, leaving a gap in understanding wave scattering phenomena. Furthermore, the literature survey indicates that ocean currents play a crucial role in modifying wave propagation characteristics and can effectively dissipate wave energy towards the leeside region.

Motivated by these observations, this thesis aims to develop a more realistic and comprehensive understanding of wave scattering by incorporating porous seabed condition, employing time-domain analysis to visualize temporal behaviour, and examining the influence of ocean currents on wave dynamics.

1.5 Outline of the thesis

This thesis is structured into Eight chapters. Chapter 1 serves as a comprehensive introduction, while Chapter 2 provides an overview of the fundamental concepts and lays the

foundation for the subsequent chapters. Chapters 3–7 present the core methodologies, analyses, and findings of the research, with each chapter contributing through theoretical formulations and practical applications. Finally, Chapter 8 presents the conclusions and outlook. The rest of the thesis is organized as follows.

Chapter 2 introduces the fundamentals of water wave theory, along with the governing equation and boundary conditions, and outlines the mathematical approaches employed throughout the thesis.

Chapter 3 investigates wave scattering by a circular cylinder placed over a porous seabed. The associated BVP is solved using the EEM. The chapter explores the influence of seabed porosity on the horizontal and vertical forces exerted on the cylinder, as well as the resulting flow distribution and surface elevation. Time-domain simulations are presented to provide a dynamic view of wave-structure interactions.

Chapter 4 extends the study to multiple circular cylinders arranged over a flat porous seabed. The solution is developed using the EEM combined with Graf's addition theorem. The chapter computes the horizontal force exerted on the cylinders configured in an arrays of two, three, and four cylinders. Temporal simulations of fluid flow are also presented for various cylinder arrangements, including arrays of two, three, and four cylinders, as well as triangular and square configurations.

Chapter 5 presents the wave interaction with floating flexible circular plates positioned over a porous seabed. The EEM and Graf's addition theorem are employed to solve the problem with three types of edge conditions, namely, free, clamped, and moored-edge conditions. The heave force exerted on the plates are computed under various wave and structural parameters. Time-domain simulations of fluid flow are also shown for different plate configurations.

Chapter 6 analyzes wave–current interaction with single and double surface-piercing rectangular docks. Both analytical and numerical solutions are determined using the EEM and BEM, respectively. Reflection and transmission coefficients, as well as their surface plots, are discussed for different structural configurations. The chapter also presents the horizontal forces acting on the front and rear faces of the docks.

Chapter 7 provides a detailed study of wave–current interaction with compound inverse T-type breakwaters composed of rigid and porous components. The boundary value problem is formulated using both the EEM and BEM, and the results are compared to

evaluate the robustness and accuracy of each method. Reflection and transmission coefficients are computed for different values of structural and porosity parameters.

Chapter 8 concludes the thesis by summarizing the key outcomes and highlighting the main contributions. It also outlines potential directions for future research in the area of wave–structure interaction.

Chapter 2

Water wave theory: A recap

In this chapter, we present the fundamentals of water wave theory, including the governing equation, relevant boundary conditions, and the methodologies employed to address the physical problems explored in this thesis.

2.1 Fundamentals of water wave theory

This section introduces the fundamental definitions and concepts related to water waves, assuming a periodic wave profile to describe the regular and repeating motion of the free surface. Such periodic waves are commonly observed in marine environments and provide a useful basis for understanding wave behavior. To further illustrate these concepts, Fig. 2.1 presents a schematic representation of the free surface and its associated features, which are critical in wave dynamics. In the figure, the free-surface is depicted as the wavy line that dynamically fluctuates due to wave motion. This surface represents the actual interface between the water and the air above, where the wave's crests and troughs are observed. The crests are the highest points of the wave, while the troughs are the lowest. These features are integral in defining wave characteristics such as wave height (H)—the vertical distance between a crest and a trough—and wavelength (λ)—the horizontal

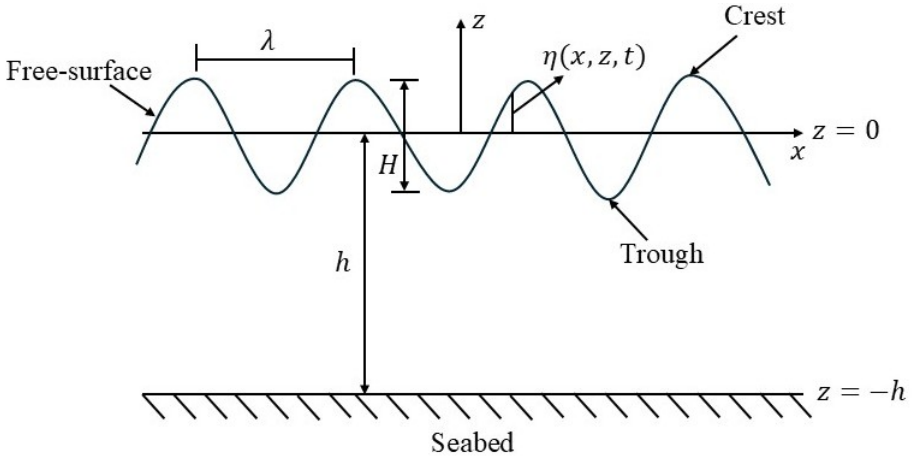

Figure 2.1: Illustration of the free-surface and associated wave characteristics.

distance between two successive crests or troughs. The mean free surface (at $z = 0$) represents the equilibrium position of the water surface in the absence of wave disturbances. This hypothetical surface is used as a reference to measure the displacement of the free surface at any point in space (x, z) and time t, denoted by $\eta(x, z, t)$. The commonly used notations related to water waves are as follows: wave amplitude $A = H/2$, wavenumber $k = 2\pi/\lambda$, wave period T and angular frequency $\omega = 2\pi/T$. The seabed is also marked at the bottom of the figure, with a water depth h measured from the mean free surface. Waves are classified based on the relation between the wavelength and water depth into three categories: shallow water waves (where the wavelength is much greater than the water depth), deep water waves (where the wavelength is much less than the water depth), and intermediate waves that do not fit neatly into either category. When the amplitude of water wave is small compared to its wavelength, it is analyzed using linear water wave theory. Despite the fact that ocean waves are typically nonlinear, linear theory provides accurate results for most engineering applications. Thus, this thesis uses linearized water wave theory for the analysis of water waves.

2.2 Relevant equations and pertaining boundary conditions

In this section, we provide a detailed discussion on the equations of motion governing the fluid domain. Utilizing the principles of linearized water wave theory, we systematically derive various boundary conditions that are essential for describing the behavior of water waves.

2.2.1 Governing equation

In this thesis, the fluid is assumed to be incompressible and inviscid, and the flow is considered irrotational. Additionally, it is assumed that the effect of surface tension on the free surface is negligible. Owing to irrotational nature, a velocity potential $\Phi(x, y, z, t)$ exists within the fluid domain, where x, y, z represent the spatial coordinates and t denotes the time. The fluid velocity at any point in the domain is denoted by $\boldsymbol{q} = \begin{bmatrix} u & v & w \end{bmatrix}^{\mathsf{T}}$, and it can be expressed as

$$\boldsymbol{q} = \boldsymbol{\nabla}\Phi, \tag{2.1}$$

where T denotes the transpose of the matrix. Since the fluid is incompressible, the continuity equation yields

$$\boldsymbol{\nabla} \cdot \boldsymbol{q} = 0. \tag{2.2}$$

By combining Eqs. (2.1) and (2.2), the resulting equation, known as the Laplace equation, is obtained. This equation serves as the governing equation within the fluid domain and is expressed as

$$\nabla^2 \Phi = 0 \quad \text{or} \quad \frac{\partial^2 \Phi}{\partial x^2} + \frac{\partial^2 \Phi}{\partial y^2} + \frac{\partial^2 \Phi}{\partial z^2} = 0. \tag{2.3}$$

By substituting $x = r\cos\theta$, $y = r\sin\theta$ and $z = z$ into the Eq. (2.3), the equation is transformed into the cylindrical coordinate system (r, θ, z), and reads

$$\frac{\partial^2 \Phi}{\partial r^2} + \frac{1}{r}\frac{\partial \Phi}{\partial r} + \frac{1}{r^2}\frac{\partial^2 \Phi}{\partial \theta^2} + \frac{\partial^2 \Phi}{\partial z^2} = 0. \tag{2.4}$$

2.2.2 Derivation of the Bernoulli equation in terms of the velocity potential

To describe the motion of a fluid, it is necessary to apply fundamental principles of mechanics—specifically, the conservation of mass and momentum. These principles are mathematically formulated through the *Navier-Stokes equations*, which govern the behavior of viscous and compressible flows. For inviscid and incompressible fluids, the *Navier–Stokes equations* simplify to the *Euler equations*. The corresponding momentum equation in the vector form is given by

$$\frac{\partial \boldsymbol{q}}{\partial t} + (\boldsymbol{q} \cdot \boldsymbol{\nabla})\boldsymbol{q} = \boldsymbol{g} - \frac{1}{\rho}\boldsymbol{\nabla} p, \tag{2.5}$$

where p is the pressure, and ρ the fluid density. If gravity acts in the z-direction, it can be expressed as

$$\boldsymbol{g} = g\hat{k} = \boldsymbol{\nabla}(gz). \tag{2.6}$$

Substituting Eqs. (2.1) and (2.6) into Eq. (2.5) leads to the Euler equation, which is:

$$\boldsymbol{\nabla}\left(\frac{\partial \Phi}{\partial t} + \frac{1}{2}\boldsymbol{\nabla}\Phi \cdot \boldsymbol{\nabla}\Phi - gz + \frac{p}{\rho}\right) = 0. \tag{2.7}$$

Since the gradient of a scalar field vanishes only when the field is constant in space, the quantity inside the parentheses must be independent of spatial coordinates. Therefore,

Eq. (2.7) can be rewritten as

$$\frac{\partial \Phi}{\partial t} + \frac{1}{2}\boldsymbol{\nabla}\Phi \cdot \boldsymbol{\nabla}\Phi - gz + \frac{p}{\rho} = \mathscr{C}(t), \tag{2.8}$$

for some function $\mathscr{C}(t)$. However, for simplicity, we take $\mathscr{C}(t) = 0$ by using the transformation [129]

$$\Phi = \Phi + \int_0^t \mathscr{C}(l)dl,$$

which does not affect the velocity field. Thus, we get the Bernoulli equation which is given by

$$\frac{\partial \Phi}{\partial t} + \frac{1}{2}\boldsymbol{\nabla}\Phi \cdot \boldsymbol{\nabla}\Phi - gz + \frac{p}{\rho} = 0. \tag{2.9}$$

As per the linearized water wave theory, the second-order velocity components can be disregarded to derive the linearized form of the Bernoulli equation, which is given as:

$$\frac{\partial \Phi}{\partial t} - gz + \frac{p}{\rho} = 0. \tag{2.10}$$

2.2.3 Kinematic boundary condition

The kinematic boundary condition states that the surface separating two fluids (such as air and water) or a fluid and a solid (water and a solid wall) moves with the fluid itself, ensuring that there is no gap between the fluid and the boundary. Mathematically, if $\mathscr{F}(x, y, z, t) = 0$ represents the surface that comprises of fixed or moving boundary, the kinematic boundary condition requires that [40]

$$\frac{D\mathscr{F}}{Dt} = 0, \tag{2.11}$$

where $\frac{D}{Dt} \equiv \frac{\partial}{\partial t} + u\frac{\partial}{\partial x} + v\frac{\partial}{\partial y} + w\frac{\partial}{\partial z}$ is the total (material) derivative, and ensures that fluid particles on the surface remain on the surface over time. Consequently, the total derivative of $\mathscr{F} = z - \eta(x, y, t)$, is equal to zero. Therefore, we get

$$-\frac{\partial \eta}{\partial t} - u\frac{\partial \eta}{\partial x} - v\frac{\partial \eta}{\partial y} + w = 0. \tag{2.12}$$

Since $\boldsymbol{q} = \begin{bmatrix} u & v & w \end{bmatrix}^{\mathsf{T}}$ is velocity vector that satisfies Eq. (2.1) which gives

$$u = \frac{\partial \phi}{\partial x}, \quad v = \frac{\partial \phi}{\partial y} \quad \text{and} \quad w = \frac{\partial \phi}{\partial z}. \tag{2.13}$$

Substituting Eq. (2.13) into Eq. (2.12), then we get

$$-\frac{\partial \eta}{\partial t} - \frac{\partial \Phi}{\partial x}\frac{\partial \eta}{\partial x} - \frac{\partial \Phi}{\partial y}\frac{\partial \eta}{\partial y} + \frac{\partial \Phi}{\partial z} = 0. \tag{2.14}$$

We define $L(x, y, z, t) = -\frac{\partial \eta}{\partial t} - \frac{\partial \Phi}{\partial x}\frac{\partial \eta}{\partial x} - \frac{\partial \Phi}{\partial y}\frac{\partial \eta}{\partial y} + \frac{\partial \Phi}{\partial z}$. We have $L(x, y, \eta, t) = 0$ and the Taylor series expansion of L around $z = 0$ evaluated at $z = \eta$, is given by

$$\begin{aligned}
L(x, y, \eta, t) &= L(x, y, 0, t) + (\eta - 0)\frac{\partial L}{\partial z}\bigg|_{z=0} + \frac{(\eta - 0)^2}{2}\frac{\partial^2 L}{\partial z^2}\bigg|_{z=0} + \ldots, \\
0 &= L(x, y, 0, t) + \eta\frac{\partial L}{\partial z}\bigg|_{z=0} + \frac{\eta^2}{2}\frac{\partial^2 L}{\partial z^2}\bigg|_{z=0} + \ldots, \\
0 &= \left(-\frac{\partial \eta}{\partial t} - \frac{\partial \Phi}{\partial x}\frac{\partial \eta}{\partial x} - \frac{\partial \Phi}{\partial y}\frac{\partial \eta}{\partial y} + \frac{\partial \Phi}{\partial z}\right)\bigg|_{z=0} \\
&\quad + \eta\frac{\partial}{\partial z}\left(-\frac{\partial \eta}{\partial t} - \frac{\partial \Phi}{\partial x}\frac{\partial \eta}{\partial x} - \frac{\partial \Phi}{\partial y}\frac{\partial \eta}{\partial y} + \frac{\partial \Phi}{\partial z}\right)\bigg|_{z=0} + \ldots.
\end{aligned} \tag{2.15}$$

The elevation η, its derivatives and the velocity components, are considered small quantities under the assumptions of linear water wave theory. Under these assumptions, Eq. (2.15) simplifies to yield the linearized kinematic boundary condition, which reads

$$\frac{\partial \Phi}{\partial z} = \frac{\partial \eta}{\partial t} \quad \text{at} \quad z = 0. \tag{2.16}$$

2.2.4 Dynamic boundary condition

The dynamic boundary condition on the free surface $z = \eta$ as in Fig. 2.2 represents the physical requirement that pressure must be continuous across the interface between water and air. To make the problem simpler, we consider the pressure at the free surface of water equaling the atmospheric pressure, which is constant and it can be conveniently set to zero [40]. From the linearized Bernoulli equation (2.10) applied at the free surface, the dynamic boundary condition can be written as

$$\frac{\partial \Phi}{\partial t} - g\eta = 0 \quad \text{at} \quad z = \eta(x, y, t). \tag{2.17}$$

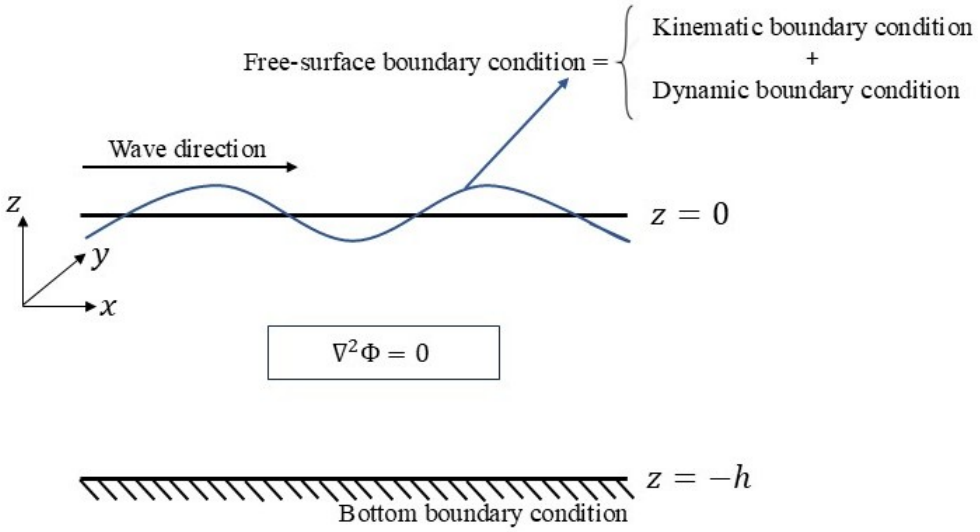

Figure 2.2: Schematic depiction of the fluid domain with governing equation and boundary conditions.

We define $\mathcal{L}(x, y, z, t) = \frac{\partial \Phi}{\partial t} - g\eta$. Now, the Taylor series expansion of $\mathcal{L}$ around $z = 0$ evaluated at $z = \eta$, is given as

$$\mathcal{L}(x, y, \eta, t) = \mathcal{L}(x, y, 0, t) + (\eta - 0)\frac{\partial \mathcal{L}}{\partial z}\bigg|_{z=0} + \frac{(\eta - 0)^2}{2}\frac{\partial^2 \mathcal{L}}{\partial z^2}\bigg|_{z=0} + \dots . \tag{2.18}$$

Since $\mathcal{L}(x, y, \eta, t) = 0$ at $z = \eta$, we get

$$0 = \left[\frac{\partial \Phi}{\partial t} - g\eta\right]_{z=0} + \eta\frac{\partial}{\partial z}\left[\frac{\partial \Phi}{\partial t} - g\eta\right]_{z=0} + \dots . \tag{2.19}$$

Since $\partial\eta/\partial z = 0$ (η does not depend on z), we have

$$0 = \left[\frac{\partial \Phi}{\partial t} - g\eta\right]_{z=0} + \eta\frac{\partial^2 \Phi}{\partial z \partial t}\bigg|_{z=0} + \frac{\eta^2}{2}\frac{\partial^3 \Phi}{\partial z^2 \partial t}\bigg|_{z=0} + \dots \tag{2.20}$$

In the framework of linearized water wave theory, Eq. (2.20) is simplified by discarding the nonlinear terms—such as those involving products of velocity components or surface elevation—which leads to the linearized dynamic boundary condition, which reads

$$\frac{\partial \Phi}{\partial t} = g\eta \quad \text{at} \quad z = 0. \tag{2.21}$$

2.2.5 Free-surface boundary condition

Taking the partial derivative with respect to time of the dynamic boundary condition (2.21), we obtain

$$\frac{\partial^2 \Phi}{\partial t^2} = g\frac{\partial \eta}{\partial t} \quad \text{at} \quad z = 0. \tag{2.22}$$

Using the kinematic boundary condition (2.16), the above equation becomes

$$\frac{\partial^2 \Phi}{\partial t^2} - g\frac{\partial \Phi}{\partial z} = 0 \quad \text{at} \quad z = 0. \tag{2.23}$$

Equation (2.23) is referred to as the free-surface boundary condition, which is derived by combining the dynamic and kinematic boundary conditions at $z = 0$.

2.2.6 Bottom boundary condition

In numerous studies, researchers have modeled the seabed of oceans and seas with various characteristics, such as rigid, undulating, or porous surfaces, depending on the specific problem being addressed. In this thesis, we focus on two specific types of seabeds: rigid and porous. Accurately incorporating these seabed types into the analysis of water wave phenomena necessitates the formulation of suitable bottom boundary conditions. To address this, we derive and present the bottom boundary conditions for both rigid and porous seabeds below.

Case 1: Rigid bed

Mathematically, if the seabed is at $z = -h$, the surface is described by $\mathcal{Q} = z + h(x, y, t) = 0$. The no-penetration condition at the seabed requires the material derivative of $\mathcal{Q}$ to be zero, satisfying Eq. (2.11) which is given by

$$\frac{\partial h}{\partial t} + u\frac{\partial h}{\partial x} + v\frac{\partial h}{\partial y} + w = 0. \tag{2.24}$$

For a flat and static rigid seabed, $h(x, y, t)$ is constant and satisfies $\frac{\partial h}{\partial t} = 0$, $\frac{\partial h}{\partial x} = 0$ and $\frac{\partial h}{\partial y} = 0$, and hence Eq. (2.24) reduces to

$$w = 0 \quad \text{at} \quad z = -h. \tag{2.25}$$

In terms of the velocity potential Φ, where $w = \frac{\partial \Phi}{\partial z}$, the bottom bed condition for rigid bed becomes:

$$\frac{\partial \Phi}{\partial z} = 0 \quad \text{at} \quad z = -h. \tag{2.26}$$

Case 2: Porous bed

The porous seabed is modeled as a homogeneous medium with uniform porosity, wherein fluid motion follows simple harmonic motion. The velocity potential $\Phi(x,y,z,t)$, the dynamic pressure $P(x,y,z,t)$ and normal velocity $W(x,y,z,t)$ within the porous layer are expressed as [11]

$$\begin{aligned}
&\Phi(x,y,z,t) = \mathrm{Re}\left\{\phi(x,y,z)e^{-\mathrm{i}\omega t}\right\}, \quad P(x,y,z,t) = \mathrm{Re}\left\{p(x,y,z)e^{-\mathrm{i}\omega t}\right\}, \\
&W(x,y,z,t) = \mathrm{Re}\left\{w(x,y,z)e^{-\mathrm{i}\omega t}\right\},
\end{aligned} \tag{2.27}$$

where ω is the angular frequency and $\phi(x,y,z)$, $p(x,y,z)$ and $w(x,y,z)$ represent time-independent the spatial velocity potential, dynamic pressure and normal fluid velocity, respectively.

From the linearized Bernoulli equation (2.10), the dynamic pressure relates to the velocity potential $\Phi(x,y,z,t)$ as

$$P(x,y,z,t) = -\rho\frac{\partial\Phi(x,y,z,t)}{\partial t}. \tag{2.28}$$

Let us denote the dynamic pressure on the positive side (fluid-side) of the porous layer by p^+ and that on the negative side (opposite side) of the porous layer by p^-. The dynamic pressures p^+ and p^- on the porous layer at $z=-h$ are related via [31]

$$P^+(x,y,z) = -P^-(x,y,z) = P(x,y,z) \quad \text{at} \quad z=-h. \tag{2.29}$$

The normal velocity w through the porous layer is proportional to the pressure gradient [142], i.e.

$$w(x,y,z) = \frac{\mathcal{C}}{\mu}\left[P^+(x,y,z) - P^-(x,y,z)\right] \quad \text{at} \quad z=-h, \tag{2.30}$$

where μ is the dynamic viscosity and $\mathcal{C}$ is the coefficient having the dimension of length. Substituting Eq. (2.29) into Eq. (2.30), we get

$$w(x,y,z) = \frac{2\mathcal{C}}{\mu}P(x,y,z) \quad \text{at} \quad z=-h. \tag{2.31}$$

From Eq. (2.28), substituting the value of $P(x,y,z)$ into the Eq. (2.31), we obtain

$$w(x,y,z) = \frac{2\mathcal{C}\rho}{\mu}\frac{\partial\Phi}{\partial t} \quad \text{at} \quad z=-h, \tag{2.32}$$

which further gives

$$w(x,y,z) = -G\,\phi(x,y,z) \quad \text{at} \quad z=-h, \tag{2.33}$$

where $G = 2\mathrm{i}\rho\omega\mathcal{C}/\mu$ is the porous effect parameter having the dimension of (1/length). Inside the porous layer, the normal velocity satisfies

$$\frac{\partial\phi}{\partial z} = w(x,y,z). \tag{2.34}$$

Thus, from Eqs. (2.33) and (2.34), the boundary condition at a porous seabed becomes

$$\frac{\partial\phi}{\partial z} + G\phi = 0 \quad \text{at} \quad z=-h. \tag{2.35}$$

Equation (2.35) represents the boundary condition at a porous seabed. In the special case where $G = 0$, this condition simplifies to boundary condition (2.26) for a rigid seabed.

2.3 Boundary value problem

Throughout this thesis, the primary governing equation is the Laplace equation, which is coupled with specific boundary conditions outlined in the preceding subsection 2.2. To derive the boundary value problem (BVP) incorporating the rigid bed condition, it is essential to consider the physical and mathematical constraints imposed by the system. By doing so, a BVP can be formulated and expressed in the cylindrical coordinate as follows

$$\frac{\partial^2\Phi}{\partial r^2} + \frac{1}{r}\frac{\partial\Phi}{\partial r} + \frac{1}{r^2}\frac{\partial^2\Phi}{\partial\theta^2} + \frac{\partial^2\Phi}{\partial z^2} = 0 \quad \text{in the whole fluid domain,} \tag{2.36}$$

$$\frac{\partial^2\Phi}{\partial t^2} - g\frac{\partial\Phi}{\partial z} = 0 \quad \text{at} \quad z=0, \tag{2.37}$$

$$\frac{\partial\Phi}{\partial z} = 0 \quad \text{at} \quad z=-h. \tag{2.38}$$

Since the equation of motion exhibits simple harmonic behavior in time with the angular frequency ω, the velocity potential can be written as

$$\Phi(r,\theta,z,t) = \mathrm{Re}\left\{\phi(r,\theta,z)e^{-\mathrm{i}\omega t}\right\}. \tag{2.39}$$

Substituting Eq. (2.39) into the BVP defined by Eqs. (2.36)–(2.38), the resulting BVP can be formulated as:

$$\frac{\partial^2\phi}{\partial r^2} + \frac{1}{r}\frac{\partial\phi}{\partial r} + \frac{1}{r^2}\frac{\partial^2\phi}{\partial\theta^2} + \frac{\partial^2\phi}{\partial z^2} = 0 \quad \text{in the whole fluid domain,} \tag{2.40}$$

$$\frac{\partial \Phi}{\partial z} - \frac{\omega^2}{g}\phi = 0 \quad \text{at} \quad z = 0, \tag{2.41}$$

$$\frac{\partial \phi}{\partial z} = 0 \quad \text{at} \quad z = -h. \tag{2.42}$$

This BVP can be solved using the method of separation of variables, leading to an explicit form of the velocity potential that involves a set of unknown coefficients [129]. These coefficients arise due to the general solution of the Laplace equation in cylindrical coordinates and the expansion over vertical, radial, and angular modes. To determine these unknown coefficients, the methodologies employed and discussed in the subsequent subsection.

2.4 Solution techniques

Fluid-structure interaction problems pose significant challenges, largely due to the need for selecting appropriate solution methodologies and computational tools tailored to the specific characteristics of each problem. The choice of these methods is critical for accurately capturing the complex interactions between fluid and structural domains. In this thesis, the following methodologies are considered to tackle a range of boundary value problems.

2.4.1 Eigenfunction expansion method

The Laplace equation serves as the governing equation for all the physical problems examined in this thesis. In this context, the velocity potential is a harmonic function that satisfies the Laplace equation, making it essential for analyzing a wide range of scientific and engineering problems. Beyond its applications in water wave modeling, the Laplace equation is utilized in disciplines such as mechanics, electromagnetics, quantum physics, biology etc. A particularly effective approach for solving boundary value problems associated with the Laplace equation is the eigenfunction expansion method (EEM). This mathematical technique is widely used in wave scattering problems, where the wave field is represented in terms of eigenfunctions that satisfy both the governing differential equations and the associated boundary conditions [127]. In this method, the fluid domain is typically partitioned into multiple regions based on the geometry and configuration of the problem—for example, interior and exterior regions around structures—and the velocity potential in each region is expanded as a series of eigenfunctions that inherently satisfy the

Laplace equation. These expansions are then matched at the interfaces between regions by enforcing continuity of velocity and pressure. Substitution of the velocity potentials into these matching conditions leads to a system of algebraic equations, which can be efficiently solved using computer algebra systems. Once the unknown coefficients are determined, the velocity potential in each region is fully determined.

2.4.2 Boundary element method

This section offers a concise introduction to the boundary element method (BEM), a numerical technique for solving the two-dimensional Laplace equation. For a comprehensive discussion, the reader may refer to Refs. [6, 20]. The BEM is a numerical technique for solving linear partial differential equations by transforming them into boundary integral equations. Unlike domain-based methods like the Finite Element Method (FEM), the BEM only requires discretization only of the outer surface enclosing the domain, making it particularly efficient for problems with infinite domains or complex geometries. The BEM is also frequently referred to as the "boundary integral equation method", emphasizing its foundation in integral equation formulations. This approach leverages the properties of Green's functions and fundamental solutions to reformulate partial differential equations into integral equations. By doing so, it eliminates the need to discretize the entire domain, focusing computational efforts on the boundary of the domain. To transform the BVP outlined in Sec. 2.3 into integral equations for numerical solutions, the fundamental solution (or Green's function) of the associated differential operator along with Green's identities are essential. In this thesis, we focus specifically on two-dimensional problems, and the formulation of the BEM presented here is developed accordingly.

The Green's function $G(x, z; \xi, \nu)$, satisfies the equation

$$\mathscr{L}\mathcal{G} = \delta(x - \xi, z - \nu), \tag{2.43}$$

where $\mathscr{L}$ is the linear differential operator and $\delta(x - \xi, z - \nu) = \delta(x - \xi)\delta(z - \nu)$ is the two-dimensional Dirac delta function with field point (x, z) and source point (ξ, ν). The Dirac delta function has the following key properties

$$\int_{-\infty}^{\infty} \delta(x)\,\mathrm{d}x = 1 \quad \text{and} \quad \int_{a}^{b} \delta(x - \xi) f(x)\,\mathrm{d}x = \begin{cases} f(\xi) & \text{if } \xi \in [a, b], \\ 0, & \text{if } \xi \notin [a, b], \end{cases} \tag{2.44}$$

where $f(x)$ is a continuous function at ξ. For the Laplace equation, the operator $\mathscr{L}$ corresponds to the Laplacian which, in two dimensions, is given as

$$\mathscr{L} = \nabla^2 = \frac{\partial^2}{\partial x^2} + \frac{\partial^2}{\partial z^2}. \tag{2.45}$$

Substituting Eq. (2.45) into Eq. (2.43), we get

$$\nabla^2 \mathcal{G} = \delta(x - \xi, z - \nu). \tag{2.46}$$

The solution to Eq. (2.46) is the two-dimensional Green's function, which is given by [6]

$$\mathcal{G}(x, z; \xi, \nu) = -\frac{1}{2\pi} \ln \tilde{r}, \tag{2.47}$$

where $\tilde{r} = \sqrt{(x-\xi)^2 + (z-\nu)^2}$. The fundamental solution serves as a crucial tool for transferring boundary value problems into integral equations. Moreover, Green's identities are necessary for this transformation. To state these identities precisely, let $\Omega \subset \mathbb{R}^n$ be a bounded domain with a piecewise smooth boundary $\partial\Omega$, denoting the set of points that form the boundary of Ω. Let u and v be scalar functions that are continuously differentiable at least twice in Ω. Green's identities involve the gradient (∇), Laplacian (∇^2), and normal derivative ($\frac{\partial}{\partial n}$) of these functions. Green's first identity is given by [48]

$$\int_\Omega \left(u \nabla^2 v + \nabla u \cdot \nabla v \right) \, \mathrm{d}V = \int_{\partial\Omega} u \frac{\partial v}{\partial n} \, \mathrm{d}\Omega \tag{2.48}$$

and the Green's second identity is given by [48]

$$\int_\Omega \left(u \nabla^2 v - v \nabla^2 u \right) \, \mathrm{d}V = \int_{\partial\Omega} \left(u \frac{\partial v}{\partial n} - v \frac{\partial u}{\partial n} \right) \, \mathrm{d}\Omega. \tag{2.49}$$

The fundamental solution, which satisfies the Laplace equation and Green's second identity, is subsequently employed to derive boundary integral equations, as discussed below.

Boundary integral equation formulation

The boundary integral equation formulation for the two-dimensional Laplace equation has been thoroughly discussed in [6, 20]. To derive this formulation, we consider the fluid region Γ bounded by Ω shown schematically in Fig. 2.3. Within this region, we introduce a source point (ξ, ν), at which the fundamental solution is singular and therefore not well-defined. Everywhere else in the domain Γ, the fundamental solution satisfies the Laplace

equation. Now, we consider a circular disc centered at (ξ, ν) with radius $\epsilon > 0$, chosen such that its boundary Ω_ϵ lies entirely within Ω. The interior domain of the circular disc is Γ_ϵ. The fundamental solution $\mathcal{G}$ then satisfies the Laplace equation over the domain $\Gamma - \Gamma_\epsilon$. After applying Green's second identity over the domain $\Gamma - \Gamma_\epsilon$, we obtain

$$\begin{aligned}&\int_{\Gamma-\Gamma_\epsilon} \left(\phi(x,z)\nabla^2\mathcal{G}(x,z;\xi,\nu) - \mathcal{G}(x,z;\xi,\nu)\nabla^2\phi(x,z)\right) \mathrm{d}V \\ &= \int_{\Omega\cup\Omega_\epsilon} \left(\phi(x,z)\frac{\partial\mathcal{G}(x,z;\xi,\nu)}{\partial n} - \mathcal{G}(x,z;\xi,\nu)\frac{\partial\phi(x,z)}{\partial n}\right) \mathrm{d}\Omega. \end{aligned} \tag{2.50}$$

In Eq. (2.50), the left-hand side of the equation equals zero because both $\phi(x,z)$ and $\mathcal{G}(x,z;\xi,\nu)$ satisfy the Laplace equation, resulting in $\nabla^2\phi(x,z) = 0$ and $\nabla^2\mathcal{G}(x,z;\xi,\nu) = 0$. For the sake of simplicity, we omit the explicit notations (x,z) and $(x,z;\xi,\nu)$. Then, we have

$$\int_{\Omega\cup\Omega_\epsilon} \left(\phi\frac{\partial\mathcal{G}}{\partial n} - \mathcal{G}\frac{\partial\phi}{\partial n}\right) \mathrm{d}\Omega = 0 \tag{2.51}$$

or

$$\int_{\Omega} \left(\phi\frac{\partial\mathcal{G}}{\partial n} - \mathcal{G}\frac{\partial\phi}{\partial n}\right) \mathrm{d}\Omega = -\int_{\Omega_\epsilon} \left(\phi\frac{\partial\mathcal{G}}{\partial n} - \mathcal{G}\frac{\partial\phi}{\partial n}\right) \mathrm{d}\Omega. \tag{2.52}$$

Eq. (2.52) holds for any $\epsilon > 0$, so long as the circle Ω_ϵ lies completely inside the region bounded by Ω. Thus, we let $\epsilon \to 0^+$ in Eq. (2.52) to analyze the limiting behavior as the

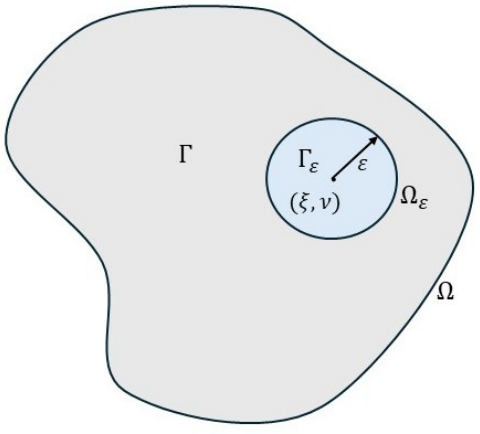

Figure 2.3: Schematic of the two-dimensional fluid region Γ enclosed by the boundary Ω, where the source point (ξ, ν) lies inside Γ, and Ω_ϵ denotes a small circular subregion of radius ϵ centered at (ξ, ν) with Γ_ϵ representing its boundary.

disc shrinks to the point (ξ, ν). This gives

$$\int_{\Omega} \left(\phi \frac{\partial \mathcal{G}}{\partial n} - \mathcal{G} \frac{\partial \phi}{\partial n} \right) \mathrm{d}\Omega = - \lim_{\epsilon \to 0^+} \int_{\Omega_\epsilon} \left(\phi \frac{\partial \mathcal{G}}{\partial n} - \mathcal{G} \frac{\partial \phi}{\partial n} \right) \mathrm{d}\Omega. \tag{2.53}$$

For $(\xi, \nu) \in \Gamma$, the right hand side of Eq. (2.53) gives [20]

$$\begin{aligned} - \lim_{\epsilon \to 0^+} \int_{\Omega_\epsilon} \left(\phi \frac{\partial \mathcal{G}}{\partial n} - \mathcal{G} \frac{\partial \phi}{\partial n} \right) \mathrm{d}\Omega &= - \lim_{\epsilon \to 0^+} \int_{\Omega_\epsilon} \phi \frac{\partial \mathcal{G}}{\partial n} \, \mathrm{d}\Omega + \lim_{\epsilon \to 0^+} \int_{\Omega_\epsilon} \mathcal{G} \frac{\partial \phi}{\partial n} \, \mathrm{d}\Omega = 0 \\ &= \phi(\xi, \nu) + 0 \\ &= \phi(\xi, \nu). \end{aligned} \tag{2.54}$$

Thus, Eq. (2.53) can be further rewritten as

$$\int_{\Omega} \left(\phi \frac{\partial \mathcal{G}}{\partial n} - \mathcal{G} \frac{\partial \phi}{\partial n} \right) \mathrm{d}\Omega = \phi(\xi, \nu). \tag{2.55}$$

Similarly, if $(\xi, \nu) \notin \Gamma \cup \Omega$ and $(\xi, \nu) \in \Omega$, we have [20]

$$\beta(\xi, \nu) \phi(\xi, \nu) = \int_{\Omega} \left(\phi \frac{\partial \mathcal{G}}{\partial n} - \mathcal{G} \frac{\partial \phi}{\partial n} \right) \mathrm{d}\Omega, \tag{2.56}$$

where

$$\beta(\xi, \nu) = \begin{cases} 0 & \text{if } (\xi, \nu) \notin \Gamma \cup \Omega, \\ \dfrac{1}{2} & \text{if } (\xi, \nu) \in \Omega \text{ for smooth } \Omega, \\ \dfrac{\alpha}{2\pi} & \text{if } (\xi, \nu) \in \Omega \text{ for non-smooth } \Omega, \end{cases} \tag{2.57}$$

where α is the aperture angle. Equations (2.55) and (2.56) represent the boundary integral equations derived for solving the Laplace equation. These integral equations (2.55) and (2.56) are solved using the BEM, which employs numerical technique to evaluate the unknown boundary values. To implement the BEM, the boundary is typically discretized using one of three common types of elements; namely, constant, linear, or quadratic. In the present thesis, the boundary integral equations are discretized using constant elements.

BEM based on constant-element approach

We consider a two-dimensional region whose boundary Ω is discretized into N number of segments, commonly referred to as boundary elements. Mathematically, the boundary

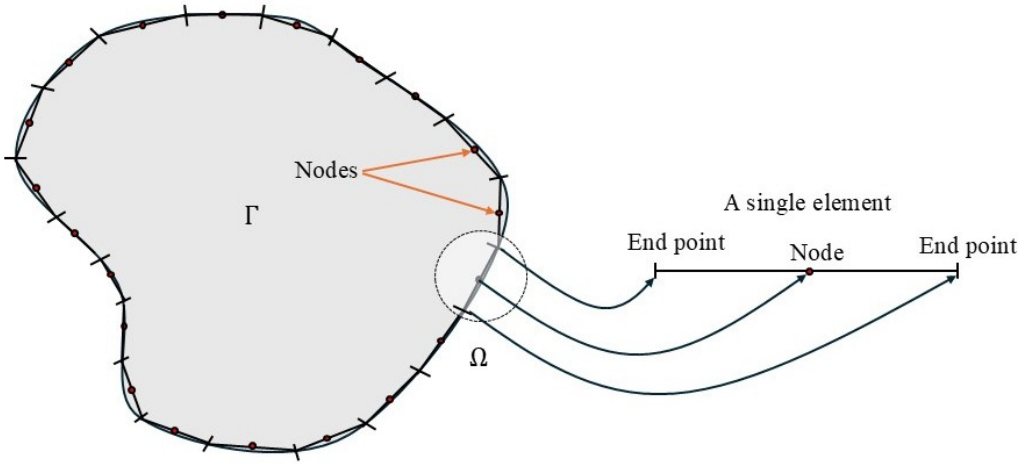

Figure 2.4: Schematic of the discretization of boundary using constant elements.

can be expressed as

$$\Omega = \bigcup_{j=1}^{N} \Omega_j, \tag{2.58}$$

where Ω_j denotes the j^{th} boundary element. The points where the unknown values are considered are called 'nodes' and taken to be in the middle of the element as shown in Fig. 2.4. The constant boundary element method assumes that both ϕ and its normal derivative $\frac{\partial \phi}{\partial n}$ are uniform over each boundary element. Additionally, for constant elements, the boundary is treated as smooth, and the value at the midpoint (node) of each element is used to approximate the value throughout the entire element [6, 20]. Based on these assumptions, the boundary integral equation is discretized by applying the fundamental solution $\mathcal{G}$ centered at the node of the i^{th} element, which is treated as the source point (ξ, ν). For smooth boundary, the discretized form of Eq. (2.56) for the i^{th} element can be written as

$$-\frac{1}{2}\phi_i(\xi,\nu) + \sum_{j=1}^{N} \int_{\Omega_j} \phi_j \frac{\partial \mathcal{G}_{ij}}{\partial n}\, d\Omega = \sum_{j=1}^{N} \int_{\Omega_j} \mathcal{G}_{ij} \frac{\partial \phi_j}{\partial n}\, d\Omega, \tag{2.59}$$

where Ω_j is the length of the element j and N is the total number of segments. According to the assumption of constant boundary element, ϕ and $\frac{\partial \phi}{\partial n}$ are constant over each

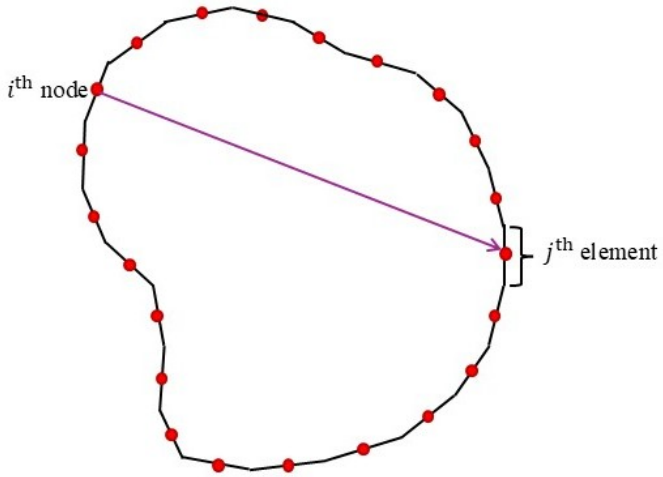

Figure 2.5: Schematic of the discretized boundary of the domain, where red dots represent nodes with the i^{th} node and j^{th} boundary element being marked explicitly, and connecting arrow indicating their geometric relationship.

boundary element, then Eq. (2.59) simplifies to [20]

$$-\frac{1}{2}\phi_i(\xi,\nu)+\sum_{j=1}^{N}\phi_j\int_{\Omega_j}\frac{\partial\mathcal{G}_{ij}}{\partial n}\,\mathrm{d}\Omega=\sum_{j=1}^{N}\frac{\partial\phi_j}{\partial n}\int_{\Omega_j}\mathcal{G}_{ij}\,\mathrm{d}\Omega, \tag{2.60}$$

where ϕ_j and $\frac{\partial\phi_j}{\partial n}$ denote the unknown coefficients over the j^{th} boundary element. The relationship between the i^{th} node (where the fundamental solution is applied) and the j^{th} boundary element is illustrated in Fig. 2.5. In Eq. (2.60), the fundamental solution $\mathcal{G}_{ij}$ is centered at the i^{th} node and the boundary integrals are evaluated over all elements $j = 1, 2, \ldots, N$, including the case $i = j$. Repeating this process for all nodes $i = 1, 2, 3, \ldots, N$ as a source point results in a complete system of N equations. For simplicity, we define

$$\mathcal{M}_{ij}:=-\frac{1}{2}\delta_{ij}+\int_{\Omega_j}\frac{\partial\mathcal{G}_{ij}}{\partial n}\,\mathrm{d}\Omega\quad\text{and}\quad G_{ij}:=\int_{\Omega_j}\mathcal{G}_{ij}\,\mathrm{d}\Omega, \tag{2.61}$$

where δ_{ij} represents the Kronecker delta function, which equals 1 when $i = j$ and 0 when $i \neq j$, M_{ij} and G_{ij} are called as influence coefficients. When $i = j$, the field point (x, z) and the source point (ξ, ν) lie on the same boundary element and in this case integrals become singular and the coefficients $\mathcal{M}_{ij}$ and G_{ij} are evaluated using Gauss–Legendre quadrature method. In contrast, when $i \neq j$, the source and field points lie on different boundary elements, and the integrals associated with $\mathcal{M}_{ij}$ and G_{ij} in this case

are computed analytically. Further, substituting Eq. (2.61) into Eq. (2.60), we obtain

$$\sum_{j=1}^{N} \mathcal{M}_{ij}\phi_j \sum_{j=1}^{N} G_{ij}\frac{\partial \phi_j}{\partial n} \quad \text{for } i = 1, 2, 3, \ldots, N. \tag{2.62}$$

The above system of equations can be written in the matrix form as

$$\mathcal{M}\boldsymbol{U} = B\boldsymbol{V}, \tag{2.63}$$

where

$$\mathcal{M} = \begin{bmatrix} \mathcal{M}_{11} & \mathcal{M}_{12} & \mathcal{M}_{13} & \cdots & \mathcal{M}_{1N} \\ \mathcal{M}_{21} & \mathcal{M}_{22} & \mathcal{M}_{23} & \cdots & \mathcal{M}_{2N} \\ \vdots & \vdots & \vdots & \ddots & \vdots \\ \mathcal{M}_{N1} & \mathcal{M}_{N2} & \mathcal{M}_{N3} & \cdots & \mathcal{M}_{NN} \end{bmatrix}, \quad B = \begin{bmatrix} G_{11} & G_{12} & G_{13} & \cdots & G_{1N} \\ G_{21} & G_{22} & G_{23} & \cdots & G_{2N} \\ \vdots & \vdots & \vdots & \ddots & \vdots \\ G_{N1} & G_{N2} & G_{N3} & \cdots & G_{NN} \end{bmatrix},$$

$$\boldsymbol{U} = \begin{bmatrix} \phi_1 & \phi_2 & \cdots & \phi_N \end{bmatrix}^{\mathsf{T}}, \quad \text{and} \quad \boldsymbol{V} = \begin{bmatrix} \frac{\partial \phi_1}{\partial n} & \frac{\partial \phi_2}{\partial n} & \ldots & \frac{\partial \phi_N}{\partial n} \end{bmatrix}^{\mathsf{T}}.$$

In matrix equation (2.63), depending on the prescribed boundary conditions, some components of $\boldsymbol{U}$ (i.e., values of ϕ) and some components of $\boldsymbol{V}$ (i.e., values of $\frac{\partial \phi}{\partial n}$) are known, while the remaining components are unknown. In order to solve matrix equation (2.63), we will have to get all of the unknowns on the left-hand side of the equation and the knowns on the right-hand side. This is accomplished by shuffling the columns of the matrix. To understand the rearrangement of boundary values, let us look at a simple example where the boundary is divided into 8 elements. Suppose the values of ϕ are known on the first 4 elements, i.e., $\phi_i = \hat{\phi}_i$ for $i = 1, \ldots, 4$, and the values of $\frac{\partial \phi}{\partial n}$ are known on the remaining elements, i.e., $\frac{\partial \phi_i}{\partial n} = \frac{\partial \hat{\phi}_i}{\partial n}$ for $i = 5, \ldots, 8$. Then Eq. (2.63) would read

$$\mathcal{M} = \begin{bmatrix} \mathcal{M}_{11} & \mathcal{M}_{12} & \mathcal{M}_{13} & \cdots & \mathcal{M}_{18} \\ \mathcal{M}_{21} & \mathcal{M}_{22} & \mathcal{M}_{23} & \cdots & \mathcal{M}_{28} \\ \vdots & \vdots & \vdots & \ddots & \vdots \\ \mathcal{M}_{81} & \mathcal{M}_{82} & \mathcal{M}_{83} & \cdots & \mathcal{M}_{88} \end{bmatrix} \begin{bmatrix} \hat{\phi}_1 \\ \vdots \\ \hat{\phi}_4 \\ \phi_5 \\ \vdots \\ \phi_8 \end{bmatrix} = \begin{bmatrix} G_{11} & G_{12} & G_{13} & \cdots & G_{18} \\ G_{21} & G_{22} & G_{23} & \cdots & G_{28} \\ \vdots & \vdots & \vdots & \ddots & \vdots \\ G_{81} & G_{82} & G_{83} & \cdots & G_{88} \end{bmatrix} \begin{bmatrix} \frac{\partial \phi_1}{\partial n} \\ \vdots \\ \frac{\partial \phi_4}{\partial n} \\ \frac{\partial \hat{\phi}_5}{\partial n} \\ \vdots \\ \frac{\partial \hat{\phi}_8}{\partial n} \end{bmatrix}. \tag{2.64}$$

In Eq. (2.64), ϕ_5 to ϕ_8 and $\frac{\partial \phi_1}{\partial n}$ to $\frac{\partial \phi_4}{\partial n}$ are the unknowns. The equation must be rearranged so that all the unknowns are isolated on the left-hand side, and the known values are shifted to the right-hand side for solution. After shuffling columns, Eq. (2.64) gives

$$\begin{bmatrix} G_{11} & \cdots & G_{14} & -\mathcal{M}_{15} & \cdots & -\mathcal{M}_{18} \\ \vdots & \ddots & \vdots & \vdots & \ddots & \vdots \\ G_{81} & \cdots & G_{84} & -\mathcal{M}_{85} & \cdots & -\mathcal{M}_{88} \end{bmatrix} \boldsymbol{b_1} = \begin{bmatrix} \mathcal{M}_{11} & \cdots & \mathcal{M}_{14} & -G_{15} & \cdots & -G_{18} \\ \vdots & \ddots & \vdots & \vdots & \ddots & \vdots \\ \mathcal{M}_{81} & \cdots & \mathcal{M}_{84} & -G_{85} & \cdots & -G_{88} \end{bmatrix} \boldsymbol{b_2}, \tag{2.65}$$

where $\boldsymbol{b_1} = \begin{bmatrix} \frac{\partial \phi_1}{\partial n} & \cdots & \frac{\partial \phi_4}{\partial n} & \phi_5 & \cdots & \phi_8 \end{bmatrix}^\mathsf{T}$ and $\boldsymbol{b_2} = \begin{bmatrix} \hat{\phi}_1 & \cdots \hat{\phi}_4 & \frac{\partial \hat{\phi}_5}{\partial n} & \cdots & \frac{\partial \hat{\phi}_8}{\partial n} \end{bmatrix}^\mathsf{T}$, respectively, show the set of unknown and known values. This leads to a linear system of equations of the form $A\boldsymbol{x} = \boldsymbol{b}$ where A contains the influence coefficients obtained from the boundary integrals, and $\boldsymbol{x}$ represents the vector containing the unknowns. The solution $\boldsymbol{x}$ is then determined from $\boldsymbol{x} = A^{-1}\boldsymbol{b}$. After obtaining the boundary values, the potential ϕ at any point in the interior of the domain can be evaluated using Eq. (2.55).

Chapter 3

Wave interaction with a cylinder

This chapter investigates the impact of the porous seabed on the hydrodynamic forces acting on a circular cylinder, the flow distribution around the cylinder, and the surface elevation. The chapter also presents temporal simulations of the fluid flow at various time intervals.

3.1 Mathematical framework

3.1.1 Problem description

We consider a rigid circular cylinder, which floats just under the open-water surface and is located above a porous seabed. The problem is described mathematically using the cylindrical coordinate system (r, θ, z). The coordinates r and θ lie on the horizontal surface of the cylinder, while the positive z-axis runs vertically upwards. The axes of the circular cylinder at $r = 0$ and the free surface of the water at $z = 0$ are shown in Fig. 3.1. The parameter h denotes the total water depth, which is taken to be positive in this chapter and throughout the thesis, while a and d represent the radius and height of the cylinder, respectively. The entire fluid domain surrounding the structure is divided into two regions: region 1, the open-water region ($a > 0$), and region 2, the interior region ($a < 0$).

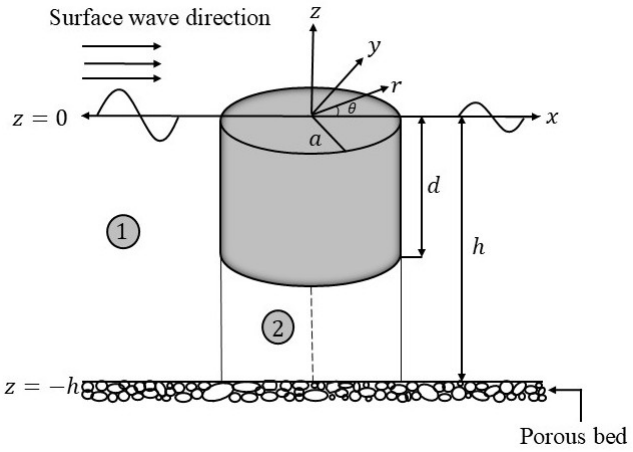

Figure 3.1: Schematic of a rigid circular cylinder floating over a porous bed.

3.1.2 Governing equation and boundary conditions

Under the assumption of irrotational flow, a velocity potential $\Phi(x, y, z, t)$ exists, which corresponds to the velocity components in each region of the domain. Furthermore, it is assumed that the fluid motion exhibits simple harmonic behavior with an angular frequency ω. As a result, the velocity potentials and the free surface elevation can be expressed in time-harmonic form. Specifically, the velocity potential in region j ($j = 1, 2$) is of the form $\Phi_j(r, \theta, z, t) = \mathrm{Re}\{\phi_j(r, \theta, z)e^{-\mathrm{i}\omega t}\}$ for $j = 1, 2$ and the corresponding free surface elevation is expressed as $\eta = \mathrm{Re}\{A\eta_1(r, \theta, z)e^{-\mathrm{i}\omega t}\}$, where Re$\cdot$ denotes the real part of a complex quantity, $\phi_j(r, \theta, z)$ is the spatial (time-independent) component of the velocity potential in the j^{th} (for $j = 1, 2$), A is the amplitude of the incident wave, and $\eta_1(r, \theta)$ is the dimensionless (also time-independent) surface elevation in region 1. Utilizing this, the continuity equation yields the Laplace equation, which works as the governing equation and is expressed in cylindrical coordinates as

$$\frac{\partial^2\phi_j}{\partial r^2} + \frac{1}{r}\frac{\partial\phi_j}{\partial r} + \frac{1}{r^2}\frac{\partial^2\phi_j}{\partial\theta^2} + \frac{\partial^2\phi_j}{\partial z^2} = 0 \quad \text{for} \quad j = 1, 2. \tag{3.1}$$

Owing to the porosity of the seabed, the boundary condition at the seabed reads [23]

$$\frac{\partial\phi_j}{\partial z} + G\,\phi_j = 0 \quad \text{at} \quad z = -h, \quad j \in \{1, 2\}, \tag{3.2}$$

where the parameter G in boundary condition (3.2) is referred to as the porosity parameter having the dimension of 1/length. The porosity parameter G is typically a complex number $G := G_r + \mathrm{i}\,G_i$, where its real part G_r represents the resistance effects while its imaginary part G_i represents the inertial effects [155, 156]. The real part of the porosity parameter G_r is often referred to as the slip parameter in the community working on hydrodynamic stability analysis of flows over a slippery porous bottom; see, e.g., [109, 124]. Furthermore, the slip parameter is related to a dimensionless parameter α_p, characterizing the structure of the permeable material, via $G_r \approx \alpha_p/\sqrt{\epsilon}$, with ϵ being the permeability of the material. Beavers & Joseph [10] found experimentally that the value of the parameter α_p lies within 0.1 and 4. However, to the best of the author's knowledge, no such experimental or theoretical works on the range of the imaginary part of the porosity parameter (or on physically acceptable values of the complex porosity parameter for that matter) are available in the existing literature. Therefore, the values

of the complex porosity parameter in the this chapter and throughout the thesis have been taken randomly following some earlier works, e.g., [14, 23, 82, 86].

The free-surface boundary condition at $z = 0$ for the open-water region is [163, 171]

$$\frac{\partial \phi_1}{\partial z} - \frac{\omega^2}{g}\phi_1 = 0. \tag{3.3}$$

The velocity potential for the open-water region is the superposition of the potentials for the incident and scattered waves [85], i.e.,

$$\phi_1 = \phi_I + \phi_S, \tag{3.4}$$

where ϕ_I is the velocity potential for the incident plane wave and ϕ_S is the velocity potential for the scattered waves. The velocity potential for the incident wave ϕ_I is defined as

$$\phi_I = -\frac{\mathrm{i}gA}{2\omega}\frac{k_0\cosh\big(k_0(h+z)\big) - G\sinh\big(k_0(h+z)\big)}{\cosh\left(k_0h\right) - G\sinh\left(k_0h\right)}\sum_{m=0}^{\infty}\varepsilon_m J_m\left(k_0r\right)\cos\left(m\theta\right), \tag{3.5}$$

where $J_m(\cdot)$ denotes the Bessel function of the first kind of order m and $\varepsilon_0 = 1$, $\varepsilon_m = 2$ for $m \geq 1$. The velocity potential for the scattered waves ϕ_S in Eq. (3.4) satisfies the far-field radiation condition as $r \to \infty$. This condition is given by

$$\lim_{r\to\infty}\sqrt{r}\left[\frac{\partial}{\partial r}(\phi_1 - \phi_I) - \mathrm{i}k_0(\phi_1 - \phi_I)\right] = 0, \tag{3.6}$$

where k_0 represents the wavenumber of the incident wave in region 1 and satisfies the dispersion relation [14]

$$k_0\big[k_0\tanh\left(k_0h\right) - G\big] = \frac{\omega^2}{g}\big[k_0 - G\tanh\left(k_0h\right)\big]. \tag{3.7}$$

3.2 Solution method

The spatial velocity potential in region 1, $\phi_1(r,\theta,z)$, satisfying the governing equation (3.1) and boundary conditions (3.2), (3.5) and (3.6), is given by [85]

$$\begin{aligned}\phi_1 = &-\frac{\mathrm{i}gA}{2\omega}f_0(z)\sum_{m=0}^{\infty}\varepsilon_m e^{\mathrm{i}m\pi/2}\left\{J_m(k_0r) + A_{m0}H_m^{(1)}(k_0r)\right\}\cos\left(m\theta\right)\\ &+\sum_{m=0}^{\infty}\sum_{n=1}^{\infty}A_{mn}\varepsilon_m e^{\mathrm{i}m\pi/2}K_m(k_nr)f_n(z)\cos\left(m\theta\right),\end{aligned} \tag{3.8}$$

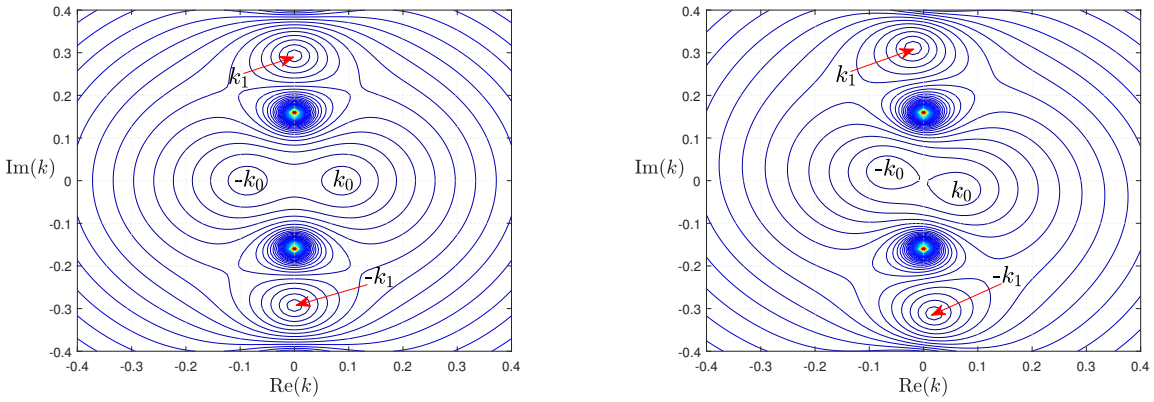

Figure 3.2: Contour plots of the roots of dispersion relation (3.9) in the open-water region for (a) rigid bed ($Gh = 0$) and (b) porous bed ($Gh = 0.5 + 0.6\mathrm{i}$) with fixed values of $h = 10$ m and time period $T = 8$ s.

where $H_m^{(1)}(\cdot)$ denotes the Hankel function of the first kind of order m; $K_m(\cdot)$ denotes the modified Bessel function of the second kind of order m; A_{mn} (for $m, n = 0, 1, 2, \dots$) are the unknown coefficients; k_n (for $n = 0, 1, 2, \dots$) are the wavenumbers of the scattered waves; and $f_n(z)$ (for $n = 0, 1, 2, \dots$) are the eigenfunctions in region 1. The wavenumbers k_n (for $n = 0, 1, 2, \dots$) satisfy the dispersion relation [14]

$$k_n\big[k_n \tanh(k_n h) - G\big] = \frac{\omega^2}{g}\big[k_n - G\tanh(k_n h)\big] \tag{3.9}$$

and the eigenfunctions $f_n(z)$ (for $n = 0, 1, 2, \dots$) are given by [14, 130]

$$f_n(z) = \frac{k_n \cosh\big(k_n(h+z)\big) - G\sinh\big(k_n(h+z)\big)}{k_n\cosh(k_n h) - G\sinh(k_n h)}. \tag{3.10}$$

It may be noted that when $G = 0$, dispersion relation (3.9) and the eigenfunctions, defined in Eq. (3.10), reduce to those for a rigid bottom; see, e.g., Refs. [54, 71, 106]. For $G = 0$, the dispersion relation has two real roots, namely $-k_0$ and k_0, and infinitely many purely imaginary roots $\pm k_n$, $n = 1, 2, 3, \dots$. Figure 3.2 illustrates the roots of dispersion relation (3.9) for (a) rigid bed ($Gh = 0$) and (b) porous bed ($Gh = 0.5 + 0.6\mathrm{i}$) via contour plots. Figure 3.2a (the case of $Gh = 0$) clearly exhibits two real roots, one lying on the positive real axis and the other on the negative real axis. Furthermore, some of the infinitely many purely imaginary roots are also shown in Fig. 3.2a, which illustrate the existence of evanescent modes. In the case of a porous bed ($Gh \neq 0$), all the roots of dispersion relation (3.9) are complex in nature, as can also be seen from

Fig. 3.2b. Figure 3.2 also shows that all the roots of dispersion relation (3.9) in the case of a porous bed are in close proximity to the corresponding roots of dispersion relation (3.9) in the case of rigid bed (cf. the contour plots in Figs. 3.2a and 3.2b). The roots of the dispersion relation that are in close proximity to the real axis are identified as the most predominant progressive wave modes for our computation. To actually find the roots of dispersion relation (3.9), we have employed the Newton–Raphson method, wherein the initial guesses are chosen with the help of the contour plots.

Similarly to the above, the velocity potential ϕ_2 in region 2 turns out to be [85]

$$\phi_2 = -\frac{\mathrm{i}gA}{2\omega}\sum_{m=0}^{\infty}\sum_{n=0}^{\infty} B_{mn}\varepsilon_m e^{\mathrm{i}m\pi/2} I_m(p_n r) g_n(z)\cos(m\theta), \tag{3.11}$$

where $I_m(\cdot)$ denotes the modified Bessel function of the first kind of order m; B_{mn} (for $m, n = 0, 1, 2, \dots$) are the unknown coefficients; p_n (for $n = 0, 1, 2, \dots$) are the wavenumbers in region 2; and $g_n(z)$ (for $n = 0, 1, 2, \dots$) are the eigenfunctions in region 2. The wave numbers p_n (for $n = 0, 1, 2, \dots$) in region 2 satisfy the dispersion relation

$$p_n \tanh\big(p_n(h-d)\big) = G, \tag{3.12}$$

and the eigenfunctions $g_n(z)$ (for $n = 0, 1, 2, \dots$) are given by

$$g_n(z) = \frac{p_n \cosh\big(p_n(h+z)\big) - G\sinh\big(p_n(h+z)\big)}{p_n}. \tag{3.13}$$

It is worth noting again that when $G = 0$, the dispersion relation (3.12) and eigenfunctions (3.13) are the same as those for the region covered by a cylinder over a rigid bottom [50, 67].

The velocity and pressure continuities near the fluid interface at $r = a$ in the region $-h \le z \le -d$ lead to the so-called matching conditions, given by

$$\frac{\partial \phi_1}{\partial r} = \frac{\partial \phi_2}{\partial r} \tag{3.14}$$

and

$$\phi_1 = \phi_2, \tag{3.15}$$

respectively. Furthermore, the structural boundary condition at $r = a$ where the radial velocity is zero due to the rigid structure in the region in the region $-d \le z \le 0$, is given

by

$$\frac{\partial \phi_1}{\partial r} = 0. \tag{3.16}$$

We substitute the velocity potentials from Eqs. (3.8) and (3.11) into boundary conditions (3.14)–(3.16). The resulting equations are multiplied by $f_q(z)\cos(l\theta)$ and integrated subsequently over θ in $[0, 2\pi]$ and over z in the respective domains of boundary conditions (3.14)–(3.16) in order to exploit the orthogonality of the trigonometric functions in $[0, 2\pi]$. Employing the orthogonality of the trigonometric functions, the resulting equations respectively yield

$$\begin{aligned} &\alpha J_m'(k_0 a) S(f_0, f_q) + \alpha A_{m0} H_m^{(1)\prime}(k_0 a)\, S(f_0, f_q) + \sum_{n=1}^{\infty} A_{mn} K_m'(k_n a) S(f_n, f_q) \\ &\qquad = \alpha \sum_{n=0}^{\infty} B_{mn} I_m'(p_n a) \int_{-h}^{-d} f_q(z) g_n(z)\, \mathrm{d}z, \end{aligned} \tag{3.17}$$

$$\begin{aligned} &\alpha J_m(k_0 a) S(f_0, f_q) + \alpha A_{l0} H_m^{(1)}(k_0 a)\, S(f_0, f_q) + \sum_{n=1}^{\infty} A_{mn} K_m(k_n a) S(f_n, f_q) \\ &\qquad = \alpha \sum_{n=0}^{\infty} B_{mn} I_m(p_n a) \int_{-h}^{-d} f_q(z) g_n(z)\, \mathrm{d}z, \end{aligned} \tag{3.18}$$

$$\alpha J_m'(k_0 a) T(f_0, f_q) + \alpha A_{m0} H_m^{(1)\prime}(k_0 a)\, T(f_0, f_q) + \sum_{n=1}^{\infty} A_{mn} K_m'(k_n a) T(f_n, f_q) = 0, \tag{3.19}$$

where $\alpha = -\mathrm{i}gA/(2\omega)$,

$$S(f_n, f_q) = \int_{-h}^{-d} f_n(z) f_q(z)\, \mathrm{d}z,$$

$$T(f_n, f_q) = \int_{-d}^{0} f_n(z) f_q(z)\, \mathrm{d}z,$$

with $n, q = \{0\} \cup \mathbb{N}$. The eigenfunctions f_n also satisfies the orthogonality condition

$$\int_{-h}^{0} f_n(z) f_q(z)\, \mathrm{d}z = \begin{cases} X(f_q) & \text{for} \quad n = q, \\ 0 & \text{for} \quad n \neq q, \end{cases} \quad \text{with} \quad X(f_q) = \int_{-h}^{0} f_q^2(z)\, \mathrm{d}z. \tag{3.20}$$

Adding Eqs. (3.17) and (3.19), and exploiting orthogonality condition (3.20), we obtain

$$\alpha J'_m(k_0a)X(f_0) + \alpha A_{m0}H_m^{(1)'}(k_0a)\,X(f_0) + \sum_{n=1}^{\infty} A_{mn}K'_m(k_na)X(f_q) = \alpha \sum_{n=0}^{\infty} B_{mn}I'_m(p_na)\int_{-h}^{-d} f_q(z)g_n(z)\,\mathrm{d}z. \quad (3.21)$$

Note that q and m are given non-negative integers. For fixed values of q and m Eqs. (3.18) and (3.21) form a system of two simultaneous linear algebraic equations containing infinite unknown coefficients A_{mn} and B_{mn} $(n = 0, 1, 2, \dots)$. Nevertheless, for all practical purposes, we can deal only with a finite number of unknowns. To this end, the series in Eqs. (3.18) and (3.21) are truncated at a reasonable value for n, let us say N, so that the system has a total of $2(N + 1)$ unknown coefficients. Corresponding to these $n = 0, 1, \dots, N$, each of dispersion relations (3.9) and (3.12) gives $N + 1$ wavenumbers, namely $k_0, k_1, \dots, k_N$ and $p_0, p_1, \dots, p_N$, which in turn give eigenfunctions, namely $f_0(z), f_1(z), \dots, f_N(z)$ and $g_0(z), g_1(z), \dots, g_N(z)$. Consequently, by choosing $q = 0, 1, \dots, N$ in Eqs. (3.18) and (3.21), we shall get $2(N+1)$ equations in $2(N+1)$ unknown coefficients that can be solved numerically using any computer algebra software. In this work, we have taken $m = 10$ and $N = 7$ for both regions 1 and 2, and solved the resulting system of linear equations in Matlab®. Substituting the determined coefficients in Eqs. (3.8) and (3.11), the velocity potentials can be obtained explicitly.

3.3 Results and discussions

All numerical computations presented in this chapter and throughout the thesis have been carried out using Matlab®. First of all, the unknown coefficients in Eqs. (3.18) and (3.21) have been determined by truncating the series in Eqs. (3.18) and (3.21) at a certain value of n. With the determined coefficients, the velocity potentials in regions 1 and 2 have been computed. The computed velocity potentials are then exploited to find the horizontal and vertical forces and flow distribution around the cylinder. In addition, time-domain simulations have been performed to visualize the temporal evolution of the wave interacting with the structure. For all numerical computations, the following physical

parameter values have been used: water depth $h = 20\,\mathrm{m}$, incident wave amplitude $A = 1\,\mathrm{m}$, gravitational acceleration $g = 9.81\,\mathrm{m/s^2}$, and water density $\rho = 1025\,\mathrm{kg/m^3}$.

3.3.1 Code validation

It is important to note that for $G = 0$ the seabed acts as a rigid bottom. Hence the results obtained in the present study for $G = 0$ must agree with the existing results on wave scattering by a circular cylinder over a rigid bottom. Therefore, to validate our code, we compare the horizontal force exerted on the cylinder for $G = 0$ from the present study with that reported in Ref. [50]. Figure 3.3 exhibits the (dimensionless) horizontal force exerted on the cylinder against the (dimensionless) wavenumber $k_0 a$ for the porosity parameter $G = 0$. The solid black line denotes the analytical results obtained in the present work and the symbols denote the result reported in Ref. [50]. The agreement between the results on the horizontal force exerted on the cylinder from the present work for $G = 0$ and from Ref. [50] is evident in the figure. This validates our code.

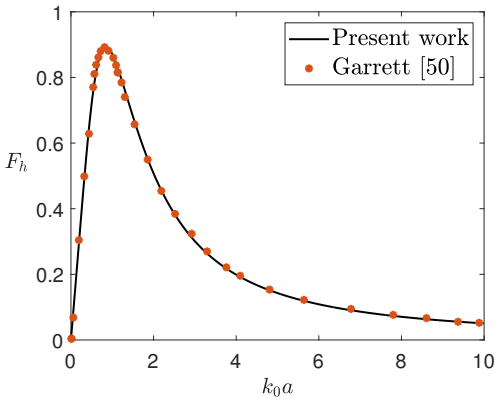

Figure 3.3: Horizontal force exerted on the cylinder by the wave plotted against the (dimensionless) wavenumber for $d/h = 0$, $a/h = 4/3$. The solid black line denotes the result for $G = 0$ obtained in the present study and symbols depict the results reported in Ref. [50].

3.3.2 Wave forces

The horizontal (in the x-direction) and vertical (in the z-direction) forces exerted on the circular cylinder are given by [67]

$$F_x = -\mathrm{i}\rho\omega a \int_0^{2\pi} \int_{-d}^{0} \phi_1(a, \theta, z) \cos\theta \, \mathrm{d}z \, \mathrm{d}\theta, \tag{3.22}$$

and

$$F_z = \mathrm{i}\rho\omega \int_0^{2\pi} \int_0^a \phi_2(r, \theta, -d) r \, \mathrm{d}r \, \mathrm{d}\theta, \tag{3.23}$$

respectively. These forces can be determined readily by inserting ϕ_1 and ϕ_2 computed above in Eqs. (3.22) and (3.23) and performing the integrals numerically. For a better understanding, we compute the dimensionless magnitudes of the horizontal and vertical forces [17, 50, 67]:

$$F_h = \frac{|F_x|}{\pi\rho g a^2 A} \quad \text{and} \quad F_v = \frac{|F_z|}{\pi\rho g a^2 A}, \tag{3.24}$$

and refer to F_h and F_v as the (dimensionless) horizontal and vertical forces, respectively.

Figure 3.4 illustrates the (dimensionless) horizontal force exerted on the circular cylinder with variation in the (dimensionless) wavenumber $k_0 h$. Figure 3.4a displays the plot of the horizontal force for different values of the length of cylinder d/h, while keeping a fixed value of the cylinder radius $a/h = 1$ and a fixed value of the porosity parameter $Gh = 2 + 2\mathrm{i}$. It can be noted from Fig. 3.4a that as the wavenumber increases, the horizontal force first increases but after attaining a maximum value it starts decreasing with a further increase in the wavenumber. Figure 3.4a also shows that as the length of the cylinder (d/h) increases, the magnitude of the horizontal force reduces due to the fact that wave forces are now distributed at an increased surface area in the vertical direction. Figure 3.4b delineates the variation of the horizontal force with respect to the wavenumber $k_0 h$ on varying the radius of the cylinder (a/h) for a fixed value of $d/h = 0.6$ and a fixed value of the porosity parameter $Gh = 2+2\mathrm{i}$. In Fig. 3.4b, the magnitude of the horizontal force also decreases with an increase in the radius of the cylinder. This is attributed to the fact that an increase in the radius of the cylinder increases the surface of the cylinder in the horizontal directions and, hence the structure now applies more resistance to the pounding waves. Figure 3.4c portrays the horizontal force exerted on the cylinder with respect to the wavenumber $k_0 h$ for different values of the porosity parameter Gh and for fixed values of $d/h = 0.6$ and $a/h = 1$. Figure 3.4c shows that the horizontal force exerted on the cylinder decreases with an increase in the modulus of the porosity parameter Gh. This is due to the fact that with an increased porosity the bottom bed absorbs more wave energy.

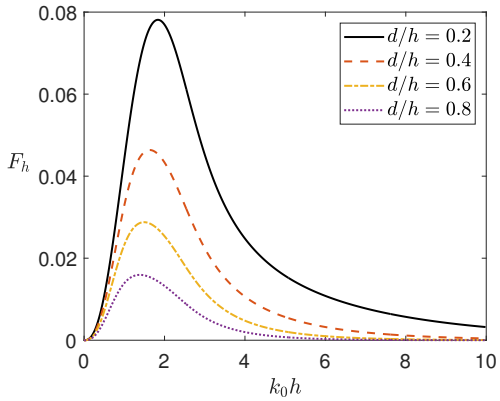

(a) $a/h = 1$, $Gh = 2 + 2\mathrm{i}$

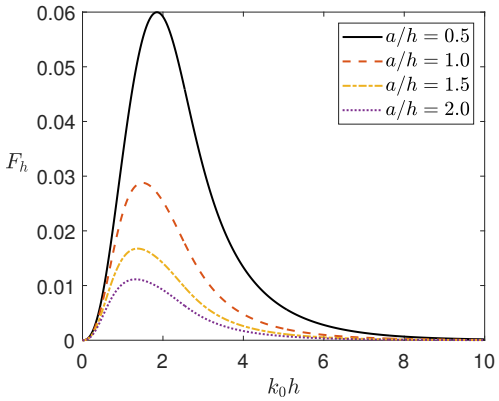

(b) $d/h = 0.6$, $Gh = 2 + 2\mathrm{i}$

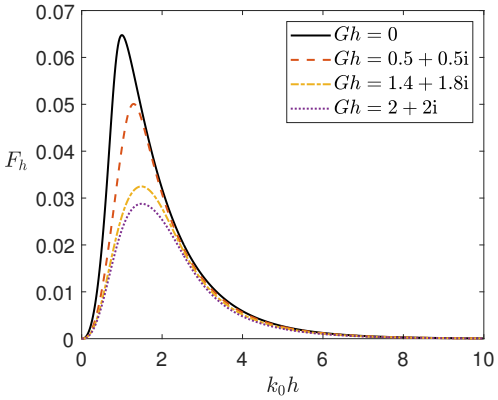

(c) $d/h = 0.6$, $a/h = 1$

Figure 3.4: Horizontal force on the cylinder with respect to the (dimensionless) wavenumber k_0h for (a) different lengths of the cylinder (d/h) and fixed radius and porosity parameter, $a/h = 1$ and $Gh = 2 + 2\mathrm{i}$ (b) different radii of the cylinder (a/h) and fixed length and porosity parameter, $d/h = 0.6$ and $Gh = 2 + 2\mathrm{i}$ and (c) different values of the porosity parameter G and fixed length and radius of the cylinder, $d/h = 0.6$ and $a/h = 1$.

Figure 3.5 illustrates the (dimensionless) vertical force exerted on the cylinder with respect to the (dimensionless) wavenumber k_0h. The figure shows that, similarly to Fig. 3.4, the vertical force also first increases with increasing the wavenumber but starts decreasing after attaining a maximum value with a further increase in the wavenumber. Figure 3.5a exhibits the change in the vertical force on changing the length of the cylinder while keeping its radius and the porosity parameter fixed ($a/h = 1$ and $Gh = 2 + 2\mathrm{i}$). A comparison of Figs. 3.4a and 3.5a reveals that, in contrast to the horizontal force, the magnitude of the vertical force on the cylinder actually increases with increasing the length of the cylinder. Figure 3.5b displays the change in the vertical force on changing the radius of

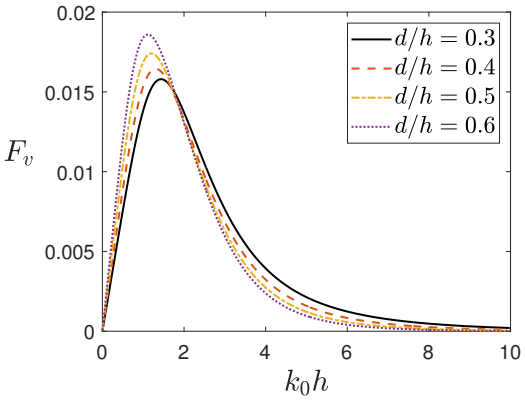

(a) $a/h = 1$, $Gh = 2 + 2\mathrm{i}$

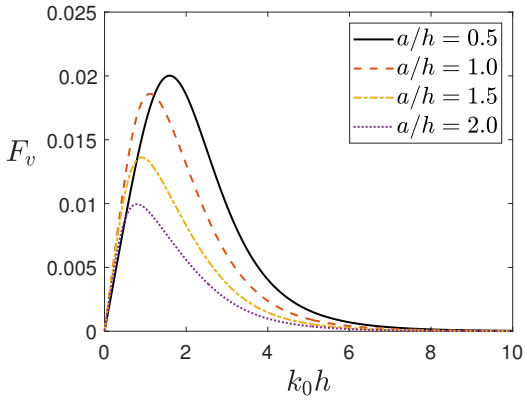

(b) $d/h = 0.6$, $Gh = 2 + 2\mathrm{i}$

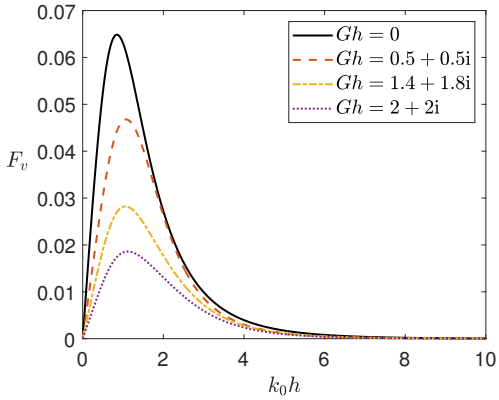

(c) $d/h = 0.6$, $a/h = 1$

Figure 3.5: Vertical force on the cylinder with respect to the (dimensionless) wavenumber k_0h for (a) different lengths of the cylinder (d/h) and fixed radius and porosity parameter, $a/h = 1$ and $Gh = 2 + 2\mathrm{i}$ (b) different radii of the cylinder (a/h) and fixed length and porosity parameter, $d/h = 0.6$ and $Gh = 2 + 2\mathrm{i}$ and (c) different values of the porosity parameter Gh and fixed length and radius of the cylinder, $d/h = 0.6$ and $a/h = 1$.

the cylinder while keeping its length and the porosity parameter fixed ($d/h = 0.6$ and $Gh = 2 + 2\mathrm{i}$). A comparison of Figs. 3.4b and 3.5b shows that, similarly to the horizontal force, the magnitude of the vertical force on the cylinder also decreases with increasing the radius of the cylinder. Figure 3.5c presents the change in the vertical force on changing the porosity parameter for a given cylinder ($d/h = 0.6$ and $a/h = 1$). A comparison of Figs. 3.4c and 3.5c shows that similarly to the horizontal force, the magnitude of the vertical force on the cylinder decreases with increasing values of the modulus of the porosity parameter. This also shows that a porous seabed helps reducing not only the horizontal forces but also the vertical forces exerted by the waves.

3.3.3 Flow distribution around the cylinder

The surface elevation, which represents the flow distribution, is given by

$$\eta_1(x, y, z) = \left| \frac{\mathrm{i}}{A\omega} \frac{\partial \phi_1}{\partial z} \right| \quad \text{at} \quad z = 0. \tag{3.25}$$

The surface elevation of the water around a cylinder (with fixed length and radius $d/h = 0.8$ and $a/h = 2$) has been computed using Eq. (3.25). Figure 3.6 presents the contour plots of the resulting surface elevation for various values of the porosity parameter Gh. The wavenumber corresponding to the incident wave is set as $k_0 h = 1.9$. Specifically, Fig. 3.6a illustrates the flow field in the case of a rigid seabed ($Gh = 0$), while Figs. 3.6b–3.6d correspond to cases with a porous seabed ($Gh \neq 0$). It is clearly observed that the surface elevation on the leeside of the cylinder reaches its maximum for the rigid-bottom scenario. As the modulus value of porosity parameter Gh increases, the magnitude of the

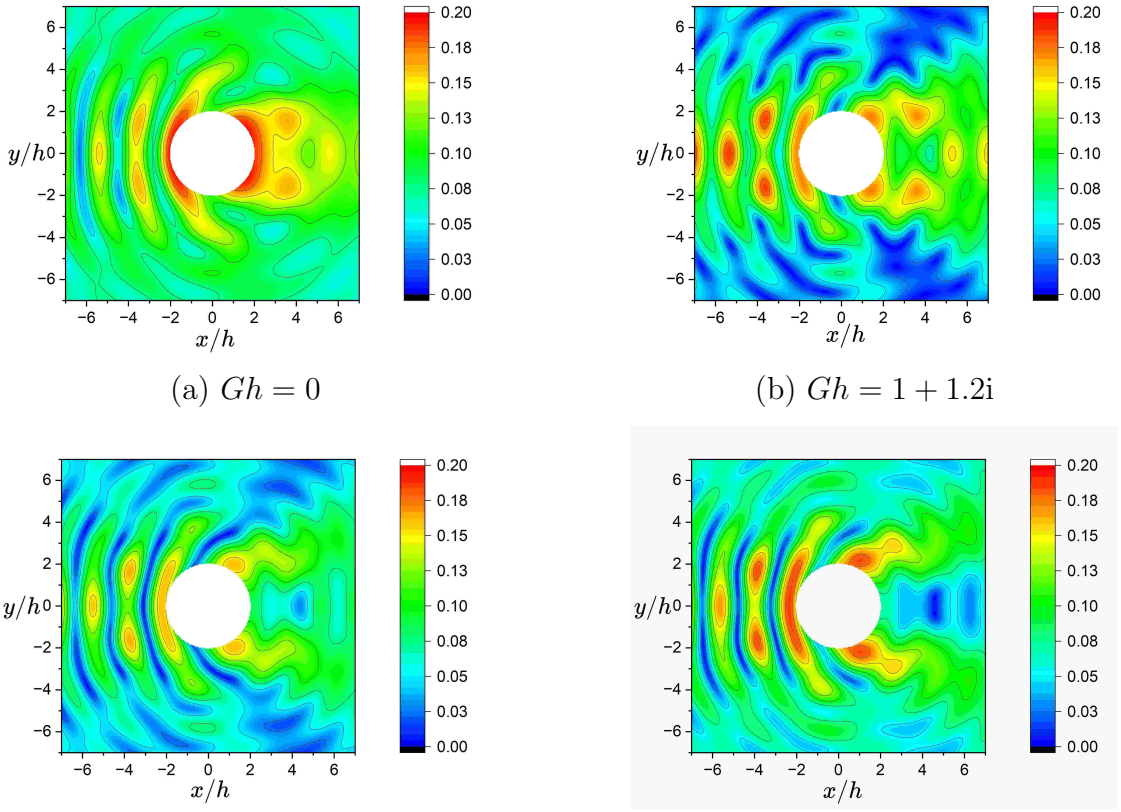

(a) $Gh = 0$ (b) $Gh = 1 + 1.2\mathrm{i}$

(c) $Gh = 1.4 + 1.8\mathrm{i}$ (d) $Gh = 2 + 2\mathrm{i}$

Figure 3.6: Contour plots of the surface elevation around a given cylinder ($d/h = 0.8$ and $a/h = 2$) for different values of the porosity parameter Gh. The wavenumber for the incident wave is taken as $k_0 h = 1.9$.

surface elevation progressively decreases. This attenuation is attributed to the increased absorption of wave energy by the more porous seabed. These findings highlight the significant role of seabed porosity in dissipating wave energy and mitigating wave-induced effects.

Figure 3.7 illustrates the free-surface elevation $\eta_1(x, y, z)$—computed using Eq. (3.25)—at $y = z = 0$ as a function of x for three cylinder radii (a) $a/h = 0.5$, (b) $a/h = 1$ and (c) $a/h = 2$ and for several values of the porosity parameter Gh. The figure shows that the free-surface elevation is the highest in the case of a rigid bottom ($Gh = 0$) in comparison to that in the case of a porous bed ($Gh \neq 0$) in both sides (i.e. for both positive and negative values of x) of the cylinders and that the free-surface elevation decreases with

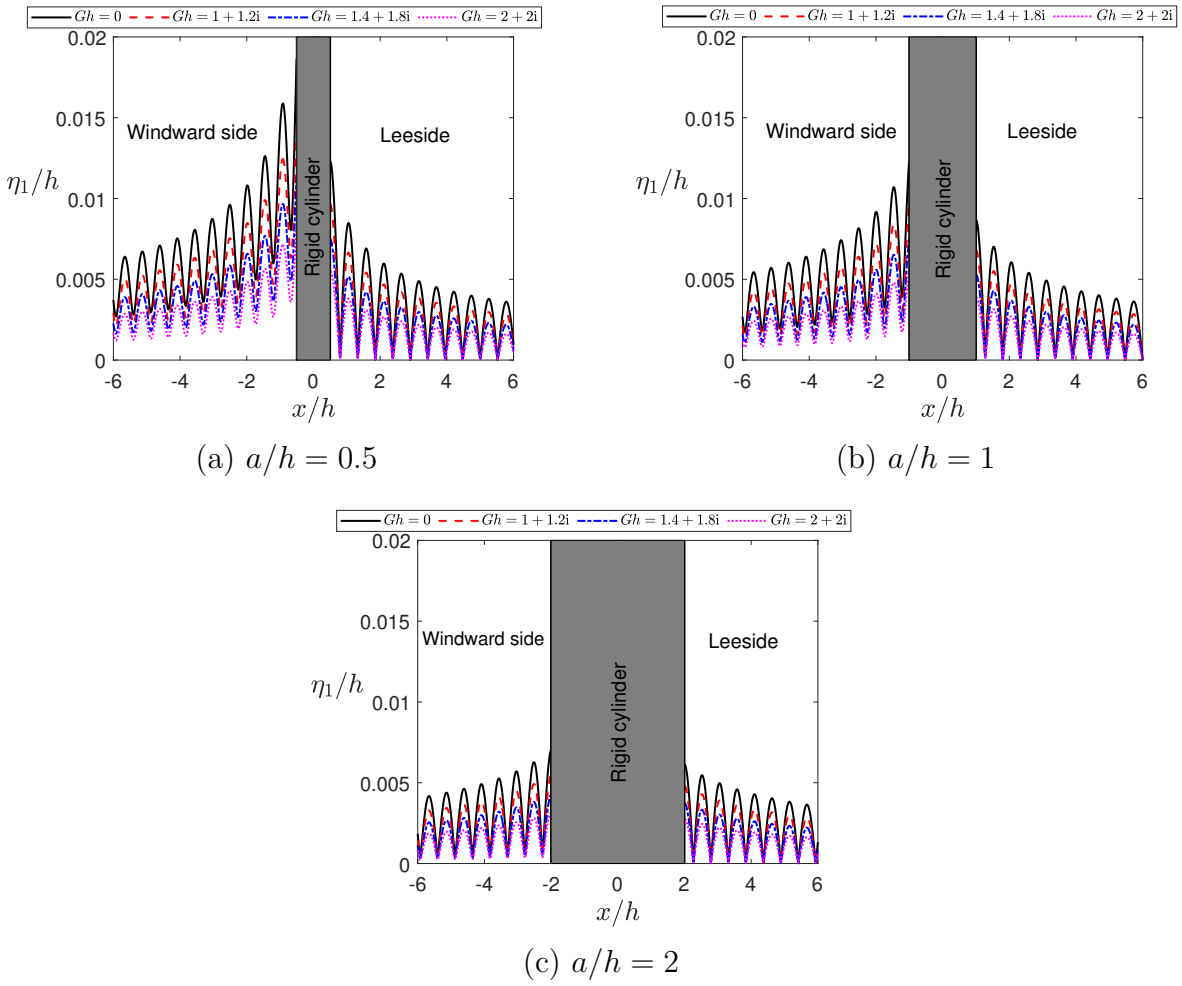

(a) $a/h = 0.5$

(b) $a/h = 1$

(c) $a/h = 2$

Figure 3.7: Free-surface elevation $\eta_1(x, y, z)$ as a function of x at $y = z = 0$ for the cylinder radii (a) $a/h = 0.5$, (b) $a/h = 1$ and (c) $a/h = 2$ for different values of the porosity parameter Gh. The height of the cylinder is fixed at $d/h = 0.6$ and the wavenumber for the incident wave is taken as $k_0h = 0.4$.

an increase in the absolute value of the porosity parameter due to the fact that a porous bed absorbs more energy than a rigid bed. Furthermore, the figure clearly illustrates a significant reduction in the surface elevation following the interaction of the incident wave with the cylinder. This attenuation becomes more pronounced in the lee side region as the radius of the cylinder increases. The observed reduction in wave height is a result of increased energy dissipation by the larger surface area of the cylinder, which obstructs and scatters more of the incoming wave energy. This effect is evident from Figs. 3.7a, 3.7b, and 3.7c, where further lowering of the surface elevation behind the cylinder is observed with increasing radius. Hence, the radius of the cylinder is another influential parameter in mitigating wave-induced forces exerted on a structure.

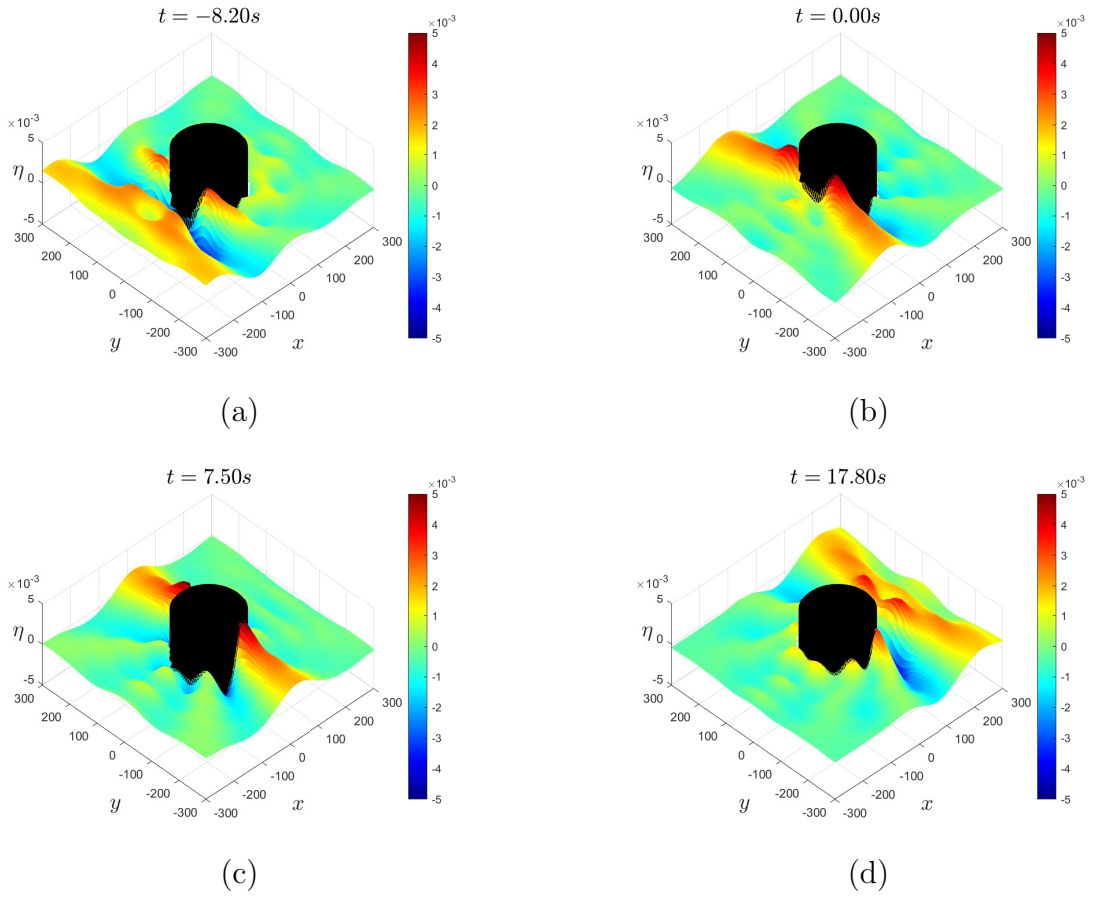

Figure 3.8: Snapshots of the water wave interaction with a given cylinder ($d/h = 0.8$ and $a/h = 2$) floating over a rigid bottom ($Gh = 0$) depicting the surface elevation at different times. The wavenumber for the incident wave is taken as $k_0 h = 1.9$.

3.3.4 Temporal simulations of the flow

In this subsection, we present the evolution of the surface elevation with time. To this end, we utilize a formula for computing the surface elevation proposed recently by Meylan [93] and Selvan *et al.* [133]. This formula reads

$$\eta(x,y,0,t) = \mathrm{Re}\left[2A\sqrt{\pi f_s}\int_{-\infty}^{\infty}\eta_1(x,y,0)\,\exp\left\{-f_s(\bar{k}-\bar{k}_c)^2-\mathrm{i}\omega t\right)\right\}\mathrm{d}\bar{k}\Bigg], \tag{3.26}$$

where A, f_s and $\bar{k}_c$ denote the amplitude of the incident wave, spreading function, and center wavenumber, respectively; and $\eta_1(x,y,0)$ is the surface elevation obtained from Eq. (3.25).

We estimate the integral in Eq. (3.26) for a fixed domain by using the midpoint rule of numerical integration. For our simulations, the amplitude of the incident wave A has been

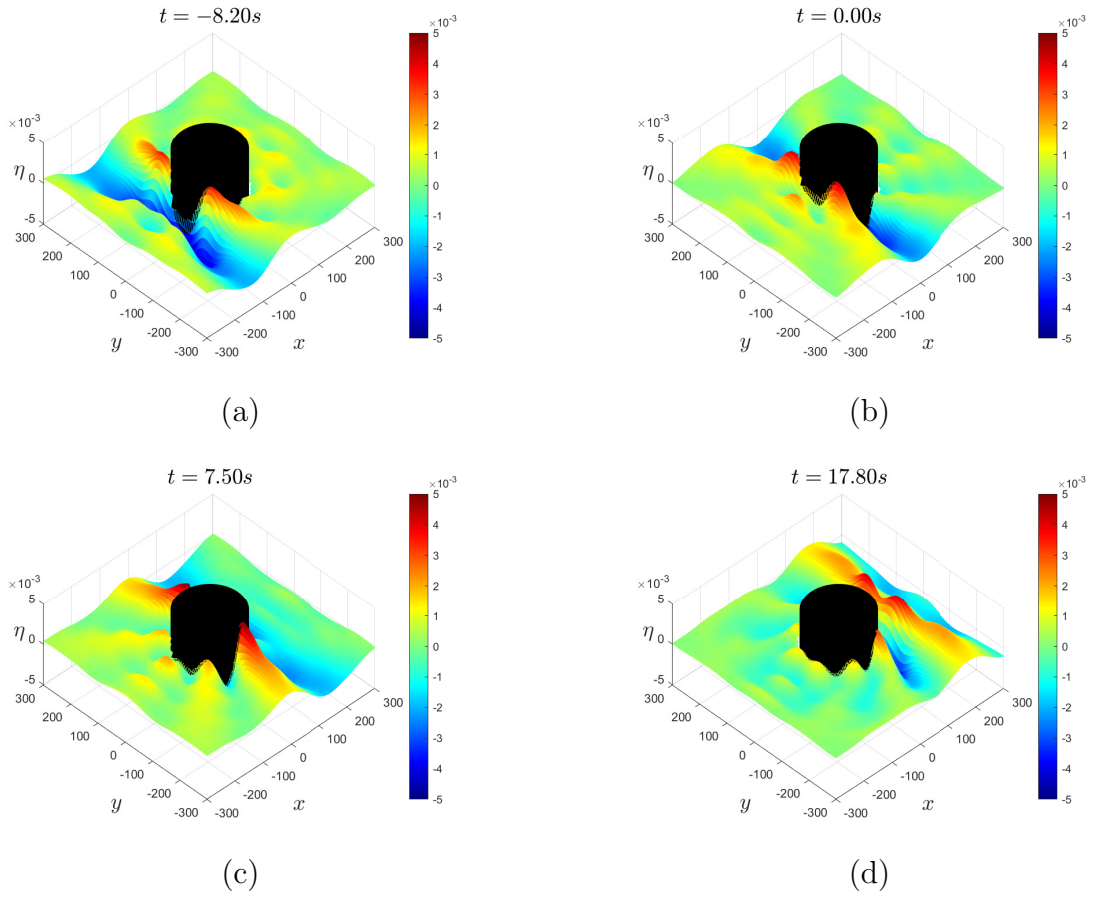

Figure 3.9: Snapshots of the water wave interaction with a given cylinder ($d/h = 0.8$ and $a/h = 2$) floating over a porous seabed ($Gh = 2 + 2\mathrm{i}$) depicting the surface elevation at different times. The wavenumber for the incident wave is taken as $k_0 h = 1.9$.

taken as 1 m, the value of the spreading function s has been taken as $2\,\mathrm{m}^2$ and the value of the parameter $\bar{k}_c$ has been taken as $\bar{k}_c = 1/h$ following [93]. The static representations of the time simulations of wave scattering by a given cylinder ($d/h = 0.8$ and $a/h = 2$) are illustrated in Fig. 3.8 for the rigid bottom ($Gh = 0$) and in Fig. 3.9 for a porous seabed ($Gh = 2 + 2\mathrm{i}$). Both figures reveal that the surface elevation reduces after the wave hits the structure and it further reduces steadily with time as the wave propagates behind the structure creating a calm zone behind the structure. Furthermore, a comparison of the corresponding sub-figures in Fig. 3.8 and Fig. 3.9 shows that the surface elevation is lesser in the porous-seabed case in comparison to that in the rigid-bottom case at all times. This substantiates the fact that the porosity of the seabed plays an important role in reducing the wave energy.

3.4 Conclusion

This chapter investigates the interaction of a water wave with a right circular surface-piercing rigid cylinder mathematically via the EEM. The resulting system of equations have been solved numerically to determine the velocity potentials both regions. The velocity potentials have then been utilized to compute the horizontal and vertical forces exerted on the cylinder and to gain deeper insights into the flow distribution at the surface. It is observed that in the presence of a porous seabed, the wave forces exerted on the cylinder are reduced compared to the rigid seabed case. Similarly, the surface elevation on the leeside is lower, the flow distribution around the cylinder is weaker, and the time-domain simulations further confirm that the free-surface elevation decreases when a porous seabed is considered instead of a rigid one. It has been found that for a fixed radius the horizontal force exerted on the cylinder decreases with increasing the length of the cylinder whereas the vertical force behaves the other way round. Moreover, both the horizontal and vertical forces exerted on the cylinder with a fixed radius and length, decrease with increasing the modulus of the porosity parameter. Thus, the porous seabed plays an important role in reducing wave forces on a circular cylinder. The temporal simulations presented in Figs. 3.8 and 3.9 illustrate that a rigid cylindrical structure is capable of reducing the wave energy and a porous seabed helps in reducing the wave energy even more.

Chapter 4

Wave interaction with multiple cylinders

This chapter explores the effectiveness of multiple circular cylinders placed over a porous bottom in reducing wave energy directed toward the leeside zone. Specifically, we investigate the horizontal forces exerted on the cylinders and temporal simulations of the fluid flow for different values of wave and structural parameters. Additionally, the study provides a comprehensive analysis of the flow field around the cylinders to gain deeper insights into the dynamics of wave-structure interactions. This chapter can be regarded as an Chapter 3.

4.1 Mathematical framework

4.1.1 Problem overview

In a global Cartesian coordinate system with its origin O being fixed at a point situated at the still water level and its positive z-axis being directed in the vertically upward direction, we consider the problem of surface wave scattering by N equidistantly-placed identical right circular cylinders of height d and radius a—with their axes being in the direction parallel to the z-axis—floating over a porous seabed located at the water depth h. A schematic of the problem when the cylinders are placed in a straight-line configuration is exhibited in Fig. 4.1. Towards the latter part of this chapter, we shall also investigate the problem when four cylinders are placed in a rectangular configuration. The problem domain is comprised of the $N + 1$ regions: (i) the N interior regions, i.e., the regions beneath all N cylinders, and (ii) the exterior region, i.e., the remaining region (above which no structure is present).

To tackle the problem further, corresponding to the global Cartesian coordinate system (x, y, z), we also define a tantamount global cylindrical coordinate system (r, θ, z) such that $x = r\cos\theta$ and $y = r\sin\theta$. Moreover, we also introduce N local Cartesian (and equivalent cylindrical) coordinate systems, each associated with one of the N cylinders.

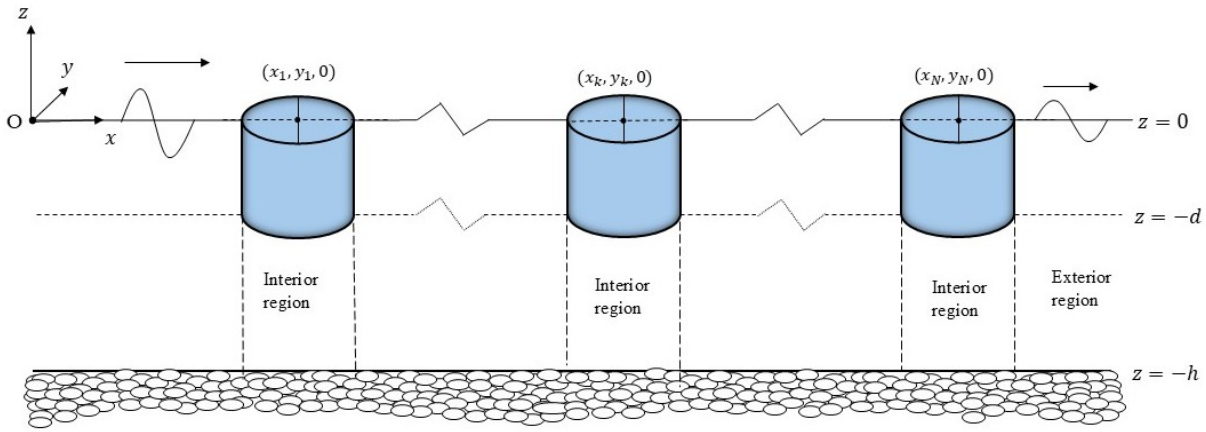

Figure 4.1: Schematic diagram of multiple circular cylinders placed in a straight line arrangement over a porous seabed.

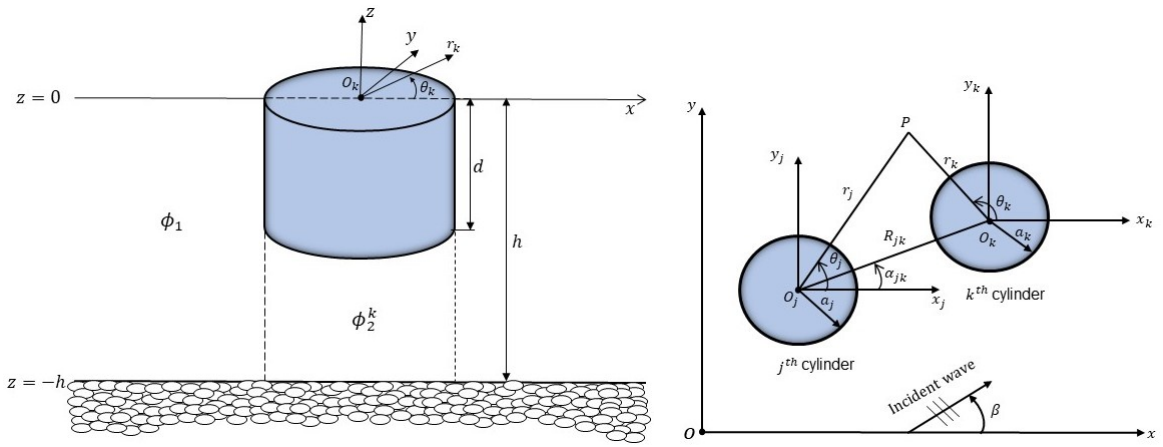

(a) (b)

Figure 4.2: (a) Depiction of the local coordinate system for the k^{th} cylinder, and (b) top view of the local coordinate systems for the j^{th} and k^{th} cylinders along with the global Cartesian coordinate system and with the incident wave propagating at angle β.

For the k^{th} cylinder, the local Cartesian coordinate system (x_k, y_k, z) and an equivalent cylindrical coordinate system (r_k, θ_k, z) are such that the z-axes of both coordinate systems coincide with the axis of the cylinder, the origin O_k of both coordinate systems is at the center of the upper cross-section of the cylinder (situated at the still water level) as shown in Fig. 4.2a, and $x_k = r_k \cos\theta$ and $y_k = r_k \sin\theta$. A top view of the local coordinate systems for the j^{th} and k^{th} cylinders along with the global Cartesian coordinate system is depicted in Fig. 4.2b. The figure also sketches the direction of the incoming wave propagating at angle β.

4.1.2 Governing equation and boundary conditions

Since the flow is considered irrotational, it can be characterized by a velocity potential function, denoted by $\Phi(r, \theta, z, t)$. Assuming the fluid motion follows simple harmonic behavior with angular frequency ω, the velocity potential is expressed in the form $\Phi(r, \theta, z, t) = \mathrm{Re}\{\phi(r, \theta, z)\, \mathrm{e}^{-\mathrm{i}\omega t}\}$. With the assumptions of an incompressible fluid and irrotational flow, the equation of continuity reduces to the Laplace equation $\nabla^2\Phi = 0$, which with the above form of Φ yields $\nabla^2\phi = 0$ and that in the cylindrical coordinate system reads

$$\frac{\partial^2\phi}{\partial r^2} + \frac{1}{r}\frac{\partial\phi}{\partial r} + \frac{1}{r^2}\frac{\partial^2\phi}{\partial\theta^2} + \frac{\partial^2\phi}{\partial z^2} = 0. \tag{4.1}$$

Owing to the porous nature of the seabed, the boundary condition applied at the ocean or sea bottom is governed by Eq. (3.2). To distinguish the velocity potentials in different regions, let us denote the spatial velocity potential in the exterior region by $\phi_1(r, \theta, z)$ and that in the k^{th} interior region (i.e., in the region below the k^{th} cylinder) by $\phi_2^k(r, \theta, z)$. It is, however, worthwhile noting that, owing to the presence of the cylinders and owing to the relation between the global and local coordinate systems, ϕ_1 and ϕ_2^k both also depend on r_j and θ_j for all $j = 1, 2, \ldots, N$. To determine the velocity potential in different regions, the required boundary conditions are as follows.

The (linearized) free-surface boundary condition at $z = 0$ defined in Eq. (3.3). Due to the rigid body of the cylinder, the boundary condition at the bottom of the k^{th} (for $k = 1, 2, 3, \ldots, N$) cylinder, i.e., $z = -d$ reads

$$\left.\frac{\partial\phi_2^k}{\partial z}\right|_{z=-d} = 0, \quad r \le a. \tag{4.2}$$

To write the other boundary conditions, it is convenient to divide the flow domain vertically into two parts, namely $\Omega_1 = \{z : -d \le z \le 0\}$ and $\Omega_2 = \{z : -h \le 0 \le -d\}$. The structural boundary condition at the fluid-cylinder interface $r_k = a_k$ of the k^{th} cylinder ($k = 1, 2, \ldots, N$) is given by

$$\frac{\partial\phi_1}{\partial r_k} = 0 \quad \forall \quad z \in \Omega_1. \tag{4.3}$$

The matching conditions for the pressure continuity in the domain Ω_2 for the k^{th} cylinder $(k = 1, 2, \ldots, N)$ is given by

$$\phi_1 = \phi_2^k \quad \text{at} \quad r_k = a_k \quad \forall \quad z \in \Omega_2 \tag{4.4}$$

and the radial velocity continuity in the domain Ω_2 for the k^{th} cylinder $(k = 1, 2, \ldots, N)$ is given by

$$\frac{\partial \phi_1}{\partial r_k} = \frac{\partial \phi_2^k}{\partial r_k} \quad \text{at} \quad r_k = a_k \quad \forall \quad z \in \Omega_2. \tag{4.5}$$

Furthermore, in the exterior region, the diffracted part of the velocity potential is required to meet the far-field boundary condition [130]

$$\lim_{r\to\infty} \sqrt{r} \left(\frac{\partial}{\partial r}(\phi_1 - \phi_I) - \mathrm{i}k_0(\phi_1 - \phi_I) \right) = 0, \tag{4.6}$$

where r represents the global polar coordinate, k_0 denotes the wavenumber of the progressive mode and obeys to the dispersion relation [82]

$$k_0(k_0 \tanh(k_0 h) - G) = \frac{\omega^2}{g}\big(k_0 - G \tanh(k_0 h)\big), \tag{4.7}$$

and ϕ_I is the velocity potential for the incident wave. In the general Cartesian coordinate system $Oxyz$, the expression of ϕ_I—as discussed in Refs. [168]—is given by

$$\phi_I(x, y, z) = -\frac{\mathrm{i}gA}{\omega} \frac{k_0 \cosh(k_0(h + z)) - G \sinh(k_0(h + z))}{k_0 \cosh(k_0 h) - G \sinh(k_0 h)} e^{\mathrm{i}k_0(x \cos\beta + y \sin\beta)} \tag{4.8}$$

and in the local cylindrical coordinate system $O_k r_k \theta_k z$ is given by

$$\begin{aligned} \phi_I(r_k, \theta_k, z) = &- \frac{\mathrm{i}gA}{\omega} \frac{k_0 \cosh(k_0(h + z)) - G \sinh(k_0(h + z))}{k_0 \cosh(k_0 h) - G \sinh(k_0 h)} e^{\mathrm{i}k_0(x_k \cos\beta + y_k \sin\beta)} \\ &\times \sum_{m=-\infty}^{\infty} \mathrm{i}^m e^{-\mathrm{i}m\beta} J_m(k_0 r_k) e^{\mathrm{i}m\theta_k}. \end{aligned} \tag{4.9}$$

4.2 Solution method

4.2.1 Velocity potential in the exterior region

The velocity potential in the exterior region is represented as the superposition of the incident wave potential, ϕ_I, and the scattered wave potential, ϕ_S, i.e.,

$$\phi_1 = \phi_I + \phi_S. \tag{4.10}$$

In the local coordinate system corresponding to the k^{th} cylinder, the velocity potential of the scattered waves is expressed mathematically as [167, 170]

$$\phi_S(r_k,\theta_k,z)=\sum_{k=1}^{N}\sum_{m=-\infty}^{\infty}\sum_{n=0}^{\infty}\mathcal{A}_{mn}^{k}H_m^{(1)}(k_nr_k)\mathrm{e}^{\mathrm{i}m\theta_k}\,f_n(z), \tag{4.11}$$

where $\mathcal{A}_{mn}^{k}$ for $k=1,2,3,\ldots,N$ and $m,n\in\mathbb{N}$ denote the unknown coefficients and the functions [130]

$$f_n(z)=\frac{k_n\cosh\left(k_n(h+z)\right)-G\sinh\left(k_n(h+z)\right)}{k_n\cosh\left(k_nh\right)-G\sinh\left(k_nh\right)}\quad\text{for}\quad n=0,1,2,3,\ldots \tag{4.12}$$

are the eigenfunctions, and the parameters k_n denote the wavenumbers that satisfy the dispersion relation

$$\frac{\omega^2}{g}\Big(k_n-G\tanh\left(k_nh\right)\Big)=k_n\Big(k_n\tanh\left(k_nh\right)-G\Big). \tag{4.13}$$

Here, Eqs. (4.12) and (4.13) are identical to Eqs. (3.10) and (3.9), respectively. Applying Graf's addition theorem [1] in Eq. (4.11), it becomes [164, 166]

$$\begin{aligned}\phi_S(r_k,\theta_k,z)=&\sum_{m=-\infty}^{\infty}\sum_{n=0}^{\infty}\mathcal{A}_{mn}^{k}H_m^{(1)}(k_nr_k)\mathrm{e}^{\mathrm{i}m\theta_k}f_n(z)\\&+\sum_{\substack{j=1\\j\neq k}}^{N}\sum_{m=-\infty}^{\infty}\sum_{n=0}^{\infty}\sum_{m_1=-\infty}^{\infty}(-1)^{m_1}\mathcal{A}_{mn}^{j}H_{m-m_1}^{(1)}(k_nR_{jk})\mathrm{e}^{\mathrm{i}(m\alpha_{kj}-m_1\alpha_{jk})}\\&\times J_{m_1}(k_nr_k)\mathrm{e}^{\mathrm{i}m_1\theta_k}f_n(z)\quad\text{for } r_k<R_{jk}\ (\text{for } j=1,2,3,\ldots,N \text{ and } j\neq k),\end{aligned} \tag{4.14}$$

where R_{jk} is the distance between the centers of the j^{th} and k^{th} cylinders, α_{jk} is the angle of the line joining the centers of the j^{th} and k^{th} cylinders from the positive x_k-axis of the k^{th} cylinder so that $(R_{jk},\alpha_{jk},0)$ are the coordinates of the point O_j (the center of the j^{th} cylinder) in the cylindrical coordinate system associated with the k^{th} cylinder. Substituting ϕ_I and ϕ_S from Eqs. (4.9) and (4.14) in Eq. (4.10), the spatial velocity potential in the exterior region becomes

$$\phi_1(r_k,\theta_k,z)=\sum_{m=-\infty}^{\infty}\left(\mathbf{I}_k\mathrm{i}^mJ_m(k_0r_k)\mathrm{e}^{-\mathrm{i}m\beta}\mathrm{e}^{\mathrm{i}m\theta_k}f_0(z)+\sum_{n=0}^{\infty}\mathcal{A}_{mn}^{k}H_m^{(1)}(k_nr_k)\mathrm{e}^{\mathrm{i}m\theta_k}f_n(z)\right.$$

$$+\sum_{\substack{j=1\\ j\neq k}}^{N}\sum_{n=0}^{\infty}\sum_{m_1=-\infty}^{\infty}\mathcal{A}_{mn}^{j}H_{m-m_1}^{(1)}(k_nR_{jk})\mathrm{e}^{\mathrm{i}(m\alpha_{kj}-m_1\alpha_{jk})}J_{m_1}(k_nr_k)\mathrm{e}^{\mathrm{i}m_1\theta_k}f_n(z)\Bigg), \tag{4.15}$$

where $\mathbf{I}_k = (-\mathrm{i}gA/\omega)\mathrm{e}^{\mathrm{i}k_0(x_k\cos\beta+y_k\sin\beta)}$.

For further simplification of the above expression, the wavenumbers k_n need to be determined from dispersion relation (4.13) first. Nevertheless, before determining the wavenumbers, it is worthwhile noting that for $G = 0$ (the case of a rigid bottom), the dispersion relation (4.13) and the eigenfunctions given in Eq. (4.12) reduce to the dispersion relation and the eigenfunctions corresponding to the rigid-bottom condition as given, for example, in [54, 105]. The wavenumbers k_n are determined from dispersion relation (4.13) in this chapter and through out this thesis numerically using the Newton–Raphson method but an appropriate initial guess is required for the convergence of the method. Therefore, to get a suitable initial guess and to understand the characteristics of the roots, we draw the contour plots of dispersion relation (4.13) in Fig. 4.3 in the case of a rigid seabed ($G = 0$) as well as in the case of a porous seabed ($G \neq 0$). Figure 4.3 illustrates that exactly two roots are located near the real axis, while the other roots are located close to the imaginary axis in both scenarios ($G = 0$ and $G \neq 0$). From Fig. 4.3, it is now easy to take astute initial guesses for the roots. It turns out that the two roots near the real axis are actually purely real roots $\pm k_0$.

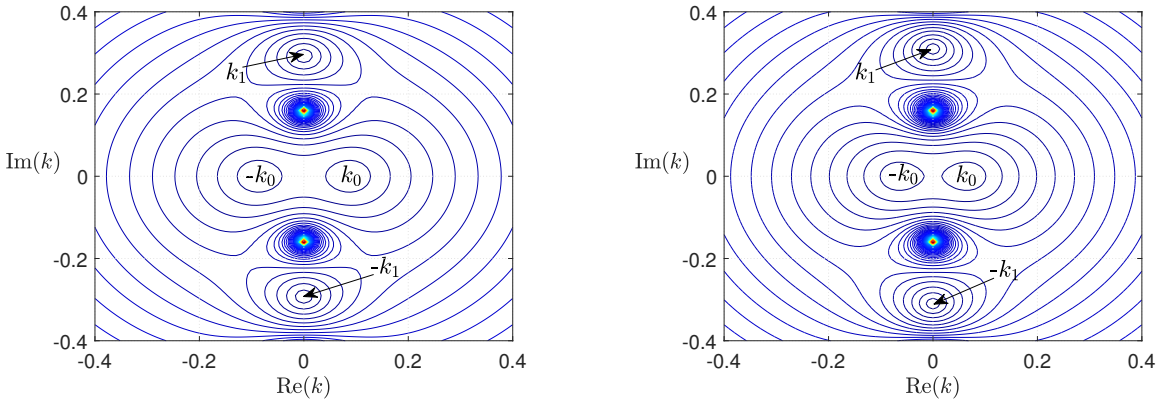

(a) (b)

Figure 4.3: Contour plots of dispersion equation (4.13)—in the exterior region—for (a) rigid bottom ($Gh = 0$) and (b) porous bottom ($Gh = 0.5$). The values of water depth (h) and time period (T) are fixed as $h = 10$m and $T = 8$s, respectively.

4.2.2 Velocity potential in the interior regions

For the interior region under the k^{th} cylinder ($k = 1, 2, 3, \ldots, N$), governing equation (4.1) along with the bottom boundary condition (3.2) gives the spatial velocity potential in the interior region under the k^{th} cylinder [133]

$$\phi_2^k = \sum_{m=-\infty}^{\infty} \sum_{n=0}^{\infty} \mathcal{B}_{mn}^k I_m(p_n r_k)\, g_n(z)\, \mathrm{e}^{\mathrm{i}m\theta_k}, \tag{4.16}$$

where $\mathcal{B}_{mn}^k$ are the unknown coefficients, the wavenumbers p_n and the eigenfunctions g_n satisfy Eqs. (3.12) and (3.13), respectively. Similarly to that for the exterior region, for further simplification of Eq. (4.16), we first determine the wavenumbers p_n from dispersion relation (3.12) numerically using the Newton–Raphson method.

4.2.3 Computation of velocity potential in all regions simultaneously

The unknown coefficients in the spatial velocity potentials given in Eqs. (4.15) and (4.16) are determined using the remaining boundary conditions (4.3)–(4.5), which indeed couple all these spatial velocity potentials. On substituting the spatial velocity potentials ϕ_1 and ϕ_2^k from Eqs. (4.15) and (4.16) in boundary conditions (4.3)–(4.5) and exploiting the orthogonality conditions of trigonometric functions in the region $[0, 2\pi]$, the resulting system of (algebraic) equations reads

$$\begin{aligned}
&\mathbf{I}_k \mathrm{i}^q e^{-\mathrm{i}q\beta} J_q(k_0 a_k) X_{0l} + \sum_{n=0}^{\infty} \mathcal{A}_{qn}^k H_q^{(1)}(k_n a_k) X_{nl} \\
&+ \sum_{\substack{j=1 \\ j\neq k}}^{N} \sum_{m=-\infty}^{\infty} \sum_{n=0}^{\infty} \left((-1)^q \mathcal{A}_{mn}^j H_{m-q}^{(1)}(k_n R_{kj}) e^{\mathrm{i}(m\alpha_{jk} - q\alpha_{kj})} J_q(k_n a_k) X_{nl} \right) = \mathcal{B}_{ql}^k I_q(p_l a_k) \delta_{0l} Y_l,
\end{aligned} \tag{4.17}$$

$$\begin{aligned}
&\mathbf{I}_k \mathrm{i}^q e^{-\mathrm{i}q\beta} k_0 J_q'(k_0 a_k) \delta_{0l} Z_l + \mathcal{A}_{ql}^k k_l H_q^{(1)'}(k_l a_k) Z_l \\
&+ \sum_{\substack{j=1 \\ j\neq k}}^{N} \sum_{m=-\infty}^{\infty} \left((-1)^q \mathcal{A}_{ml}^j H_{m-q}^{(1)}(k_l R_{kj}) e^{\mathrm{i}(m\alpha_{jk} - q\alpha_{kj})} k_l J_q'(k_l a_k) Z_l \right) = \sum_{n=0}^{\infty} \left(\mathcal{B}_{qn}^k p_n I_q'(p_n a_k) Y_{1nl} \right),
\end{aligned} \tag{4.18}$$

where $'$ denotes the derivative with respect to r_k and

$$X_{nl} = \int_{\Omega_2} f_n(z) g_l(z) \mathrm{d}z, \quad Y_l = \int_{\Omega_2} g_l^2(z) \mathrm{d}z,$$

$$Z_l = \int_{\Omega_1+\Omega_2} f_l^2(z)\mathrm{d}z, \quad Y_{1nl} = \int_{\Omega_2} g_n(z) f_l(z)\mathrm{d}z, \tag{4.19}$$

for $l, n = 0, 1, 2, 3, \ldots$ and $k = 1, 2, \ldots, N$. A detailed derivation of Eqs. (4.17) and (4.18) are given in Appendix A. Note that the system of simultaneous equations formed by Eqs. (4.17) and (4.18) contains an infinite number of unknowns $\mathcal{A}_{qn}^k$ and $\mathcal{B}_{qn}^k$. However, finding all infinite unknowns is impracticable. Thus, it is quite typical to truncate the series in Eqs. (4.17) and (4.18). To truncate the series for n and m involved in Eqs. (4.17) and (4.18), we set $n = \mathsf{N}^*$ for some $\mathsf{N}^* \in 0 \cup \mathbb{N}$ and $m \in \{-M, \ldots, 0, \ldots, M\}$ for some value of $M \in 0 \cup \mathbb{N}$. In addition, the ranges of q and l are specified as $q = \{-M, \ldots, 0, \ldots, M\}$ and $l = \mathsf{N}^*$ for some $\mathsf{N}^* \in 0 \cup \mathbb{N}$ in Eqs. (4.17) and (4.18). After solving the system of equations, the unknown coefficients are determined. Equations (4.15) and (4.16) on substituting the determined unknowns give the velocity potentials in both regions, i.e., in the exterior region and interior regions.

4.3 Results and discussions

We have validated our code by computing the horizontal force in the limiting case of a single cylinder over a rigid bottom and comparing it with the theoretical and experimental results available in the literature. To show the comparison, let us first define the horizontal force. The horizontal force $\mathcal{F}_h^k$ exerted on the k^{th} cylinder is defined as [73]

$$\mathcal{F}_h^k = -\mathrm{i}\rho\omega a_k \int_0^{2\pi} \int_{\Omega_1} \phi_1(a_k, \theta_k, z)\, \cos\theta_k \, \mathrm{d}z \, \mathrm{d}\theta_k \tag{4.20}$$

and the dimensionless horizontal force F_h^k exerted on the k^{th} cylinder as

$$F_h^k = \left| \frac{\mathcal{F}_h^k}{F^*} \right|, \tag{4.21}$$

where F^* is a reference force used for dimensionless scaling. We have taken the reference force $F^* = \rho g a^2 d$ in the present chapter. The physical parameters used in the calculations are as follows: water depth $h = 20\,\mathrm{m}$, the incident amplitude $A = 1\,\mathrm{m}$, the fluid density $\rho = 1025\,\mathrm{kg/m^3}$ and acceleration due to gravity $g = 9.8\,\mathrm{m/s^2}$.

4.3.1 Code validation

To validate our code, we examine the limiting case of a single cylinder (i.e., $N = 1$) floating above a rigid seabed ($G = 0$). For this scenario, Fig. 4.4 presents the horizontal

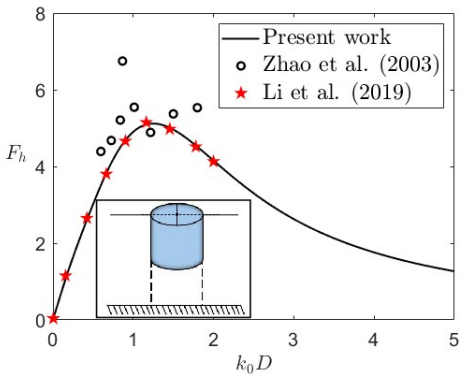

Fig

Figure 4.4: Dimensionless horizontal force F_h^k exerted on a single cylinder over a rigid seabed ($G = 0$) plotted against the dimensionless wavenumber k_0D. The circular markers show the experimental results of Zhao *et al.* [159] and the red stars depict the dimensionless horizontal force obtained analytically by Li & Liu [67]

force calculated using our code (shown as a solid line) as a function of the dimensionless wavenumber k_0D, where $D = 2a$ is the cylinder diameter. For comparison, the figure also includes experimental results from [159] (represented by circular markers) and the analytical solution from [67] (indicated by stars). The horizontal force calculated in the present work (solid lines) shows excellent agreement with the analytical solution in [67], and also aligns reasonably well with the experimental data given in [159], thereby confirming the accuracy and reliability of our numerical code.

4.3.2 Temporal simulations of the fluid flow

To gain a deeper understanding of the interaction between the fluid and the cylinders, we present time-domain simulations that show the variation of wave height over time. For this purpose, we employ the transformation formula for the free surface elevation η, as given in Eq. (3.26). In simulations, the spreading function f_s has been set to $2\,\mathrm{m}^2$ and the parameter k_c has been assigned a value of $k_c = 1/h$. The integration in Eq. (3.26) has been computed numerically by restricting the domain of $\bar{k}$ to $[-10, 40]$ per meter and using the midpoint rule of numerical integration.

4.3.3 Horizontal force on the cylinders and the temporal simulations

In this subsection, we present the horizontal forces exerted on the cylinders placed in different configurations and the temporal simulations of the fluid flow. Several cases

N^*	1^{st} **cylinder**		2^{nd} **cylinder**	
	$k_0h = 2.5$	$k_0h = 4$	$k_0h = 2.5$	$k_0h = 4$
1	0.040770	0.031421	0.025142	0.008863
2	0.040024	0.030148	0.023671	0.008734
3	0.038165	0.029251	0.025812	0.008802
5	0.037924	0.028481	0.024308	0.008950
7	0.036771	0.028230	0.024015	0.009045
9	0.036770	0.028233	0.024019	0.009045

Table 4.1: Variation of the horizontal force F_h^k for different values of the evanescent mode N^* with fixed values of $Gh = 0.5$, $a/h = 0.5$, $d/h = 0.4$, $\beta = 30^\circ$ and $M = 5$ for two cylinders in a horizontal array.

exhibiting the results for a rigid seabed ($G = 0$), for a porous bottom ($G \neq 0$) with different values of the porous-effect parameter, and for cylinders of various radii and heights are also considered in the following illustrations. Note that the still water depth h has been used for the non-dimensionalization of the porous-effect parameter, wavenumber, radius, and height of each cylinder.

In Table 4.1, we present a convergence study of the horizontal force F_h^k for two values of the dimensionless wavenumber, $k_0h = 2.5$ and $k_0h = 4$, considering an array of two cylinders with a fixed value of $M = 5$. The table demonstrates that the proposed analytic solution converges rapidly, achieving five-decimal points accuracy already for $\mathsf{N}^* = 7$. Hence, these values will be used in the subsequent analyses.

Case 1: Two cylinders placed in a horizontal array configuration

We consider the case of two cylinders placed at a (axis-to-axis) distance $2h$ apart in an array configuration. Figures 4.5–4.8 exhibit the (dimensionless) horizontal forces exerted on the first and second cylinders in sub-figures (a) and (b), respectively, plotted against the (dimensionless) wavenumber k_0h for different parameters. Figure 4.5 illustrates the horizontal forces on the cylinders for the rigid seabed ($G = 0$) as well as for porous seabeds ($G \neq 0$) when the angle of the incident wave is fixed to $\beta = 30^\circ$ and the (dimensionless) radii and heights of both cylinders are fixed to $a/h = 0.5$ and $d/h = 0.4$. The figure shows that the horizontal forces exerted on both cylinders are the highest when the seabed is rigid (i.e., when $G = 0$) in comparison to that when the seabed is porous (i.e. when $G \neq 0$). Moreover, the horizontal forces exerted on both cylinders decrease with increasing the porosity of the seabed. This is because as the porosity parameter increases, the void spaces

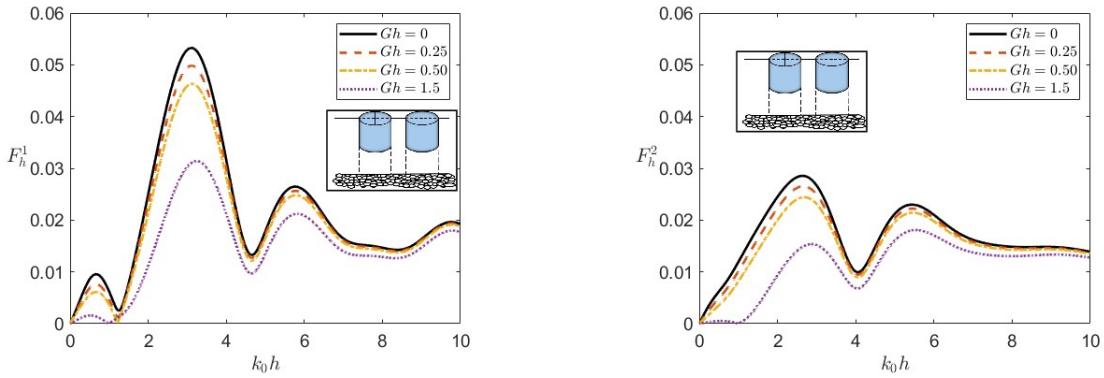

(a) (b)

Figure 4.5: Horizontal force on the (a) first and (b) second cylinders placed in an array plotted with respect to the wavenumber k_0h for different values of the porous-effect parameter Gh. The remaining parameters are set as $a/h = 0.5$, $d/h = 0.4$ and $\beta = 30°$.

between the solid particles in the seabed become larger, allowing the porous medium to behave like a sponge, absorbing more wave energy as the fluid passes through it.

A comparison between sub-figures (a) and (b) of Fig. 4.5 reveals that the horizontal force exerted on the second cylinder is generally less than that exerted on the first cylinder for all values of the porosity parameter. This is due to the fact that when the incident wave interacts with the first cylinder, a portion of the incident wave is reflected back into the water and the remaining portion is transmitted past the first cylinder. The transmitted portion of the wave, however, carries lesser energy and hence has a reduced amplitude in comparison to the energy and amplitude of the incident wave due to energy dissipation and scattering effects. The transmitted wave continues from the first cylinder onward, reaches the second cylinder, and interacts with it. Hence the horizontal force experienced by the second cylinder is less than that experienced by the first cylinder.

Figure 4.6 displays the variation in the horizontal forces on the cylinders on changing the heights of the cylinders while keeping their radii fixed to $a/h = 0.5$ for the angle of the incident wave $\beta = 30°$ and (dimensionless) porosity parameter $Gh = 0.5$. The figure shows that the horizontal forces on both cylinders decrease with an increase in the height of the cylinders, which is due to the fact that the wave force exerted on a cylinder is distributed over a larger surface area on increasing the height of the cylinder. Similarly to Fig. 4.5, a comparison between figures (a) and (b) of Fig. 4.6 also shows that the horizontal force on the second cylinder is in general less than that on the first cylinder.

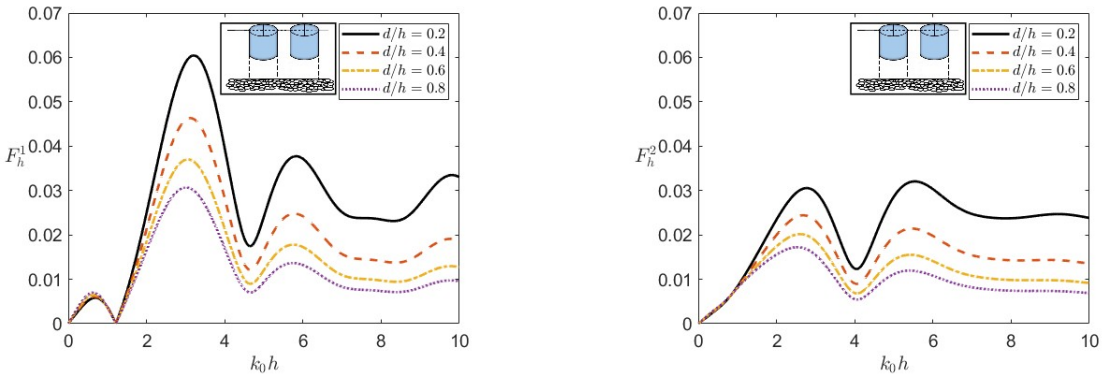

(a) (b)

Figure 4.6: Same as Fig 4.6 but for different d/h.

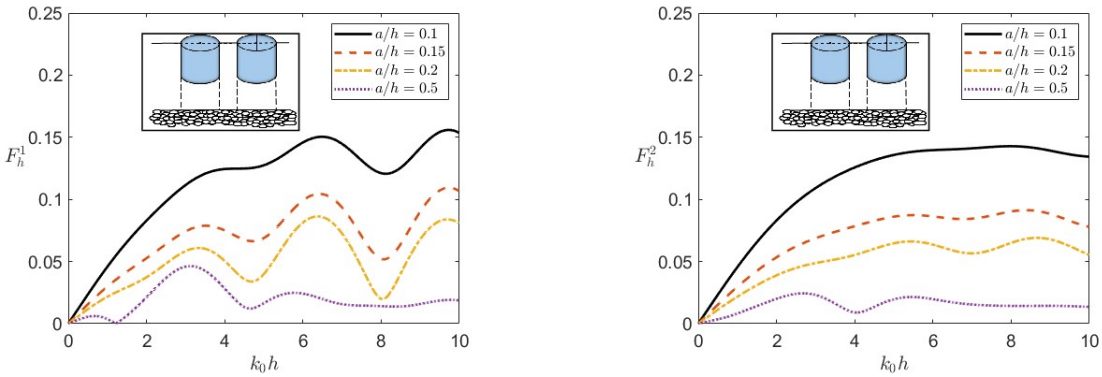

(a) (b)

Figure 4.7: Same as Fig 4.6 but for different a/h.

Figure 4.7 delineates the variation in the horizontal forces exerted on the cylinders on varying the radii of the cylinders while keeping their heights fixed to $d/h = 0.4$ for the angle of the incident wave $\beta = 30°$ and (dimensionless) porosity parameter $Gh = 0.5$. The figure shows the decrease in horizontal forces on both cylinders with an increase in the radii of the cylinders in general, which is consequent to the fact that enlarging the radius of a cylinder also expands its surface area on which the horizontal force is distributed. Decay in the horizontal force on the second cylinder in comparison to that on the first cylinder is also evident from the figure (cf. figures (a) and (b) of Fig. 4.7) due to the same reason as mentioned above.

Figure 4.8 depicts the change in the horizontal forces exerted on the cylinders of fixed radii and heights ($a/h = 0.5$ and $d/h = 0.4$) with change in the angle of the incident wave β for the (dimensionless) porosity parameter $Gh = 0.5$. Similarly to Figs. 4.5–4.7,

Fig. 4.8 also shows that the horizontal force of the second cylinder is generally less than that on the first cylinder Nevertheless, in contrast to Figs. 4.5–4.7, there is no harmony

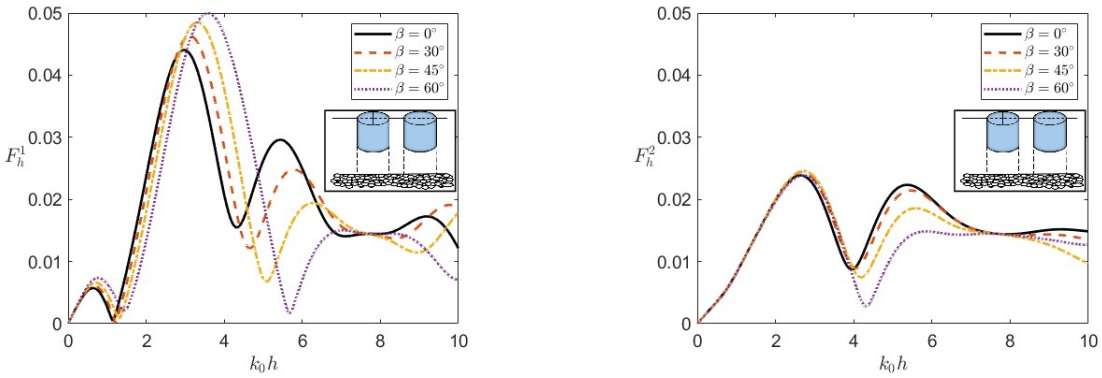

(a) (b)

Figure 4.8: Same as Fig 4.6 but for different β.

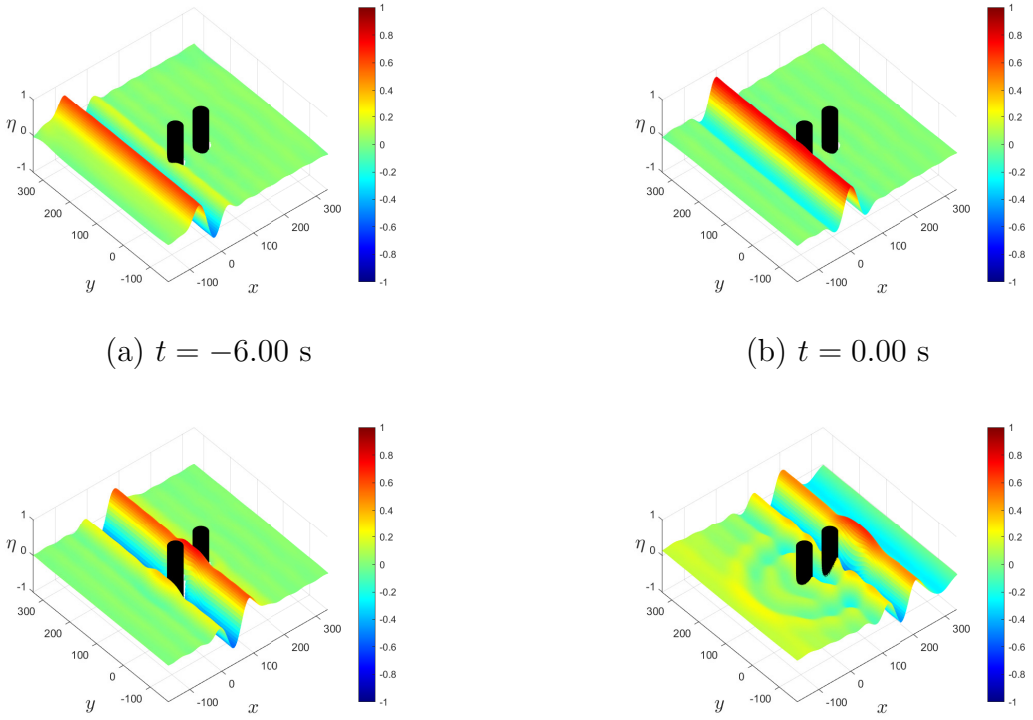

(a) $t = -6.00$ s (b) $t = 0.00$ s

(c) $t = 7.20$ s (d) $t = 28.40$ s

Figure 4.9: Snapshots of a simulation at different time instances illustrating the variation in the height of the water surface when a water wave approaching at an incident angle $\beta = 0°$ interacts with two cylinders of (dimensionless) radii $a/h = 0.5$ and (dimensionless) heights $d/h = 0.4$ placed at a distance $2h$ apart in a horizontal array configuration over a rigid seabed ($G = 0$).

in the profiles of the horizontal forces on changing the incident angle. A possible reason for this could be the implicit dependence of the horizontal force on the incident angle β through the velocity potential ϕ_1 (see, Eq. (4.20)), which depends on β in an involved way.

For a comprehensive understanding of wave interaction with two cylinders of fixed radii and heights ($a/h = 0.5$ and $d/h = 0.8$) placed at a (axis-to-axis) distance $2h$ apart (with $h = 50\,\mathrm{m}$) in an array configuration and to perceive the effect of a porous seabed on the wave motion, static representations of time-dependent simulations at four distinct time instances are illustrated.

For Figs. 4.9 and 4.10, the incident wave angle is set to $\beta = 0°$ but to show the effect of a porous seabed, the porosity parameter is taken as $G = 0$ (rigid seabed) and $Gh = 0.5$ (porous seabed) in Figs. 4.9 and 4.10, respectively. Figure 4.10 and Fig. 4.11 display the results for different angles of the incident wave ($\beta = 0°$ in Fig. 4.10 and $\beta = 30°$ in Fig. 4.11) while keeping all other physical characteristics the same ($Gh = 0.5$, $a/h = 0.5$ and $d/h = 0.8$ and $h = 50\,\mathrm{m}$ for both figures). The snapshots in each of

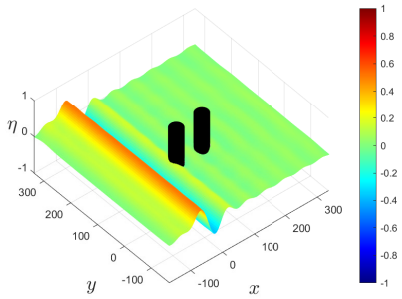

(a) $t = -6.00$ s

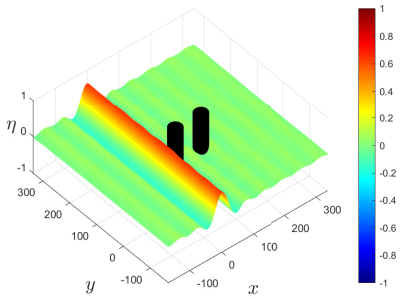

(b) $t = 0.00$ s

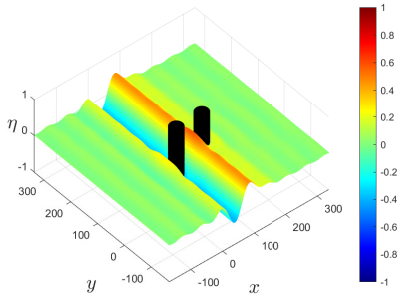

(c) $t = 7.40$ s

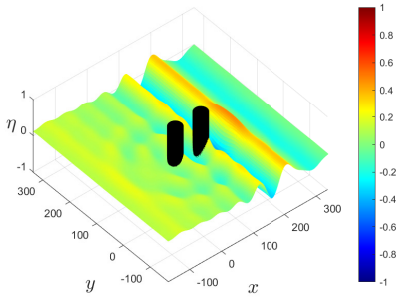

(d) $t = 28.40$ s

Figure 4.10: Same as Fig 4.9 but for the porosity parameter $Gh = 0.5$.

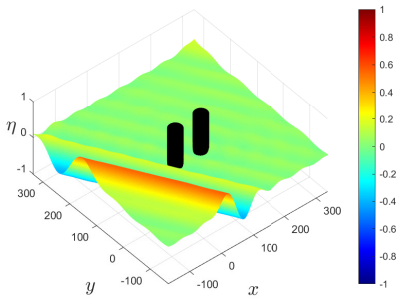

(a) $t = -6.00$ s

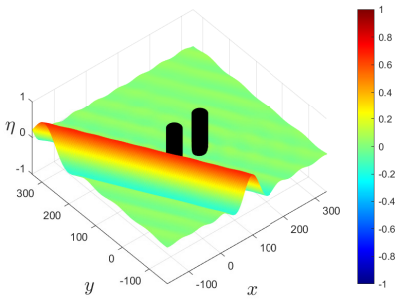

(b) $t = 0.00$ s

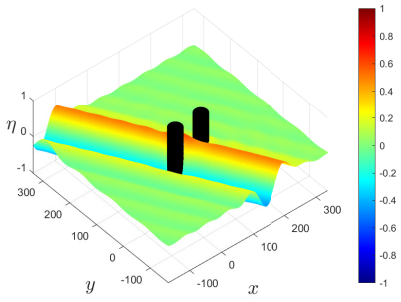

(c) $t = 7.20$ s

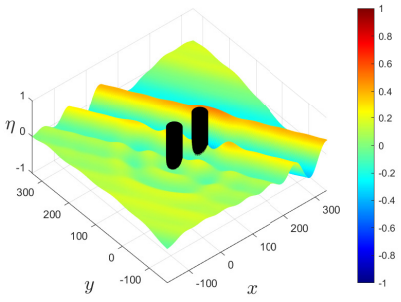

(d) $t = 28.40$ s

Figure 4.11: Same as Fig 4.10 but for incident angle $\beta = 30°$.

Figs. 4.9–4.11 exhibit the gradual decrease in the elevation of the water surface with time after the interaction of the wave with the cylinders. A visual comparison between the corresponding sub-figures of Figs. 4.9 and 4.10 shows the decrease in the elevation of the water surface due to the porosity of the seabed. Similarly to Fig. 4.10, Fig. 4.11 also bespeaks a significant reduction in the elevation of the wave amplitude towards the back side of the second cylinder due to the porosity of the seabed.

Case 2: Three cylinders in a horizontal array configuration

We now consider the case of three cylinders placed at a (axis-to-axis) distance $2h$ apart from each other in an array configuration. Figure 4.12 illustrates the horizontal forces exerted on the three cylinders plotted against the wavenumber k_0h, and figures (a) and (b) in the figure exhibit the horizontal forces for the porous seabed with the (dimensionless) porosity parameter $Gh = 0.25$ and $Gh = 0.5$, respectively. The figure shows that the peaks in the horizontal forces are reduced as one moves from the first cylinder to the second cylinder to the third cylinder indicating a gradual decay in the horizontal forces due to partial reflection of the wave energy on encounter with each

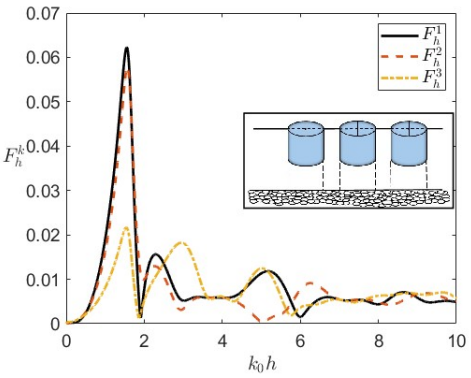

(a)

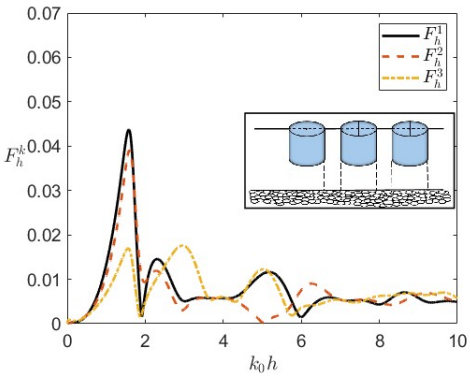

(b)

Figure 4.12: Horizontal forces exerted on the three cylinders of dimensionless radii $a/h = 0.5$ and dimensionless heights $d/h = 0.4$ kept in a horizontal array configuration for the angle of the incident wave $\beta = 30°$ and for the porous parameters (a) $Gh = 0.25$ and (b) $Gh = 0.5$.

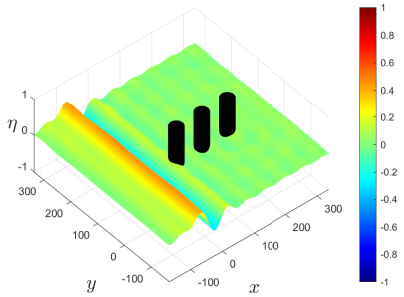

(a) $t = -6.00$ s

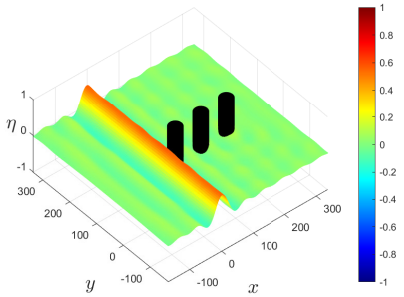

(b) $t = 0.00$ s

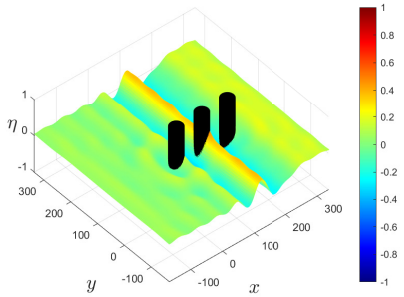

(c) $t = 19.20$ s

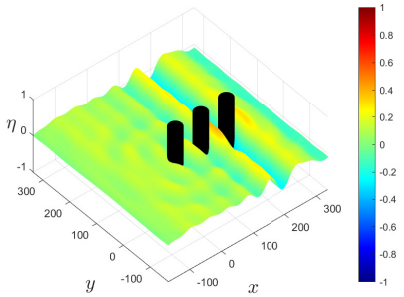

(d) $t = 28.60$ s

Figure 4.13: Snapshots of a simulation at different time instances illustrating the variation in the height of the water surface when a water wave approaching at an incident angle $\beta = 0°$ interacts with three cylinders of $a/h = 0.5$ and $d/h = 0.8$ placed in a horizontal array configuration over a porous seabed ($Gh = 0.5$).

cylinder. Furthermore, a comparison between figures (a) and (b) of the figure reconfirms

the decay in the horizontal forces on increasing the porous-effect parameter.

Figures 4.13 and 4.14 display snapshots from temporal simulations in the case of three identical cylinders placed equidistantly in an array for the incident wave angles $\beta = 0°$ and $\beta = 30°$, respectively. Both figures show the decay in the surface elevation towards the leeward side due to the same reason as mentioned above.

Furthermore, a careful comparison of the corresponding sub-figures in Figs. 4.10 and 4.13 and those in Figs. 4.11 and 4.14 reveals that the surface elevation in Figs. 4.13 and 4.14 has been reduced further in comparison to that in Figs. 4.10 and 4.11, respectively. This means that the inclusion of more structures along with a porous seabed can help reduce wave energy significantly on the leeward side.

In addition to the configuration of three cylinders in an array, Fig. 4.15 presents snapshots of the time-domain simulations for the triangular arrangement of cylinders, placed at a distance of $3h$ apart from each other. Compared to Figs. 4.13 and 4.14, the wave energy reduction in Fig. 4.15 is more pronounced. This occurs because, in the array arrangement, the wave first impacts a single cylinder, whereas, in the triangular arrangement, it

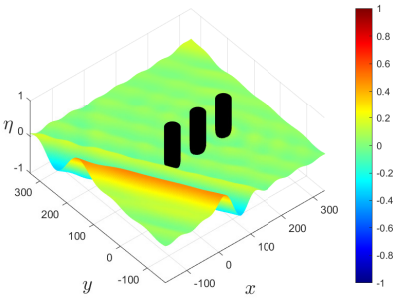

(a) $t = -6.00$ s

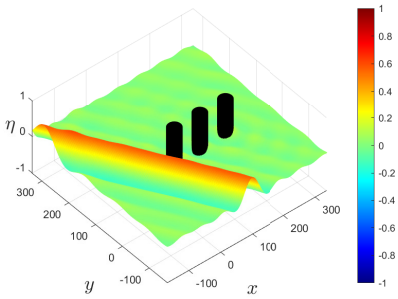

(b) $t = 0.00$ s

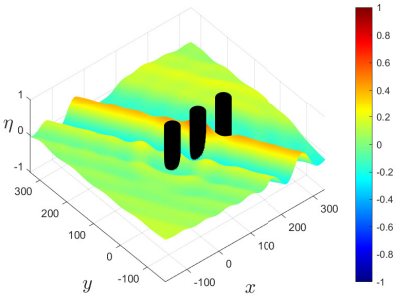

(c) $t = 19.20$ s

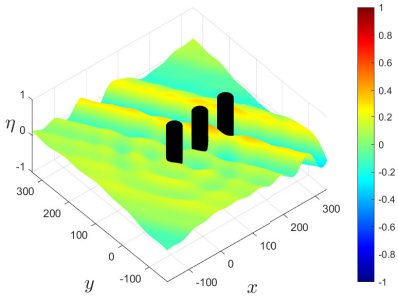

(d) $t = 28.60$ s

Figure 4.14: Same as Fig 4.13 but for incident angle $\beta = 30°$.

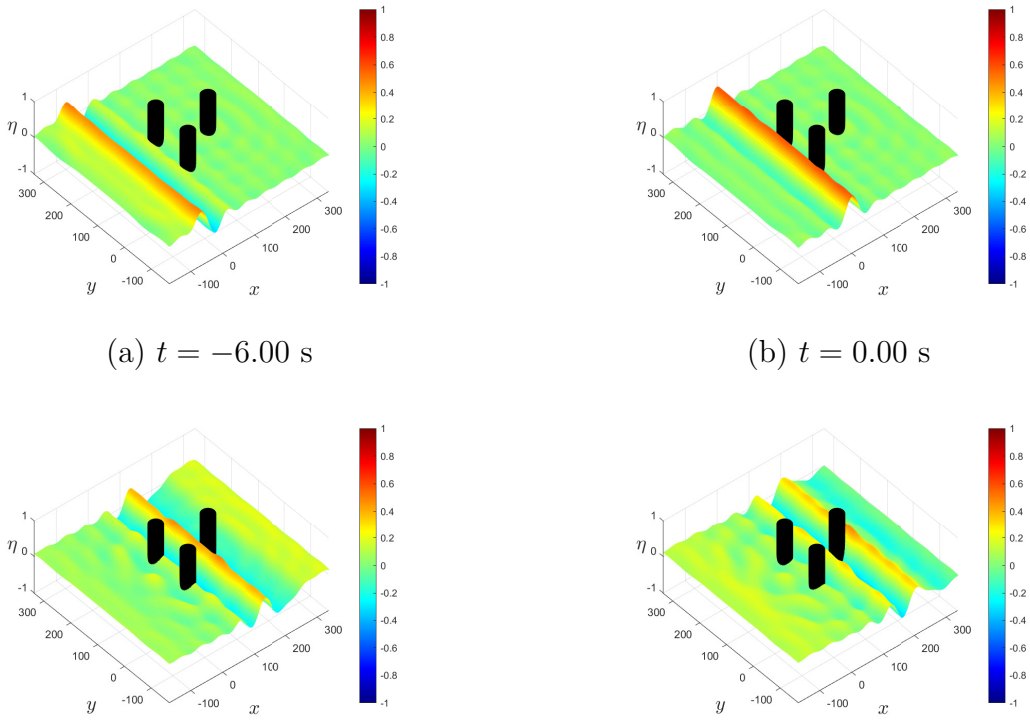

(a) $t = -6.00$ s (b) $t = 0.00$ s

(c) $t = 19.20$ s (d) $t = 28.60$ s

Figure 4.15: Snapshots of a simulation at different time instances illustrating the variation in the height of the water surface when a water wave approaching at an incident angle $\beta = 0°$ interacts with three cylinders of $a/h = 0.5$ and $d/h = 0.8$ placed in triangular configuration over a porous seabed ($Gh = 0.5$).

simultaneously strikes two cylinders. This results in greater wave dissipation and reduced energy transmission. Therefore, the arrangement of the cylinders has a significant impact on reducing wave energy in the leeside zone, with the triangular configuration proving more effective at attenuating wave forces.

Case 3: Four cylinders in a horizontal array and in a square configuration

To further explore the effects of increasing the number of cylinders beyond those in cases 1 and 2, we examine the scenarios involving four identical cylinders arranged in a horizontal array configuration and in a square configuration. In the array configuration, the (axis-to-axis) distance between each cylinder is set as $2h$, whereas in the square arrangement, the (axis-to-axis) distance between the cylinders on one side of the square is fixed as $3h$.

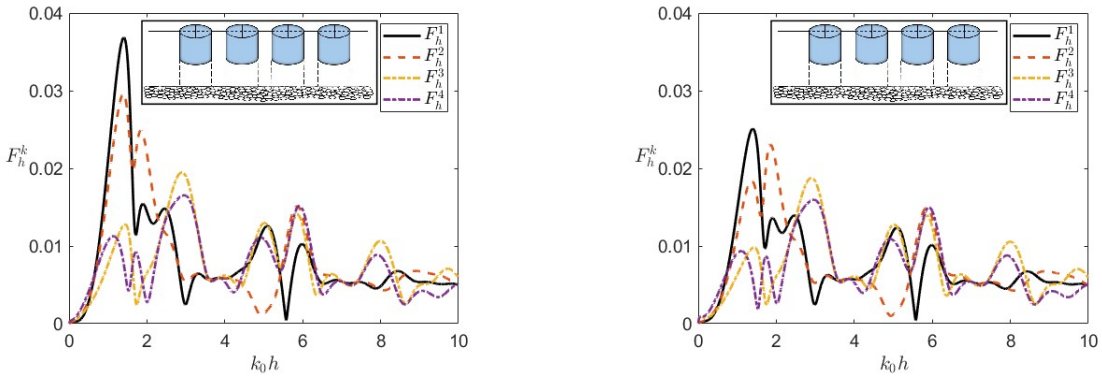

(a) (b)

Figure 4.16: Horizontal forces exerted on the four cylinders of $a/h = 0.5$ and $d/h = 0.4$ kept in a horizontal array configuration for $\beta = 30°$ and for the porous parameters (a) $Gh = 0.25$ and (b) $Gh = 0.5$.

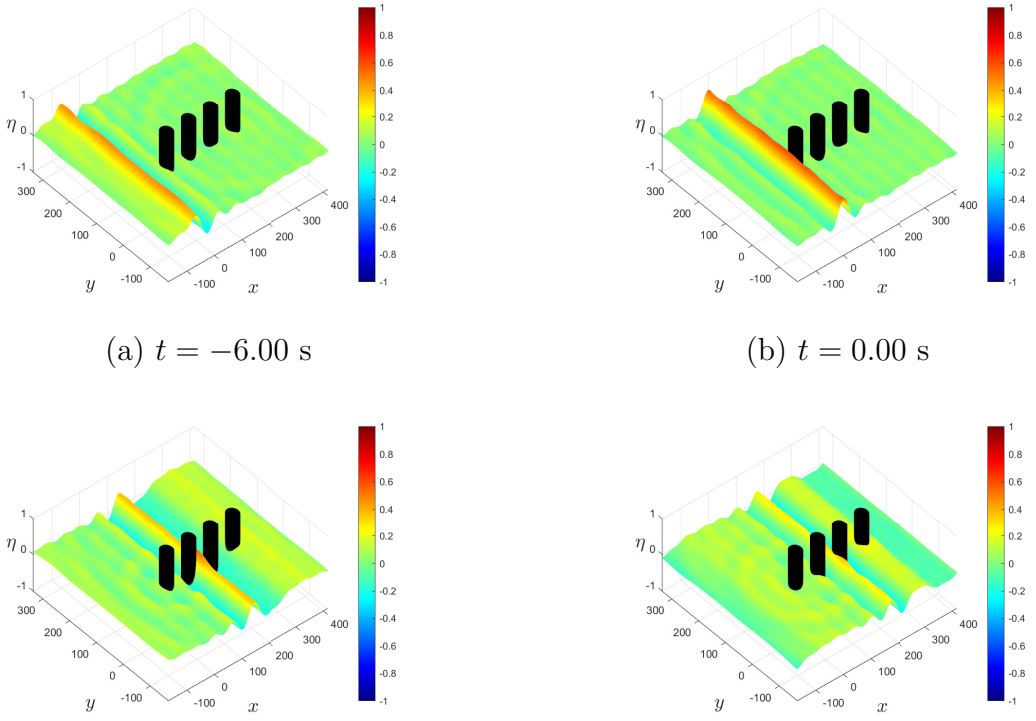

(a) $t = -6.00$ s (b) $t = 0.00$ s

(c) $t = 18.40$ s (d) $t = 30.00$ s

Figure 4.17: Snapshots of a simulation at different time instances illustrating the variation in the height of the water surface when a water wave approaching at an incident angle $\beta = 0°$ interacts with four cylinders of $a/h = 0.5$ and $d/h = 0.8$ over a porous seabed ($Gh = 0.5$).

Figure 4.16 delineates the horizontal forces exerted on the four cylinders plotted against the wavenumber k_0h, and figures (a) and (b) in the figure again display the horizontal forces for the porous seabed with the (dimensionless) porosity parameter $Gh = 0.25$ and $Gh = 0.5$, respectively. The figure, in a general sense, shows that the peaks in the horizontal force are getting reduced as one moves from the first cylinder towards the fourth cylinder. Similarly to Figs. 4.5 and 4.12, a comparison between sub-figures (a) and (b) of Fig. 4.16 also reconfirms the decay in the horizontal forces on increasing the porosity of the seabed.

To understand the wave dynamics around four cylinders in an array configuration, Figs. 4.17 and 4.18 depict the static visualizations of time-dependent simulations at four distinct time instances. In Figs.4.17 and 4.18, each cylinder (dimensionless) has a radius of $a/h = 0.5$ and a height of $d/h = 0.5$, and is placed over a porous seabed with a dimensionless porosity of $Gh = 0.5$. The cylinders are arranged in a horizontal array configuration with equal spacing of $2h$ between them. The angle of the incident wave is set to $\beta = 0°$ in Fig.4.17 and $\beta = 30°$ in Fig. 4.18. Similarly to case 2, Figs. 4.17

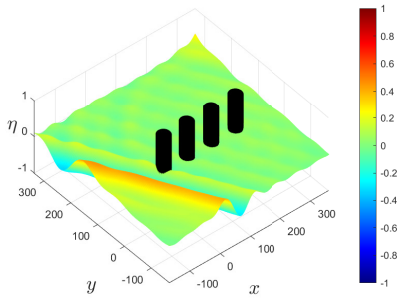

(a) $t = -6.00$ s

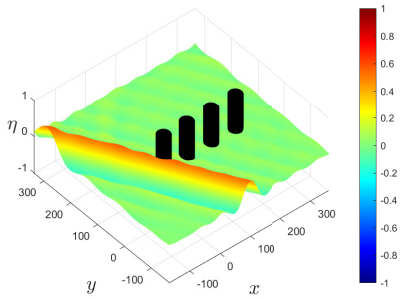

(b) $t = 0.00$ s

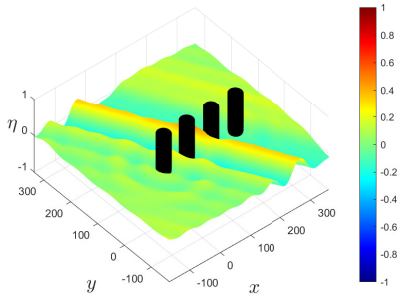

(c) $t = 18.40$ s

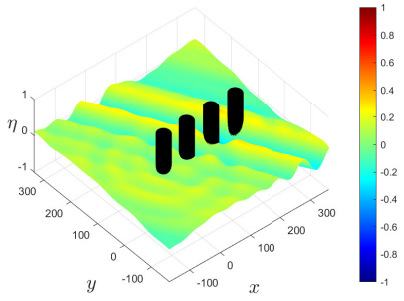

(d) $t = 30.00$ s

Figure 4.18: Same as Fig 4.17 but for incident angle $\beta = 30°$.

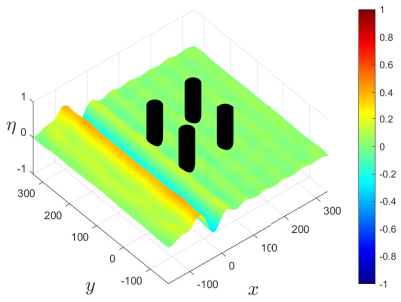

(a) $t = -6.00$ s

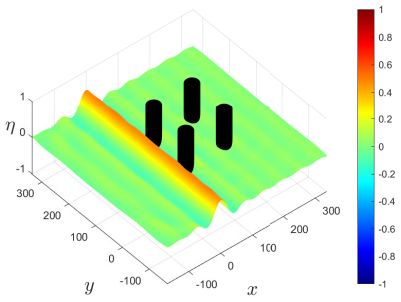

(b) $t = 0.00$ s

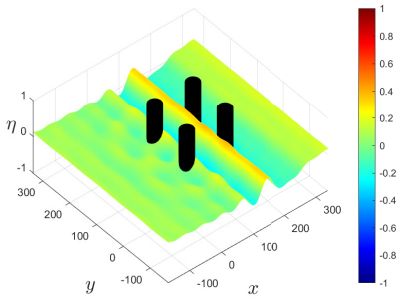

(c) $t = 15.40$ s

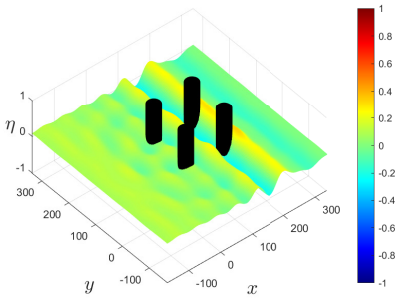

(d) $t = 25.20$ s

Figure 4.19: Snapshots of a simulation at different time instances illustrating the variation in the height of the water surface when the incident wave approaching at an angle $\beta = 0°$ interacts with four cylinders of $a/h = 0.5$ and $d/h = 0.8$ placed in a square configuration over a porous bottom ($Gh = 0.5$).

and 4.18 also show the decay in the surface elevation towards the leeward side due to the same reason as mentioned above. Again, a careful comparison of corresponding subfigures in Figs. 4.10, 4.13 and 4.17 and those in Figs. 4.11, 4.14 and 4.18 show that the surface elevation in Figs. 4.17 and 4.18 is reduced even more in comparison to that in Figs. 4.13 and 4.14, respectively. It is also observed that the configuration with four cylinders, compared to the three-cylinder arrangement, is more effective in reducing wave energy. This is because the additional cylinder in the arrangement contributes to a more significant dissipation of wave energy, particularly in the leeside zone.

Figure 4.19 and Fig. 4.20, on the other hand, illustrate the snapshots from the simulation when the cylinders are placed in a square configuration where the axis-to-axis distance between the cylinders placed on a side of the square is $3h$, and the angle of the incident wave in Figs. 4.19 and 4.20 has again been set to $\beta = 0°$ and $\beta = 30°$, respectively. The figures again asserts that the inclusion of more structures along with a porous

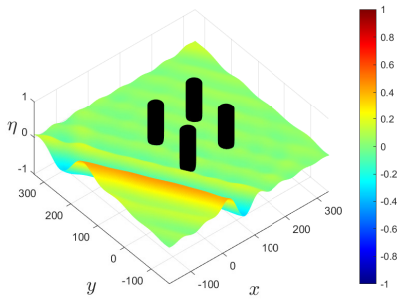

(a) $t = -6.00$ s

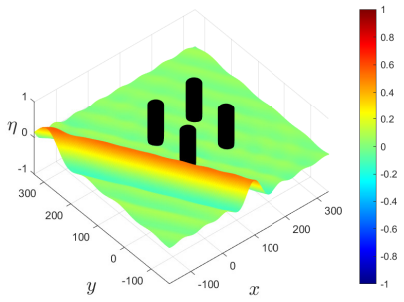

(b) $t = 0.00$ s

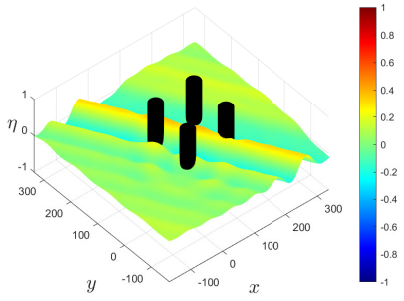

(c) $t = 15.40$ s

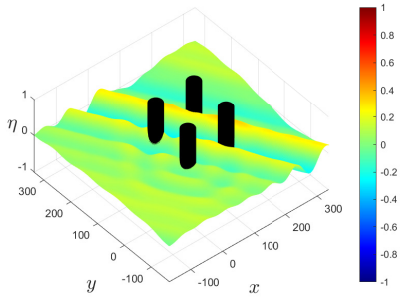

(d) $t = 25.20$ s

Figure 4.20: Same as Fig 4.19 but for incident angle $\beta = 30°$.

seabed can help reduce wave energy significantly on the leeward side. Similarly to other figures on temporal simulations, Figs. 4.19 and 4.20 also illustrate the decay in the elevation of the water surface towards the leeward side due to the presence of the cylinders. Upon closely examining both horizontal array (Figs. 4.17–4.18) and square arrangements (Figs. 4.19–4.20), it becomes evident that the wave elevation is reduced more significantly in the square arrangement. This is because, in the array arrangement, the incident wave first interacts with a single cylinder before propagating to the subsequent cylinders. On the other hand, in the square arrangement, the incident wave simultaneously interacts with two cylinders, resulting in greater energy dissipation and less energy transmission to the downstream cylinders compared to the array configuration.

4.3.4 Flow field around the cylinders

This subsection presents a detailed investigation of the velocity vector field around both single and multiple circular cylinders arranged in a horizontal array configuration. Figure 4.21 provides visual representations of the flow behavior, where in Fig. 4.21a shows

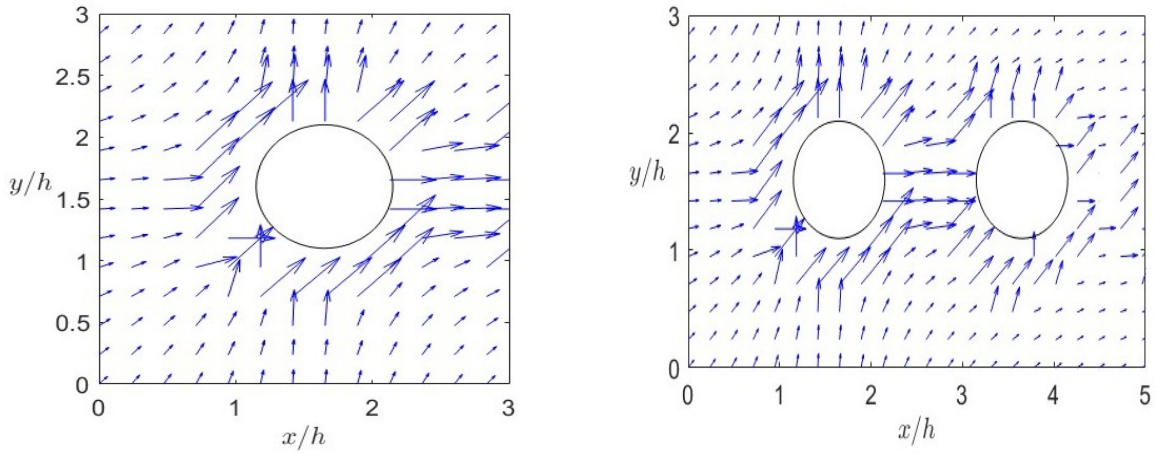

(a) (b)

Figure 4.21: Flow field around (a) single cylinder and (b) two cylinders in a horizontal array arrangement. The remaining parameters are set as $a/h = 0.5$, $d/h = 0.4$, $\beta = 30°$ and $Gh = 0.5$.

the velocity field around a single cylinder, and Fig. 4.21b illustrates the flow around two cylinders placed in a horizontal array. As observed, the velocity field around the back side of the cylinders due to the obstruction of incident waves, leading to higher velocities along the cylinder surfaces. In the case of a single cylinder, the approaching flow splits and speeds up along the curved surface, followed by a reduction in velocity in the downstream region. When two cylinders are placed in line, the first cylinder disrupts the incoming flow, scattering the velocity field and weakening the flow that reaches the second cylinder. As a result, the interaction with the second cylinder further slows down the flow compared to the first one, creating an even more pronounced low-velocity region behind it. This behavior confirms the cumulative impact of multiple cylinders, where each structure successively modifies the velocity field, leading to a progressive reduction in wave-induced flow. Ultimately, the inclusion of more cylinders further increases the disturbance in the flow pattern, resulting in more complex vector fields and greater energy dissipation due to repeated wave-structure interactions.

Following the previous analysis, the velocity vector fields for cases with three and four cylinders arranged in horizontal array are presented in Figs. 4.22 and 4.23, respectively. In both cases, the incoming fluid gains speed as it moves toward the first cylinder, reaching its maximum just before contact. This behavior is consistent with earlier observations, where the highest velocity appears near the front of the first cylinder. It is evident that

as the number of cylinders increases, the flow pattern becomes increasingly intricate, and the reduction in velocity becomes more pronounced, indicating a greater effectiveness of the cylinder array in dissipating wave energy and diminishing the strength of the flow reaching the downstream region.

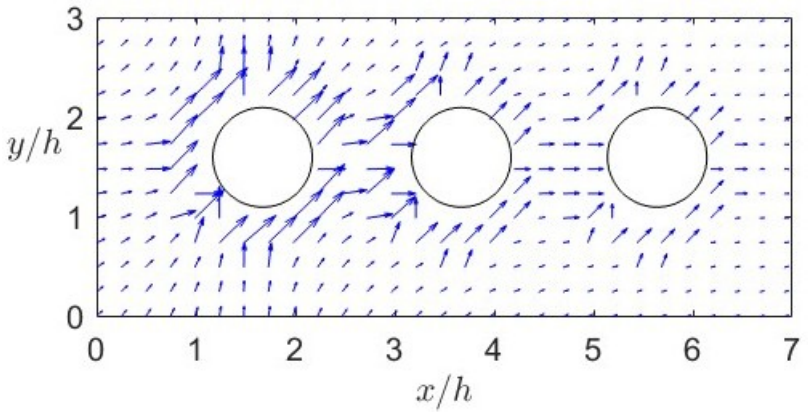

Figure 4.22: Same as Fig. 4.21 but for three cylinders.

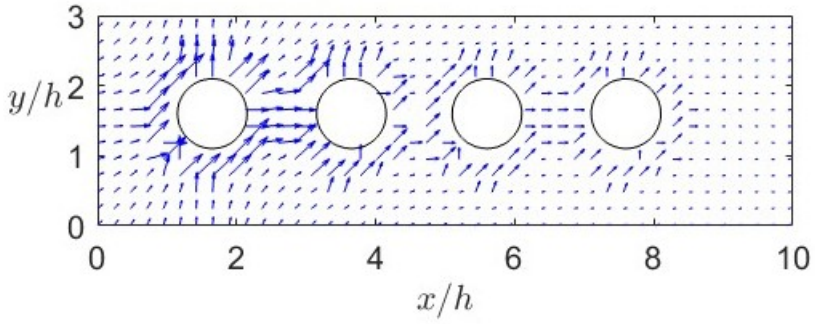

Figure 4.23: Same as Fig. 4.21 but for four cylinders.

4.4 Conclusion

This chapter investigates the impact of a permeable seabed on wave scattering by multiple circular cylinders through a temporal study. The equations derived in the present study have been solved numerically to determine the velocity potentials in the exterior region as well as in the regions covered by the cylinders. The determined velocity potentials have subsequently been employed to calculate the horizontal force exerted on the cylinders. It has been found that, with fixed radii (heights) of the cylinders, the horizontal force on a cylinder decreases as the heights (radii) of the cylinders increase due to the fact that the

impact of the wave is distributed over a larger surface area. Furthermore, as the porosity of the seabed increases, the horizontal forces exerted on the cylinders also diminish. Hence, the porosity of the seabed also contributes significantly to diminishing wave force exerted on the cylinders. Furthermore, temporal simulations depicting wave interaction with the cylinders in various cases have been presented, which provide a comprehensive understanding of how a porous bed attenuates wave energy compared to a rigid bed. In the static figures of the temporal simulations, the incident wave elevation is observed to be higher before its interaction with the cylinder (i.e., for $t < 0$) compared to its elevation afterward (i.e., for $t > 0$). Over time, the wave elevation gradually decreases toward the leeside zone after interacting with the cylinders. Furthermore, the velocity vector fields also provide valuable insights into the fluid flow behavior around single and multiple circular cylinders. Consequently, a porous bed combined with multiple structures can help weaken the impact of pounding waves multifold and hence can help protect coastal areas effectively.

Chapter 5

Wave interaction with floating plates

In this chapter, the scattering of waves by multiple floating circular flexible plates over a porous seabed is analyzed using the EEM. To investigate the effects of seabed porosity, the heave force exerted on the plate(s), the flow distribution around the plate(s), and the temporal simulations of the fluid flow are presented for various wave and structural parameters.

5.1 Mathematical framework

5.1.1 Problem overview

We consider a system of N floating, flexible, circular thin plates arranged over a flat porous seabed, in a global Cartesian coordinate system $Oxyz$, where the origin O is located at the still water surface. The plates are equally spaced along the horizontal direction, and specific plates such as the j^{th} and k^{th} are highlighted in the figure for illustrative purposes (see Fig. 5.1a). In this system, the xy-plane represents the horizontal surface

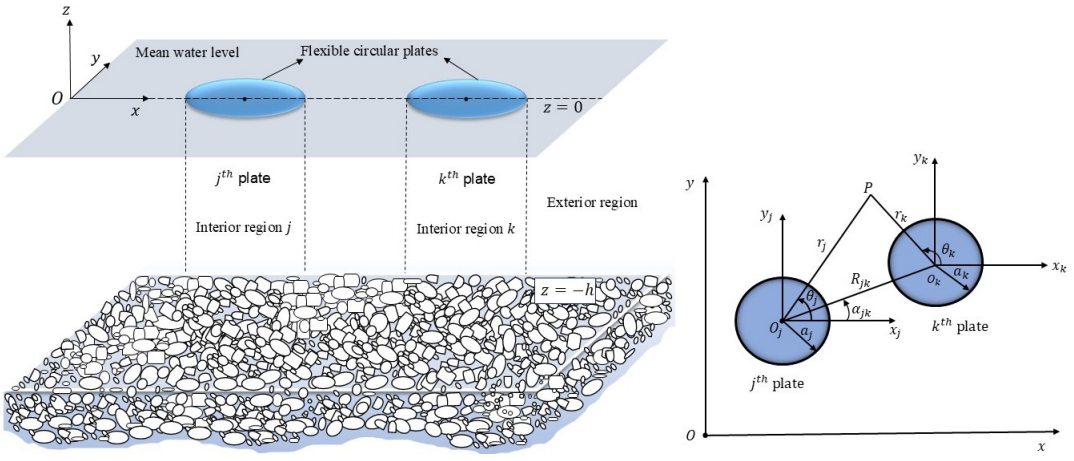

Figure 5.1: Schematic of (a) lateral view of multiple floating circular elastic plates over a porous bed and (b) top view of the local coordinate systems for the j^{th} and k^{th} cylinders along with the global Cartesian coordinate system.

of the fluid domain, while the positive z-axis is directed vertically upwards. The water

depth is denoted by h. The entire fluid domain is divided into two distinct regions: the exterior region, which lies outside the circular plates, and N interior regions, which are the regions beneath each of the N floating plates. To describe the interaction between incident wave and each plate more effectively, N local cylindrical coordinate systems $O_j r_j \theta_j z$ are introduced, where each system is centered at the origin O_j corresponding to the j^{th} plate, for $j = 1, 2, 3, \ldots, N$ as shown in Fig. 5.1b. In this local cylindrical coordinate system, the positions of the j^{th} and k^{th} plates are given as (r_j, θ_j) and (r_k, θ_k), respectively. Here, θ_j and θ_k are the angular coordinates measured counterclockwise from the positive x-axis. The points O_j and O_k denote the centers of the j^{th} and k^{th} plates, while a_j and a_k represent their respective radii. The distance between the centers of the two plates is represented by R_{jk}.

5.1.2 Governing equation and boundary conditions

The governing equation and the corresponding bottom boundary condition used in this chapter are the same as those defined in Eq. (4.1) and Eq. (3.2), respectively. Additionally, in the local polar coordinate system, the spatial velocity potential for the exterior region is represented as $\phi_1(r_j, \theta_j, z)$, and the regions covered by the circular plates are denoted as $\phi_2^j(r_j, \theta_j, z)$. The entire fluid domain is characterized by $\Omega = \{z : -h \leq z \leq 0\}$, representing both the exterior and interior regions. The linearized free-surface boundary condition in the exterior region given in Eq. (3.2). Assuming simple harmonic motion, the free surface elevation is represented by $\zeta_j(r, \theta, t) = \text{Re}\{\eta_j(r, \theta) e^{-\text{i}\omega t}\}$, where ζ_0 corresponds to the free surface elevation in the exterior region, and ζ_j (for $j = 1, 2, 3, \ldots, N$) denotes the deflection of the j^{th} plate. The linearized kinematic boundary condition at the free surface is expressed as

$$\frac{\partial \phi_2^j}{\partial z} = -\text{i}\omega\eta_j \quad \text{for } j = 1, 2, \ldots, N \text{ on } z = 0. \tag{5.1}$$

The hydrodynamic pressure $P_j(r_j, \theta_j, z, t) = \text{Re}\{p_j(r_j, \theta_j, z) e^{-\text{i}\omega t}\}$ exerted on the j^{th} plate is given by [14]

$$p_j(r_j, \theta_j, z) = \text{i}\omega\rho\phi_2^j - \rho g \eta_j \quad \text{at} \quad z = 0. \tag{5.2}$$

Further, the dynamic condition for the j^{th} circular plate takes the form

$$\left[EI(\nabla^4\eta_j) + \mathcal{N}(\nabla^2\eta_j) - \rho_c d\omega^2\eta_j\right] = p_j(r_j, \theta_j, z) \quad \text{at } z = 0, \tag{5.3}$$

where

$$\nabla^2 = \frac{\partial^2}{\partial r_j^2} + \frac{1}{r_j}\frac{\partial}{\partial r_j} + \frac{1}{r_j^2}\frac{\partial^2}{\partial \theta_j^2}, \tag{5.4}$$

$\nabla^4 = (\nabla^2)^2$, E denotes Young's modulus, ρ_c is the density of the plate material, $\mathcal{N}$ is the uniform compressive force, and $I = d_j^3/(12(1-\nu^2))$ is the moment of inertia of the plate with ν being the Poisson's ratio and d_j being the plate thickness of the j^{th} plate. Substituting Eq. (5.2) into Eq. (5.3), the resultant equation yields

$$\left[EI(\nabla^4\eta_j) + \mathcal{N}(\nabla^2\eta_j) + \rho g\eta_j - \rho_c d_j\omega^2\eta_j\right] = \mathrm{i}\omega\rho\phi_2^j \quad \text{on } z = 0. \tag{5.5}$$

Eliminating η_j from the Eq. (5.5) using Eq. (5.1), the obtained plate-covered boundary condition for j^{th} plate is

$$\left[EI\nabla^4 + \mathcal{N}\nabla^2 + \rho g - \rho_c d_j\omega^2\right]\frac{\partial\phi_2^j}{\partial z} = \omega^2\rho\phi_2^j \quad \text{on } z = 0. \tag{5.6}$$

Using Eq. (4.1), the dynamic boundary conditions on the plates, i.e., Eq. (5.6), are rewritten as follows:

$$\left(\mathbb{D}\frac{\partial^5}{\partial z^5} - \mathbb{Q}\frac{\partial^3}{\partial z^3} + \frac{\partial}{\partial z} - \mathbb{M}K\right)\phi_2^j = K\phi_2^j \quad \text{on } z = 0, \tag{5.7}$$

where

$$\mathbb{D} = \frac{EI}{\mathbb{T}}, \quad \mathbb{Q} = \frac{\mathcal{N}}{\mathbb{T}}, \quad K = \frac{\omega^2}{g}, \quad \mathbb{T} = \rho g \quad \text{and} \quad \mathbb{M} = \frac{\rho_c d_j}{\rho}. \tag{5.8}$$

To ensure the stability and realistic response of floating plates, appropriate edge conditions are applied and categorized as clamped, moored, and free, as illustrated in Fig. 5.2. These edge conditions are incorporated into the mathematical model by prescribing suitable boundary conditions for each case, as described below.

Clamped-edge condition:

A clamped edge is fully restrained such that the plate cannot deflect or rotate at the boundary. Physically, this represents a rigid connection at the edge, enforcing both

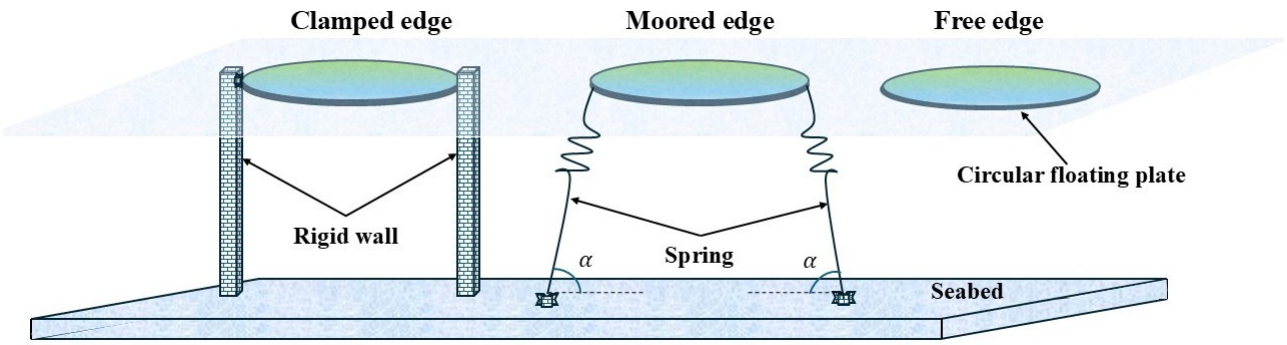

Figure 5.2: Schematic of different edge conditions on circular plates.

zero vertical displacement and zero slope. The mathematical boundary conditions for a clamped edge at $r_j = a_j$ are given by [118]

$$\begin{cases} \dfrac{\partial \phi_2^j}{\partial z} = 0 \\ \dfrac{\partial^2 \phi_2^j}{\partial r \partial z} = 0 \end{cases}. \tag{5.9}$$

Moored-edge condition:

A moored or spring-supported is connected to the seabed via vertical mooring lines or springs. This allows the edge to rotate freely, while vertical displacement is resisted by an elastic restoring force proportional to the displacement. Mathematically, the moored-edge boundary condition at $r_j = a_j$, the vertical shear force and bending moment vanish, and the condition reads [93, 132]

$$\begin{cases} \left[\dfrac{\partial^2}{\partial r_j^2} + \nu \left(\dfrac{1}{r_j} \dfrac{\partial}{\partial r_j} + \dfrac{1}{r_j^2} \dfrac{\partial^2}{\partial \theta_j^2} \right) \right] \eta_j = 0 \\ \left[EI \left\{ \dfrac{\partial}{\partial r_j} \nabla^2 + \dfrac{(1-\nu)}{r_j^2} \left(\dfrac{\partial}{\partial r_j} - \dfrac{1}{r_j} \right) \dfrac{\partial^2}{\partial \theta_j^2} \right\} + \mathcal{N} \dfrac{\partial}{\partial r_j} - W \right] \eta_j = 0, \end{cases} \tag{5.10}$$

where $W = p_s \sin^2 \alpha$ with p_s and α being the spring constant and mooring angle, respectively [131]. In this study, the mooring angle is taken as $\alpha = 90°$.

Free-edge condition:

A free edge implies that the plate is not subjected to any constraints at the boundary—it is free to deflect and rotate under wave forcing. Physically, this means no bending moment or no vertical shear force is transmitted across the edge. Setting $p_s = 0$ in Eq. (5.10) yields the boundary condition corresponding to a free-edge conditions.

The matching conditions for pressure and velocity continuities at the fluid–structure interface for the j^{th} plate are given by

$$\phi_1 = \phi_2^j \quad \text{at } r_j = a_j \text{ for } z \in \Omega, \tag{5.11}$$

$$\frac{\partial \phi_1}{\partial r_j} = \frac{\partial \phi_2^j}{\partial r_j} \quad \text{at } r_j = a_j \text{ for } z \in \Omega. \tag{5.12}$$

Furthermore, in the exterior region, the diffracted velocity potential must satisfy the far-field boundary condition (4.6).

5.2 Solution method

5.2.1 Velocity potential for the exterior region

The total velocity potential in the open-water region is assumed to be formed by adding together the velocity potentials of the incident and scattered waves [84], i.e.,

$$\phi_1 = \phi_I + \phi_S, \tag{5.13}$$

where the explicit form of ϕ_I and ϕ_S are defined in Eq. (4.8) and Eq. (4.11), respectively. By utilizing the Graf's addition theorem, Eq. (5.13) can be redefined as

$$\begin{aligned}\phi_1(r_j, \theta_j, z) = \sum_{m=-\infty}^{\infty} \Bigg(\mathbf{I}_j \mathrm{i}^m e^{-\mathrm{i}m\beta} J_m(k_0 r_j) e^{\mathrm{i}m\theta_j} f_{10}(z) + \sum_{n=0}^{\infty} \mathcal{A}_{mn}^j H_m^{(1)}(k_n r_j) f_n(z) \\ + \sum_{\substack{k=1 \\ k\neq j}}^{N} \sum_{n=0}^{\infty} \sum_{m_1=-\infty}^{\infty} (-1)^{m_1} \mathcal{A}_{mn}^k H_{m-m_1}^{(1)}(k_n R_{jk}) e^{\mathrm{i}(m\alpha_{jk} - m_1\alpha_{kj})} J_{m_1}(k_n r_j) e^{\mathrm{i}m_1\theta_j} f_n(z) \Bigg)\end{aligned} \tag{5.14}$$

for $r_j < R_{jk}$ (for $k = 1, 2, \ldots, N$ and $k \neq j$) where $\mathbf{I}_j = e^{\mathrm{i}k_0(x_j \cos\beta + y_j \sin\beta)}$. In Eq. (5.14), $\mathcal{A}_{mn}^j$ for $j = 1, 2, 3, \ldots, N$ are the unknown coefficients, $f_n(z)$ and k_n are defined in Eqs. (4.12) and (4.13), respectively.

5.2.2 Velocity potentials for the interior regions

In the interior regions, once governing equation (4.1) is solved alongside the bottom-boundary condition (3.2), the spatial velocity potentials are obtained as

$$\phi_2^j = \sum_{m=-\infty}^{\infty} \left(\sum_{n=-2}^{\infty} \mathcal{B}_{mn}^j J_m(\mu_n r_j) g_n(z) \right) e^{\mathrm{i}m\theta_j}, \tag{5.15}$$

where $\mathcal{B}^j_{mn}$ are the unknown coefficients for $j = 1, 2, 3, \ldots, N$, $g_n(z)$ denote the eigenfunctions, given by

$$g_n(z) = \frac{\mu_n \cosh\left(\mu_n(h+z)\right) - G \sinh\left(\mu_n(h+z)\right)}{\mu_n \cosh\left(\mu_n h\right) - G \sinh\left(\mu_n h\right)} \quad \text{for} \quad n = 0, 1, 2, 3, \ldots, \tag{5.16}$$

and μ_n are the wavenumbers which satisfy the dispersion relation [14]

$$(\mathbb{D}\mu_n^4 - \mathbb{Q}\mu_n^2 - \mathbb{M}K + 1)(\mu_n^2 \tanh \mu_n h - \mu_n G) = K(\mu_n - G \tanh \mu_n h). \tag{5.17}$$

When $G = 0$, Eq. (5.17) reduces to a dispersion relation for the regions covered by plates over the rigid bed [92, 144]. In this scenario ($G = 0$), dispersion relation (5.17) possesses two real roots, denoted by μ_0 and $-\mu_0$. Additionally, there are four complex roots, represented by μ_{-1}, μ_{-2}, their complex conjugates $\bar{\mu}_{-1}$ and $\bar{\mu}_{-2}$, and countably infinite number of purely imaginary roots. In the present study, it is important to highlight that, in order to ensure the propagation of progressive waves at the far field in the open-water region, the porous-effect parameter (G) is assumed to be a real number as discussed in Ref. [82]. Under these conditions, for $G \in \mathbb{R}$ and $G \neq 0$, the dispersion relation (5.17) also exhibits two real roots (μ_0 and $-\mu_0$), four complex roots (μ_{-1}, μ_{-2}, $\bar{\mu}_{-1}$ and $\bar{\mu}_{-2}$) and countably infinite purely imaginary roots, maintaining the same characteristics as in the scenario of $G = 0$. However, when the porous-effect parameter G is a complex number, all the roots of dispersion relation (5.17) become complex.

5.2.3 Velocity potential evaluation in all regions simultaneously

The unknown coefficients in the spatial velocity potentials given in Eqs. (5.14) and (5.15) are determined using the matching conditions ((5.11) and (5.12)). On substituting the spatial velocity potentials ϕ_1 and ϕ_2^k from Eqs. (5.14) and (5.15) in boundary conditions (5.14) and (5.15) and exploiting the orthogonality conditions of the eigenfunction and trigonometric functions, the resulting system of algebraic equations reads

$$\begin{aligned}
&\mathbf{I}_j \mathrm{i}^s e^{-\mathrm{i}s\beta} J_s(k_0 a_j)\delta_{0,l} Z_l + \mathcal{A}^j_{sl} H^{(1)}_s(k_l a_j) Z_l \\
&+ \sum_{\substack{k=1 \\ k\neq j}}^{N} \sum_{m=-\infty}^{\infty} \left((-1)^s \mathcal{A}^k_{ml} H^{(1)}_{m-s}(k_l R_{kj}) e^{\mathrm{i}(m\alpha_{jk} - s\alpha_{kj})} J_s(k_l a_j) Z_l \right) = \sum_{n=-2}^{\infty} \mathcal{B}^j_{sn} J_s(\mu_n a_j) Y_{nl},
\end{aligned} \tag{5.18}$$

$$\mathbf{I}_j \mathrm{i}^s e^{-\mathrm{i}s\beta} k_0 J_s^{'}(k_0 a_j)\delta_{0,l} Z_l + \mathcal{A}_{sl}^j k_l H_s^{(1)^{'}}(k_l a_j) Z_l$$
$$+ \sum_{\substack{k=1 \\ k\neq j}}^{N} \sum_{m=-\infty}^{\infty} \left((-1)^s \mathcal{A}_{ml}^k H_{m-s}^{(1)}(k_l R_{kj}) e^{\mathrm{i}(m\alpha_{jk} - s\alpha_{kj})} k_l J_s^{'}(k_l a_j) Z_l \right) = \sum_{n=-2}^{\infty} \mathcal{B}_{sn}^j \mu_n J_s^{'}(\mu_n a_j) Y_{nl}, \tag{5.19}$$

where $\delta_{0,l}$ is the Kronecker delta function and

$$Z_l = \int_\Omega f_l^2(z)\mathrm{d}z, \quad Y_{nl} = \int_\Omega g_n(z) f_l(z)\mathrm{d}z. \tag{5.20}$$

Furthermore, to deduce the system of equation for the moored-edge boundary condition, we put the spatial velocity potentials ϕ_2^k as defined in Eq. (5.15) and applying the orthogonality condition of the trigonometric functions in $[0\ 2\pi]$, the resulting equations are obtained as

$$\sum_{n=-2}^{\infty} \mathcal{B}_{sn}^j \left[a_j^2 \mu_n^2 J_s^{''}(\mu_n a_j) + \nu \left\{ a_j \mu_n J_s^{'}(\mu_n a_j) - s^2 J_s(\mu_n a_j) \right\} \right] \psi(\mu_n) = 0, \tag{5.21}$$

$$\sum_{n=-2}^{\infty} \mathcal{B}_{sn}^j \Bigg[EI \Bigg\{ a_j^3 \mu_n^3 J_s^{'''}(\mu_n a_j) + a_j^2 \mu_n^2 J_s^{''}(\mu_n a_j) - [1 + (2-\nu)s^2] \mu_n J_s^{'}(\mu_n a_j)$$
$$+ (3-\nu) s^2 J_s(\mu_n a_j) \Bigg\} + a_j^3 \mathcal{N} \mu_n J_s^{'}(\mu_n a_j) - p_s \Bigg] \psi(\mu_n) = 0, \tag{5.22}$$

where

$$\psi(\mu_n) = \frac{\mu_n^2 \sinh(\mu_n h) + G\mu_n \cosh(\mu_n h)}{G \sinh(\mu_n h) - \mu_n \cosh(\mu_n h)}.$$

When $p_s = 0$, Eqs. (5.21) and (5.22) transform into the system of equations for free-edge conditions. For the system of equations for the clamped-edge conditions, we again put the spatial velocity potentials ϕ_2^k as defined in Eq. (5.15) and applying the orthogonality condition of the trigonometric functions in $[02\pi]$, the resulting equations are obtained as

$$\sum_{n=-2}^{\infty} \mathcal{B}_{sn}^j J_s(\mu_n a_j) \psi(\mu_n) = 0, \tag{5.23}$$

$$\sum_{n=-2}^{\infty} \mathcal{B}_{sn}^j \mu_n J_s^{'}(\mu_n a_j) \psi(\mu_n) = 0. \tag{5.24}$$

A detailed derivation of Eqs. (5.18)–(5.19), Eqs. (5.21)–(5.22) and Eqs. (5.23)–(5.24) are given in Appendix B. Combining Eqs. (5.18) and (5.19) with those derived from the

free-edge conditions (Eqs. (5.21) and (5.22)) or the clamped-edge conditions (Eqs. (5.23) and (5.24)), we obtain a system of equations. This system encompasses infinitely many unknown coefficients. To evaluate the unknown coefficients, we truncate the infinite series for m to the range $\{-M, \ldots, 0, \ldots, M\}$, using a fixed value of M. For the series of vertical eigenfunctions, the range of n for $\mathcal{A}^j_{mn}$ is $\{0, 1, 2, 3, \ldots, N_1\}$, while for $\mathcal{B}^j_{mn}$, the range of n is $\{-2, -1, 0, 1, 2, \ldots, N_1\}$. Additionally, the ranges of s and l are defined as $l = 0, 1, 2, \ldots, N_1$ and $s = -M, \ldots, 0, \ldots, M$, respectively, in Eqs. (5.18) and (5.19), (5.21) and (5.22) and (5.23) and (5.24). To ascertain these unknown coefficients, one can employ any available computer algebra software. After substituting the calculated coefficients into Eqs. (5.14) and (5.15), the complete velocity potentials throughout the entire domain can be explicitly determined.

5.2.4 Time-dependent fluid flow simulations

In this section, we delve into the dynamic interaction that occurs when a fluid flow interacts with multiple circular plates that are floating and flexible. This exploration aims to understand how the height of the waves on the fluid surface changes over time. To perform this time-dependent simulation, we employ (3.26) a specific transformation rule for the free surface elevation η.

5.3 Results and discussions

This section analyzes the effects of varying wave characteristics, porous seabed properties, and structural parameters of the plates on their dynamic response. To run the simulations, we adopted the following fixed parameters: $h = 30$ m, $\rho = 1025$ kg/m^3, $\nu = 0.1$, $\beta = 30^\circ$ and $E = 1$ GPa for the plates unless mentioned otherwise. Additionally, all plates are assumed to have the same density $\rho_c = 922.5$ kg/m^3, the same dimensionless thickness $d_j/h = d/h = 0.05$, the same dimensionless radius $a_j/h = a/h = 2$ and the same uniform compressive force $\mathcal{N} = 0.1\sqrt{EI\rho g}$. The heave force exerted on the j^{th} plate can be determined by following the formula [132]:

$$F_j = \mathrm{i}\rho\omega \int_0^{2\pi} \int_0^{a_j} \phi_2^j(r_j, \theta_j, 0) r_j \mathrm{d}r_j \mathrm{d}\theta_j \quad \text{for } j = 1, 2, 3, \ldots, N. \tag{5.25}$$

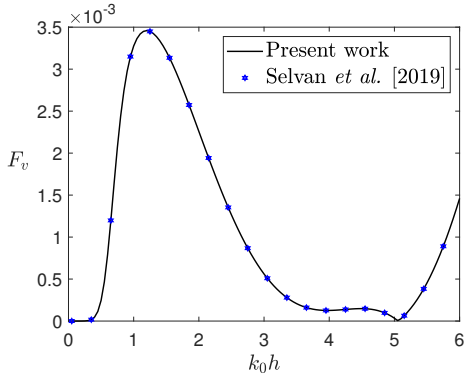

Figure 5.3: Dimensionless vertical force F_v exerted on the single circular flexible plate plotted against the dimensionless wavenumber k_0h for fixed values of $a_1/h = 2$, $d_1/h = 0.01$, $E = 2 \times 10^9$, $\nu = 0.3$ and $Gh = 0$. The analytical result reported in Selvan *et al.* [132] is represented by the blue stars, whereas the black solid line corresponds to the findings of the present study.

The non-dimensional heave force exerted on the j^{th} plate is given by

$$F_{v_j} = \frac{F_j}{\rho g a_j^2 h} \quad \text{for } j = 1, 2, 3, \ldots, N. \tag{5.26}$$

5.3.1 Validation

It is important to note that when the porosity parameter $G = 0$, the seabed behaves as a rigid surface. Under this condition, the problem should reproduces results consistent with those available in the literature for wave interaction with a single circular flexible plate resting on a rigid bottom. To validate the accuracy of our code, we compare the heave force exerted on the single circular plate over a rigid bed ($G = 0$) with the analytical solution calculated by Selvan *et al.* [132] in Fig. 5.3. Our results for $G = 0$ align well with those previously reported in [132]. This confirms the correctness of the code.

5.3.2 Effect of the heave force along with time-dependent simulations

In this subsection, we investigate the influence of systems comprising of two, three, and four circular flexible plates on the heave force, considering a range of wave and structural parameters. Furthermore, time-dependent simulations based on Eq. (3.26) are presented to demonstrate the temporal simulations of wave-structure interactions, providing deeper insights into the dynamic behavior of the fluid flow around the plates.

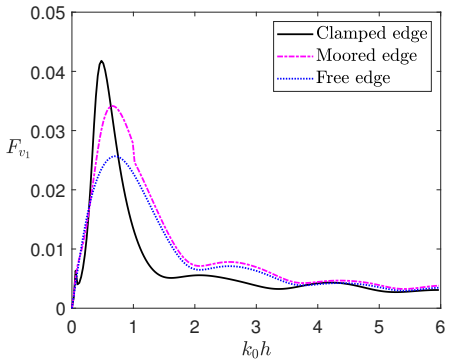

(a)

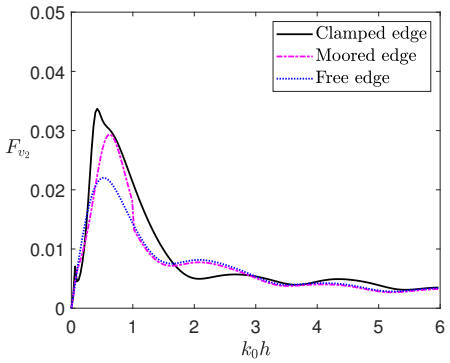

(b)

Figure 5.4: The dimensionless heave force (F_v) acting on (a) the first circular flexible plate and (b) the second circular flexible plate plotted against the dimensionless wavenumber (k_0h). The plates have clamped, moored and free edge conditions with fixed parameters $d/h = 0.05$, $a/h = 2$, $\beta = 30°$ and $Gh = 0.5$.

5.3.2.1 Presence of two circular plates

The non-dimensional heave force exerted on each circular flexible plates under three distinct edge boundary conditions—free edge, moored, and clamped—are presented in Fig. 5.4. It is evident that plates with free edges experience the lowest heave force, followed by moored, and then clamped edges. This trend stems from the increasing rigidity imposed by the edge conditions. A free edge allows maximum flexibility, enabling the plate to deform more easily and absorb wave energy efficiently, thus reducing the applied force. The moored edge restricts displacement but permits rotation, resulting in moderate stiffness and a higher heave force than the free edge. The clamped edge, which constrains both displacement and rotation, introduces the highest stiffness and stress concentration, leading to the greatest force required for comparable motion. Additionally, it can be seen that the heave force on the second circular (Fig. 5.4a) plate is reduced more compared to the heave force on the first plate (Fig. 5.4b) due to the wave interaction and porous bed. Based on these findings, free-edge conditions on the plates are adopted throughout this chapter for their effectiveness in minimizing heave force.

The variation of the heave force experienced by each circular plate over both rigid and porous seabeds is illustrated in Fig. 5.5 as a function of the dimensionless wavenumber (k_0h). For a rigid seabed ($Gh = 0$), Fig. 5.5a shows that the heave force on the first plate initially increases with the dimensionless wavenumber (k_0h), reaches a maximum value,

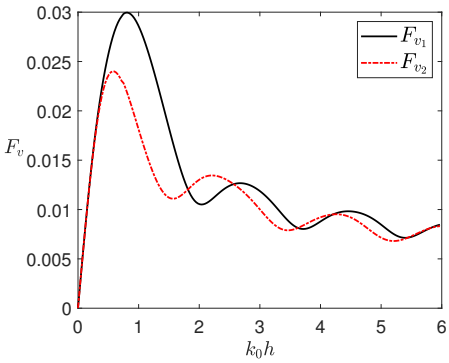

(a) $Gh = 0$

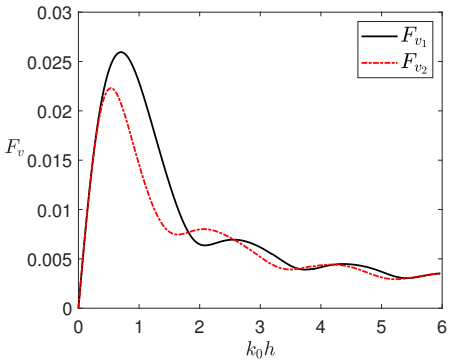

(b) $Gh = 0.5$

Figure 5.5: The dimensionless heave force (F_v), acting on a pair of two circular flexible plates in a horizontal array configuration is plotted against the dimensionless wavenumber (k_0h). Results are shown for (a) a rigid bottom condition ($Gh = 0$) and (b) a porous bottom condition ($Gh = 0.5$) with fixed parameters $a/h = 2$, $d/h = 0.05$ and $\beta = 30°$.

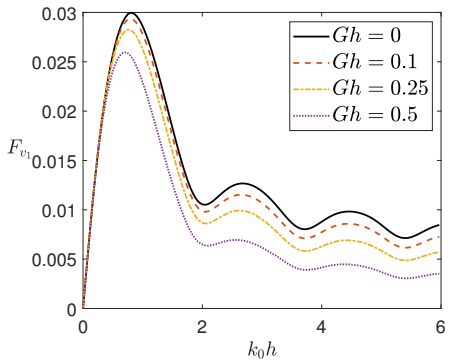

(a)

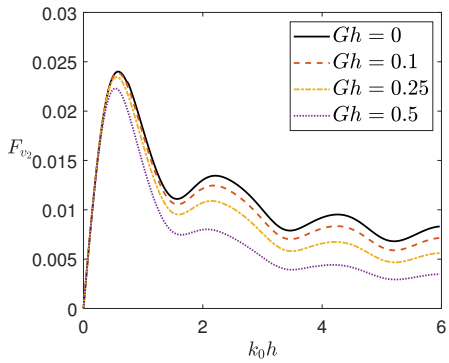

(b)

Figure 5.6: The dimensionless heave force (F_v), acting on (a) the first circular plate (F_{v_1}) and (b) the second circular plate (F_{v_2}) plotted against the dimensionless wavenumber (k_0h). The plots illustrate variations across different porosity parameters Gh while keeping fixed parameters of $d/h = 0.05$, $a/h = 2$ and $\beta = 30°$.

and then gradually decreases. The transmitted waves, weakened by interaction with the first plate, exert a lower force on the second plate. In the porous-bed case ($Gh = 0.5$), shown in Fig. 5.5b, the heave forces are further reduced due to wave energy absorption by the porous seabed.

Figure 5.6 presents the variation of heave force on the first plate (Fig. 5.6a) with respect to the dimensionless wavenumber (k_0h) for different porosity parameters (Gh). As observed, the heave force decreases progressively with increasing porosity, owing to the

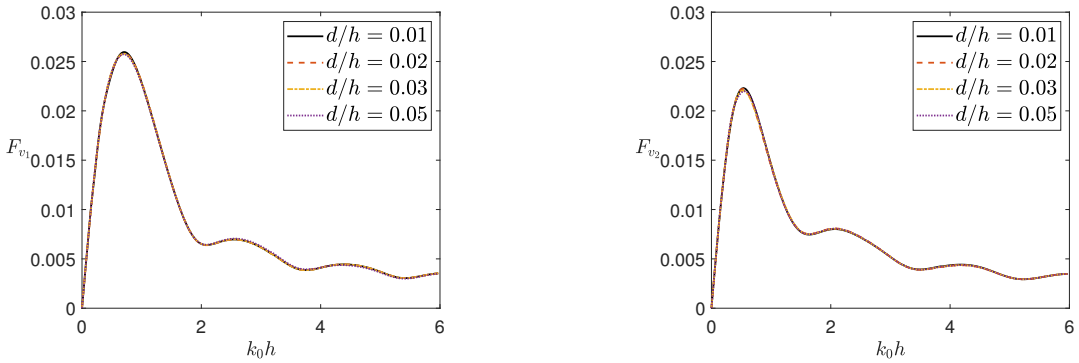

(a) (b)

Figure 5.7: The dimensionless heave force (F_v) acting on (a) first circular plate (F_{v_1}) and (b) second circular plate (F_{v_2}) plotted against the wavenumber (k_0h) for various values of thickness of the plates d/h with fixed parameters $a/h = 2$ and $\beta = 30°$ and $Gh = 0.5$.

combined energy dissipation effects of the porous seabed and wave-plate interaction. The transmitted wave, weakened after passing the first plate and interacting with the porous bed, induces an even lower heave force on the second plate, as shown in Fig. 5.6b. This highlights the significant role of seabed porosity in reducing wave energy and protecting the leeside region from strong wave action.

Figure 5.7 illustrates the variation in the heave force with the dimensionless wavenumber (k_0h) for different plate thicknesses. For very thin plates, only minor deviations in heave force are observed around $k_0h \approx 0.8$. Additionally, the porosity of the seabed significantly reduces the heave force on the second plate (F_{v_2}) compared to the first (F_{v_1}), as part of the wave energy is absorbed by the porous medium.

Figure 5.8 illustrates the variation in heave force with radii of the circular plates. Unlike the trends observed in Fig. 5.7, both Figs. 5.8a and 5.8b show that the heave force increases with larger plate radii due to the greater surface area exposed to wave action. Moreover, Fig. 5.8b clearly shows lower heave forces compared to Fig. 5.8a, which is attributed to the energy-absorbing effect of the porous seabed, along with the energy dissipated during wave interaction with the first plate.

The influence of Young's modulus on the heave force with respect to the dimensionless wavenumber is illustrated in Fig. 5.9, with detailed results shown in Figs. 5.9a and 5.9b for the first and second plates, respectively. The figures demonstrate a consistent trend: as Young's modulus increases, the heave force decreases, particularly within the range

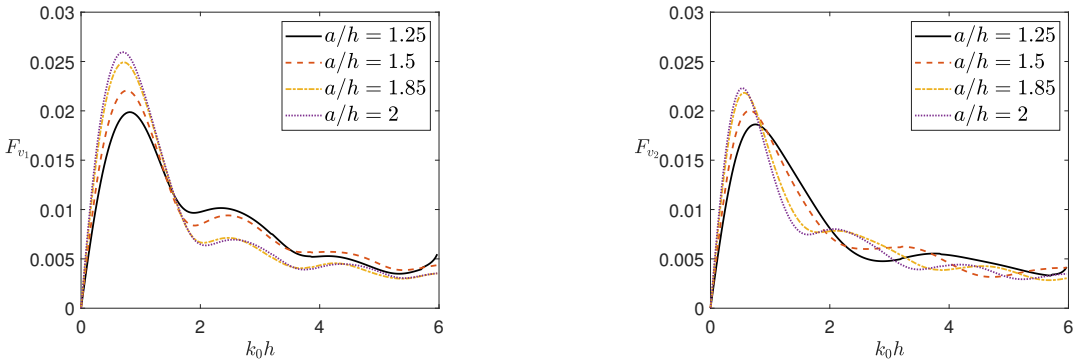

(a) (b)

Figure 5.8: The dimensionless heave force (F_v) acting on (a) the first circular plate (F_{v_1}) and (b) the second circular plate (F_{v_2}) plotted versus k_0h for different radii of the circular plates a/h with fixed parameters $d/h = 0.05$, $\beta = 30°$ and $Gh = 0.5$.

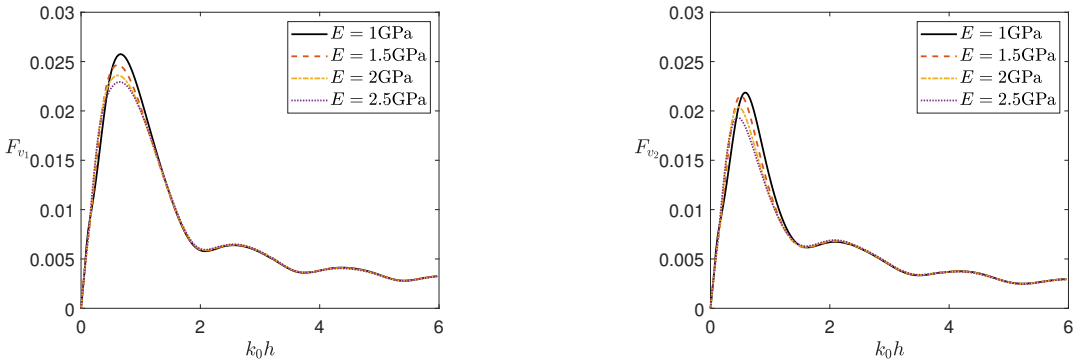

(a) (b)

Figure 5.9: The dimensionless heave force (F_v) acting on (a) the first circular plate (F_{v_1}) and (b) the second circular plate (F_{v_2}) as a function of the dimensionless wavenumber (k_0h) for various values of Young's modulus of the plates E with fixed parameters $a/h = 2$, $d/h = 0.05$, $\beta = 30°$ and $Gh = 0.5$.

$0 \leq k_0h \leq 1.5$. This reduction is due to the increased stiffness of the plates, which limits their deformation and, therefore, reduces the heave force induced by wave interaction. Notably, the decrease in heave force is more significant for the second plate. The combined effects of increased structural rigidity and seabed porosity result in a more pronounced attenuation of the heave response in the downstream plate.

To investigate the influence of different incident wave propagation angles on the plates, the heave force is plotted against the dimensionless wavenumber in Fig. 5.10. Figures 5.10a and 5.10b show the heave forces acting on the first and second plates, respectively, for

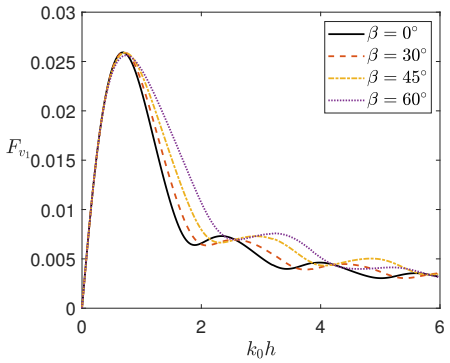

(a)

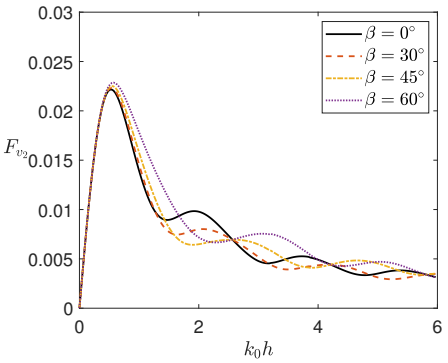

(b)

Figure 5.10: The dimensionless heave force (F_v) acting on (a) the first circular plate (F_{v_1}) and (b) the second circular plate (F_{v_2}) as a function of the dimensionless wavenumber (k_0h) for various values of incident angles β with fixed parameters $a/h = 2$, $d/h = 0.05$ and $Gh = 0.5$.

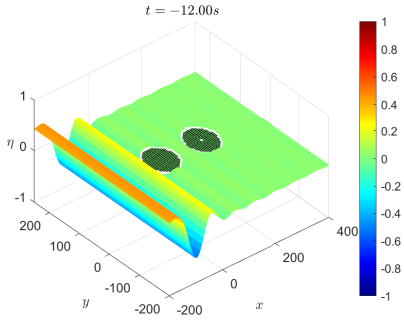

(a)

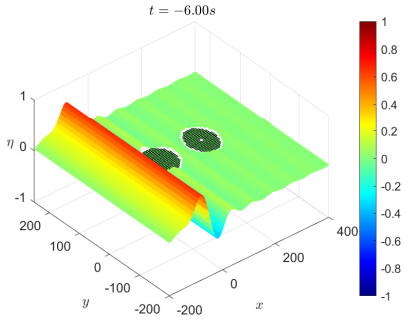

(b)

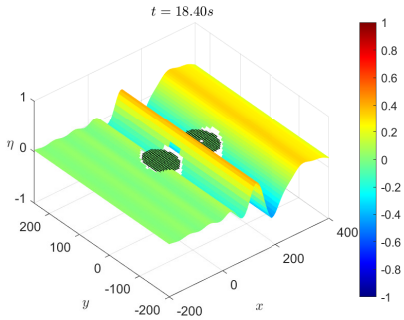

(c)

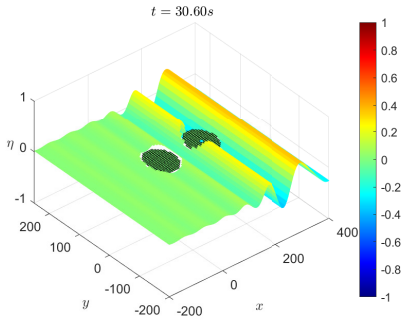

(d)

Figure 5.11: Snapshots of water wave interaction with two plates in horizontal array configuration with free edge conditions over a porous seabed ($Gh = 0.25$), showing changes in surface elevation changes over time. The distance between the plates is fixed as $3h$. The other parameters are fixed as $a/h = 2$, $d/h = 0.05$, $\beta = 0°$, $E = 1$ GPa and $\nu = 0.1$.

various angles of wave incidence. Consistent with earlier observations (Figs. 5.4–5.9), the heave force on the second plate is generally lower than that on the first plate, due to wave energy loss after interaction with the first plate and the porous bed. In Fig. 5.10a, a noticeable increase in the heave force is observed within the range $1 \leq k_0 h \leq 1.8$ as the incident wave angle becomes steeper. A similar rising trend is visible in Fig. 5.10b, though the increase is confined to a slightly narrower range, $1 \leq k_0 h \leq 1.6$. This trend might be attributed to the complex relationship between the incident angle β and the heave force, which is implicitly influenced by the velocity potential ϕ_1 (as described in Eq. (5.14)).

While the preceding discussion has focused on the heave forces acting on circular plates, a more practical insight into wave behavior around flexible circular plates over a porous bed can be achieved through temporal simulations of the fluid flow using the transformation given in Eq. (3.26). Figure 5.11 illustrates snapshots of these simulations at various time instances. The simulation reveals that the fluid flow carries higher energy before encountering the plate. Upon interaction, the wave energy is partially dissipated

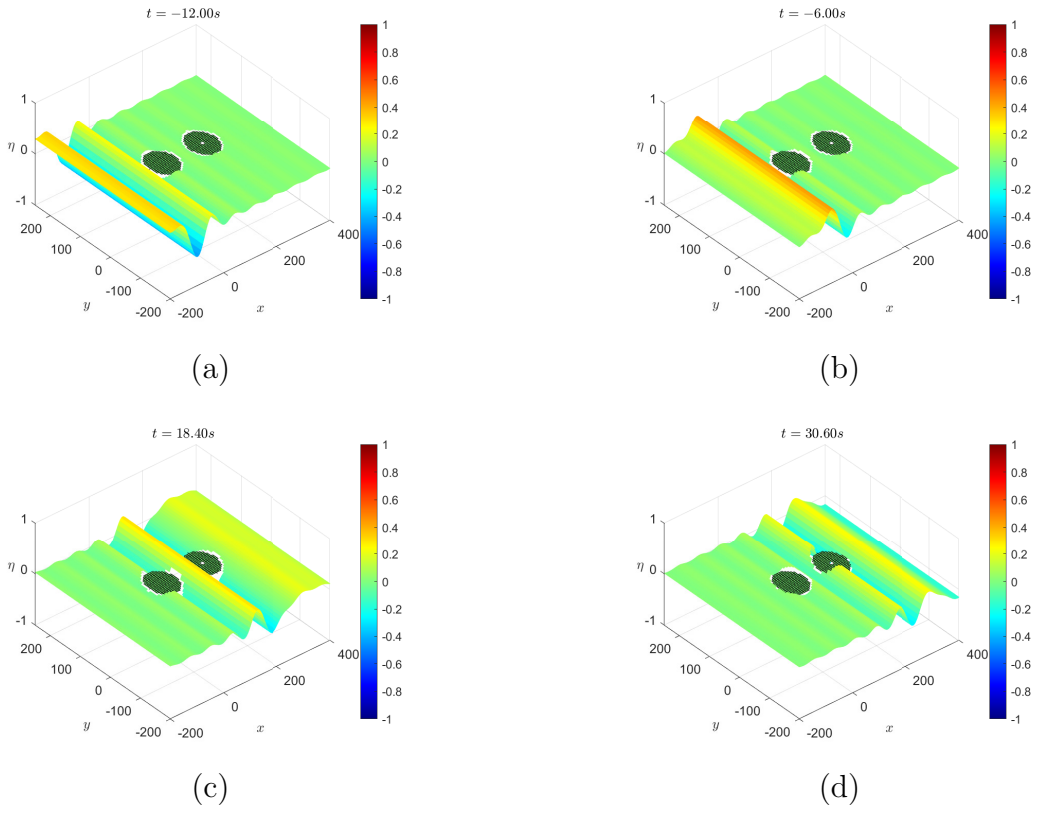

Figure 5.12: Same as Fig. 5.11 but for $Gh = 0.5$ and $\beta = 0°$.

due to the plate's deformation, partially transmitted, and further influenced by the porous seabed beneath. The porous bed plays a vital role in absorbing and scattering wave energy, thereby reducing the magnitude of the transmitted waves. As a result, the wave elevation on the leeside of the plates is significantly lowered. This combined interaction between the plate and the porous bed leads to effective attenuation of wave energy, offering enhanced protection for the leeside zone.

Figure 5.12 presents snapshots from time-dependent simulations of fluid flow for an incident wave angle of $\beta = 30°$. In comparison to Fig. 5.11, where the incident wave angle is $\beta = 0°$, a significant reduction in fluid surface elevation is observed. This attenuation is primarily attributed to the increased influence of the porous seabed at oblique wave incidence. As the porosity effect parameter increases, the seabed's capacity to absorb and dissipate wave energy becomes more effective, resulting in lower wave amplitudes towards the leeside zone. A comparison between Figs. 5.11 and 5.12 underscores the crucial role of seabed porosity in mitigating wave impact.

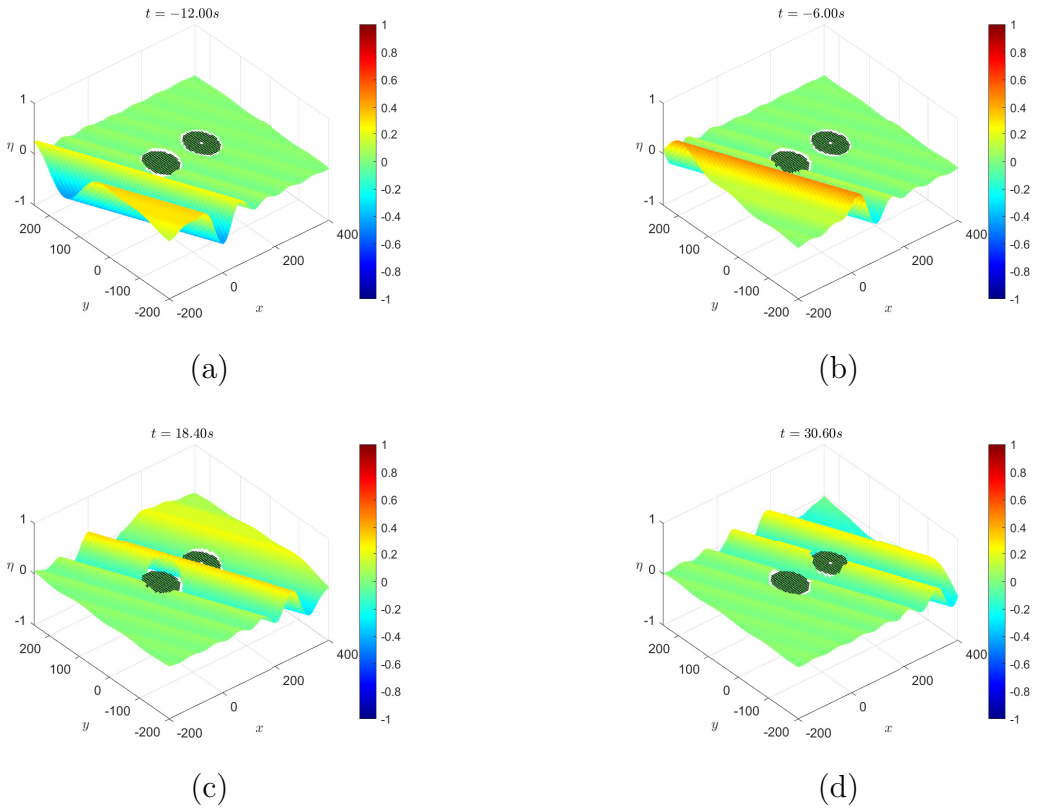

Figure 5.13: Same as Fig. 5.11 but for $Gh = 0.5$ and $\beta = 30°$.

Building upon the observations from Figs. 5.11 and 5.12, Fig. 5.13 presents snapshots from time-domain simulations at various time instances, where the incident wave approaches at an oblique angle of $\beta = 30°$ with respect to the positive x-axis, in contrast to the normal incidence considered previously. Similar to earlier results, a noticeable reduction in surface elevation is observed towards the leeside zone, indicating effective attenuation of wave energy.

5.3.2.2 Presence of three circular plates

The investigation of heave force is extended to three circular plates in horizontal array configuration, incorporating time-dependent simulations to assess the effects of seabed porosity. Figure 5.14 compares the heave forces on the plates for two different values of the porosity parameter (Gh), as shown in Figs. 5.14a and 5.14b. The results reveal a marked difference in the heave forces experienced by each plate, with Fig. 5.14b exhibiting significantly reduced values due to the higher porosity parameter. This increased porosity enhances energy dissipation within the seabed, resulting in diminished hydrodynamic loads on the plates. Furthermore, increasing the number of plates leads to a cumulative reduction in transmitted wave energy, further decreasing the heave forces on downstream plates. These findings underscore the effectiveness of a more porous bed and

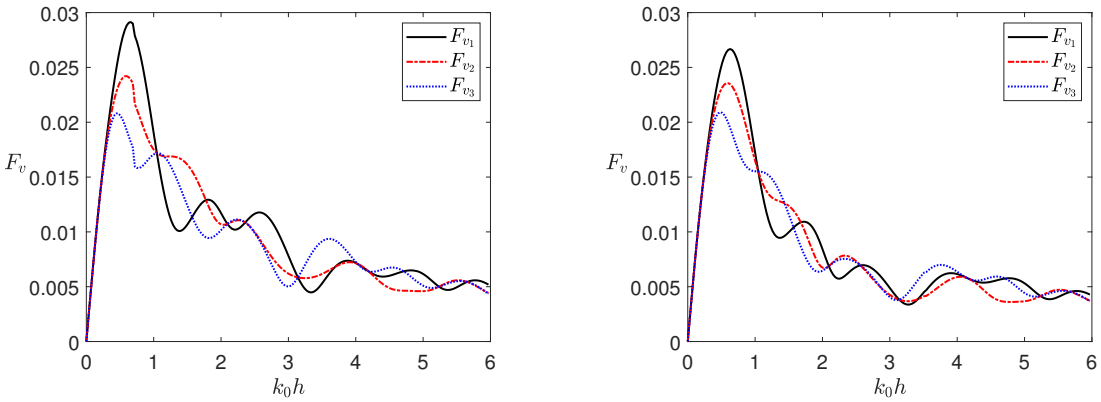

(a) $Gh = 0$ (b) $Gh = 0.5$

Figure 5.14: The dimensionless heave force (F_v) acting on the three circular flexible plates in a horizontal array configuration against the dimensionless wavenumber (k_0h). Results are shown for (a) rigid bottom ($Gh = 0$) and (b) porous bottom ($Gh = 0.5$) with fixed parameters $d/h = 0.05$, $a/h = 2$ and $\beta = 30°$.

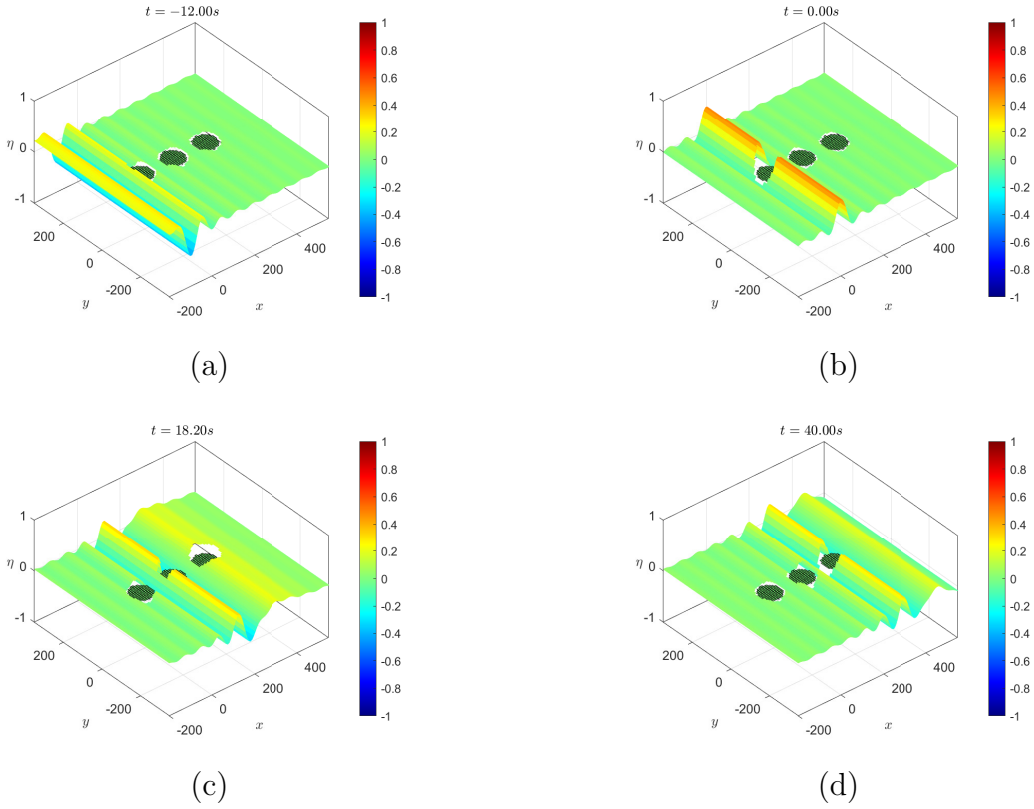

Figure 5.15: Snapshots of water wave interaction with three circular plates in horizontal array configuration with free edge conditions over a porous seabed ($Gh = 0.25$), showing changes in surface elevation over time. The distance between the plates is fixed as $3h$. The other parameters are fixed as $a/h = 2$, $d/h = 0.05$, $\beta = 0°$, $E = 1$ GPa and $\nu = 0.1$

the presence of multiple plates in absorbing wave energy and mitigating the impact on floating structures.

Figure 5.15 presents a static snapshot from time-dependent simulations, illustrating wave interaction with three flexible circular plates arranged in horizontal array over a porous bed. Before encountering the plates, the wave energy is high, but as waves pass through the plates, energy is progressively dissipated, transmitted, and absorbed by the porous bed. This results in a noticeable reduction in wave elevation on the leeside. Compared to Fig. 5.11, the lower wave heights in Fig. 5.15 can be attributed to the increased number of plates, which enhances energy dissipation through repeated wave-structure interactions, leading to a calmer water surface behind the structures.

As shown in Fig. 5.16, the wave elevation is further reduced compared to Figs. 5.12 and 5.15, due to the combined effects of increased seabed porosity, a higher porosity parameter (Gh), and the presence of additional circular plates. These factors enhance

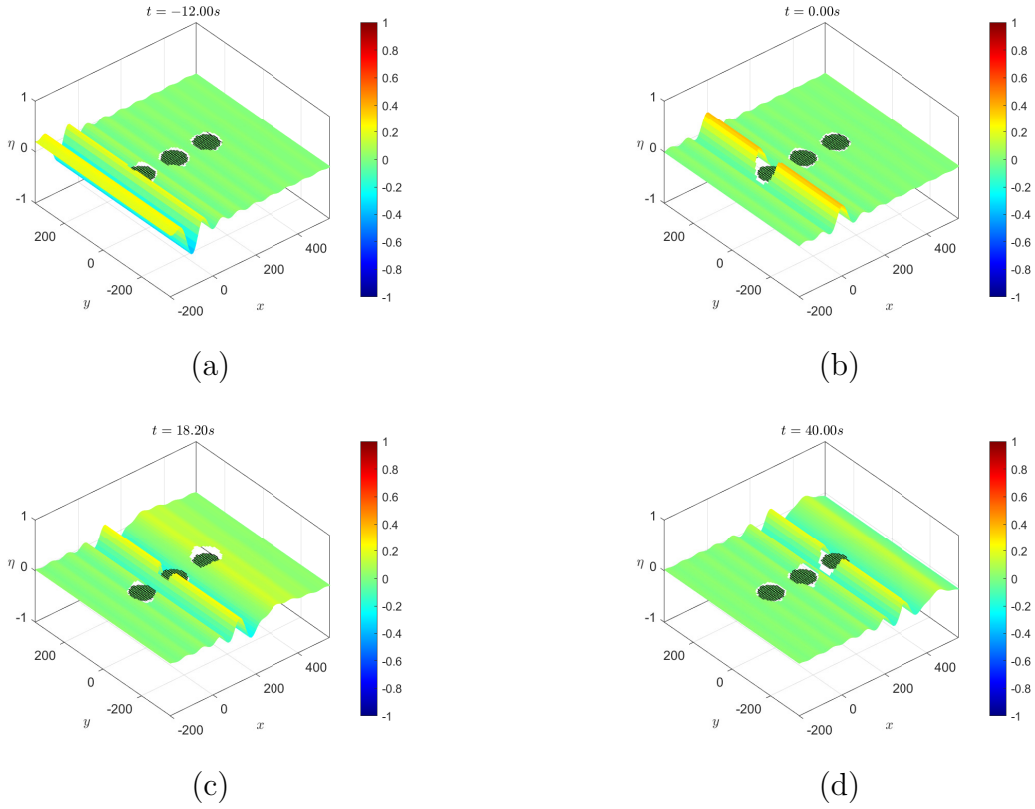

Figure 5.16: Same as Fig. 5.15 but for $Gh = 0.5$ and $\beta = 0°$.

energy dissipation and absorption, resulting in a more pronounced attenuation of wave energy.

In addition to Figs. 5.15 and 5.16, to examine the effect of an obliquely incident wave—rather than a normally incident wave—on an array of three circular floating elastic plates, Fig. 5.17 illustrates the temporal evolution of wave patterns at different time instances. The figure captures the wave behavior as an incident wave approaches the plate array at an angle of $\beta = 30°$, showing the interaction both before and after wave impact. As seen consistently across the time-domain results (Figs. 5.11, 5.12, 5.13, 5.15), Fig. 5.17 also highlights a clear reduction in wave elevation on the leeward side of the plates. This trend reaffirms the role of the porous bed in energy dissipation and the additional wave attenuation due to scattering and diffraction caused by the flexible plates. The results emphasize that both wave direction and seabed porosity are significant factors in reducing transmitted wave energy, thereby improving protection for the region behind the plate array.

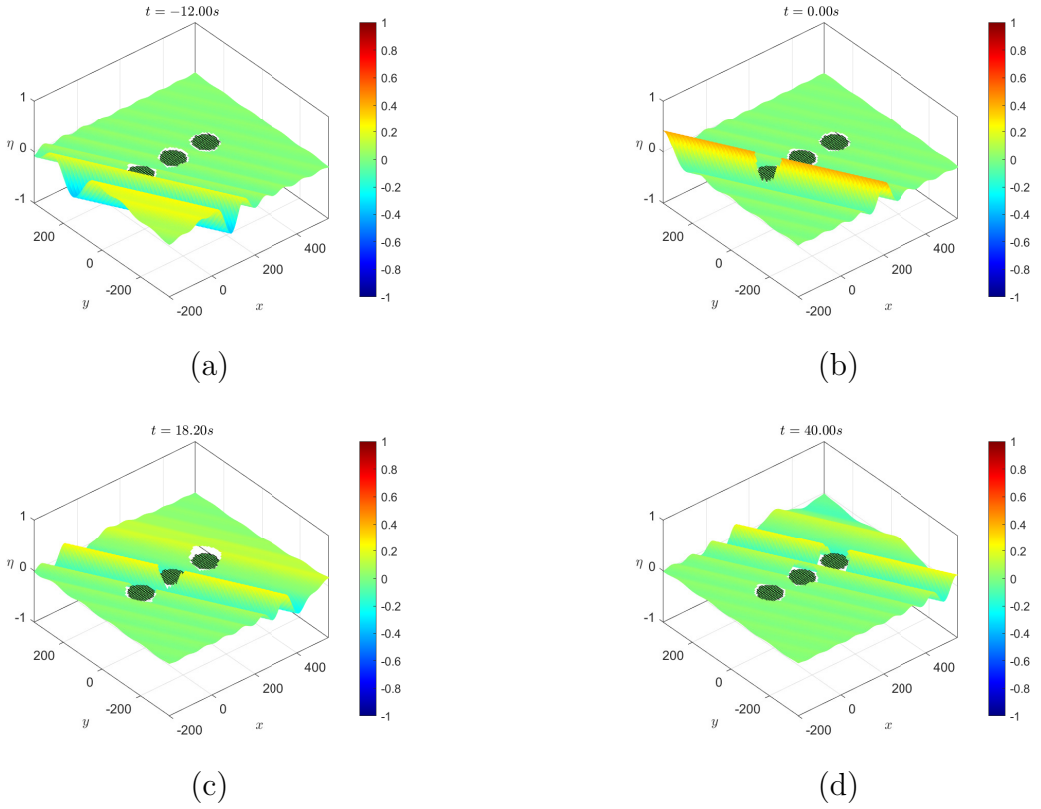

Figure 5.17: Same as Fig. 5.15 but for $Gh = 0.5$ and $\beta = 30°$.

5.3.2.3 Presence of four circular plates

After analyzing the effects of heave force on configurations involving two and three circular plates, the investigation is extended to examine its impact on a system comprising four circular flexible plates. In this context, two distinct arrangements are considered: Case 1: involving a horizontal array configuration and Case 2: a square configuration.

Case 1: Horizontal array configuration

Figure 5.18 explores the influence of four circular flexible plates in a horizontal array configuration on the heave forces experienced by each plate as a function of the wavenumber. The figure presents two scenarios (Figs. 5.18a and 5.18b) corresponding to different characteristics of the sea bed $Gh = 0$ (rigid bed) and $Gh = 0.5$ (porous bed), with fixed values of radii of each plate ($a/h = 2$) and thickness of each plate ($d/h = 0.05$). In both scenarios, a significant reduction in heave force is observed due to the individual interaction with the water wave and the plates. This interaction disrupts the flow patterns around each plate, leading to a decrease in the overall force experienced. The results

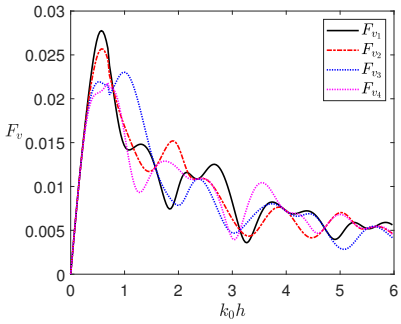

(a) $Gh = 0$

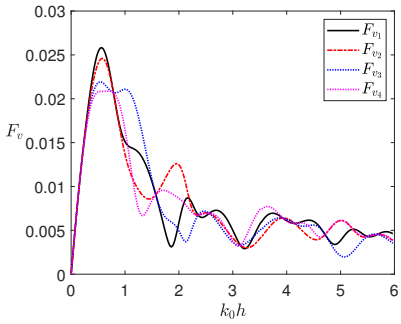

(b) $Gh = 0.5$

Figure 5.18: The dimensionless heave force (F_v) acting on the four circular flexible plates in a horizontal array configuration plotted against the dimensionless wavenumber (k_0h). Results are shown for (a) rigid bottom ($Gh = 0$) and (b) porous bottom ($Gh = 0.5$) with fixed parameters $d/h = 0.05$, $a/h = 2$ and $\beta = 30°$.

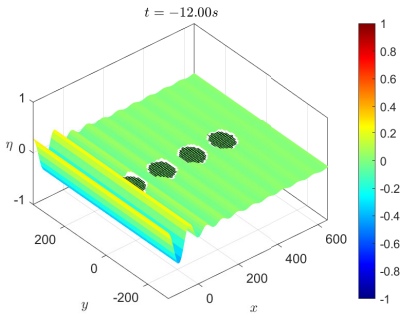

(a)

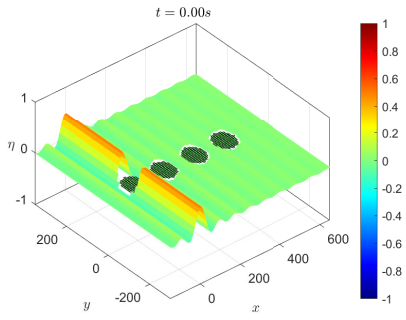

(b)

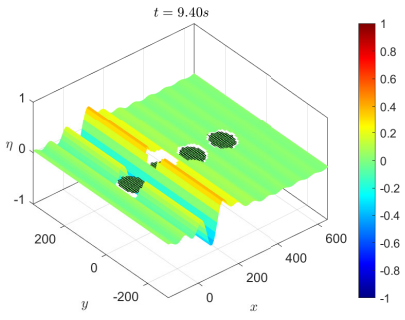

(c)

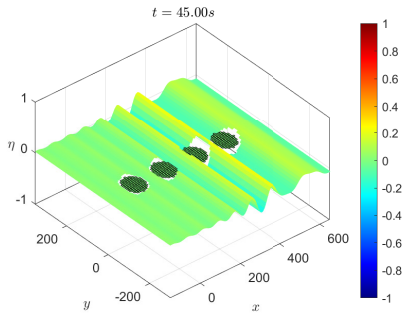

(d)

Figure 5.19: Snapshots of water wave interaction with four circular plates in horizontal array configuration with free edge conditions over a porous seabed ($Gh = 0.25$), showing changes in surface elevation over time. The distance between each plate is fixed as $3h$. The other fixed parameters are fixed as $a/h = 2$, $d/h = 0.05$, $\beta = 0°$, $E = 1$ GPa and $\nu = 0.1$.

suggest that increasing the number of circular flexible plates in conjunction with a higher porosity parameter leads to a significant reduction in the heave force experienced on the leeside zone. This highlights the critical role of porosity in creating a calmer region behind the circular flexible plates.

Figure 5.19 illustrates the interaction of waves with four floating circular flexible plates arranged in a horizontal array over a porous seabed, captured at various time instances from the simulation. Notably, the wave height on the leeward side in Fig. 5.19 is visibly reduced compared to those in Figs. 5.15 and 5.11. This reduction in wave elevation can be attributed to the increased number of circular plates in the configuration shown in Fig. 5.19, which enhances wave energy dissipation and attenuation.

Figure 5.20 demonstrates the effect of a higher porosity parameter on the temporal evolution of fluid flow in the presence of four floating circular elastic plates over a porous seabed. As the porosity parameter increases, the void spaces between the solid particles in the seabed become larger, allowing the porous medium to behave like a sponge, absorbing more wave energy as the fluid passes through it. This enhanced energy dissipation is

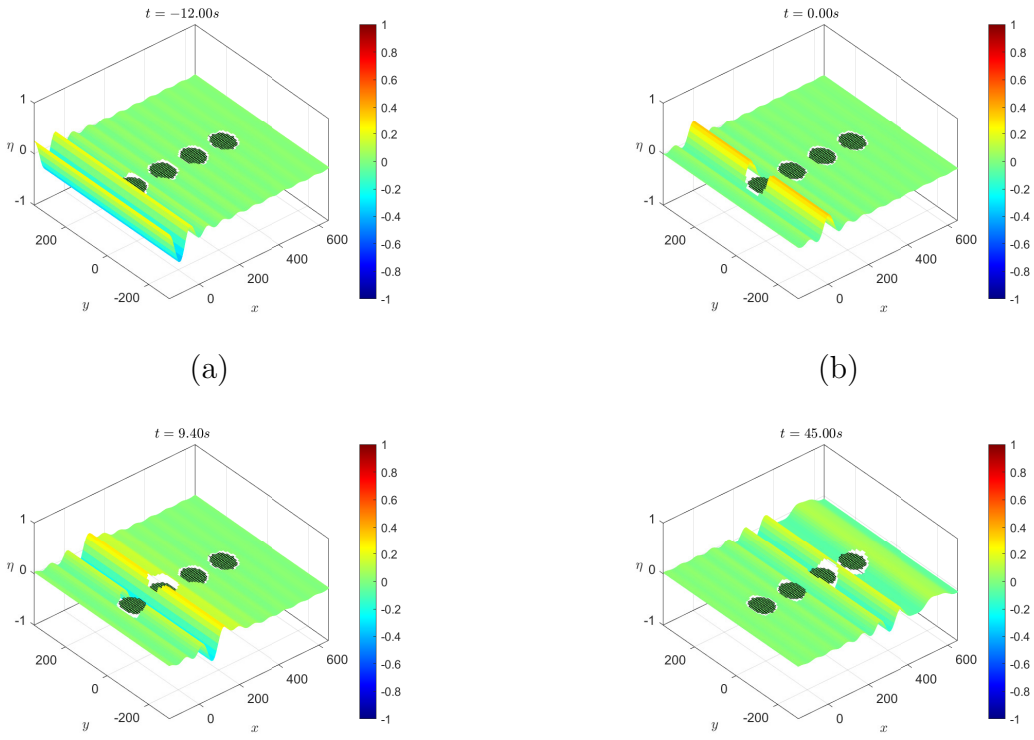

Figure 5.20: Same as Fig. 5.19 but for $Gh = 0.5$ and $\beta = 0°$.

evident in Fig. 5.20, where a noticeable reduction in wave elevation is observed compared to Fig. 5.19, which corresponds to a case with a lower porosity value. The decreased wave heights in Fig. 5.20 can be directly attributed to the increased energy absorption by the more permeable seabed.

Case 2: Square configuration

In addition to the time-dependent simulations of the horizontal array configuration of four circular flexible plates presented in Figs. 5.19 and 5.20, Fig. 5.21 illustrates a square configuration of the same number of plates. This figure captures still images from time-domain simulations, depicting the temporal evolution of fluid flow over and around the plates. The square configuration appears to enhance the attenuation effect, resulting in a more significant reduction in wave elevation on the leeward side compared to the horizontal array setup. Across all configurations, the presence of a porous seabed

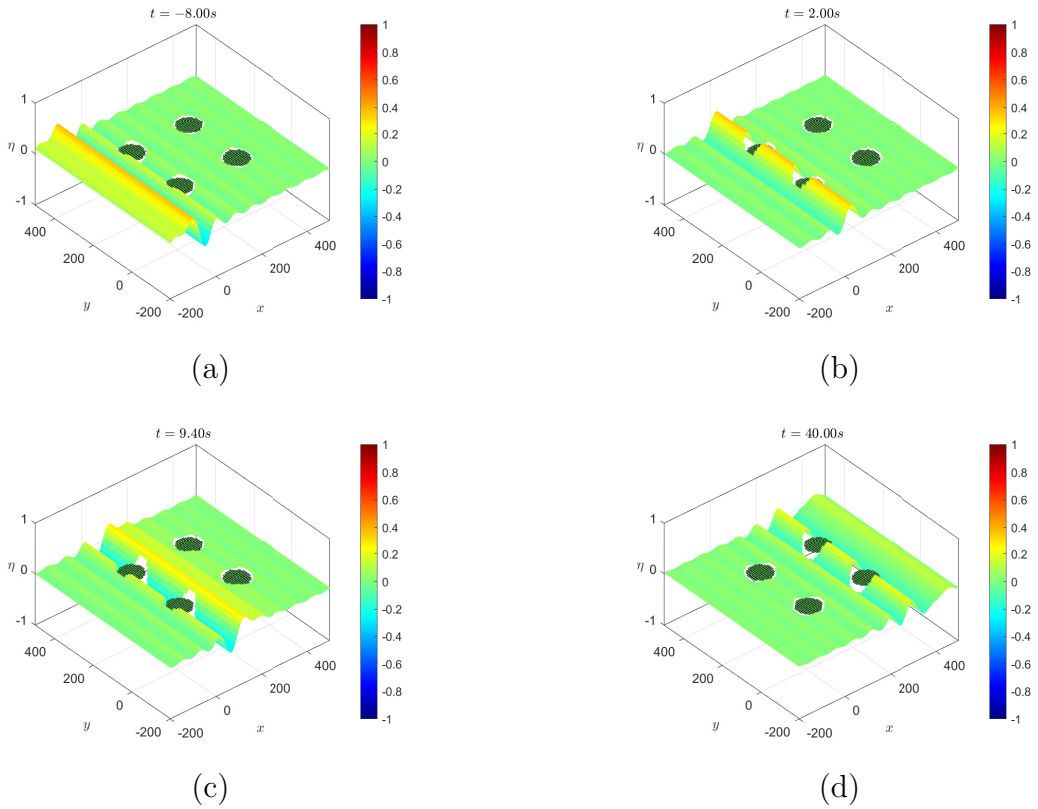

Figure 5.21: Snapshots of water wave interaction with four floating flexible circular plates with free-edge conditions in a square arrangement over a porous seabed ($Gh = 0.5$), showing changes in surface elevation over time. The distance between each plate (axis to axis) is fixed as $4h$. The other parameters are fixed as $a/h = 2$, $d/h = 0.05$, $\beta = 0°$, $E = 1$ GPa and $\nu = 0.1$.

consistently contributes to lower wave elevation behind the plates due to its ability to absorb and dissipate wave energy. Furthermore, increasing the number of circular flexible plates leads to cumulative energy loss through successive wave-structure interactions, which effectively mitigates wave impact and improves protection in the leeside region.

An alternative perspective on temporal simulations of fluid flow under oblique incidence, corresponding to an incident angle of $\beta = 30°$ in contrast to normal incidence ($\beta = 0°$), is depicted in Fig. 5.22. The figure offers a detailed visualization of wave interactions with a square configuration of floating circular elastic plates situated above a porous seabed. It demonstrates how the direction of wave incidence significantly affects the wave field and energy distribution, particularly as the obliquely incident waves propagate through the porous medium and interact with the plates.

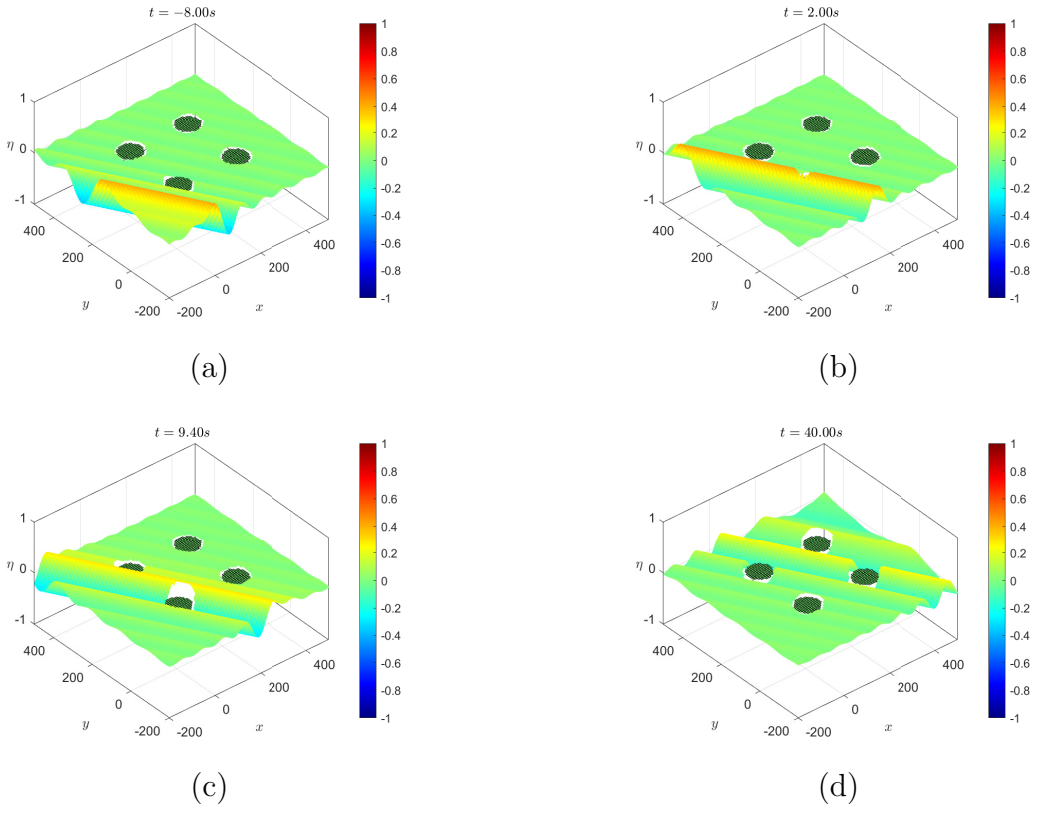

Figure 5.22: Same as Fig. 5.21 but for $Gh = 0.5$ and $\beta = 30°$.

5.3.3 Comparison of flow distributions around the circular plates

The surface elevation, which serves as a visual representation of the flow distribution across a given area, plays a crucial role in understanding fluid dynamics and wave behavior. To

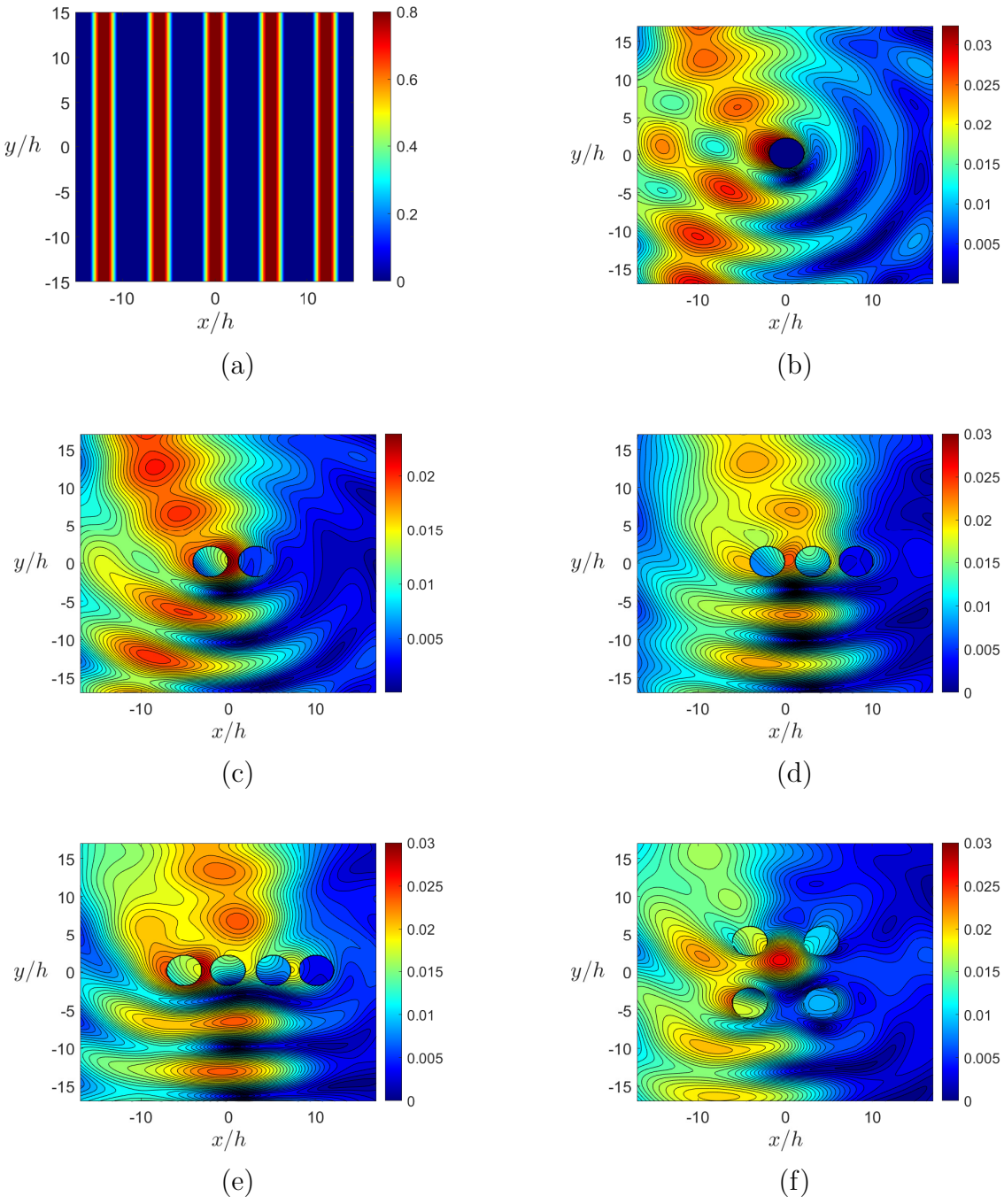

Figure 5.23: Contour plots of the surface elevation around (a) without plate (b) single plate (c) two plates in horizontal array configuration (d) three plates in horizontal array configuration (e) four plates in horizontal array configuration and (f) four plates in a square arrangement over a porous bed $Gh = 0.5$ with fixed wavenumber $k_0h = 0.5$. The other fixed parameters are fixed as $a/h = 2$, $d/h = 0.05$, $\beta = 0°$, $E = 1$ GPa and $\nu = 0.1$.

analyze the flow characteristics around the plates, the following mathematical expression

is employed to compute the free surface elevation

$$\eta_0(x,y,z) = \left| \frac{\mathrm{i}}{A\omega} \frac{\partial \phi_1}{\partial z} \right| \quad \text{at} \quad z = 0 \tag{5.27}$$

and

$$\eta_j(x,y,z) = \left| \frac{\mathrm{i}}{A\omega} \frac{\partial \phi_2^j}{\partial z} \right| \quad \text{at} \quad z = 0 \quad \text{for } j = 1,2,3,\ldots,N. \tag{5.28}$$

It is observed from Fig. 5.23 that increasing the number of circular flexible plates leads to a noticeable decrease in surface elevation on the leeside of the structure compared to the elevation observed in the incident wave region, before interaction with the plates. This attenuation in wave height is primarily due to two key factors: the porosity of the seabed and the wave-structure interactions. Furthermore, the spatial arrangement of the plates plays a critical role in determining the extent of wave attenuation. A square configuration leads to more effective disruption of the wave elevation compared to a horizontal array configuration on the leeside zone. Therefore, the combined effect of a larger number of plates, the presence of a porous seabed, and an optimized plate configuration—such as the square arrangement—significantly improves wave mitigation and promotes a more stable and protected marine environment behind the structure.

5.4 Conclusion

This paper investigates the wave scattering by multiple floating circular elastic plates over a porous seabed is analyzed using the EEM and Graf's addition theorem. The velocity potentials for incident plane wave and scattered waves are expressed in each region through expansions involving Bessel and Hankel functions. Three edge boundary conditions—clamped, moored, and free—are considered to capture different structural responses. It is observed that increasing the porosity of the seabed significantly reduces the heave force on the plates, while plates with free edges experience lower heave forces than clamped or moored plates. For horizontal arrays of two, three, or four plates, the heave force on each successive plate decreases relative to the previous one, reflecting the shielding effect of upstream plates. As the plate radii increase, the heave force initially rises in the long-wave region, reaches a peak, and then declines. In this region, increasing the Young's modulus (E) reduces the peak of heave force, highlighting the influence

of structural stiffness. Temporal simulations further reveal that higher seabed porosity lowers wave amplitude in the lee-side zone, and flow distributions, with and without the plates, further demonstrate the attenuation of wave amplitude due to the combined effects of the porous seabed and plate configuration.

Chapter 6

Wave interaction with surface-piercing structures under the effect of ocean current

This chapter investigates the role of ocean current in reducing wave energy towards the leeside zone by examining the influence of rectangular docks. Both analytical and numerical approaches are applied to tackle the problem.

6.1 Mathematical framework

The problem is setup in a Cartesian coordinate system, considering the interaction of rigid, rectangular docks placed over a rigid bed. The physical setup is illustrated in Fig. 6.1, where the docks are floating at the free surface of water (at $z = 0$). The xy-plane lies horizontally, while the z-axis points vertically upward. The total water depth is denoted by h, measured vertically downward from the free surface to the seabed. In this schematic, the heights of the docks are denoted by a_1 and a_2, and their widths by b_1 and b_2, respectively. The horizontal gap between the docks is represented by L. An incoming wave of amplitude A approaches from the negative x-direction, making an angle β with the positive x-axis (measured anticlockwise). Furthermore, we assume that uniform ocean current with constant velocity U is flowing parallel to the y-axis, directed from the negative to positive y-direction.

6.1.1 Problem setup for the EEM

For the analytical approach, The fluid domain is partitioned into five regions, which are defined as follows: region 1 is described by the domain $\Omega_1 = \{-\infty < x < 0, -\infty < y < \infty, -h \leq z \leq 0\}$; region 2 is defined by the domain; $\Omega_2 = \{0 < x < b_1, -\infty < y < \infty, -h \leq z \leq -a_1\}$; region 3 is represented by the domain $\Omega_3 = \{b_1 < x < s_1, -\infty < y < \infty, -h \leq z \leq 0\}$; region 4 is defined by the domain $\Omega_4 = \{s_1 < x < s_2, -\infty < y <$

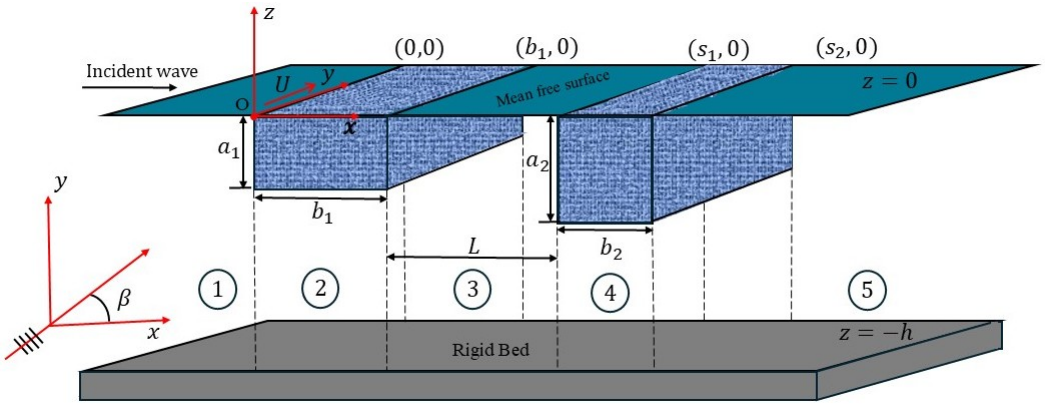

Figure 6.1: Schematic of the surface-piercing rectangular docks.

$\infty, -h \leq z \leq -a_2\}$ and region 5 is classified by the domain $\Omega_5 = \{s_2 < x < \infty, -\infty < y < \infty, -h \leq z \leq 0\}$.

6.1.2 Problem setup for the BEM

To ensure an accurate and well-posed BEM formulation, it is crucial to completely enclose the entire computational domain. This is achieved by introducing two auxiliary boundaries—$\mathscr{B}_l$ and $\mathscr{B}_r$—which are placed at the far left ($x = -l_0$) and far right ($x = r_0$) of the domain, respectively, where $l_0 > 0$ and $r_0 > 0$, as further illustrated in Fig. 6.2. To formulate the boundary integral equations used in the BEM, the fluid domain is fully bounded by a compound boundary $\mathscr{B} = \mathscr{B}_l \cup \mathscr{B}_1 \cup \mathscr{B}_2 \cup \mathscr{B}_3 \cup \mathscr{B}_4 \cup \mathscr{B}_5 \cup \mathscr{B}_6 \cup \mathscr{B}_7 \cup \mathscr{B}_8 \cup \mathscr{B}_9 \cup \mathscr{B}_b \cup \mathscr{B}_r$, where each segment is described as follows: $\mathscr{B}_l = \{x = -l_0,\ z| -h < z < 0\}$, $\mathscr{B}_1 = \{x| -l_0 < x < 0,\ z = 0\}$, $\mathscr{B}_2 = \{x = 0,\ z| -a_1 < z < 0\}$, $\mathscr{B}_3 = \{x| 0 < x < b_1,\ z = -a_1\}$, $\mathscr{B}_4 = \{x = b_1,\ z| -a_1 < z < 0\}$, $\mathscr{B}_5 = \{x| b_1 < x < s_1,\ z = 0\}$, $\mathscr{B}_6 = \{x = s_1,\ z| -a_2 < z < 0\}$, $\mathscr{B}_7 = \{x| s_1 < x < s_2,\ z = -a_2\}$, $\mathscr{B}_8 = \{x = s_2,\ z| -a_2 < z < 0\}$, $\mathscr{B}_9 = \{x| s_2 < x < r_0,\ z = 0\}$, $\mathscr{B}_r = \{x = r_0,\ z| -h < z < 0\}$ and $\mathscr{B}_b = \{x| -l_0 < x < r_0,\ z = -h\}$. This closed boundary setup defines the complete geometric model needed for the BEM implementation.

6.1.3 Governing equation and boundary conditions

The total velocity potentials in each region are defined as $\Psi_j(x, y, z, t) = Uy + \Phi_j(x, y, z, t)$ for $j = 1, 2, \ldots, 5$ where $\Phi_j(x, y, z, t) = \mathrm{Re}\left[\phi_j(x, z)e^{-\mathrm{i}(k_y y - \omega t)}\right]$ for $j = 1, 2, \ldots, 5$. Here, $k_y = k_0 \sin\beta$, with k_0 being the progressive wavenumber. In every region of the fluid domain, the spatial velocity potentials $\phi_j(x, z)$ satisfy the Helmholtz equation, which is

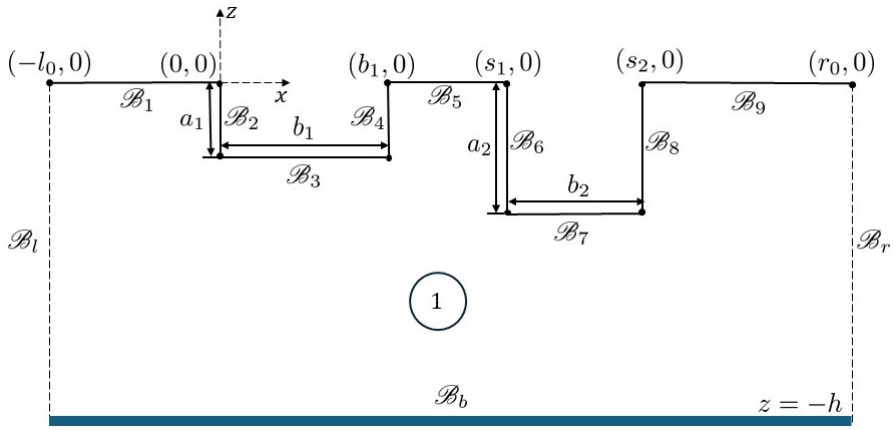

Figure 6.2: Schematic depiction of surface-piercing rectangular docks for the BEM.

expressed as

$$\frac{\partial^2 \phi_j}{\partial x^2} + \frac{\partial^2 \phi_j}{\partial z^2} - k_y^2 \phi_j = 0 \quad \text{for } j = 1, 2, \ldots, 5. \tag{6.1}$$

Owing to the impermeable nature of the seabed, the bottom-boundary condition reads

$$\frac{\partial \phi_j}{\partial z} = 0 \quad \text{at } z = -h \quad \text{for } j = 1, 2, \ldots, 5. \tag{6.2}$$

The linearized free-surface boundary condition is given by

$$\frac{\partial \phi_j}{\partial z} - \frac{(\omega - U k_y)^2}{g} \phi_j = 0 \quad \text{at } z = 0 \quad \text{for } j = 1, 3, 5. \tag{6.3}$$

The matching conditions for the pressure and velocity continuities are given by

$$\left.\begin{aligned} \phi_1 &= \phi_2 \\ \frac{\partial \phi_1}{\partial x} &= \frac{\partial \phi_2}{\partial x} \end{aligned}\right\} \quad \text{at } x = 0 \quad \text{for } z \in (-h, -a_1), \tag{6.4}$$

$$\left.\begin{aligned} \phi_2 &= \phi_3 \\ \frac{\partial \phi_2}{\partial x} &= \frac{\partial \phi_3}{\partial x} \end{aligned}\right\} \quad \text{at } x = b_1 \quad \text{for } z \in (-h, -a_1), \tag{6.5}$$

$$\left.\begin{aligned} \phi_3 &= \phi_4 \\ \frac{\partial \phi_3}{\partial x} &= \frac{\partial \phi_4}{\partial x} \end{aligned}\right\} \quad \text{at } x = s_1 \quad \text{for } z \in (-h, -a_2), \tag{6.6}$$

$$\left.\begin{aligned} \phi_4 &= \phi_5 \\ \frac{\partial \phi_4}{\partial x} &= \frac{\partial \phi_5}{\partial x} \end{aligned}\right\} \quad \text{at } x = s_2 \quad \text{for } z \in (-h, -a_2). \tag{6.7}$$

The structural boundary conditions at $x = 0$ and $x = b_1$ within the region $z \in [-a_1, 0]$ for $j = 1$ and $j = 3$, respectively, while at $x = s_1$ and $x = s_2$ within the region $z \in [-a_2, 0]$ for $j = 3$ and $j = 5$, respectively, are given by

$$\frac{\partial \phi_j}{\partial x} = 0 \quad \text{for } j = \{1, 3, 5\}. \tag{6.8}$$

As $x \to \pm\infty$, the boundary conditions are given by the Sommerfeld radiation condition, which read

$$\phi_1 = (e^{-\mathrm{i}q_0 x} + R_0 e^{\mathrm{i}q_0 x}) f_{10}(z) \quad \text{as } x \to -\infty, \tag{6.9}$$

$$\phi_5 = (T_0 e^{-\mathrm{i}q_0 (x - s_2)}) f_{10}(z) \quad \text{as } x \to \infty, \tag{6.10}$$

where $f_{10}(z)$ is the vertical eigenfunction, defined as [46]

$$f_{10}(z) = \frac{\mathrm{i}gA}{\omega - Uk_y} \frac{\cosh k_0 (h + z)}{\cosh k_0 h}, \tag{6.11}$$

the coefficients R_0 and T_0 are unknown reflected and transmitted waves, respectively, $q_0 = \sqrt{k_0^2 - k_y^2}$.

6.2 Solution method

The detailed formulation and solution procedures for both the EEM and BEM are presented in the following subsections. Each method is applied independently to solve the problem.

6.2.1 Analytic solution by the EEM

To obtain an analytical solution to the BVP, it is necessary to determine the spatial velocity potentials $\phi_j(x, z)$ for $j = 1, 2, 3, 4, 5$, which satisfy the Helmholtz equation (6.1), along with the relevant boundary conditions ((6.2) and (6.3)). The general expressions for the velocity potentials $\phi_j(x, z)$ in each region are expressed in the following form:

$$\phi_1 = A e^{-\mathrm{i}q_0 x} f_{10}(z) + \sum_{n=0}^{\infty} R_n e^{\mathrm{i}q_n x} f_{1n}(z), \tag{6.12}$$

$$\phi_2 = \sum_{n=0}^{\infty} \left[A_n e^{-\mathrm{i}Q_n x} + B_n e^{\mathrm{i}Q_n x}\right] f_{2n}(z), \tag{6.13}$$

$$\phi_3 = \sum_{n=0}^{\infty} \left[C_n e^{-\mathrm{i}q_n x} + D_n e^{\mathrm{i}q_n x}\right] f_{1n}(z), \tag{6.14}$$

$$\phi_4 = \sum_{n=0}^{\infty} \left[E_n e^{-\mathrm{i}\Theta_n x} + F_n e^{\mathrm{i}\Theta_n x}\right] f_{3n}(z), \tag{6.15}$$

$$\phi_5 = \sum_{n=0}^{\infty} T_n e^{-\mathrm{i}q_n x} f_{1n}(z), \tag{6.16}$$

where R_n, A_n, B_n, C_n, D_n, E_n, F_n, and T_n (for $n = 0, 1, 2, 3, \dots$) are the unknown coefficients; $q_n = \sqrt{k_n^2 - k_y^2}$ (for $n = 0, 1, 2, 3, \dots$); the wavenumbers k_n satisfy the dispersion relation [46]

$$k_n \tanh(k_n h) = \frac{(\omega - U k_y)^2}{g} \tag{6.17}$$

and $Q_n = \sqrt{p_n^2 - k_y^2}$ where $p_0 = 0$ and $p_n = n\pi/(h - a_1)$ for $n = 1, 2, 3, \dots$, $\Theta_n = \sqrt{\mu_n^2 - k_y^2}$ where $\mu_0 = 0$ and $\mu_n = n\pi/(h - a_2)$ for $n = 1, 2, 3, \dots$, the eigenfunctions $f_{1n}(z)$ (in the regions 1, 3 and 5), $f_{2n}(z)$ (in the region 2) and $f_{3n}(z)$ (in the region 4) for $n = 0, 1, 2, \dots$, respectively, are defined as

$$f_{1n}(z) = \frac{\mathrm{i}gA}{\omega - U k_y} \frac{\cosh k_n(h + z)}{\cosh k_n h}, \tag{6.18}$$

$$f_{2n}(z) = \cosh\big(p_n(h + z)\big), \tag{6.19}$$

$$f_{3n}(z) = \cosh(\mu_n(h + z)). \tag{6.20}$$

The eigenfunctions $f_{1n}(z)$, $f_{2n}(z)$ and $f_{3n}(z)$ for $n = 0, 1, 2, 3, \dots$ satisfy the orthogonality conditions, given as

$$\langle f_{1n}(z), f_{1m}(z)\rangle = \int_{-h}^{0} f_{1n}(z) f_{1m}(z) \mathrm{d}z = \begin{cases} X_{nn} & \text{if } n = m, \\ 0 & \text{if } n \neq m, \end{cases} \tag{6.21}$$

$$\langle f_{2n}(z), f_{2m}(z)\rangle = \int_{-h}^{-a_1} f_{2n}(z) f_{2m}(z) \mathrm{d}z = \begin{cases} Y_{nn} & \text{if } n = m, \\ 0 & \text{if } n \neq m, \end{cases} \tag{6.22}$$

$$\langle f_{3n}(z), f_{3m}(z)\rangle = \int_{-h}^{-a_2} f_{3n}(z) f_{3m}(z)\mathrm{d}z = \begin{cases} \xi_{nn} & \text{if } n = m, \\ 0 & \text{if } n \neq m, \end{cases} \tag{6.23}$$

where

$$X_{nn} = \left(\frac{\mathrm{i}g}{\omega - Uk_y}\right)^2 \frac{2k_n h + \sinh 2k_n h}{4k_n \cosh^2 k_n h} \quad \text{for } n = 0, 1, 2, 3, \ldots, \tag{6.24}$$

$$Y_{nn} = \begin{cases} h\left(1 - \dfrac{a_1}{h}\right) & \text{for } n = 0, \\ \dfrac{h}{2}\left(1 - \dfrac{a_1}{h}\right) & \text{for } n = 1, 2, 3, \ldots, \end{cases} \tag{6.25}$$

$$\xi_{nn} = \begin{cases} h\left(1 - \dfrac{a_2}{h}\right) & \text{for } n = 0, \\ \dfrac{h}{2}\left(1 - \dfrac{a_2}{h}\right) & \text{for } n = 1, 2, 3, \ldots. \end{cases} \tag{6.26}$$

By substituting the velocity potentials given in Eqs.(6.12)–(6.16) into the matching and structural boundary conditions defined in Eqs.(6.4)–(6.8), and utilizing the orthogonality of the eigenfunctions introduced in Eqs. (6.21)–(6.23), a system of infinite equations is obtained. The resulting equations are as follows.

$$\sum_{n=0}^{\infty} \tilde{X}_{mn} R_n - \sum_{n=0}^{\infty} \left[A_n + B_n\right] Y_{mn} = -A\tilde{X}_{m0}, \tag{6.27}$$

$$\sum_{n=0}^{\infty} -\mathrm{i}q_n X_{mn} R_n - \sum_{n=0}^{\infty} \mathrm{i}Q_n \left[-A_n + B_n\right] \tilde{X}_{mn} = \mathrm{i}q_0 A X_{m0}, \tag{6.28}$$

$$\sum_{n=0}^{\infty} \left[A_n e^{-\mathrm{i}Q_n b_1} + B_n e^{\mathrm{i}Q_n b_1}\right] Y_{mn} - \sum_{n=0}^{\infty} \left[C_n e^{-\mathrm{i}q_n b_1} + D_n e^{\mathrm{i}q_n b_1}\right] \tilde{X}_{mn} = 0, \tag{6.29}$$

$$\sum_{n=0}^{\infty} \mathrm{i}Q_n \left[-A_n e^{-\mathrm{i}Q_n b_1} + B_n e^{\mathrm{i}Q_n b_1}\right] \tilde{X}_{mn} - \sum_{n=0}^{\infty} \mathrm{i}q_n \left[-C_n e^{-\mathrm{i}q_n b_1} + D_n e^{\mathrm{i}q_n b_1}\right] X_{mn} = 0, \tag{6.30}$$

$$\sum_{n=0}^{\infty} \left[C_n e^{-\mathrm{i}q_n s_1} + D_n e^{\mathrm{i}q_n s_1}\right] Z_{mn} - \sum_{n=0}^{\infty} \left[E_n e^{-\mathrm{i}\Theta_n s_1} + F_n e^{\mathrm{i}\Theta_n s_1}\right] \tilde{Z}_{mn} = 0, \tag{6.31}$$

$$\sum_{n=0}^{\infty} \mathrm{i}q_n \left[-C_n e^{-\mathrm{i}q_n s_1} + D_n e^{\mathrm{i}q_n s_1}\right] X_{mn} - \sum_{n=0}^{\infty} \mathrm{i}\Theta_n \left[-E_n e^{-\mathrm{i}\Theta_n s_1} + F_n e^{\mathrm{i}\Theta_n s_1}\right] Z_{mn} = 0, \tag{6.32}$$

$$\sum_{n=0}^{\infty} \left[E_n e^{-\mathrm{i}\Theta_n s_2} + F_n e^{\mathrm{i}\Theta_n s_2}\right] \tilde{Z}_{mn} - \sum_{n=0}^{\infty} e^{-\mathrm{i}q_n s_2} T_n Z_{mn} = 0, \tag{6.33}$$

$$\sum_{n=0}^{\infty} \mathrm{i}\Theta_n \left[-E_n e^{-\mathrm{i}\Theta_n s_2} + F_n e^{\mathrm{i}\Theta_n s_2}\right] \tilde{Z}_{mn} + \sum_{n=0}^{\infty} \mathrm{i}q_n e^{-\mathrm{i}q_n s_2} T_n X_{mn} = 0, \tag{6.34}$$

for $n, m = 0, 1, 2, 3, \ldots$ and

$$\tilde{X}_{mn} = \int_{-h}^{-a_1} f_{1n}(z) f_{2m}(z) \mathrm{d}z, \quad X_{mn} = \int_{-h}^{0} f_{1n}(z) f_{1m}(z) \mathrm{d}z, \quad Y_{mn} = \int_{-h}^{-a_1} f_{2n}(z) f_{2m}(z) \mathrm{d}z,$$

$$Z_{mn} = \int_{-h}^{-a_2} f_{1n}(z) f_{3m}(z) \mathrm{d}z \quad \text{and} \quad \tilde{Z}_{mn} = \int_{-h}^{-a_2} f_{3n}(z) f_{3m}(z) \mathrm{d}z.$$

Note that m is given non-negative integers and for fixed value of m, Eqs. (6.27)–(6.34) form a system of simultaneous linear equations involves an infinite number of unknowns, namely R_n, A_n, B_n, C_n, D_n, E_n, F_n, and T_n for $n = 0, 1, 2, 3, \ldots$. Solving for all these infinite unknowns is impractical. Therefore, the series is truncated by retaining only a finite number of terms, up to $n = N$, which makes the system solvable using computational methods. After solving for the unknowns, substituting them back into Eqs. (6.12)–(6.16) gives the explicit expressions for the velocity potentials in each region.

6.2.2 Numerical solution by the BEM

In this subsection, we derive the integral equation corresponding to the two-dimensional BVP. To apply the BEM, the domain has only one region, say region 1. Let the spatial velocity in region 1 be denoted by ϕ. Applying Green's second identity to the velocity potentail ϕ and the Greens function $\mathcal{G}$ yields the following boundary integral equation [107]

$$\frac{1}{2}\phi(\xi, \nu) = \int_{\mathscr{B}} \left(\phi \frac{\partial \mathcal{G}}{\partial \mathbf{n}}(x, z; \xi, \nu) - \mathcal{G}(x, z; \xi, \nu) \frac{\partial \phi}{\partial \mathbf{n}} \right) \mathrm{d}\mathscr{B} \quad \text{if } (x, z) \in \mathscr{B}. \tag{6.35}$$

The Greens function $\mathcal{G}(x, z; \xi, \nu)$ is the fundamental solution satisfying

$$(\nabla^2 - k_y^2)\mathcal{G} = \delta(\xi - x)\delta(\nu - z), \tag{6.36}$$

and given by

$$\mathcal{G}(x, z; \xi, \nu) = \frac{K_0(k_y r)}{2\pi}, \tag{6.37}$$

where $r = \sqrt{(\xi - x)^2 + (\nu - z)^2}$ and $K_0(\cdot)$ is the modified Bessel function of the second kind with zeroth order. The normal derivative of $\mathcal{G}$ is obtained by [65]

$$\frac{\partial \mathcal{G}}{\partial n} = \frac{k_y}{2\pi} K_1(k_y r) \frac{\partial r}{\partial n}, \tag{6.38}$$

where $K_1(\cdot)$ is the modified Bessel function of the second kind with first order. As $r \to 0$, the asymptotic behavior of $K_0(k_y r)$ is

$$K_0(k_y r) = -\gamma - \ln\left(\frac{k_y r}{2}\right), \tag{6.39}$$

with $\gamma = 0.5772$ being Euler's constant. For clarity and to facilitate the numerical implementation using the BEM, the physical boundary conditions previously described are now reformulated and applied over the discretized computational boundaries corresponding to each subdomain.

$$\frac{\partial \phi}{\partial n} = 0 \quad \text{at} \quad \mathscr{B}_p \quad \text{for } p = 2, 3, 4, 6, 7, 8, b. \tag{6.40}$$

Additionally, the linearized free-surface boundary conditions are given as

$$\frac{\partial \phi}{\partial n} - \frac{(\omega - U k_y)^2}{g}\phi = 0 \quad \text{at} \quad \mathscr{B}_p \quad \text{for } p = 1, 5, 9. \tag{6.41}$$

By imposing boundary conditions (6.40) and (6.41) into Eq. (6.35) , the integral equation is obtained as

$$\begin{aligned}
&\frac{1}{2}\phi + \int_{\mathscr{B}_l}\left(\phi\frac{\partial \mathcal{G}}{\partial n} - \mathcal{G}\frac{\partial \phi}{\partial n}\right)d\mathscr{B} + \int_{\mathscr{B}_1}\left(\phi\frac{\partial \mathcal{G}}{\partial n} - \mathcal{G}K\phi\right)d\mathscr{B} + \int_{\mathscr{B}_2}\phi\frac{\partial \mathcal{G}}{\partial n}d\mathscr{B} + \int_{\mathscr{B}_3}\phi\frac{\partial \mathcal{G}}{\partial n}d\mathscr{B} \\
&+ \int_{\mathscr{B}_4}\phi\frac{\partial \mathcal{G}}{\partial n}d\mathscr{B} + \int_{\mathscr{B}_5}\left(\phi\frac{\partial \mathcal{G}}{\partial n} - \mathcal{G}K\phi\right)d\mathscr{B} + \int_{\mathscr{B}_6}\phi\frac{\partial \mathcal{G}}{\partial n}d\mathscr{B} + \int_{\mathscr{B}_7}\phi\frac{\partial \mathcal{G}}{\partial n}d\mathscr{B} + \int_{\mathscr{B}_8}\phi\frac{\partial \mathcal{G}}{\partial n}d\mathscr{B} \\
&+ \int_{\mathscr{B}_9}\left(\phi\frac{\partial \mathcal{G}}{\partial n} - \mathcal{G}K\phi\right)d\mathscr{B} + \int_{\mathscr{B}_r}\left(\phi\frac{\partial \mathcal{G}}{\partial n} - \mathcal{G}\frac{\partial \phi}{\partial n}\right)d\mathscr{B} + \int_{\mathscr{B}_b}\phi\frac{\partial \mathcal{G}}{\partial n}d\mathscr{B} \;=\; 0.
\end{aligned} \tag{6.42}$$

To solve the integral equation (6.42), we employ the BEM. Each boundary is discretized into N segments using constant element approach. The boundary integral equation is then discretized by evaluating the fundamental solution $\mathcal{G}$, which is centered at the node of the i^{th} element—treated as the source point (ξ, ν). Then, Eq. (6.42) can be written in a discretized form for the i^{th} element as

$$\begin{aligned}
&\frac{1}{2}\phi_i + \sum_{j=1}^{N_l}\int_{\mathscr{B}_l}\left(\phi_j\frac{\partial \mathcal{G}_{ij}}{\partial n} - \mathcal{G}_{ij}\frac{\partial \phi_j}{\partial n}\right)\mathrm{d}\mathscr{B} + \sum_{j=1}^{N_1}\int_{\mathscr{B}_1}\left(\phi_j\frac{\partial \mathcal{G}_{ij}}{\partial n} - \mathcal{G}_{ij}K\phi_j\right)\mathrm{d}\mathscr{B} \\
&\quad + \sum_{j=1}^{N_2}\int_{\mathscr{B}_2}\phi_j\frac{\partial \mathcal{G}_{ij}}{\partial n}\mathrm{d}\mathscr{B} + \sum_{j=1}^{N_3}\int_{\mathscr{B}_3}\phi_j\frac{\partial \mathcal{G}_{ij}}{\partial n}\mathrm{d}\mathscr{B} + \sum_{j=1}^{N_4}\int_{\mathscr{B}_4}\phi_j\frac{\partial \mathcal{G}_{ij}}{\partial n}\mathrm{d}\mathscr{B}
\end{aligned}$$

$$+\sum_{j=1}^{N_5}\int_{\mathscr{B}_5}\left(\phi_j\frac{\partial\mathcal{G}_{ij}}{\partial n}-\mathcal{G}_{ij}K\phi_j\right)\mathrm{d}\mathscr{B}+\sum_{j=1}^{N_6}\int_{\mathscr{B}_6}\phi_j\frac{\partial\mathcal{G}_{ij}}{\partial n}\mathrm{d}\mathscr{B}+\sum_{j=1}^{N_7}\int_{\mathscr{B}_7}\phi_j\frac{\partial\mathcal{G}_{ij}}{\partial n}\mathrm{d}\mathscr{B}$$
$$+\sum_{j=1}^{N_8}\int_{\mathscr{B}_8}\phi_j\frac{\partial\mathcal{G}_{ij}}{\partial n}\mathrm{d}\mathscr{B}+\sum_{j=1}^{N_9}\int_{\mathscr{B}_9}\left(\phi_j\frac{\partial\mathcal{G}_{ij}}{\partial n}-\mathcal{G}_{ij}K\phi_j\right)\mathrm{d}\mathscr{B}+\sum_{j=1}^{N_b}\int_{\mathscr{B}_b}\phi_j\frac{\partial\mathcal{G}_{ij}}{\partial n}\mathrm{d}\mathscr{B}$$
$$+\sum_{j=1}^{N_r}\int_{\mathscr{B}_r}\left(\phi_j\frac{\partial\mathcal{G}_{ij}}{\partial n}-\mathcal{G}_{ij}\frac{\partial\phi_j}{\partial n}\right)\mathrm{d}\mathscr{B}\;=\;0, \tag{6.43}$$

where $N_l, N_1, N_2, N_3, \ldots, N_9, N_b$ and N_r, respectively, denote the total number of segments on the boundaries $\mathscr{B}_l, \mathscr{B}_1, \mathscr{B}_2, \mathscr{B}_3, \ldots, \mathscr{B}_9, \mathscr{B}_b$ and $\mathscr{B}_r$. For simplicity, we define

$$\mathcal{M}_{ij}=\alpha\delta_{ij}+\int_{\mathscr{B}_j}\frac{\partial\mathcal{G}_{ij}}{\partial n}\mathrm{d}\mathscr{B}, \tag{6.44}$$

$$G_{ij}=\int_{\mathscr{B}_j}\mathcal{G}_{ij}\mathrm{d}\mathscr{B}. \tag{6.45}$$

Substituting Eqs. (6.44) and (6.45) into Eq. (6.43), we obtain

$$\sum_{j=1}^{N_l}\left(\phi_j\mathcal{M}_{ij}-G_{ij}\frac{\partial\phi_j}{\partial n}\right)\Big|_{\mathscr{B}_l}+\sum_{j=1}^{N_1}\left(\phi_j\mathcal{M}_{ij}-G_{ij}K\phi_j\right)\Big|_{\mathscr{B}_1}+\sum_{j=1}^{N_2}\phi_j\mathcal{M}_{ij}\Big|_{\mathscr{B}_2}+\sum_{j=1}^{N_3}\phi_j\mathcal{M}_{ij}\Big|_{\mathscr{B}_3}$$
$$+\sum_{j=1}^{N_4}\phi_j\mathcal{M}_{ij}\Big|_{\mathscr{B}_4}+\sum_{j=1}^{N_5}\left(\phi_j\mathcal{M}_{ij}-G_{ij}K\phi_j\right)\Big|_{\mathscr{B}_5}+\sum_{j=1}^{N_6}\phi_j\mathcal{M}_{ij}\Big|_{\mathscr{B}_6}+\sum_{j=1}^{N_7}\phi_j\mathcal{M}_{ij}\Big|_{\mathscr{B}_7}$$
$$+\sum_{j=1}^{N_8}\phi_j\mathcal{M}_{ij}\Big|_{\mathscr{B}_8}+\sum_{j=1}^{N_9}\left(\phi_j\mathcal{M}_{ij}-G_{ij}K\phi_j\right)\Big|_{\mathscr{B}_9}+\sum_{j=1}^{N_r}\left(\phi_j\mathcal{M}_{ij}-G_{ij}\frac{\partial\phi_j}{\partial n}\right)\Big|_{\mathscr{B}_r}$$
$$+\sum_{j=1}^{N_b}\phi_j\mathcal{M}_{ij}\Big|_{\mathscr{B}_b}=0. \tag{6.46}$$

Considering the fundamental solution centered at each node on every segment, the boundary integral equation is evaluated at every node $i = 1, 2, 3, \ldots, N_p$, where $p = 1, 2, 3, \ldots, 9, l, r, b$. This leads to total of N equations corresponding to N unknowns, forming an $N \times N$ linear system, where $N = N_l + N_1 + N_2 + N_3 + \cdots + N_9 + N_r + N_b$. Solving this system of equations, we obtain the spatial velocity potential ϕ and its normal derivative $\frac{\partial\phi}{\partial n}$ at each node on the boundary element.

6.3 Results and discussions

The reflection coefficient R and the transmission coefficient T have been evaluated for various structural and wave parameters as well as for different velocities of ocean current. These coefficients are computed using the relations:

$$R = \frac{R_0}{A} \quad \text{and} \quad T = \frac{T_0}{A}. \tag{6.47}$$

The non-dimensional horizontal forces acting on the front side (F_f^j) and rear side (F_r^j) of the j^{th} dock are given by [46]

$$F_f^j = \frac{-\mathrm{i}(\omega - Uk_y)}{gh^2} \int_{-a_j}^{0} \phi_{2j-1}(l_{2j-1}, z)\, \mathrm{d}z \quad \text{for } j = 1, 2, \tag{6.48}$$

$$F_r^j = \frac{-\mathrm{i}(\omega - Uk_y)}{gh^2} \int_{-a_j}^{0} \phi_{2j+1}(l_{2j+1}, z)\, \mathrm{d}z \quad \text{for } j = 1, 2, \tag{6.49}$$

where $j = 1$ and $j = 2$ correspond to the horizontal forces on the first and second docks, respectively. In Eqs. (6.48) and (6.49), the positions are defined as $l_1 = 0$, $l_2 = b_1$, $l_3 = s_1$, and $l_4 = s_2$. For numerical simulations, unless stated otherwise, the parameters are kept consistent for both single and dual dock configurations. The chosen values are as follows: water depth $h = 10$ m, incident wave amplitude $A = 1$, dimensionless dock heights $a_1/h = a_2/h = 0.5$, gap between the docks $L/h = 1$, dimensionless dock widths $b_1/h = b_2/h = 1$, wave incident angle $\beta = 30^\circ$ and dimensionless velocity of the ocean current $U/\sqrt{gh} = 0.5$.

6.3.1 Validation

It is important to note that the present study reduces to the classical problem of wave scattering by rectangular structures in the absence of an ocean current, as reported in Ref. [169]. To validate the accuracy of the code, the reflection coefficient as a function of the dimensionless wavenumber k_0h using both the EEM and BEM is calculated. In Fig. 6.3, we compare these results with the analytical solution provided by Zheng & Zhang [169]. In this figure, the star symbols indicate data obtained from the Ref. [169], while the solid line and circles correspond to the present results obtained from the EEM and BEM, respectively. It is evident from both figures that the results obtained using the EEM and

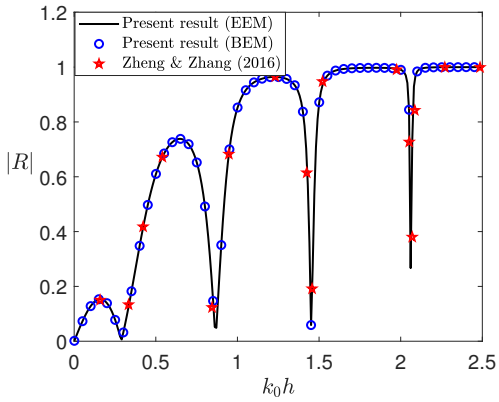

Figure 6.3: The reflection coefficient against the dimensionless wavenumber k_0h for fixed values of $a_1/h = a_2/h = 0.25$, $b_1/h = b_2/h = 1$, $L/h = 4.25$ and $U = 0$.

BEM are in excellent agreement with the existing studies. This confirms the accuracy of the code.

6.3.2 Convergence analysis in the BEM

This subsection presents the convergence analysis of numerical solutions based on BEM. Convergence is assessed by examining the behavior of the reflected and transmitted coefficients as the number of evanescent modes, N, increases. As shown in Table 6.1, the values of the reflection and transmission coefficients stabilize, converging up to three decimal places when $N = 10$. Therefore, for all subsequent numerical computations, the number of evanescent modes is fixed at $N = 10$, ensuring both computational efficiency.

6.3.3 Case of a single dock

In the present study, if the height of the second dock is considered negligible, the problem simplifies to the case of a single surface-piercing dock. In the following subsection, the effects of single dock on the reflection and transmission coefficients are presented.

6.3.3.1 Reflection and transmission coefficients

Figure 6.4 illustrates the variation in the reflection and transmission coefficients with the dimensionless wavenumber k_0h for different current velocities. In the figure, solid lines represent the analytical results obtained using the EEM, and symbols denote the numerical results computed via the BEM. From Fig. 6.4a, it is observed that as the velocity of ocean current increases, the reflection coefficient curves shift to the left and

N	k_0h	**BEM**	
		$\|R\|$	$\|T\|$
1	0.3	0.5564	0.8309
	0.5	0.5449	0.8385
	1	0.9920	0.1260
5	0.3	0.5493	0.8356
	0.5	0.5553	0.8317
	1	0.9931	0.1172
10	0.3	0.5336	0.8467
	0.5	0.5648	0.8251
	1	0.9945	0.1019
20	0.3	0.5332	0.8460
	0.5	0.5640	0.8257
	1	0.9941	0.1019

Table 6.1: A comparison of the reflection and transmission coefficients based on the BEM for various values of the dimensionless wavenumber k_0h, with fixed parameters: $U/\sqrt{gh} = 0.5$, $a_1/h = a_2/h = 0.5$, $b_1/h = b_2/h = 1$, $L/h = 1$, and $\beta = 30°$.

approach unity more rapidly, indicating enhanced wave reflection under stronger ocean current. On the other hand, Fig. 6.4b reveals that the transmission coefficient decreases with increasing velocity of the ocean current, signifying a reduction in the amount of wave energy passing through the structure. Furthermore, Figs. 6.4a and 6.4b clearly demonstrate that the numerical results obtained using the BEM align closely with the analytical results calculated via the EEM.

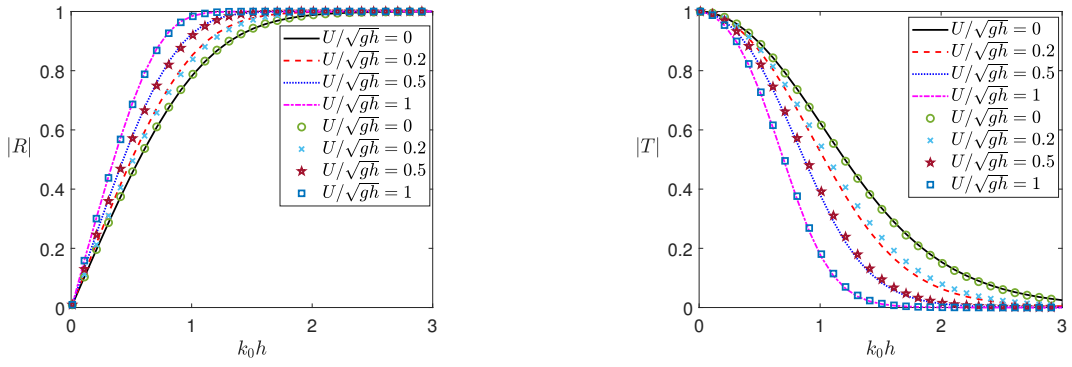

(a) (b)

Figure 6.4: (a) The reflection and (b) transmission coefficients plotted against the dimensionless wavenumber k_0h for different velocities of the ocean current $U/\sqrt{gh}$. The other fixed parameters are taken as $a_1/h = 0.5$, $b_1/h = 1$, and $\beta = 30°$. The symbols represent the results obtained using the BEM, while the solid lines depict the results obtained from the EEM.

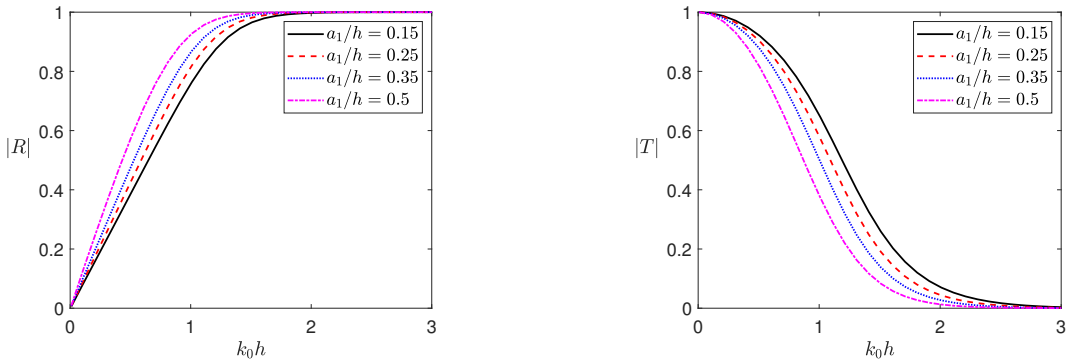

(a) (b)

Figure 6.5: (a) The reflection and (b) transmission coefficients plotted against the dimensionless wavenumber k_0h for different values of the dock height a_1/h. The other fixed parameters are taken as $b_1/h = 1$, $U/\sqrt{gh} = 0.5$, and $\beta = 30°$.

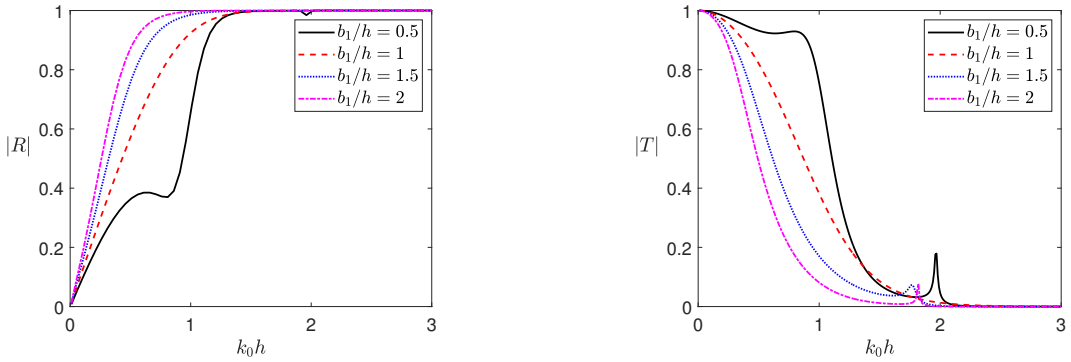

(a) (b)

Figure 6.6: (a) The reflection and (b) transmission coefficients plotted against the dimensionless wavenumber k_0h for different values of dock width b_1/h. The other fixed parameters are taken as $a_1/h = 0.5$, $U/\sqrt{gh} = 0.5$, and $\beta = 30°$.

Figure 6.5 shows the reflection (Fig. 6.5a) and transmission (Fig. 6.5b) coefficients versus k_0h for various dock heights. As seen in Fig. 6.5a, the reflection coefficient increases with increasing dock height up to $k_0h \approx 1.8$. Beyond this point ($k_0h \gtrsim 1.8$), the reflection stabilizes and approaches full reflection ($|R| \approx 1$) for all dock heights, , indicating that all of the wave energy is reflected back. In contrast, Fig. 6.5b shows that the transmission coefficient decreases consistently as the dock height increases. This behavior occurs because a taller dock presents a larger surface area to the incoming waves, blocking more of the wave energy. As a result, a greater portion of the incident wave is reflected, and only a small amount is able to pass beneath the dock.

Figure 6.6 illustrates the variations in the reflection and transmission coefficients against the dimensionless wavenumber k_0h for different dock widths. In Fig. 6.6a, the reflection coefficient generally increases with increasing k_0h for all dock widths. For wider docks (e.g., $b_1/h = 1.5$ and 2), the reflection increases smoothly and saturates near full reflection as k_0h becomes large. However, for narrower docks, particularly at $b_1/h = 0.5$, the reflection curve does not rise smoothly. Instead, it shows slight bends or irregularities in the range $0.65 \lesssim k_0h \lesssim 1.4$. These irregularities are due to wave interference beneath the dock. In narrower docks, part of the wave passes through and reflects within the gap under the structure. This can cause the waves to interfere with each other—sometimes strengthening, sometimes weakening the reflection—resulting in small non-smooth variations in the curve. On the other hand, in Fig. 6.6b, for wider docks, the transmission drops smoothly as k_0h increases till $k_0h \approx 1.8$, indicating stronger wave blocking. Between $k_0h = 1.65$ and 2.2, a sudden increase appears in transmission for all dock widths, once again due to interference below the dock. The gap under the dock, in this range, allows certain wave sizes to transmit more easily as phase alignment enables more energy to pass, causing these rapid changes in the curve.

Figure 6.7 demonstrates the effect of the incident wave angle β on the reflection and transmission coefficients. At normal incidence ($\beta = 0°$), the wave directly enters the gap beneath the dock, resulting in minimal reflection and maximum transmission. As β increases, the wave strikes the dock at an angle, effectively increasing the horizontal

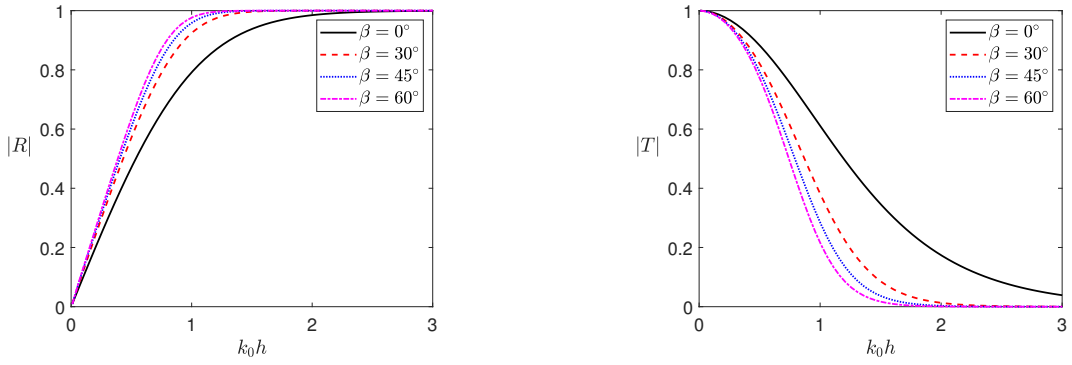

(a) (b)

Figure 6.7: (a) The reflection and (b) transmission coefficients plotted against the dimensionless wavenumber k_0h for different values of the wave propagation angle β. The other fixed parameters are taken as $a_1/h = 0.5$, $b_1/h = 1$ and $U/\sqrt{gh} = 0.5$.

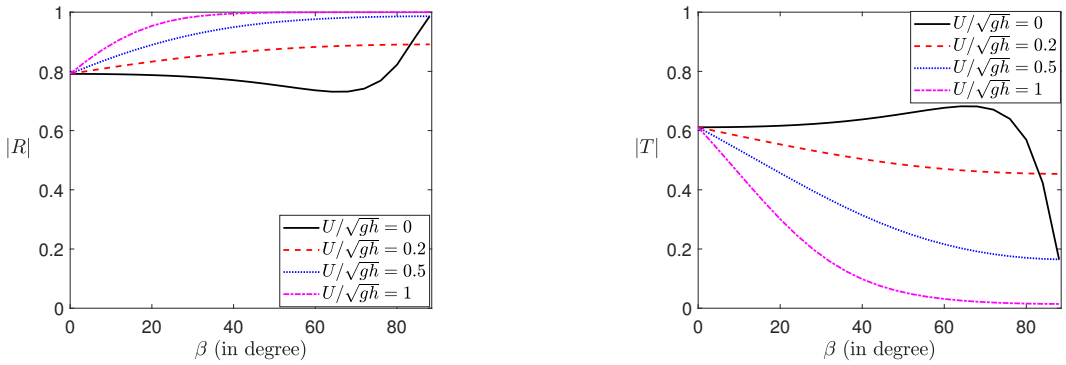

(a) (b)

Figure 6.8: (a) The reflection and (b) transmission coefficients plotted against the angle of incidence β for different values of the current velocities $U/\sqrt{gh}$. The other fixed parameters are taken as $a_1/h = 0.5$, $b_1/h = 1$, and $k_0 h = 1$.

width it encounters. This makes it harder for the wave to pass under the structure, causing more energy to be reflected. Physically, the oblique angle increases the path length across the dock and reduces the vertical component of wave motion beneath it, both of which contribute to stronger reflection and reduced transmission.

Figure 6.8 illustrates the variation of the reflection and transmission coefficients with respect to the incident wave angle β for different ocean current velocities. When the incident angle reaches $\beta = 90°$, the reflection coefficient approaches its maximum value, indicating complete reflection, while the transmission coefficient drops to zero. This occurs because at $\beta = 90°$, the waves travel parallel to the dock, causing the entire wave front to interact with the structure. As a result, nearly all wave energy is reflected, and no transmission occurs.

6.3.3.2 Horizontal forces on the front and rear faces of the dock

Figure 6.9 displays the variation in the horizontal force acting on the front face of the dock as a function of the dimensionless wavenumber $k_0 h$. In Fig. 6.9a, the horizontal force is plotted for increasing values of the velocity of ocean current. It is observed that as the current velocity rises, the horizontal force initially increases within the range $0 \leq k_0 h \leq 0.8$, reaching a peak before gradually declining. Notably, higher current velocities lead to a more significant reduction in the horizontal force after the peak. Figure 6.9b shows that the horizontal wave force initially increases with dock height due to stronger interaction with surface waves. However, beyond a certain height, the force

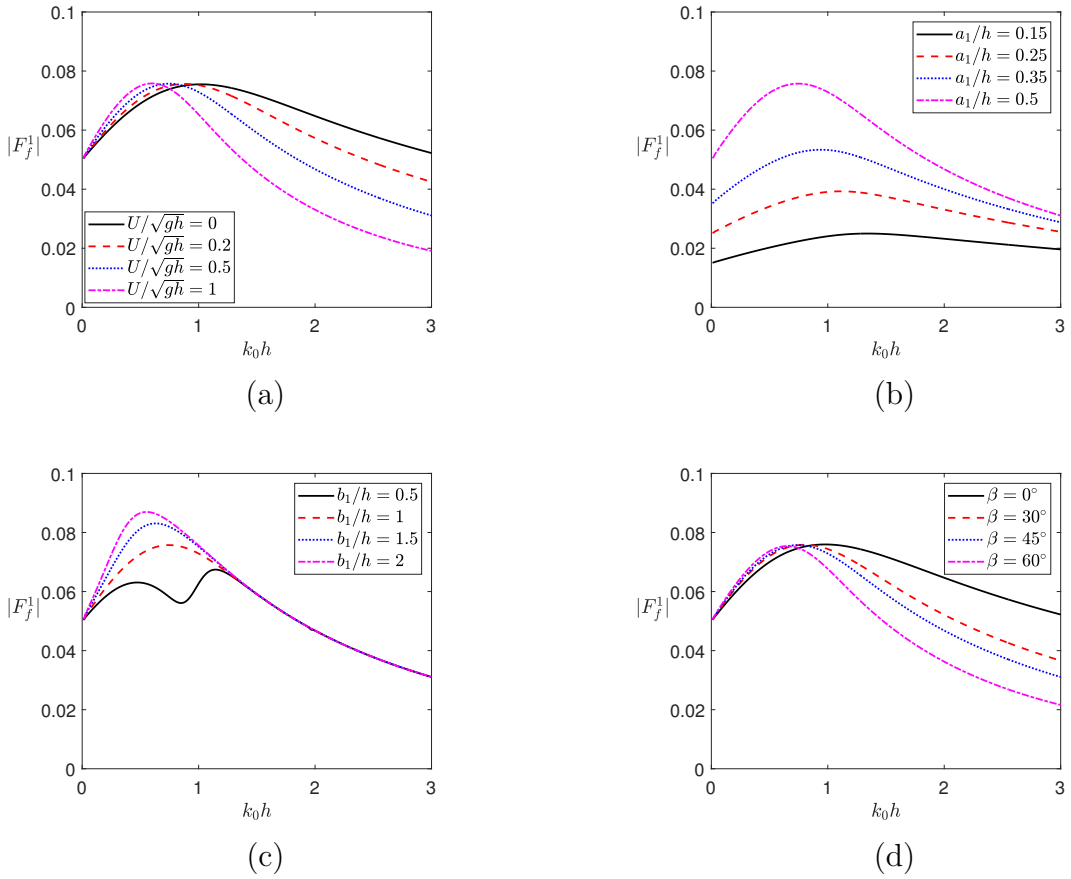

Figure 6.9: The dimensionless horizontal force exerted on the front face (F_f^1) of the dock plotted against the dimensionless wavenumber k_0h for different values of (a) $U/\sqrt{gh}$, (b) a_1/h, (c) b_1/h and (d) β.

decreases as the structure extends. In Fig. 6.9c, the horizontal force grows with dock width across $0 \leq k_0h \leq 1.2$, due to the larger surface area facing incoming waves. Fig. 6.9d shows that the force decreases after $k_0h \geq 0.8$ with increasing wave angle β, as waves strike less directly, reducing the horizontal force component.

Figure 6.10 illustrates the dimensionless horizontal force on the rear face of the dock as a function of the dimensionless wavenumber k_0h. In Fig. 6.10a, the horizontal force decreases as current velocity increases. Figure 6.10b shows that the force rises with increasing dock height due to enhanced structure height in vertical direction. Figures 6.10c and 6.10d reveal similar behavior: the force on the rear face decreases with greater dock width and larger wave propagation angles, consistent with the trend in Fig. 6.10a. A comparison of Figs. 6.9 and 6.10 shows that the horizontal force on the rear face is consistently lower than that on the front face. This reduction results from wave energy reflection from the front face of the dock, leaving less wave to act on the rear face.

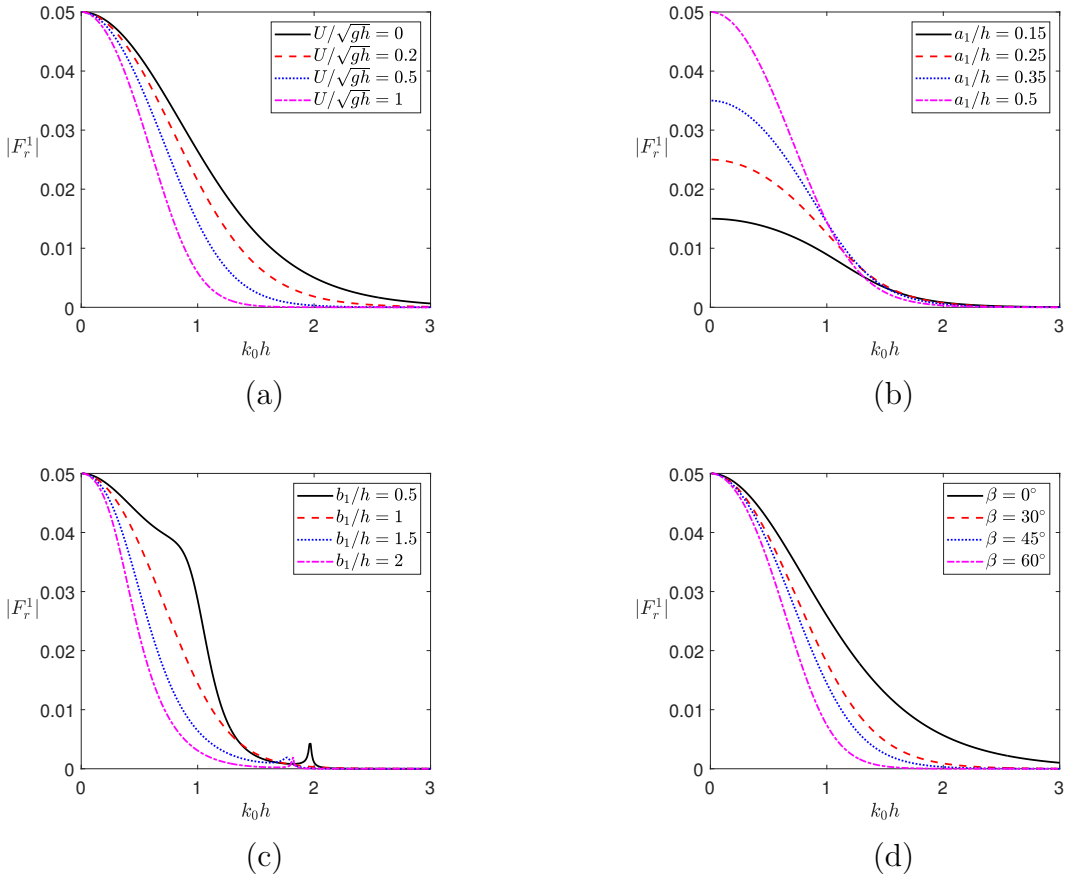

Figure 6.10: The dimensionless horizontal force exerted on the rear face of the dock plotted against the dimensionless wavenumber k_0h for different values of (a) $U/\sqrt{gh}$, (b) a_1/h, (c) b_1/h and (d) β.

6.3.4 Comparison of single and dual docks on reflection and transmission coefficients

To compare the reflection and transmission coefficients for single and dual dock configurations, Fig. 6.11 is presented. In Fig. 6.11a, the dual dock setup shows higher reflection in the long-wave region, while Fig. 6.11b displays a corresponding decrease in transmission. A sharp drop and rise around $k_0h \approx 0.7$ is observed for the dual dock case, attributed to a resonance effect—where the frequency of the trapped waves between the docks aligns with that of the incoming waves, enhancing wave interaction. These results confirm that the dual docks configuration is more effective than the single dock in reducing wave transmission and protecting the leeside region. Furthermore, Figs. 6.11a and 6.11b demonstrate excellent agreement between numerical results obtained via the BEM and the analytical solutions obtained from the EEM. The next subsection presents the influence of dual

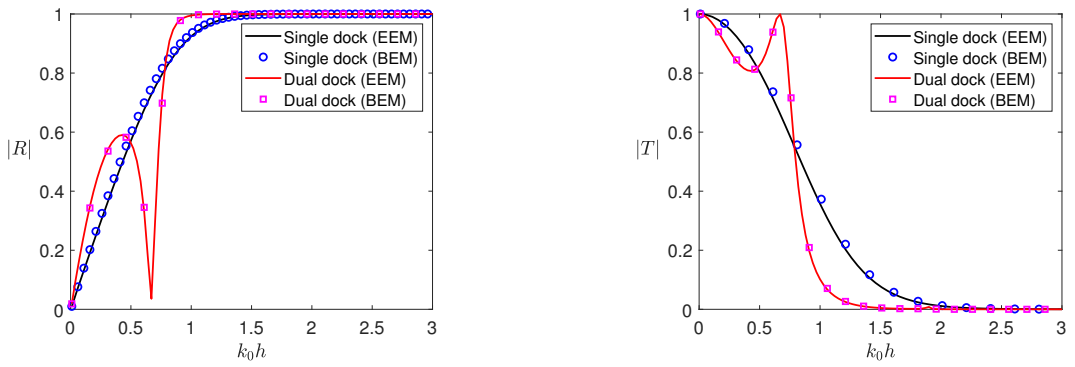

Figure 6.11: (a) The reflection and (b) transmission coefficients plotted against the dimensionless wavenumber k_0h in the presence of single and dual docks for a fixed value of the dimensionless current velocity $U = 0.5\sqrt{gh}$. The other fixed parameters are taken as $a_1/h = a_2/h = 0.5$, $b_1/h = b_2/h = 1$, and $\beta = 30°$. The solid line presents the result obtained using the EEM, while the symbols present the result obtained using the BEM.

dock configurations on the reflection and transmission coefficients for a range of wave and structural parameters.

6.3.5 Case of dual docks

To calculate the reflection and transmission coefficients, as well as the horizontal force in the case of dual docks, the spacing between the docks is fixed at a non-dimensional ratio of $L/h = 1$ for all subsequent analyses.

6.3.5.1 Reflection and transmission coefficients

To see the effect of different values of the dimensionless velocity of ocean current, Fig. 6.12 depicts the reflection and transmission coefficients as functions of the dimensionless wavenumber k_0h. In Fig. 6.12a, the reflection coefficient is plotted for various values of the current velocity. The plot reveals that as the current velocity increases, the reflection curves shift leftward, indicating higher reflection. This trend suggests that a stronger current enhances wave reflection by amplifying wave-current interactions. On the other hand, Fig. 6.12b illustrates the transmission coefficients for various current velocity values. In contrast to the trend observed in Fig. 6.12a, the curves in Fig. 6.12b show a decrease as the current velocity increases. This indicates that higher current velocities result in less wave transmission toward the leeward side.

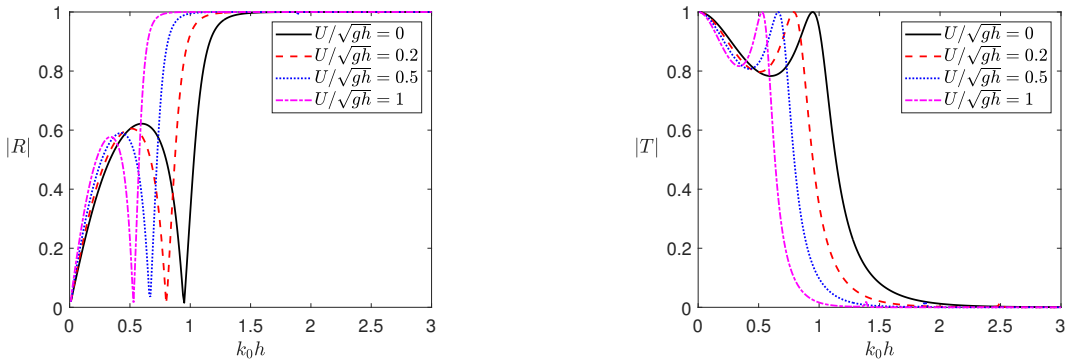

Figure 6.12: (a) The reflection and (b) transmission coefficients plotted against the dimensionless wavenumber k_0h for different values of the dimensionless current velocities $U/\sqrt{gh}$. The other fixed parameters are taken as $a_1/h = a_2/h = 0.5$, $b_1/h = b_2/h = 1$, $L/h = 1$, and $\beta = 30°$.

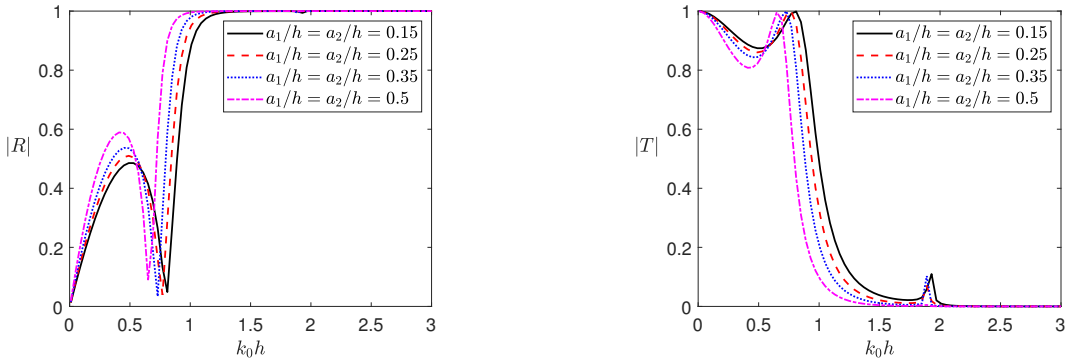

Figure 6.13: (a) The reflection and (b) transmission coefficients plotted against the dimensionless wavenumber k_0h for different values of the dimensionless dock heights. The other fixed parameters are taken as $b_1/h = b_2/h = 1$, $U/\sqrt{gh} = 0.5$, $L/h = 1$ and $\beta = 30°$.

Figure 6.13 portrays the reflection and transmission coefficients as functions of the dimensionless wavenumber for different values of the dimensionless dock height. In Fig. 6.13a, an increase in the height of the docks leads to a notable enhancement in the reflection curve within the wavenumber range $0 \lesssim k_0h \lesssim 0.5$. This indicates that more wave energy is being reflected in this region as the docks become taller, primarily due to the larger surface area in the vertical direction. Simultaneously, the reflection curve exhibits a noticeable leftward shift in the range $0.7 \lesssim k_0h \lesssim 1$, signifying that the onset of higher reflection occurs at lower wavenumbers as the dock height increases. Finally, for wavenumber $k_0h \gtrsim 1.5$, the reflection reaches its maximum value, indicating full wave

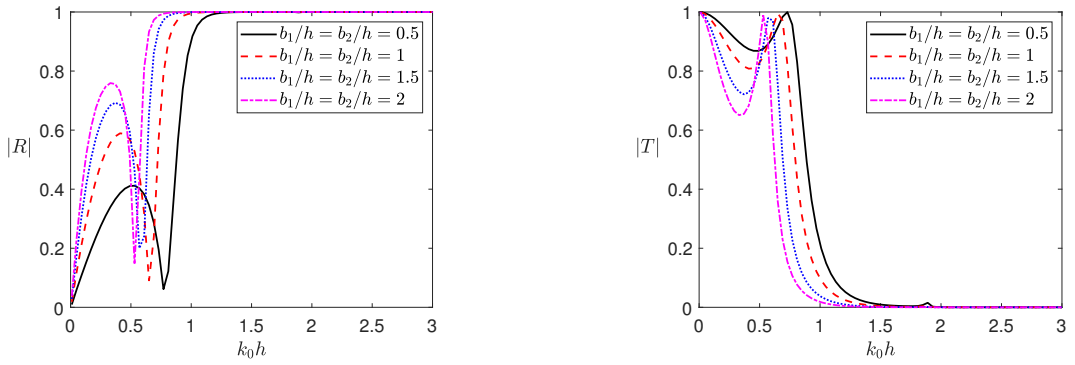

(a) (b)

Figure 6.14: (a) The reflection and (b) transmission coefficients plotted against the dimensionless wavenumber k_0h for different values of the dimensionless width of the docks. The other fixed parameters are taken as $a_1/h = a_2/h = 0.5$, $U/\sqrt{gh} = 0.5$, $L/h = 1$ and $\beta = 30°$.

reflection. In this region, the wave energy is almost entirely reflected by the docks. On the contrary, Fig. 6.13b shows a complementary pattern due to an inverse relationship between reflection and transmission. As the reflection increases with dock height, the transmission correspondingly decreases. In this figure, the reduced transmission signifies that less wave energy is passing through the docks. This occurs because the taller docks limit the propagation of wave energy across the structure by reflecting a larger fraction of the incident wave energy.

Figure 6.14 illustrates the reflection and transmission coefficients as functions of the dimensionless wavenumber k_0h for different values of the dimensionless width of the dock. In Fig. 6.14a, as the width of the dock increase, the reflection coefficient exhibits a noticeable rise in the long-wave region, where the dimensionless wavenumber k_0h is relatively small. This behavior indicates that wider docks are more effective at obstructing and reflecting wave energy in this regime. Additionally, for larger dock widths, the reflection approaches full reflection more rapidly in the region $0.5 \lesssim k_0h \lesssim 1$. Figure 6.14b illustrates that the transmission curve decreases with increasing dock widths. This reduction occurs because a larger proportion of wave energy is reflected back, as explained in Figure 6.14a.

Figure 6.15 illustrates the variation of the reflection and transmission coefficients with the dimensionless wavenumber k_0h for different wave propagation angles, β. A similar trend can also be observed in the reflection and transmission coefficients shown in

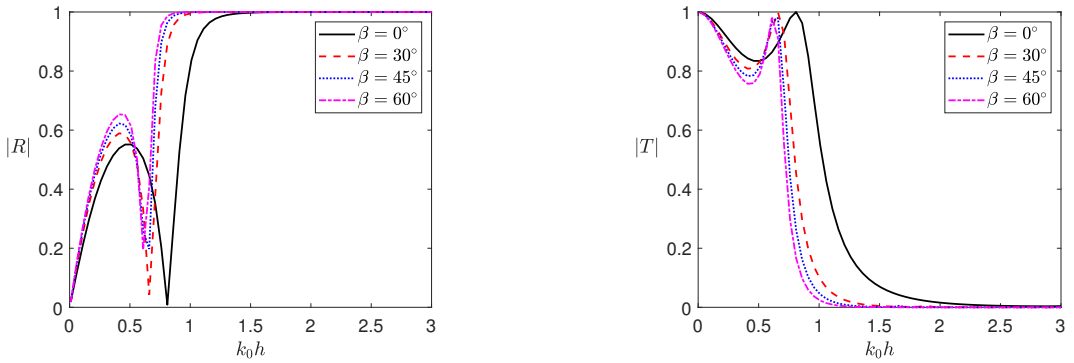

(a) (b)

Figure 6.15: (a) The reflection and (b) transmission coefficients plotted against the dimensionless wavenumber k_0h for different values of the wave propagation angle β. The other fixed parameters are taken as $a_1/h = a_2/h = 0.5$, $b_1/h = b_2/h = 1$, $L/h = 1$ and $U/\sqrt{gh} = 0.5$.

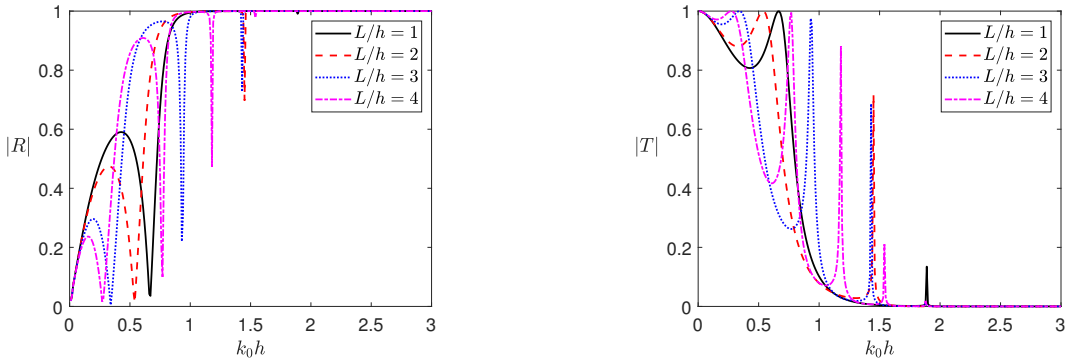

(a) (b)

Figure 6.16: (a) The reflection and (b) transmission coefficients plotted against the dimensionless wavenumber k_0h for different values of the gap between the docks L/h. The other fixed parameters are taken as $a_1/h = a_2/h = 0.5$, $b_1/h = b_2/h = 1$, $\beta = 30°$ and $U/\sqrt{gh} = 0.5$.

Figs. 6.15a and 6.15b, respectively, which mirror the patterns seen in Figs. 6.12–6.14. In all these figures, the general behavior of the reflection and transmission coefficients is influenced by varying factors such as dock height, width, and wave propagation angle. Despite the different parameters being analyzed, the overall trends reveal consistent relationships, where increase in one variable tend to enhance reflection while decreasing transmission.

Figure 6.16 illustrates the reflection (Fig. 6.16a) and transmission coefficients (Fig. 6.16b) as functions of the dimensionless wavenumber k_0h for various gap widths between the docks. For small values of k_0h (representing long waves), the reflection coefficient remains

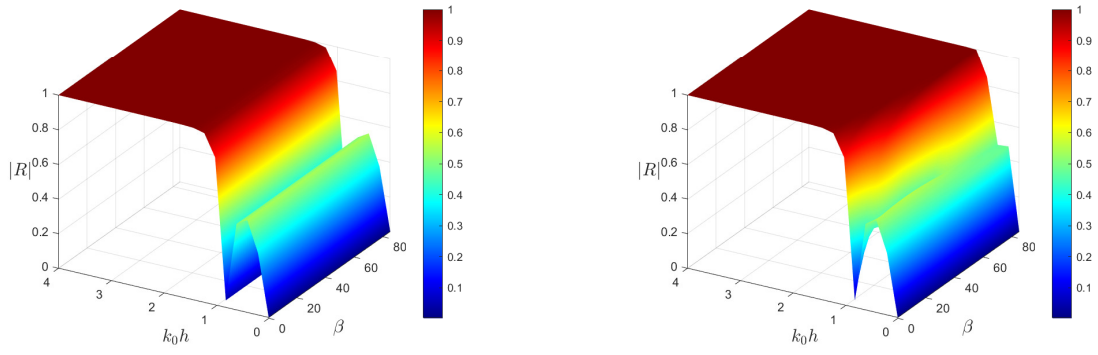

(a) $U/\sqrt{gh} = 0$ (b) $U/\sqrt{gh} = 0.5$

Figure 6.17: Surface plot of the reflection coefficient against the dimensionless wavenumber k_0h and wave propagation angle β for different values of current velocity (a) $U/\sqrt{gh} = 0$ and (b) $U/\sqrt{gh} = 0.5$, with fixed parameters $a_1/h = a_2/h = 0.5$ and $b_1/h = b_2/h = 1$.

relatively low across all gap sizes, indicating that long waves pass through the gap with minimal reflection. As k_0h increases, the reflection coefficient rises sharply and exhibits oscillatory behavior. These oscillations become more frequent and pronounced with increasing gap size (L/h), signifying resonance phenomena, where specific wavelengths are either strongly reflected or transmitted depending on the gap width. At low k_0h, the transmission coefficient is high—particularly for wider gaps—indicating efficient transmission of long waves. At large k_0h (short waves), the transmission coefficient approaches zero for all gap sizes, indicating that short waves are predominantly reflected by the dock structure. Overall, the results demonstrate that the gap between docks also plays a crucial role in wave reflection and transmission, with resonance effects becoming increasingly significant as the gap widens.

To provide a more comprehensive view beyond the earlier two-dimensional plots of reflection coefficient versus wavenumber or wave angle, a three-dimensional surface plot is presented to simultaneously capture the influence of both parameters. This plot provides a fuller view by showing the variation of the reflection coefficient with both k_0h and β. This combined representation makes the pattern of wave reflection more visible and easier to understand across the entire range of parameters. Figure 6.17 shows the variation of the reflection coefficient with respect to the dimensionless wavenumber k_0h and the wave propagation angle β for two different current velocities. Figure 6.17a corresponds to the case with no ocean current ($U/\sqrt{gh} = 0$), while Fig. 6.17b corresponds to the case with

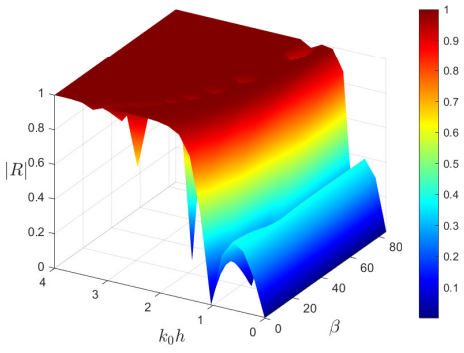

(a) $a_1/h = a_2/h = 0.1$

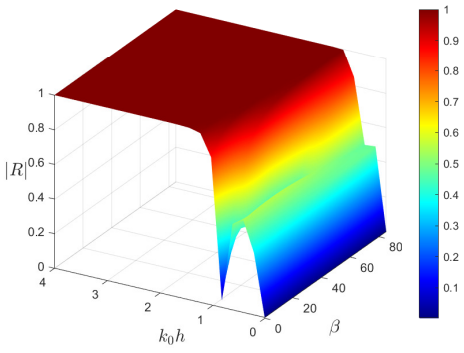

(b) $a_1/h = a_2/h = 0.5$

Figure 6.18: Surface plot of the reflection coefficient against the dimensionless wavenumber k_0h and wave propagation angle β for different dock heights, with fixed parameters $U/\sqrt{gh} = 0.5$. and $b_1/h = b_2/h = 1$.

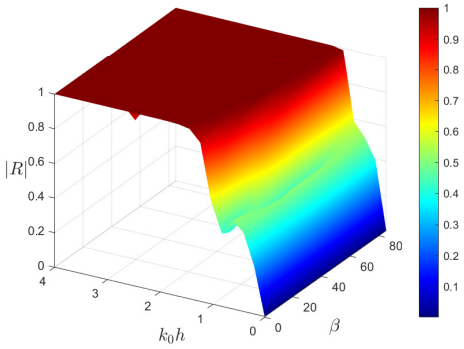

(a) $b_1/h = b_2/h = 0.5$

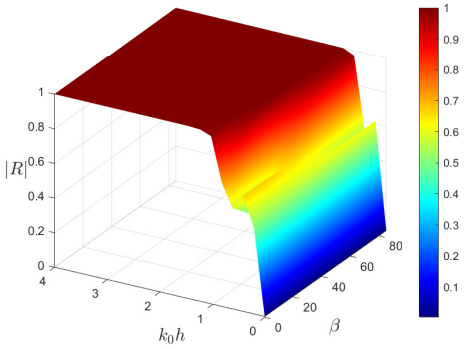

(b) $b_1/h = b_2/h = 2$

Figure 6.19: Surface plot of the reflection coefficient against the dimensionless wavenumber k_0h and wave propagation angle β for different dock widths, with fixed parameters $U/\sqrt{gh} = 0.5$. and $a_1/h = a_2/h = 0.5$.

a current velocity ($U/\sqrt{gh} = 0.5$). As previously observed in Fig. 6.12a, a leftward shift in the reflection pattern occurs with increasing current velocity, and this trend is evident across the entire range of k_0h and β.

Figure 6.18 presents the variation of the reflection coefficient as a function of k_0h and β for different dock heights. In Fig. 6.18a, which corresponds to a smaller dock height, certain regions show a noticeable drop in the reflection coefficient. This indicates that shorter docks can cause more irregular reflection patterns, depending on the wavenumber and wave angle. In contrast, Fig. 6.18b shows the results for a taller dock. Here, the

reflection coefficient appears more uniform across the (k_0h, β) domain. Notably, near-complete reflection is observed in the region where $k_0h > 1$, aligning with the trend discussed earlier in Fig. 6.13a.

Figure 6.19 displays surface plots illustrating the dependence of the reflection coefficient on the dimensionless wavenumber (k_0h) and the wave propagation angle (β) for various dock widths. For larger dock widths, in the long-wave region (i.e., for small values of k_0h), the reflection coefficient increases across the entire range of β. This behavior arises because increasing the width of the dock enhances the obstruction to incoming waves, causing more wave energy to be reflected rather than transmitted.

On the other hand, Fig. 6.20 presents surface plots of the transmission coefficient as a function of the dimensionless wavenumber (k_0h) and the wave propagation angle (β) under two different conditions: without ocean current (see Fig. 6.20a) and with ocean current (see Fig. 6.20b). It is observed that with increasing ocean current velocity, the transmission coefficient decreases noticeably in the range $0.5 \lesssim k_0h \lesssim 2$ across the entire span of β. This reduction indicates that stronger ocean current hinder the transmission of wave energy, consistent with the trend previously reported in Fig. 6.12b.

Figure 6.21 shows the surface plot of the transmission coefficient as a function of the dimensionless wavenumber (k_0h) and the wave propagation angle (β), for two different dock heights. In Fig. 6.21a, corresponding to a smaller dock height, several regions display sudden spikes in transmission across the entire range of k_0h and β, indicating irregular

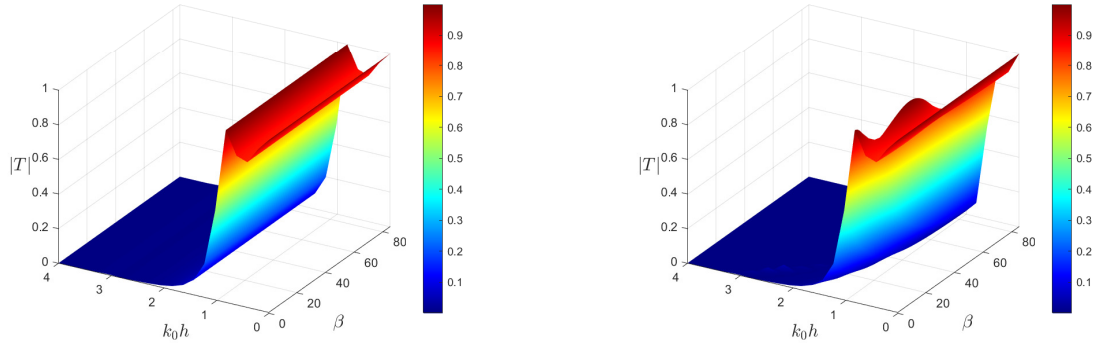

(a) $U/\sqrt{gh} = 0$ (b) $U/\sqrt{gh} = 0.5$

Figure 6.20: Surface plot of the transmission coefficient against the dimensionless wavenumber k_0h and wave propagation angle β for different values of the velocity of ocean current (a) $U/\sqrt{gh} = 0$ and (b) $U/\sqrt{gh} = 0.5$, with fixed parameters $a_1/h = a_2/h = 0.5$ and $b_1/h = b_2/h = 1$.

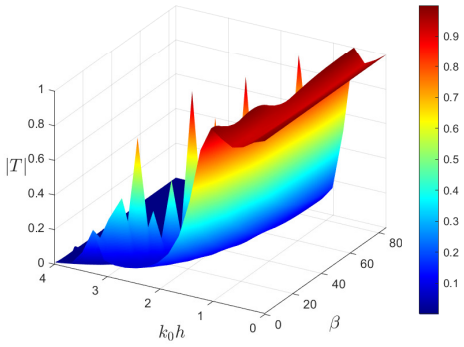

(a) $a_1/h = a_2/h = 0.1$

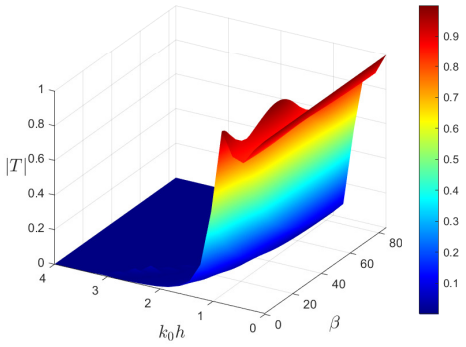

(b) $a_1/h = a_2/h = 0.5$

Figure 6.21: Surface plot of the transmission coefficient against the dimensionless wavenumber k_0h and wave propagation angle β for different dock heights, with fixed parameters $U/\sqrt{gh} = 0.5$. and $b_1/h = b_2/h = 1$.

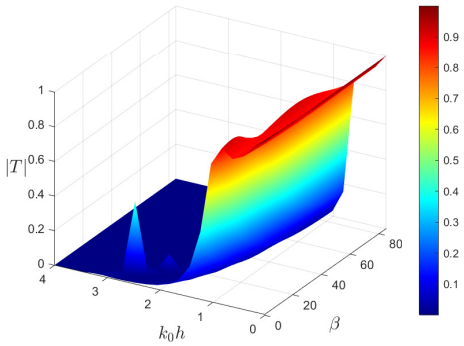

(a) $b_1/h = b_2/h = 0.5$

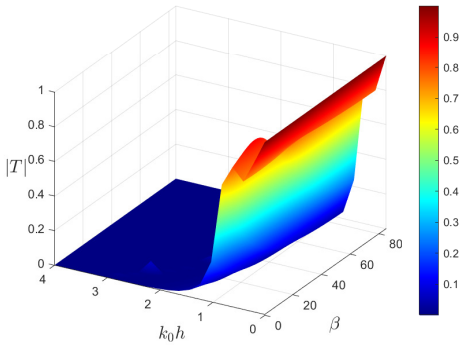

(b) $b_1/h = b_2/h = 2$

Figure 6.22: Surface plot of the transmission coefficient against the dimensionless wavenumber k_0h and wave propagation angle β for different dock widths, with fixed parameters $U/\sqrt{gh} = 0.5$. and $a_1/h = a_2/h = 0.5$.

wave behavior. In contrast, Fig. 6.21b illustrates the case of a taller dock. Here, the transmission coefficient drops significantly and consistently approaches zero beyond $k_0h > 2$, confirming the trend previously discussed in Fig. 6.13b. This suggests that taller structures are more effective at blocking wave transmission at higher wavenumbers.

Figure 6.22 illustrates the effect of varying dock widths on the surface plot of the transmission coefficient as a function of the dimensionless wavenumber (k_0h) and the wave propagation angle (β) for increasing value of the width of dock. Both Figs. 6.22a and 6.22b clearly show that increasing the dock width leads to a reduction in the transmission coefficient within the range $0 \leq k_0h \leq 2$. This behavior is consistent with the trend observed earlier in the two-dimensional plot shown in Fig. 6.14b.

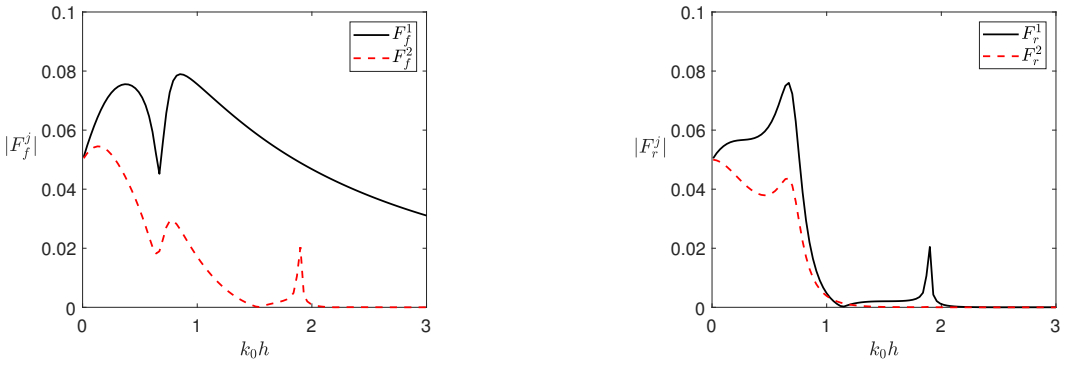

(a) (b)

Figure 6.23: Horizontal force on the (a) front side ($|F_f^j|$) and (b) rear side ($|F_r^j|$) of the single dock and dual docks plotted against the dimensionless wavenumber k_0h for a fixed value of dimensionless velocity of ocean current $U = 0$. The other fixed parameters are taken as $a_1/h = a_2/h = 0.5$, $b_1/h = b_2/h = 1$, and $\beta = 30°$.

6.3.5.2 Comparison between the horizontal forces on the front and rear faces of the single and dual docks

Figure 6.23 depicts the magnitude of horizontal force exerted on the front and rear sides of the first and second docks, plotted as a function of the dimensionless wavenumber k_0h. In Fig. 6.23a, the black and red lines represent the forces on the front faces of the first dock and second dock, respectively. The first dock experiences a consistently higher force, as it directly encounters the incoming wave energy. Due to the wave interaction with the first dock, the wave energy that reaches the second dock is reduced as a result of reflection and dissipation, leading to a comparatively lower horizontal force on the front face of the second dock. Fig. 6.23b presents the horizontal forces on the rear faces, with the black line for the first dock and the red line for the second dock. The rear face of the first dock experiences a lower force because most energy is absorbed or reflected at the front. The horizontal force on the rear face of the second dock is also reduced, as it receives weaker transmitted waves.

6.3.5.3 Horizontal force on dual docks

Figure 6.24 illustrates the influence of current velocity on the dimensionless horizontal force acting on the front faces of (a) the first dock and (b) the second dock, plotted as a function of the dimensionless wavenumber k_0h for various values of $U/\sqrt{gh}$. Fig. 6.24a

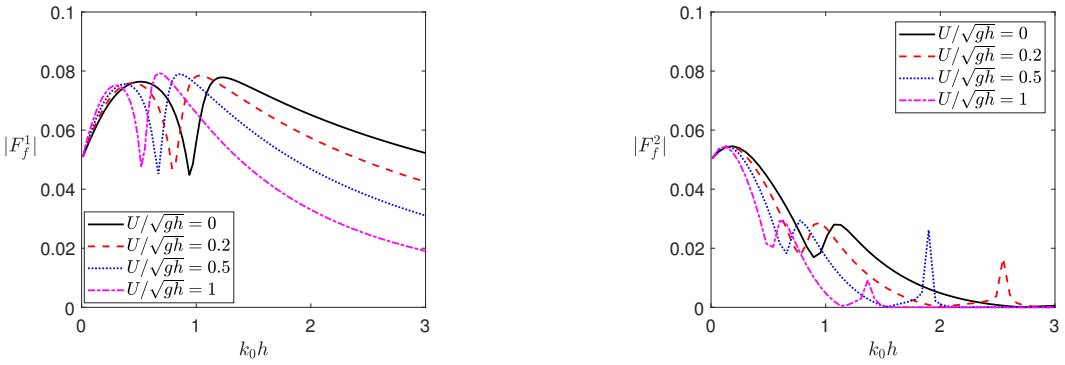

Figure 6.24: The dimensionless horizontal force on the front side of (a) the first dock $|F_f^1|$ and (b) the second dock $|F_f^2|$ with respect to the dimensionless wavenumber k_0h for various values of dimensionless current velocity $U/\sqrt{gh}$. The other fixed parameters are taken as $a_1/h = a_2/h = 0.5$, $b_1/h = b_2/h = 1$, $L/h = 1$ and $\beta = 30°$.

shows the horizontal force on the front face of the first dock, which initially increases and reaches a local maximum in the range $0.5 \leq k_0h \leq 1.2$. This is followed by a sharp drop in magnitude, after which the force gradually decreases as k_0h increases further. As the current velocity increases, the overall magnitude of the force reduces across the entire range of k_0h, and the peak shifts toward lower wavenumbers. Fig. 6.24b shows the horizontal force on the front face of the second dock. However, the force on the second dock is smaller compared to the first dock due to the wave reflection by the first dock, which reduces the wave energy reaching the second dock. The force exhibits a rise and fall pattern at intermediate k_0h values, followed by a gradual decay as k_0h increases.

Figure 6.25 illustrates the effect of dock height on the dimensionless horizontal force exerted on the front faces of (a) the first dock and (b) the second dock, plotted against the dimensionless wavenumber k_0h. In Fig. 6.25a, the horizontal force on the first dock increases consistently with dock height across the full range of k_0h. For all values of a_1/h, the force decreases monotonically after $k_0h > 1.2$. On the other hand, Figure 6.25b presents the force on the front face of the second dock. However, a sharp, narrow spike appears near $k_0h \approx 2.5$ for all dock heights. This phenomenon is attributed to a resonant effect, where the natural frequency of the wave trapped between the docks matches the frequency of the incoming wave.

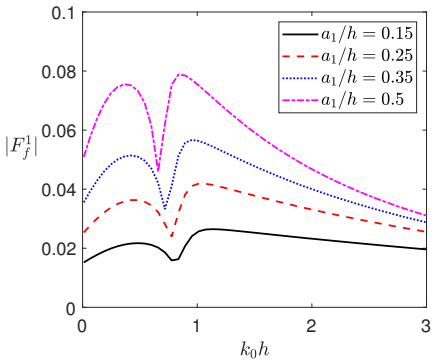

(a)

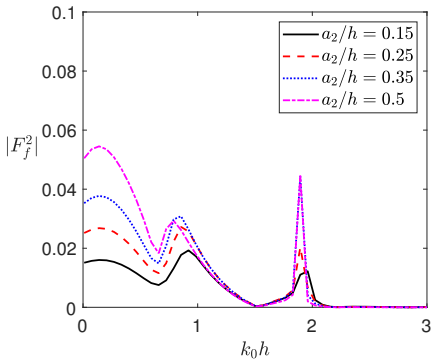

(b)

Figure 6.25: The dimensionless horizontal force on the front side of (a) the first dock $|F_f^1|$ and (b) the second dock $|F_f^2|$ plotted against the dimensionless wavenumber k_0h for various values of dock height. The other fixed parameters are taken as $U/\sqrt{gh} = 0.5$, $b_1/h = b_2/h = 1$, $L/h = 1$ and $\beta = 30°$.

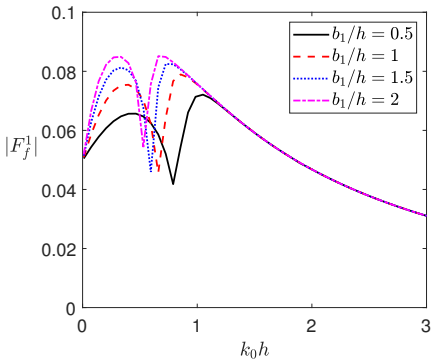

(a)

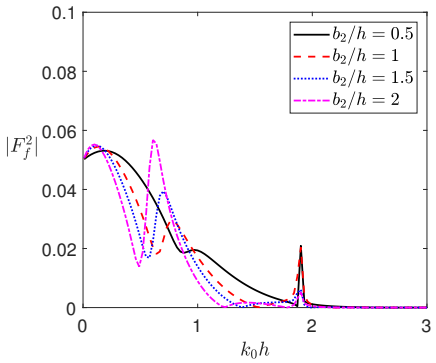

(b)

Figure 6.26: The dimensionless horizontal force on the front side of (a) the first dock $|F_f^1|$ and (b) the second dock $|F_f^2|$ plotted against the dimensionless wavenumber k_0h for various values of dock width. The other fixed parameters are taken as $U/\sqrt{gh} = 0.5$, $a_1/h = a_2/h = 0.5$, $L/h = 1$ and $\beta = 30°$.

Figure 6.26 portrays the dimensionless horizontal force on the front faces of the first and second docks as a function of k_0h for various dock widths. A similar trend is observed in Figs. 6.26a and 6.26b, consistent with the previously plotted Figs. 6.25a and 6.25b. In Fig. 6.26a, as b_1/h increases, the peaks of the force shift toward higher values of k_0h. Additionally, similar to Figs. 6.24b and 6.25b, It is also evident from Fig. 6.26b that the horizontal force exerted on the front face of the second dock is significantly smaller than the corresponding force experienced by the first dock.

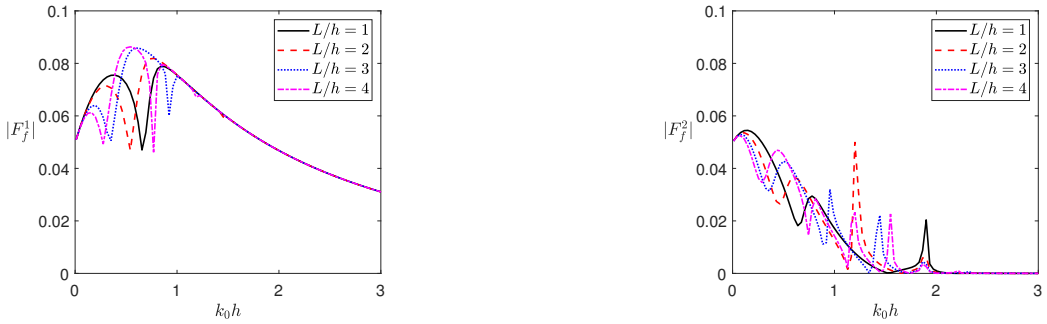

Figure 6.27: The dimensionless horizontal force on the front side of (a) the first dock $|F_f^1|$ and (b) the second dock $|F_f^2|$ plotted against the dimensionless wavenumber k_0h for various values of the gap between the docks L/h. The other fixed parameters are $U/\sqrt{gh} = 0.5$, $a_1/h = a_2/h = 0.5$, and $\beta = 30°$.

To see the impact of different values of the gap between the docks on the horizontal force on the front face of the docks, Fig. 6.27 is plotted against dimensionless wavenumber k_0h. Figure 6.27a displays the dimensionless horizontal force on the front face of the first dock as a function of k_0h for different gap ratios. The force behavior shows a complex oscillatory pattern rather than a simple rise and fall. For $L/h = 1$, the force initially increases to a peak around $k_0h \approx 0.5$, then decreases before rising again to reach its maximum around $k_0h \approx 0.8$, after which it gradually decays. For larger gap ratios ($L/h = 2, 3, 4$), the oscillatory pattern becomes more pronounced, with multiple distinct peaks occurring at regular intervals. These oscillations result from resonant interactions between the incident and reflected waves within the gap. As k_0h increases (i.e., as the wavelength decreases), additional resonant modes can form between the docks, leading to standing wave patterns consistent with previous observations [69, 160]. On the other hand, Fig. 6.27b shows the dimensionless horizontal force on the front face of the second dock, which also exhibits oscillations due to resonance effect. The second dock experiences lower overall force magnitude because the first dock partially shields it by reflecting and dissipating incoming wave energy. For higher value of the wavenumber $k_0h > 2$, the horizontal forces exerted on the front faces of the first dock and second dock are nearly zero for all gaps between the docks. Overall, increasing the gap between the docks significantly influences wave behavior, and a properly chosen gap can enhance wave energy dissipation, making the structure more effective as a breakwater for protecting coastal areas.

6.4 Conclusion

This chapter investigates the interaction of water waves with single and dual rectangular rigid docks in the presence of ocean current. The BVP associated with the study is addressed through a combination of analytical and numerical techniques, specifically utilizing the EEM for the analytical approach and the BEM for the numerical computations. After calculating the unknown coefficients, the complete velocity potentials in each region are determined. These velocity potentials have then been used to calculate the reflection and transmission coefficients, as well as the horizontal forces on the front and rear faces of single and dual docks under various structural configurations. A strong agreement has been observed between the results obtained from the EEM and the BEM, highlighting the accuracy and reliability of both approaches in addressing the problem effectively. Furthermore, the ocean current is observed to amplify wave reflection while reducing wave transmission toward the leeside region. It is also found that as the gap between the docks increases, the reflection and transmission coefficients become smaller in the long-wave region, and larger gaps cause more noticeable oscillations. Additionally, as the strength of the ocean current increases, the horizontal forces exerted on the front and rear surfaces of both single and dual docks decrease. Interestingly, the horizontal force acting on the second dock is consistently lower than that on the first dock. As the dock width for the case of a single dock increases, the horizontal force on the front face rises in the long-wave region. However, for $k_0h > 1.2$, the force on the front face converges and remains consistent across all considered dock widths. Similarly, in the case of dual docks, as the dock widths increase, the behavior aligns with that observed for a single dock. Furthermore, the surface plots of the reflection and transmission coefficients provide a detailed visual representation, effectively illustrating the influence of ocean currents and various structural parameters on wave behavior.

Chapter 7

Wave interaction with a fully-extended structure under the effect of ocean current

In this chapter, the scattering of waves by an inverse T-type compound breakwater under the influence of ocean current is examined using both the EEM and BEM. The reflection and transmission coefficients are calculated for various values of the wave and structural parameters.

7.1 Mathematical framework

The problem is setup in a Cartesian coordinate system to analyze the interaction of waves and ocean current with a fully extended inverse T-type compound breakwater placed over a rigid seabed. The physical setup is illustrated in Fig. 7.1, where the xy-plane lies horizontally and the z-axis points vertically upward. The total water depth is h, measured vertically from the free surface of water (at $z = 0$) down to the seabed (at $z = -h$). The breakwater structure consists of two components—a porous rectangular upper section and a rigid base below it. The upper section has height h_1 and width b_2, while the rigid base extends from the seabed to the bottom of the porous part, with a total height given by $-(h - h_1)$ where $h_1 > 0$. The total width of the rigid base is denoted by $s_2 = b_1 + b_2 + b_3$. An incoming wave propagates from the negative x-direction. Furthermore, we assume that a uniform ocean current with constant velocity U is flowing parallel to the x-axis, directed from the negative to positive x-direction.

7.1.1 Problem setup for the EEM

For the analytical approach, we apply the EEM by dividing the problem domain into five regions, as illustrated in Fig. 7.1. These regions are defined as follows: region 1 is $\Omega_1 = \{-\infty < x \leq 0,\ -h \leq z \leq 0\}$; region 2 is $\Omega_2 = \{0 \leq x \leq b_1,\ -h_1 \leq z \leq 0\}$; region 3

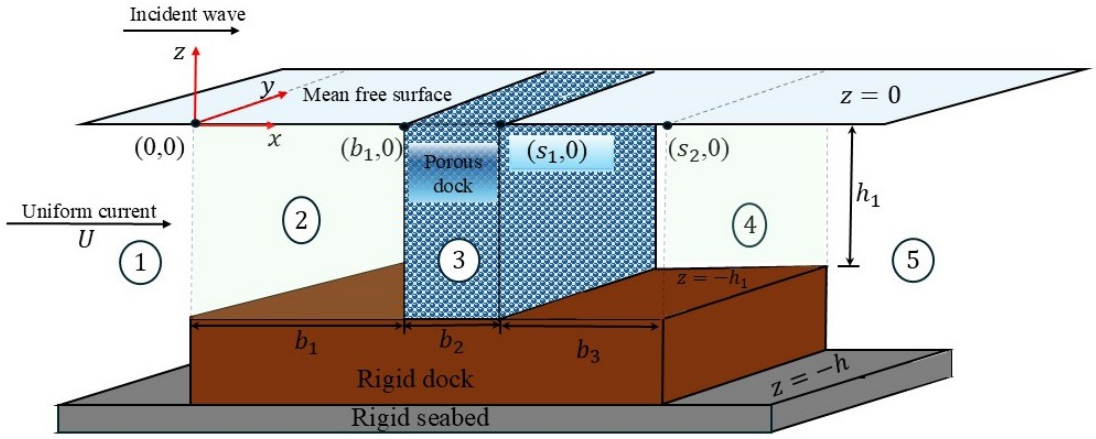

Figure 7.1: Schematic of the inverse T-type compound structure.

is $\Omega_3 = \{b_1 \leq x \leq s_1,\ -h_1 \leq z \leq 0\}$; region 4 is $\Omega_4 = \{s_1 \leq x \leq s_2,\ -h_1 \leq z \leq 0\}$; and region 5 is $\Omega_5 = \{s_2 \leq x < \infty,\ -h \leq z \leq 0\}$, where $s_1 = b_1 + b_2$.

7.1.2 Problem setup for the BEM

To investigate the problem using the BEM, it is essential to completely enclose the entire computational domain. This is accomplished by introducing two auxiliary boundaries, L_1 and L_8, positioned at $x = -l_0$ and $x = r_0$, respectively, as shown in Fig 7.2, where $l_0 > 0$ and $r_0 > 0$. The fluid domain is divided into three distinct regions, namely R_1, R_2, and R_3. To formulate the boundary integral equation used in the BEM, each region is bounded by a set of boundary segments defined as follows. Region R_1 is enclosed by the combined boundary $\mathcal{L}_{R_1} = L_1 \cup L_2 \cup L_3 \cup L_4 \cup L_{m_1} \cup L_{11} \cup L_{12}$, region R_2 is bounded by the combined boundary $\mathcal{L}_{R_2} = L_{m_1} \cup L_b \cup L_{m_2} \cup L_f$ and region R_3 is bounded by the combined boundary $\mathcal{L}_{R_3} = L_5 \cup L_6 \cup L_7 \cup L_8 \cup L_9 \cup L_{10} \cup L_{m_2}$, where each segment is described as follows: $L_1 = \{x = -l_0,\ z|\ -h < z < 0\}$; $L_2 = \{x|\ -l_0 < x < 0,\ z = -h\}$; $L_3 = \{x = 0,\ z|\ -h < z < -h_1\}$; $L_4 = \{x|\ 0 < x < b_1,\ z = -h_1\}$; $L_b = \{x|\ b_1 < x < s_1,\ z = -h_1\}$; $L_5 = \{x|\ s_1 < x < s_2,\ z = -h_1\}$; $L_6 = \{x = s_2,\ z|\ -h < z < -h_1\}$; $L_7 = \{x|\ s_2 < x < r_0,\ z = -h\}$; $L_8 = \{x = r_0,\ z|\ -h < z < 0\}$; $L_9 = \{x|\ s_2 < x < r_0,\ z = 0\}$; $L_{10} = \{x|\ s_1 < x < s_2,\ z = 0\}$; $L_f = \{x \mid b_1 < x < s_1,\ z = 0\}$; $L_{11} = \{x \mid 0 < x < b_1,\ z = 0\}$, $L_{12} = \{x|\ -l_0 < x < 0,\ z = 0\}$, $L_{m_1} = \{x = b_1,\ z|\ -h_1 < z < 0\}$ and $L_{m_2} = \{x = s_1,\ z|\ -h_1 < z < 0\}$. This closed boundary setup defines the complete geometric model needed for the BEM implementation.

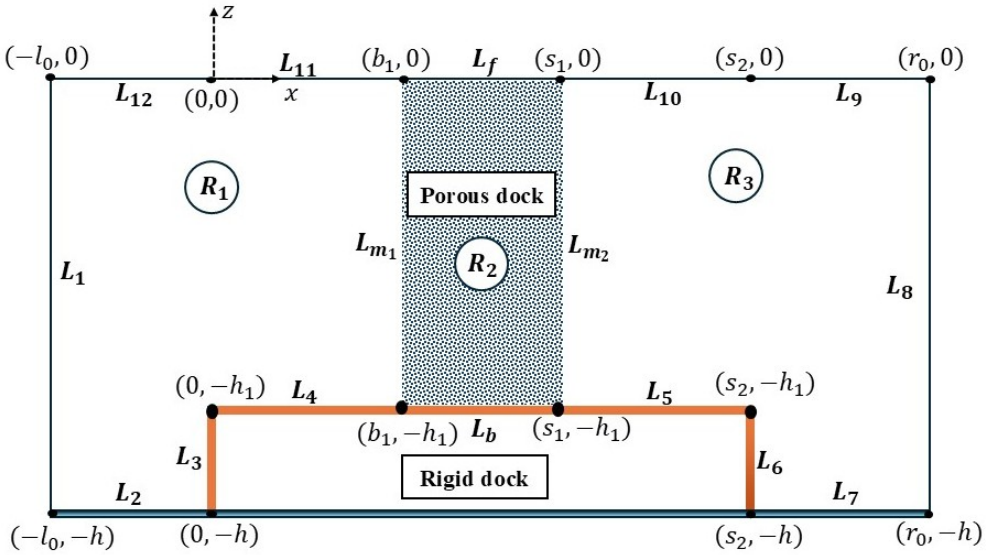

Figure 7.2: Schematic depiction of the inverse T-typed compound structure for the BEM.

7.1.3 Governing equation and boundary conditions

To incorporate the effect of the velocity of ocean current U which is parallel to the x-axis, the total velocity potentials $\Phi(x, z, t)$ is expressed as the superposition of two potential functions [4, 5, 122]

$$\Phi(x, z, t) = \Phi_c(x) + \Phi_w(x, z, t), \tag{7.1}$$

where $\Phi_c(x) = Ux$ represents the steady current potential and $\Phi_w(x, z, t) = \mathrm{Re}\left[\phi(x, z)e^{-\mathrm{i}\omega t)}\right]$ is the unsteady wave potential. In each region, the spatial velocity potential $\phi_j(x, z)$ (for $j = 1, 2, 3, 4, 5$) adheres to the Laplace equation, represented as:

$$\nabla^2\phi_j = 0 \quad \text{in the whole fluid domain,} \tag{7.2}$$

where ∇ is the Laplace operator. The seabed is considered impermeable, restricting any vertical flow across the seabed. Consequently, the boundary condition at $z = -h$ is defined in Eq. (6.2). The linearized free-surface boundary condition reads [39]

$$\frac{\partial\phi_j}{\partial z} - \frac{(\omega - Uk_0)}{g}\phi_j = 0 \quad \text{at } z = 0 \quad \text{for } j = 1, 2, 4, 5. \tag{7.3}$$

For region 3, the free-surface boundary condition is given by [46]

$$\frac{\partial\phi_3}{\partial z} = (s - \mathrm{i}f)\frac{(\omega - Uk_0)}{g}\phi_3 \quad \text{at } z = 0, \tag{7.4}$$

where s and f are the inertial and frictional coefficients, respectively. The pressure and velocity continuities at $x = 0$ and $x = s_2$ are given as

$$\left.\begin{aligned} \phi_1 &= \phi_2 \\ \frac{\partial \phi_1}{\partial x} &= \frac{\partial \phi_2}{\partial x} \end{aligned}\right\} \quad \text{at } x = 0 \quad \text{for } z \in (-h_1, 0), \tag{7.5}$$

$$\left.\begin{aligned} \phi_4 &= \phi_5 \\ \frac{\partial \phi_4}{\partial x} &= \frac{\partial \phi_5}{\partial x} \end{aligned}\right\} \quad \text{at } x = s_2 \quad \text{for } z \in (-h_1, 0), \tag{7.6}$$

and the velocity and pressure continuity at $x = b_1$ and $x = s_1$ are given as [139]

$$\left.\begin{aligned} \phi_2 &= (s - \mathrm{i}f)\phi_3 \\ \frac{\partial \phi_2}{\partial x} &= \varepsilon_p \frac{\partial \phi_3}{\partial x} \end{aligned}\right\} \quad \text{at } x = b_1 \quad \text{for } z \in (-h_1, 0), \tag{7.7}$$

$$\left.\begin{aligned} \phi_4 &= (s - \mathrm{i}f)\phi_3 \\ \frac{\partial \phi_4}{\partial x} &= \varepsilon_p \frac{\partial \phi_3}{\partial x} \end{aligned}\right\} \quad \text{at } x = s_1 \quad \text{for } z \in (-h_1, 0), \tag{7.8}$$

where ε_p is the porous-effect parameter. Additionally, the structural boundary conditions reads

$$\frac{\partial \phi_1}{\partial x} = 0 \quad \text{at } x = 0 \text{ for } z \in (-h, -h_1), \tag{7.9}$$

$$\frac{\partial \phi_5}{\partial x} = 0 \quad \text{at } x = s_2 \text{ for } z \in (-h, -h_1). \tag{7.10}$$

As $x \to \pm\infty$, the radiation condition are given by [139]

$$\phi_1 = (e^{-\mathrm{i}k_0 x} + R_0 e^{\mathrm{i}k_0 x}) f_{10}(z) \quad \text{as } x \to -\infty, \tag{7.11}$$

$$\phi_5 = T_0 e^{-\mathrm{i}k_0 x} f_{10}(z) \quad \text{as } x \to \infty, \tag{7.12}$$

where R_0 and T_0 are the reflection and transmission coefficients, respectively, $f_{10}(z)$ is the vertical eigenfunction, defined as [139]

$$f_{10}(z) = \frac{\mathrm{i}gA}{\omega - Uk_0} \frac{\cosh k_0(h + z)}{\cosh k_0 h}, \tag{7.13}$$

where k_0 is the wavenumber in regions 1 and 5, which satisfies

$$k_0 \tanh(k_0 h) = \frac{(\omega - Uk_0)^2}{g}. \tag{7.14}$$

7.2 Solution method

The detailed formulation and solution procedures for both the EEM and BEM are presented in the following subsection.

7.2.1 Analytic solution by the EEM

To obtain an analytic solution to the BVP, the velocity potentials ϕ_j in each region ($j = 1, 2, 3, \ldots, 5$) are determined. These velocity potentials satisfy the Laplace equation given in Eq. (7.2). The general expressions for ϕ_j in each region are expressed as

$$\phi_1 = Ae^{-\mathrm{i}k_0 x} f_{10}(z) + \sum_{n=0}^{\infty} R_n e^{\mathrm{i}k_n x} f_{1n}(z), \tag{7.15}$$

$$\phi_2 = \sum_{n=0}^{\infty} \left[A_n e^{-\mathrm{i}p_{1n} x} + B_n e^{\mathrm{i}p_{1n} x}\right] f_{2n}(z), \tag{7.16}$$

$$\phi_3 = \sum_{n=0}^{\infty} \left[C_n e^{-\mathrm{i}p_{2n} x} + D_n e^{\mathrm{i}p_{2n} x}\right] f_{3n}(z), \tag{7.17}$$

$$\phi_4 = \sum_{n=0}^{\infty} \left[E_n e^{-\mathrm{i}p_{1n} x} + F_n e^{\mathrm{i}p_{1n} x}\right] f_{4n}(z), \tag{7.18}$$

$$\phi_5 = \sum_{n=0}^{\infty} T_n e^{-\mathrm{i}k_n x} f_{5n}(z), \tag{7.19}$$

where R_n, A_n, B_n, C_n, D_n, E_n, F_n, and T_n (for $n = 0, 1, 2, 3, \ldots$) are unknown coefficients, k_n to be determined from the dispersion relation [122]

$$k_n \tanh(k_n h) = \frac{(\omega - Uk_0)^2}{g}, \tag{7.20}$$

the vertical eigenfunctions $f_{jn}(z)$ (for $j = 1, 2, 3, \ldots, 5$) are given by

$$f_{jn}(z) = \begin{cases} \left(\dfrac{\mathrm{i}gA}{\omega - Uk_0}\right) \dfrac{\cosh k_n(h+z)}{\cosh(k_n h)} & \text{for } j = 1, 5 \\ \left(\dfrac{\mathrm{i}gA}{\omega - Uk_0}\right) \dfrac{\cosh p_{1n}(h_1+z)}{\cosh(p_{1n} h_1)} & \text{for } j = 2, 4 \\ \left(\dfrac{\mathrm{i}gA}{\omega - Uk_0}\right) \dfrac{\cosh p_{2n}(h_1+z)}{\cosh(p_{2n} h_1)} & \text{for } j = 3 \end{cases} \tag{7.21}$$

and p_{1n} and p_{2n} satisfy the following dispersion relations

$$p_{1n} \tanh(p_{1n} h_1) = \frac{(\omega - Uk_0)^2}{g}, \tag{7.22}$$

$$p_{2n}\tanh(p_{2n}h_1) = (s - \mathrm{i}f)\frac{(\omega - Uk_0)^2}{g}, \tag{7.23}$$

We substitute the velocity potentials (7.15)–(7.19) into the matching conditions for pressure and velocity continuity (Eqs.(7.5) and (7.6)) as well as the structural boundary conditions (Eqs.(7.9) and (7.10)). By applying the orthogonality of the eigenfunctions, this leads to the following system of equations

$$A\mathcal{X}_{1m0} + \sum_{n=0}^{\infty} R_n\mathcal{X}_{1mn} = \sum_{n=0}^{\infty}\left[A_n + B_n\right]\mathcal{Y}_{mn}, \tag{7.24}$$

$$-\mathrm{i}k_0A\mathcal{Z}_{m0} + \sum_{n=0}^{\infty}\mathrm{i}k_nR_n\mathcal{Z}_{mn} = \sum_{n=0}^{\infty}\mathrm{i}p_{1n}\left[-A_n + B_n\right]\mathcal{Y}_{1mn}, \tag{7.25}$$

$$\sum_{n=0}^{\infty}\left[A_ne^{-\mathrm{i}p_{1n}b_1} + B_ne^{\mathrm{i}p_{1n}b_1}\right]\mathcal{Y}_{mn} = (s - \mathrm{i}f)\left[C_ne^{-\mathrm{i}p_{2n}b_1} + D_ne^{\mathrm{i}p_{2n}b_1}\right]\mathcal{X}_{2mn}, \tag{7.26}$$

$$\sum_{n=0}^{\infty}\left[E_ne^{-\mathrm{i}p_{1n}s_1} + F_ne^{\mathrm{i}p_{1n}s_1}\right]\mathcal{Y}_{mn} = (s - \mathrm{i}f)\left[C_ne^{-\mathrm{i}p_{2n}s_1} + D_ne^{\mathrm{i}p_{2n}s_1}\right]\mathcal{X}_{2mn}, \tag{7.27}$$

$$\sum_{n=0}^{\infty}\left[E_ne^{-\mathrm{i}p_{1n}s_2} + F_ne^{\mathrm{i}p_{1n}s_2}\right]\mathcal{Y}_{mn} = \sum_{n=0}^{\infty}T_ne^{-\mathrm{i}k_ns_2}\mathcal{X}_{1mn}, \tag{7.28}$$

$$\sum_{n=0}^{\infty}\mathrm{i}p_{1n}\left[-A_ne^{-\mathrm{i}p_{1n}b_1} + B_ne^{\mathrm{i}p_{1n}b_1}\right]\mathcal{Y}_{mn} = \sum_{n=0}^{\infty}\mathrm{i}p_{2n}\left[-C_ne^{-\mathrm{i}p_{2n}b_1} + D_ne^{\mathrm{i}p_{2n}b_1}\right]\mathcal{X}_{2mn}, \tag{7.29}$$

$$\sum_{n=0}^{\infty}\mathrm{i}p_{1n}\left[-E_ne^{-\mathrm{i}p_{1n}s_1} + F_ne^{-\mathrm{i}p_{1n}s_1}\right]\mathcal{Y}_{mn} = \sum_{n=0}^{\infty}\mathrm{i}p_{2n}\left[-C_ne^{-\mathrm{i}p_{2n}s_1} + D_ne^{\mathrm{i}p_{2n}s_1}\right]\mathcal{X}_{2mn}, \tag{7.30}$$

$$\sum_{n=0}^{\infty}\mathrm{i}p_{1n}\left[-E_ne^{-\mathrm{i}p_{1n}s_2} + F_ne^{\mathrm{i}p_{1n}s_2}\right]\mathcal{Y}_{1mn} = -\sum_{n=0}^{\infty}\mathrm{i}k_nT_ne^{-\mathrm{i}k_ns_2}\mathcal{Z}_{mn}, \tag{7.31}$$

where

$$\mathcal{X}_{1mn} = \int_{-h_1}^{0} f_{1n}(z)f_{2m}(z)\mathrm{d}z, \quad \mathcal{X}_{2mn} = \int_{-h_1}^{0} f_{3n}(z)f_{2m}(z)\mathrm{d}z, \quad \mathcal{Y}_{mn} = \int_{-h_1}^{0} f_{2n}(z)f_{2m}(z)\,\mathrm{d}z,$$

$$\mathcal{Y}_{1mn} = \int_{-h_1}^{0} f_{2n}(z)f_{1m}(z)\mathrm{d}z, \quad \mathcal{Z}_{mn} = \int_{-h}^{0} f_{1n}(z)f_{1m}(z)\mathrm{d}z$$

for $n, m = 0, 1, 2, 3, \ldots$. Note that m is given non-negative integers and for fixed value of m, Eqs. (7.24)–(7.31) form a system of simultaneous linear equations involves an infinite number of unknowns, namely R_n, A_n, B_n, C_n, D_n, E_n, F_n, and T_n for $n = 0, 1, 2, 3, \ldots$. Solving for all these infinite unknowns is impractical. Therefore, the series is truncated

by retaining only a finite number of terms, say $n = N$, which makes the system solvable using computational methods. After solving for the unknowns, substituting them back into Eqs. (7.24)–(7.31) gives the explicit expressions for the velocity potentials in each region.

7.2.2 Numerical solution by the BEM

In this subsection, we derive the integral equations corresponding to the two-dimensional BVP. Since the domain is divided into three distinct regions—R_1 and R_3 representing the fluid domains without a porous structure, and R_2 denoting the domain occupied by the porous medium—the BEM is developed as a multidomain approach [29]. Let the spatial velocity potentials in regions R_1, R_2, and R_3 be ϕ_1, ϕ_2, and ϕ_3, respectively. Applying Green's second identity to the velocity potentials ϕ_l for $l = 1, 2, 3$ and the Green's function $\mathcal{G}$ yields the following boundary integral equations

$$\frac{1}{2}\phi_l(\xi,\nu) = \int_L \left(\phi_l \frac{\partial \mathcal{G}}{\partial n}(x,z;\xi,\nu) - \mathcal{G}(x,z;\xi,\nu)\frac{\partial \phi_l}{\partial n}\right) \mathrm{d}L, \quad \text{if } (x,z) \in \mathcal{L}, \tag{7.32}$$

where $\mathcal{L}$ is the combined boundary $\mathcal{L} = \mathcal{L}_{R_1} \cup \mathcal{L}_{R_2} \cup \mathcal{L}_{R_3}$ and the Green function $\mathcal{G}$ is the fundamental solution satisfying

$$\nabla^2 \mathcal{G} = \delta(\xi - x)\delta(\nu - z), \tag{7.33}$$

and given by

$$\mathcal{G}(x,z;\xi,\nu) = -\frac{1}{2\pi}\ln(r), \tag{7.34}$$

where $\mathsf{r} = \sqrt{(\xi - x)^2 + (\nu - z)^2}$. The normal derivative of $\mathcal{G}$ is obtained by

$$\frac{\partial \mathcal{G}}{\partial n} = -\frac{1}{2\pi r}\frac{\partial \mathsf{r}}{\partial n}. \tag{7.35}$$

For clarity and to facilitate the numerical implementation using the BEM, the physical boundary conditions previously described are now reformulated and applied over the discretized computational boundaries corresponding to each subdomain. The boundary conditions on rigid boundaries for all corresponding segments are given by

$$\frac{\partial \phi_j}{\partial n} = 0 \quad \text{at } L_p \text{ for } p = 2, 3, 4, \ldots, 7, b. \tag{7.36}$$

Additionally, Eqs. (7.11) and (7.12) are written in the following form as

$$\frac{\partial}{\partial n}(\phi_1 - \phi_{inc}) = \mathrm{i}k_0(\phi_1 - \phi_{inc}) \quad \text{at } L_1, \tag{7.37}$$

$$\frac{\partial \phi_3}{\partial n} = \mathrm{i}k_0\phi_3 \quad \text{at } L_8, \tag{7.38}$$

where $\phi_{inc} = e^{\mathrm{i}k_0 x} f_{10}$ as detailed in Ref. [139]. The linearized free-surface boundary conditions in regions R_1 and R_3 are given as

$$\frac{\partial \phi_1}{\partial n} - \frac{(\omega - Uk_0)^2}{g}\phi_1 = 0 \quad \text{at } L_{11} \text{ and } L_{12}, \tag{7.39}$$

$$\frac{\partial \phi_3}{\partial n} - \frac{(\omega - Uk_0)^2}{g}\phi_3 = 0 \quad \text{at } L_9 \text{ and } L_{10}. \tag{7.40}$$

The linearized free-surface boundary condition at L_f is given as

$$\frac{\partial \phi_2}{\partial n} - (s - \mathrm{i}f)\frac{(\omega - Uk_0)^2}{g}\phi_2 = 0 \quad \text{at } L_f. \tag{7.41}$$

Finally, At the interfaces L_{m_1} and L_{m_2} between the porous and non-porous regions, the matching conditions are given by

$$\left.\begin{aligned} \phi_1 &= (s - \mathrm{i}f)\phi_2 \\ \frac{\partial \phi_1}{\partial n} &= \varepsilon_p \frac{\partial \phi_2}{\partial n} \end{aligned}\right\} \quad \text{at } L_{m_1}, \tag{7.42}$$

$$\left.\begin{aligned} \phi_3 &= (s - \mathrm{i}f)\phi_2 \\ \frac{\partial \phi_3}{\partial n} &= \varepsilon_p \frac{\partial \phi_2}{\partial n} \end{aligned}\right\} \quad \text{at } L_{m_2}. \tag{7.43}$$

By imposing the above boundary conditions as defined in Eqs. (7.36)–(7.43) into the Eq. (7.32), the integral equations in each region are obtained as follows.

For region 1:

$$\begin{aligned} \frac{1}{2}\phi_1 &+ \int_{L_1}\left(\phi_1\frac{\partial \mathcal{G}}{\partial n} - \mathcal{G}\left(\frac{\partial \phi^{inc}}{\partial n} + \mathrm{i}k_0\phi_1 - \mathrm{i}k_0\phi^{inc}\right)\right)\mathrm{d}L + \int_{L_2}\phi_1\frac{\partial \mathcal{G}}{\partial n}\,\mathrm{d}L \\ &+ \int_{L_3}\phi_1\frac{\partial \mathcal{G}}{\partial n}\,\mathrm{d}L + \int_{L_4}\phi_1\frac{\partial \mathcal{G}}{\partial n}\,\mathrm{d}L + \int_{L_{m_1}}\left((s - \mathrm{i}f)\phi_2\frac{\partial \mathcal{G}}{\partial n} - \varepsilon_p\frac{\partial \phi_2}{\partial n}\mathcal{G}\right)\mathrm{d}L \\ &+ \int_{L_{11}}\left(\frac{\partial \mathcal{G}}{\partial n} - \frac{(\omega - Uk_0)^2}{g}\mathcal{G}\right)\phi_1\,\mathrm{d}L + \int_{L_{12}}\left(\frac{\partial \mathcal{G}}{\partial n} - \frac{(\omega - Uk_0)^2}{g}\mathcal{G}\right)\phi_1\,\mathrm{d}L = 0, \end{aligned} \tag{7.44}$$

For region 2:

$$\frac{1}{2}\phi_2 + \int_{L_{m_1}} \left(\frac{1}{(s-\mathrm{i}f)} \phi_1 \frac{\partial \mathcal{G}}{\partial n} - \frac{1}{\varepsilon_p} \frac{\partial \phi_1}{\partial n} \mathcal{G} \right) \mathrm{d}L + \int_{L_{m_2}} \left(\frac{1}{(s-\mathrm{i}f)} \phi_3 \frac{\partial \mathcal{G}}{\partial n} - \frac{1}{\varepsilon_p} \frac{\partial \phi_3}{\partial n} \mathcal{G} \right) \mathrm{d}L$$
$$+ \int_{L_b} \phi_2 \frac{\partial \mathcal{G}}{\partial n} \, \mathrm{d}L + \int_{L_f} \left(\frac{\partial \mathcal{G}}{\partial n} - (s-\mathrm{i}f) \frac{(\omega - Uk_0)^2}{g} \mathcal{G} \right) \phi_2 \, \mathrm{d}L = 0, \tag{7.45}$$

For region 3:

$$\frac{1}{2}\phi_3 + \int_{L_5} \phi_3 \frac{\partial \mathcal{G}}{\partial n} \, \mathrm{d}L_5 + \int_{L_6} \phi_3 \frac{\partial \mathcal{G}}{\partial n} \, \mathrm{d}L + \int_{L_7} \phi_3 \frac{\partial \mathcal{G}}{\partial n} \, \mathrm{d}L + \int_{L_8} \left(\frac{\partial \mathcal{G}}{\partial n} - \mathrm{i}k_0 \mathcal{G} \right) \phi_3 \, \mathrm{d}L$$
$$+ \int_{L_9} \left(\frac{\partial \mathcal{G}}{\partial n} - \frac{(\omega - Uk_0)^2}{g} \mathcal{G} \right) \phi_3 \, \mathrm{d}L + \int_{L_{10}} \left(\frac{\partial \mathcal{G}}{\partial n} - \frac{(\omega - Uk_0)^2}{g} \mathcal{G} \right) \phi_3 \, \mathrm{d}L$$
$$+ \int_{L_{m_2}} \left((s-\mathrm{i}f) \phi_2 \frac{\partial \mathcal{G}}{\partial n} - \varepsilon_p \frac{\partial \phi_2}{\partial n} \mathcal{G} \right) \mathrm{d}L = 0. \tag{7.46}$$

The boundary integral equations (7.44)–(7.46) are then discretized by evaluating the fundamental solution $\mathcal{G}$, which is centered at the node of the i^{th} element—treated as the source element (ξ, ν). Then, Eqs. (7.44)–(7.46) can be written in a discretized form for the i^{th} element are given as follows.

For region 1:

$$\frac{1}{2}\phi_{1i} + \sum_{j=1}^{N_1} \int_{L_1} \left(\phi_{1j} \frac{\partial \mathcal{G}_{ij}}{\partial n} - \mathcal{G}_{ij} \left(\frac{\partial \phi_j^{inc}}{\partial n} + \mathrm{i}k_0 \phi_{1j} - \mathrm{i}k_0 \phi_j^{inc} \right) \right) \mathrm{d}L + \sum_{j=1}^{N_2} \int_{L_2} \phi_{1j} \frac{\partial \mathcal{G}_{ij}}{\partial n} \, \mathrm{d}L$$
$$+ \sum_{j=1}^{N_3} \int_{L_3} \phi_{1j} \frac{\partial \mathcal{G}_{ij}}{\partial n} \, \mathrm{d}L + \sum_{j=1}^{N_4} \int_{L_4} \phi_{1j} \frac{\partial \mathcal{G}_{ij}}{\partial n} \, \mathrm{d}L + \sum_{j=1}^{N_{m_1}} \int_{L_{m_1}} \left((s-\mathrm{i}f) \phi_{2j} \frac{\partial \mathcal{G}_{ij}}{\partial n} - \varepsilon_p \frac{\partial \phi_{2j}}{\partial n} \mathcal{G}_{ij} \right) \mathrm{d}L$$
$$+ \sum_{j=1}^{N_{11}} \int_{L_{11}} \left(\frac{\partial \mathcal{G}_{ij}}{\partial n} - \frac{(\omega - Uk_0)^2}{g} \mathcal{G}_{ij} \right) \phi_{1j} \, \mathrm{d}L + \sum_{j=1}^{N_{12}} \int_{L_{12}} \left(\frac{\partial \mathcal{G}_{ij}}{\partial n} - \frac{(\omega - Uk_0)^2}{g} \mathcal{G}_{ij} \right) \phi_{1j} \, \mathrm{d}L = 0. \tag{7.47}$$

For region 2:

$$\frac{1}{2}\phi_{2i} + \sum_{j=1}^{N_{m_1}} \int_{L_{m_1}} \left(\frac{1}{(s-\mathrm{i}f)} \phi_{1j} \frac{\partial \mathcal{G}_{ij}}{\partial n} - \frac{1}{\varepsilon_p} \frac{\partial \phi_{1j}}{\partial n} \mathcal{G}_{ij} \right) \mathrm{d}L + \sum_{j=1}^{N_b} \int_{L_b} \phi_{2j} \frac{\partial \mathcal{G}_{ij}}{\partial n} \, \mathrm{d}L$$
$$+ \sum_{j=1}^{N_{m_2}} \int_{L_{m_2}} \left(\frac{1}{(s-\mathrm{i}f)} \phi_{3j} \frac{\partial \mathcal{G}_{ij}}{\partial n} - \frac{1}{\varepsilon_p} \frac{\partial \phi_{3j}}{\partial n} \mathcal{G}_{ij} \right) \mathrm{d}L + \sum_{j=1}^{N_f} \int_{L_f} \left(\frac{\partial \mathcal{G}_{ij}}{\partial n} - (s-\mathrm{i}f) \frac{(\omega - Uk_0)^2}{g} \mathcal{G}_{ij} \right)$$
$$\times \phi_{2j} \, \mathrm{d}L = 0. \tag{7.48}$$

For region 3:

$$\frac{1}{2}\phi_{3i}+\sum_{j=1}^{N_5}\int_{L_5}\phi_{3j}\frac{\partial \mathcal{G}_{ij}}{\partial n}\,\mathrm{d}L+\sum_{j=1}^{N_6}\int_{L_6}\phi_{3j}\frac{\partial \mathcal{G}_{ij}}{\partial n}\,\mathrm{d}L+\sum_{j=1}^{N_7}\int_{L_7}\phi_{3j}\frac{\partial \mathcal{G}_{ij}}{\partial n}\,\mathrm{d}L$$
$$+\sum_{j=1}^{N_8}\int_{L_8}\left(\frac{\partial \mathcal{G}_{ij}}{\partial n}-\mathrm{i}k_0\mathcal{G}_{ij}\right)\phi_{3j}\Big)\,\mathrm{d}L+\sum_{j=1}^{N_9}\int_{L_9}\left(\frac{\partial \mathcal{G}_{ij}}{\partial n}-\frac{(\omega-Uk_0)^2}{g}\mathcal{G}_{ij}\right)\phi_{3j}\,\mathrm{d}L$$
$$+\sum_{j=1}^{N_{10}}\int_{L_{10}}\left(\frac{\partial \mathcal{G}_{ij}}{\partial n}-\frac{(\omega-Uk_0)^2}{g}\mathcal{G}_{ij}\right)\phi_{3j}\,\mathrm{d}L+\sum_{j=1}^{N_{m_2}}\int_{L_{m_2}}\left((s-\mathrm{i}f)\phi_{2j}\frac{\partial \mathcal{G}_{ij}}{\partial n}-\varepsilon_p\frac{\partial \phi_{2j}}{\partial n}\mathcal{G}_{ij}\right)$$
$$\times\,\mathrm{d}L=0. \tag{7.49}$$

In each region, $N_1, N_2, N_3, \ldots, N_{12}, N_{m_1}, N_{m_2}, N_b$ and N_f, respectively, denote the total number of segments on the boundaries $L_1, L_2, L_3, \ldots, L_{12}, L_{m_1}, L_{m_2}, L_b$ and L_f. For simplicity, we define

$$\mathcal{M}^l_{ij}=\frac{1}{2}\delta_{ij}+\int_{L_j}\frac{\partial \mathcal{G}_{ij}}{\partial n}\,\mathrm{d}L, \tag{7.50}$$

$$G^l_{ij}=\int_{L_j}\mathcal{G}_{ij}\mathrm{d}L, \tag{7.51}$$

where $l=1,2,3$ corresponds to region 1, region 2, and region 3, respectively. By substituting Eqs. (7.50) and (7.51) into Eqs. (7.47)–(7.49) for each region, the following system of equations are as follows.

For region 1:

$$\sum_{j=1}^{N_1}\left(\phi_{1j}\mathcal{M}^1_{ij}-G^1_{ij}\left(\frac{\partial \phi^{inc}_j}{\partial n}+\mathrm{i}k_0\phi_{1j}-\mathrm{i}k_0\phi^{inc}_j\right)\right)\Big|_{L_1}+\sum_{j=1}^{N_2}\phi_1\mathcal{M}^1_{ij}\Big|_{L_2}+\sum_{j=1}^{N_3}\phi_{1j}\mathcal{M}^1_{ij}\Big|_{L_3}$$
$$+\sum_{j=1}^{N_{m_1}}\left((s-\mathrm{i}f)\phi_{2j}\mathcal{M}^1_{ij}-\varepsilon_p\frac{\partial \phi_{2j}}{\partial n}G^1_{ij}\right)\Big|_{L_{m_1}}+\sum_{j=1}^{N_{11}}\left(\mathcal{M}^1_{ij}-\frac{(\omega-Uk_0)^2}{g}G^1_{ij}\right)\phi_{1j}\Big|_{L_{11}}$$
$$+\sum_{j=1}^{N_4}\phi_{1j}\mathcal{M}^1_{ij}\Big|_{L_4}+\sum_{j=1}^{N_{12}}\left(\mathcal{M}^1_{ij}-\frac{(\omega-Uk_0)^2}{g}G^1_{ij}\right)\phi_{1j}\Big|_{L_{12}}=0, \tag{7.52}$$

For region 2:

$$\sum_{j=1}^{N_{m_1}}\left(\frac{1}{(s-\mathrm{i}f)}\phi_{1j}\mathcal{M}^2_{ij}-\frac{1}{\varepsilon_p}\frac{\partial \phi_{1j}}{\partial n}G^2_{ij}\right)\Big|_{L_{m_1}}+\sum_{j=1}^{N_{m_2}}\left(\frac{1}{(s-\mathrm{i}f)}\phi_{3j}\mathcal{M}^2_{ij}-\frac{1}{\varepsilon_p}\frac{\partial \phi_{3j}}{\partial n}G^2_{ij}\right)\Big|_{L_{m_2}}$$

$$+\sum_{j=1}^{N_b}\phi_{2j}\mathcal{M}^2_{ij}\Big|_{L_b}+\sum_{j=1}^{N_f}\left(\mathcal{M}^2_{ij}-(s-\mathrm{i}f)\frac{(\omega-Uk_0)^2}{g}G^2_{ij}\right)\phi_{2j}\Big|_{L_f}=0, \tag{7.53}$$

For region 3:

$$\begin{aligned}&\sum_{j=1}^{N_5}\phi_{3j}\mathcal{M}^3_{ij}\Big|_{L_5}+\sum_{j=1}^{N_6}\phi_{3j}\mathcal{M}^3_{ij}\Big|_{L_6}+\sum_{j=1}^{N_7}\phi_{3j}\mathcal{M}^3_{ij}\Big|_{L_7}+\sum_{j=1}^{N_8}\left(\mathcal{M}^3_{ij}-\mathrm{i}k_0G^3_{ij}\right)\phi_{3j}\Big|_{L_8}\\&+\sum_{j=1}^{N_9}\left(\mathcal{M}^3_{ij}-\frac{(\omega-Uk_0)^2}{g}G^3_{ij}\right)\phi_{3j}\Big|_{L_9}+\sum_{j=1}^{N_{10}}\left(\mathcal{M}^3_{ij}-\frac{(\omega-Uk_0)^2}{g}G^3_{ij}\right)\phi_{3j}\Big|_{L_{10}}\\&+\sum_{j=1}^{N_{m_2}}\left((s-\mathrm{i}f)\phi_{2j}\mathcal{M}^3_{ij}-\varepsilon_p\frac{\partial\phi_{2j}}{\partial n}G^3_{ij}\right)\Big|_{L_{m_2}}=0.\end{aligned} \tag{7.54}$$

Considering the fundamental solution centered at each node on every segment, the boundary integral equation is evaluated at every node $i = 1, 2, 3, \ldots, N_p$, where $p = 1, 2, 3, \ldots, 12, m_1, m_2, f, b$. This leads to total of N equations corresponding to N unknowns, forming an $N \times N$ linear system, where $N = N_1 + N_2 + N_3 + \cdots + N_{12} + N_{m_1} + N_{m_2} + N_f + N_b$. Solving this system of equations, we obtain the spatial velocity potential ϕ and its normal derivative $\frac{\partial\phi}{\partial n}$ at each node on the boundary element.

7.3 Results and discussions

The reflection (R) and the transmission (T) coefficients (6.47) have been evaluated for various structural and wave parameters as well as for different velocities of ocean current. For numerical simulations, unless stated otherwise, the parameters are kept consistent. The chosen values are as follows: water depth $h = 20$ m, incident wave amplitude $A = 1$, dimensionless porous superstructure height $h_1/h = 0.5$ and dimensionless ocean current velocity $U/\sqrt{gh} = 0.5$.

7.3.1 Validation

It is important to note that, in the absence of ocean current ($U = 0$) and with a negligible height of the rigid base, the inverse T-shaped structure reduces to the case of a fully extended porous breakwater, as studied by Dalrymple *et al.* [35]. Figure 7.3 illustrates the variation of the absolute value of the reflection coefficient with respect to the dimensionless wavenumber k_0h. The results reported by Dalrymple *et al.* [35] are represented by star

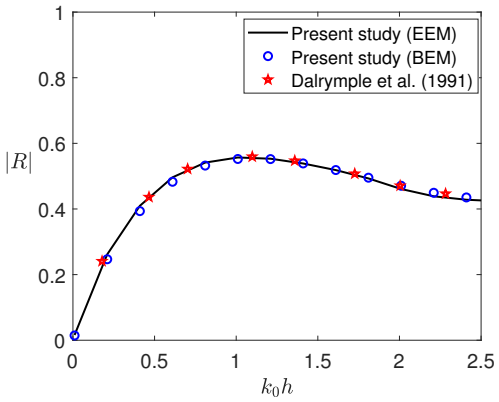

Figure 7.3: Modulus of the reflection coefficient plotted against the dimensionless wavenumber k_0h for fixed parameters: $U = 0$, $f = 1$, $s = 1$, $b_2/h = 1$, and $\varepsilon_p = 0.4$. Star symbol denotes the results reported in [35], while the black solid line and blue circles represent the present results obtained using the EEM and BEM, respectively.

symbol, while those obtained in the present study using the EEM and BEM are shown by the solid black line and blue circles, respectively. Excellent agreement among these results validates the accuracy of the present methodology.

7.3.2 Reflection and transmission coefficients

This subsection presents the influence of various structural and wave parameters on the reflection and transmission coefficients by the inverse T-type compound breakwater. Figure 7.4 displays the (a) reflection and (b) transmission coefficients as functions of the dimensionless wavenumber k_0h for different values of the current velocity. In Fig. 7.4a, the presence of the velocity of ocean current ($U/\sqrt{gh} \neq 0$) leads to distinct oscillatory behavior in the curves compared to gradually decreasing trend observed when no ocean current is present ($U/\sqrt{gh} = 0$). For cases with nonzero velocity of ocean current, both the number and prominence of local maxima in the reflection coefficient increase with the velocity of the ocean current. The narrowing of the bandwidth of curve with increasing current velocity demonstrates that strong reflection is confined to a limited range of wavenumbers, resulting in sharper and higher peaks. In contrast, the transmission coefficient plot (Fig. 7.4b) shows that, for very small wavenumber ($k_0h \to 0$), nearly full transmission is observed. As k_0h grows, the transmission coefficient gradually decreases.

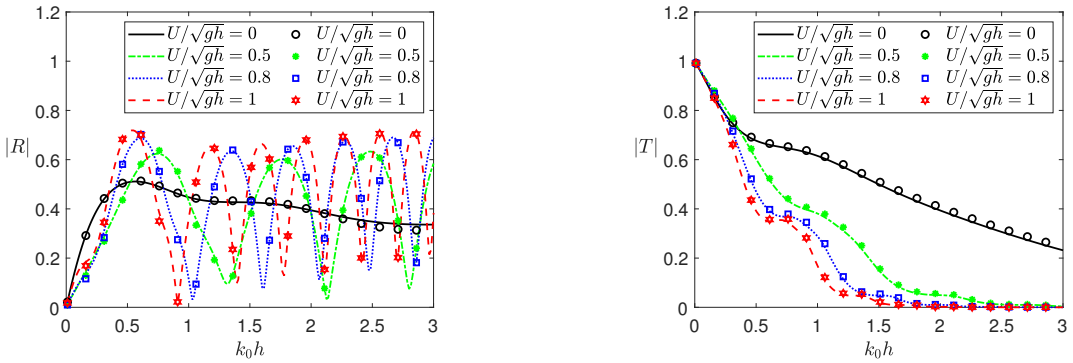

(a) (b)

Figure 7.4: (a) Reflection and (b) transmission coefficients plotted against the dimensionless wavenumber k_0h for different values of the current velocity $U/\sqrt{gh}$. The results derived from the EEM are represented by solid lines, while those obtained using the BEM are shown as symbols. The remaining fixed parameters are taken as $U/\sqrt{gh} = 0.5$, $b_2/h = 1$, $f = 0.5$, $s = 1$ and $\varepsilon_p = 0.5$.

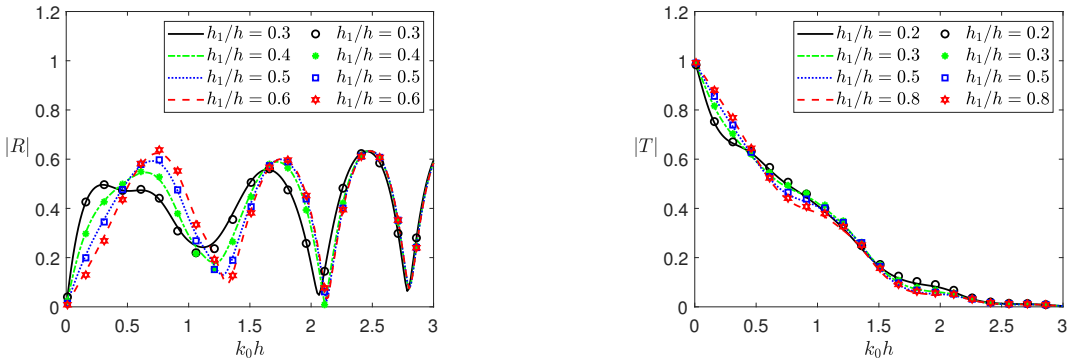

(a) (b)

Figure 7.5: (a) Reflection and (b) transmission coefficients plotted against the dimensionless wavenumber k_0h for varying values of height of the porous section h_1/h. The results derived from the EEM are represented by solid lines, while those obtained using the BEM are shown as symbols. The remaining parameters are fixed as $b_2/h = 1$, $f = 0.5$, $s = 1$ and $\varepsilon_p = 0.5$.

At higher current velocity, the transmission coefficient becomes more pronounced, confirming a greater reduction in energy passing through the structure. Across both Figs. 7.4a and 7.4b, the results from the EEM and BEM show good agreement.

Figure 7.5 presents the of modulus value of the reflection and transmission coefficients for different heights of porous vertical section of the inverse T-type structure. In Fig. 7.5a, the reflection coefficient exhibits noticeable oscillations across the range of k_0h for all values of h_1/h. As the height of porous section increases, the peak of the reflection

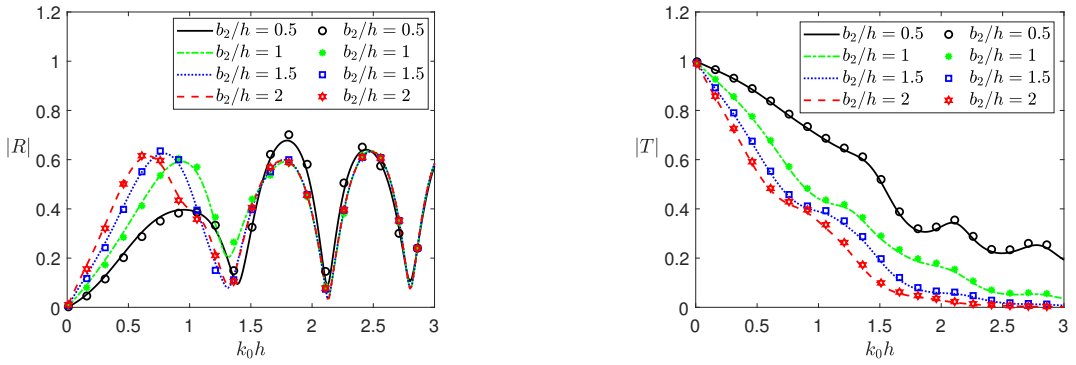

(a) (b)

Figure 7.6: (a) Reflection and (b) transmission coefficients plotted against the dimensionless wavenumber k_0h for varying rigid structure width b_2/h. The results derived from the EEM are represented by solid lines, while those obtained using the BEM are shown as symbols. The remaining parameters are fixed as $U/\sqrt{gh} = 0.5$, $h_1/h = 0.5$, $f = 0.5$, $s = 1$ and $\varepsilon_p = 0.5$

.

coefficient within the range $0.5 \lesssim k_0h \lesssim 1$ becomes more prominent, indicating a stronger reflective response in the long wave region. In Fig. 7.5b, the transmission coefficient initially increases slightly in the long-wave region ($0 \leq k_0h \lesssim 0.6$) as h_1/h increases. This trend suggests that for very low-frequency (long) waves, a taller porous section may offer less resistance, allowing more wave energy to pass through. However, this behavior reverses in the mid-frequency ranges. Specifically, in the intervals $0.5 \lesssim k_0h \lesssim 1.4$ and $1.5 \lesssim k_0h \lesssim 2.25$, the transmission coefficient consistently decreases as h_1/h increases. This implies that as waves become shorter (i.e., as k_0h increases), the porous section becomes increasingly effective at attenuating wave energy. The reduction in transmission is more significant in these intervals, showing that the taller porous section acts as a more efficient energy-absorbing or scattering barrier for intermediate to shorter waves.

The width of the porous section (b_2/h) of the inverse T-shaped structure also significantly affects wave behavior, as shown in Figure 7.6. In Fig. 7.6a, increasing the dimensionless width b_2/h of the porous section leads to noticeably higher reflection coefficients, particularly in the long-wave regime (lower k_0h values). As b_2/h increases, the initial peak and subsequent local maxima of the reflection curve rise in the long wave region. In Fig. 7.6b, a wider porous section (b_2/h) results in a more substantial and persistent reduction in the transmission coefficient across the entire wave spectrum examined. As b_2/h increases, the transmission curve consistently falls lower, demonstrating

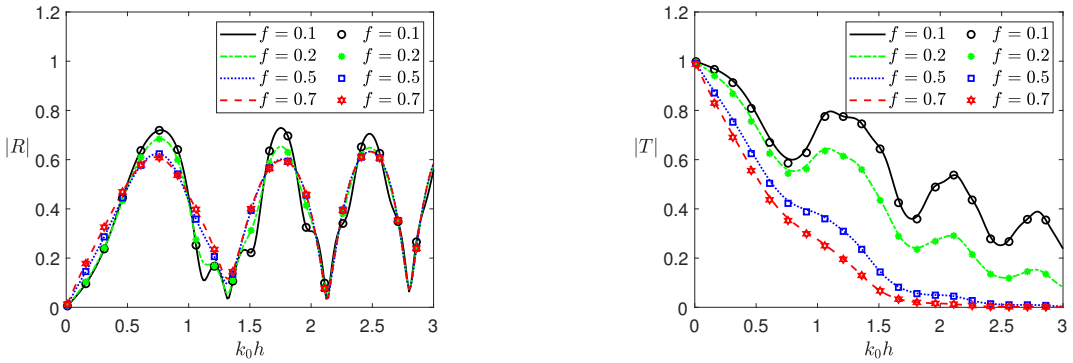

(a) (b)

Figure 7.7: (a) Reflection and (b) transmission coefficients plotted against the dimensionless wavenumber k_0h for varying friction coefficient f. The results derived from the EEM are represented by solid lines, while those obtained using the BEM are shown as symbols. The remaining parameters are fixed as $U/\sqrt{gh} = 0.5$, $h_1/h = 0.5$, $b_2/h = 1$, $s = 1$ and $\varepsilon_p = 0.5$.

that broader structures are more effective at dissipating and reflecting incoming wave energy, and thereby reducing the amount of wave energy transmitted towards the back side of the structure. These results emphasize that optimizing the width b_2/h is crucial for the design of stable and efficient coastal protection systems.

Figure 7.7 demonstrates the effect of the friction coefficient f, associated with the porous section of the structure, on wave reflection and transmission as functions of the dimensionless wavenumber k_0h. In Fig. 7.7a, the reflection coefficient exhibits oscillatory behavior for all values of f, consistent with the trends observed earlier in Figs. 7.5a and 7.6a. As the friction coefficient increases within the porous medium, the peaks of the reflection coefficient become less pronounced, indicating enhanced energy dissipation due to internal flow resistance. This reduces the amount of wave energy reflected by the structure. In Fig. 7.7b, the transmission coefficient consistently decreases with increasing f, showing that more wave energy is either reflected or absorbed within the porous layer, resulting in less energy being transmitted beyond the structure. These results highlight the important role of the porous friction coefficient in governing the dissipation characteristics of the breakwater and its overall effectiveness in attenuating wave energy on the leeside.

Figure 7.8 illustrates the effect of porosity on the reflection and transmission coefficients. As shown in Fig. 7.8a, the peak of the reflection coefficient decreases as the porosity parameter ε_p increases. This occurs because higher porosity allows more wave

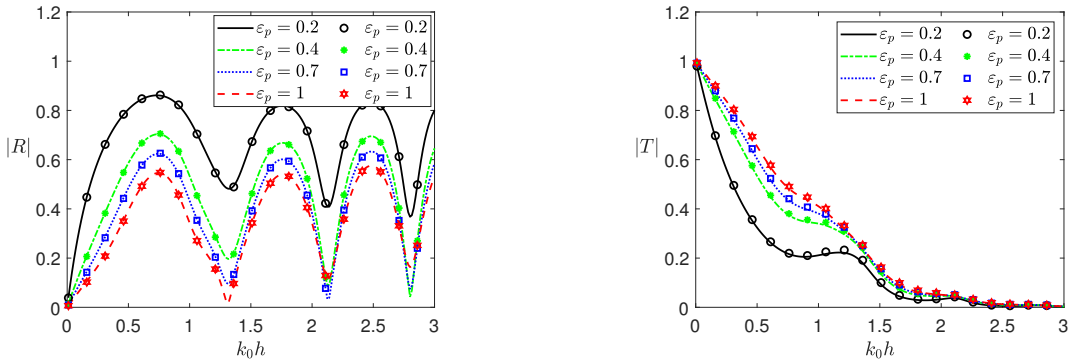

(a) (b)

Figure 7.8: (a) Reflection and (b) transmission coefficients plotted against the dimensionless wavenumber k_0h for different values of the porosity parameter ε_p. The results derived from the EEM are represented by solid lines, while those obtained using the BEM are shown as symbols. The remaining parameters are fixed as $U/\sqrt{gh} = 0.5$, $h_1/h = 0.5$, $b_2/h = 1$, $s = 1$ and $f = 0.5$.

energy to pass through the structure, reducing the amount of energy reflected back. Consequently, as seen in Fig. 7.8b, the transmission coefficient increases. The decrease in reflection directly contributes to greater transmission since more wave energy is able to traverse the porous medium. This relationship highlights the significance of the porosity parameter in controlling the balance between reflection and transmission of wave energy.

7.4 Conclusion

This chapter focuses on understanding the interaction of water waves with an inverse T-type compound breakwater under ocean current. The corresponding BVP is addressed via the analytically (EEM) and numerically (BEM). Using this method, the unknown coefficients associated with the velocity potentials are determined, and the resulting system of equations is solved computationally. The obtained velocity potentials are then used to evaluate the reflection and transmission coefficients for various structural configurations, providing deeper insight into the hydrodynamic performance of the breakwater. A comparison between analytical and numerical results demonstrates good agreement. It is observed that the presence of an ocean current in wave propagation significantly enhances water dissipation through the compound inverse T-shaped structure, leading to less wave transmission. As the current velocity $(U/\sqrt{gh})$ increases, the amplitude of the reflection curve rises, accompanied by a more noticeable decrease in wave transmission.

Furthermore, an increase in the height of the perforated section of the structure results in a higher amplitude of the reflection curve in the long-wave region, while the transmission coefficient exhibits an opposite trend in the same region. Additionally, a higher value of the friction parameter (f) consistently contributes to a reduction in the transmission coefficient across all wave conditions.

Chapter 8

Conclusions and outlook

8.1 Summary and conclusions

In this thesis, the widely adopted assumption of a rigid seabed in wave scattering problems is re-evaluated, as it does not adequately reflect the complexities of real-world marine environments. To address this limitation, a porous seabed has been introduced in Chapters 3–5, offering a more realistic depiction of the seabed. Additionally, while most existing studies consider only normal ocean wave conditions, this thesis analyzes the effects of ocean currents in Chapters 6–7, which play a significant role in altering wave behavior.

A comprehensive investigation has been carried out in this thesis on the interaction of water waves with various structural configurations. The configurations employed include single and multiple circular cylinders and multiple circular flexible plates placed over a porous seabed, surface-piercing structures, and a fully extended inverse T-type structure in the presence of ocean currents. A summary of the thesis is as follows.

- The BVPs associated with the physical problems—such as the scattering of waves by circular cylinder(s) and plates—discussed in Chapters 3–5 have been solved analytically using the EEM. Furthermore, for the problems involving the scattering of waves by rectangular and inverse T-type structures, presented in Chapters 6–7, numerical solutions have also been obtained using the BEM in addition to analytic solution through the EEM.
- In problems involving multiple circular cylinders and plates, the interaction of scattered waves with each structure complicates the analysis. To overcome this complexity, Graf's addition theorem has been employed in the open-water region to relate the scattered waves from all cylinders and plates in a global coordinate system.
- Wave interactions with a single and multiple cylinder(s), as well as flexible circular plates placed on the free surface over a porous seabed, have been investigated. The findings indicate that a porous seabed significantly reduces the wave forces acting

on the structures compared to a rigid seabed, and an increase in the modulus of the porous-effect parameter leads to a further reduction in wave forces.

- In the study of wave interaction with multiple cylinders, it has been found that, for fixed radii (or heights), the horizontal force on a cylinder decreases as the heights (or radii) of the cylinders increase.
- For the problem of floating circular plates, different edge conditions have been employed. The heave force exerted on the plates has been found to be lower in the free-edge condition compared to the clamped- and moored-edge conditions. It has also been found that as the Young's modulus of the plates increases, the heave force decreases, especially in the long-wave region.
- In the case of multiple cylinders and plates, it has been observed that the wave forces exerted on the succeeding cylinders or plates are significantly reduced compared to those on the preceding ones.
- Time-dependent simulations of fluid flow have been presented to provide realistic visualizations of wave interactions with cylinder(s)/plate(s) arranged in both array and square configurations. Additionally, flow distributions around the cylinder(s)/plate(s) have been presented to illustrate the variation in wave elevation. Furthermore, the velocity vector fields around multiple circular cylinders have also been presented.
- Ocean currents have been found to significantly reduce the transmission coefficient and increase the reflection coefficient during wave interactions with surface-piercing and fully extended inverse T-shaped compound docks. It has also been found that, as the velocity of the ocean current increases, the peak of the reflection curve increases, while the transmission coefficients gradually decrease.
- A higher velocity of the ocean current has been found to result in reduced horizontal forces on both single and dual docks, with the second dock consistently experiencing lower forces. Surface plots of the reflection and transmission coefficients, as functions of the dimensionless wavenumber and oblique wave incidence, have been presented to illustrate the combined effects of ocean currents and structural parameters.

8.2 Outlook

The present thesis, while providing valuable insights on wave-structure interactions, involves certain limitations due to simplifying assumptions made for mathematical convenience. The fluid is assumed to be inviscid and irrotational, thereby neglecting viscous and rotational effects that may influence the hydrodynamic behavior in realistic marine environments. The seabed is modeled as rigid or porous without considering internal fluid motion, which may affect wave attenuation and energy dissipation. Similarly, the analysis is confined to a single-layer fluid system, whereas oceans often exhibit stratification due to variations in temperature and salinity. The exclusion of surface tension at the free surface further simplifies the wave dynamics. Recognizing these limitations provides a clear pathway for future research. Future studies should aim to address these constraints and extend the present work toward more realistic and practically relevant scenarios. Some of the potential directions for future research are outlined below.

- The thesis considers the sea bottom as a porous seabed but does not account for fluid movement inside the it. Future studies could focus on capturing fluid movement inside the porous seabed as well.
- The problems discussed in this thesis focus on a single fluid layer, which simplifies the fluid environment. However, in real-world situations like in oceans, fluid layers often form due to differences in temperature or salt concentration. These layered fluids behave differently than a single uniform layer because waves can travel not only on the surface but also at the interfaces between layers. Future studies can extend these problems to include two- or multi-layers fluid systems, allowing the study of wave motion inside each layer as well as interactions between the layers.
- Scattering of waves by floating flexible circular plates studied in Chapter 5. This work can be further extended by replacing those plates with piezoelectric plates, which possess the ability to convert mechanical energy from wave motion into electrical energy. Investigating the interaction between ocean waves and floating piezoelectric plates would enable assessment of their potential as renewable energy harvesters.
- The analysis conducted in this thesis relies on the assumptions of inviscid and irrotational flow. For a more realistic depiction of fluid behavior, future studies

can revisit these problems by applying the Navier–Stokes equations to incorporate viscous effects.

- The problems addressed in this thesis primarily consider rigid and porous seabeds. In future studies, more realistic seabed characteristics—such as elastic, poroelastic and undulated—can be incorporated to extend the scope of the analysis.
- In this thesis, the effect of surface tension on the free surface of water has been neglected. However, the inclusion of surface tension on the free surface of water in future studies can provide a more comprehensive understanding of wave behavior.
- The scattering of waves by rectangular and inverse T-shaped structures has been examined in Chapters 6 and 7 using the BEM. Future investigations could extend the application of the BEM to more complex geometries, including arbitrarily shaped boundaries.
- The effect of ocean current in Chapters 6 and 7 has been considered parallel to the y- and x-axes, respectively. Future studies would extend these works by examining the combined effect of ocean current in both the x- and y-directions.

To address the above challenges and capture the complexity of wave–structure interactions, advanced numerical methods will be essential, especially when considering the full Navier-Stokes equations. Future studies may use techniques like the finite volume method, FEM, or coupled FEM–BEM approaches for accurate and efficient modeling of complex geometries and nonlinear wave behavior.

Appendix A: Derivation process to get a system of equations

By substituting the spatial velocity potential for the exterior region, given in Eq. (4.15), and for the interior regions, given in Eq. (4.16), into the matching condition for velocity continuity (4.4) and the matching condition for pressure continuity (4.5), we obtain

$$\sum_{m=-\infty}^{\infty}\Bigg[\mathbf{I}_k \mathrm{i}^m J_m(k_0a_k)\mathrm{e}^{-\mathrm{i}m\beta}f_0(z)+\sum_{n=0}^{\infty}\mathcal{A}_{mn}^{k}H_m^{(1)}(k_na_k)\mathrm{e}^{\mathrm{i}m\theta_k}f_n(z)$$
$$+\sum_{\substack{j=1\\ j\neq k}}^{N}\sum_{n=0}^{\infty}\sum_{m_1=-\infty}^{\infty}\Big((-1)^{m_1}\mathcal{A}_{mn}^{j}H_{m-m_1}^{(1)}(k_nR_{jk})\mathrm{e}^{\mathrm{i}(m\alpha_{kj}-m_1\alpha_{jk})}J_{m_1}(k_na_k)\mathrm{e}^{\mathrm{i}m_1\theta_k}f_n(z)\Big)\Bigg]$$
$$=\sum_{m=-\infty}^{\infty}\sum_{n=0}^{\infty}\mathcal{B}_{mn}^{k}I_m(\lambda_na_k)g_n(z)\mathrm{e}^{\mathrm{i}m\theta_k}, \tag{A.1}$$

$$\sum_{m=-\infty}^{\infty}\Bigg[\mathbf{I}_k \mathrm{i}^m k_0J_m^{'}(k_0a_k)\mathrm{e}^{-\mathrm{i}m\beta}f_0(z)+\sum_{n=0}^{\infty}\mathcal{A}_{mn}^{k}k_nH_m^{(1)^{'}}(k_na_k)\mathrm{e}^{\mathrm{i}m\theta_k}f_n(z)$$
$$+\sum_{\substack{j=1\\ j\neq k}}^{N}\sum_{n=0}^{\infty}\sum_{m_1=-\infty}^{\infty}\Big((-1)^{m_1}\mathcal{A}_{mn}^{j}H_{m-m_1}^{(1)^{'}}(k_nR_{jk})\mathrm{e}^{\mathrm{i}(m\alpha_{kj}-m_1\alpha_{jk})}k_nJ_{m_1}^{'}(k_na_k)\mathrm{e}^{\mathrm{i}m_1\theta_k}f_n(z)\Big)\Bigg]$$
$$=\sum_{m=-\infty}^{\infty}\sum_{n=0}^{\infty}\mathcal{B}_{mn}^{k}\lambda_nI_m^{'}(\lambda_na_k)g_n(z)\mathrm{e}^{\mathrm{i}m\theta_k}. \tag{A.2}$$

Inserting the expression of the spatial velocity potential for the exterior region (4.15) into the structural boundary condition (4.3), we obtain

$$\sum_{m=-\infty}^{\infty}\Bigg[\mathbf{I}_k \mathrm{i}^m k_0J_m^{'}(k_0a_k)\mathrm{e}^{-\mathrm{i}m\beta}f_0(z)+\sum_{n=0}^{\infty}\mathcal{A}_{mn}^{k}k_nH_m^{(1)^{'}}(k_na_k)\mathrm{e}^{\mathrm{i}m\theta_k}f_n(z)$$
$$+\sum_{\substack{j=1\\ j\neq k}}^{N}\sum_{n=0}^{\infty}\sum_{m_1=-\infty}^{\infty}\Big((-1)^{m_1}\mathcal{A}_{mn}^{j}H_{m-m_1}^{(1)^{'}}(k_nR_{jk})\mathrm{e}^{\mathrm{i}(m\alpha_{kj}-m_1\alpha_{jk})}k_nJ_{m_1}^{'}(k_na_k)\mathrm{e}^{\mathrm{i}m_1\theta_k}f_n(z)\Big)\Bigg]=0. \tag{A.3}$$

After multiplying both sides of Eq. (A.1) by $g_l(z)\mathrm{e}^{-\mathrm{i}q\theta_k}$ (for $l=0,1,2,3,\ldots$ and $q=\ldots,-1,0,1,\ldots$) and integrating with respect to z over the respective domain of the boundary condition in Eq. (4.4) as well as with respect to for θ_k over the interval $[0,2\pi]$, and then applying the orthogonality conditions for the eigenfunctions $g_n(z)$, the resultant

equation is obtained as

$$\mathbf{I}_k \mathrm{i}^q e^{-\mathrm{i}q\beta} J_q(k_0 a_k) X_{0l} + \sum_{n=0}^{\infty} \mathcal{A}_{qn}^k H_q^{(1)}(k_n a_k) X_{nl}$$
$$+ \sum_{\substack{j=1 \\ j\neq k}}^{N} \sum_{m=-\infty}^{\infty} \sum_{n=0}^{\infty} \left((-1)^q \mathcal{A}_{mn}^j H_{m-q}^{(1)}(k_n R_{kj}) e^{\mathrm{i}(m\alpha_{jk} - q\alpha_{kj})} J_q(k_n a_k) X_{nl} \right) = \mathcal{B}_{ql}^k I_q(\lambda_l a_k) \delta_{0l} Y_l, \tag{A.4}$$

where

$$X_{nl} = \int_{\Omega_2} f_n(z) g_l(z)\, \mathrm{d}z, \quad Y_l = \int_{\Omega_2} g_l^2(z)\, \mathrm{d}z. \tag{A.5}$$

Next, multiplying both sides of Eqs. (A.2) and (A.3) by $f_l(z)\mathrm{e}^{-\mathrm{i}q\theta_k}$ (for $l = 0, 1, 2, 3, \ldots$ and $q = \ldots, -1, 0, 1, \ldots$), integrating with respect to z in the respective domain of the boundary conditions in Eqs. (4.5) and (4.3) and for $\theta_k \in [0, 2\pi]$. After combining both Eqs. (4.5) and (4.3), we apply the orthogonality conditions for the eigenfunction $f_n(z)$. As a result, Eqs. (A.2) and (A.3) give

$$\mathbf{I}_k \mathrm{i}^q e^{-\mathrm{i}q\beta} k_0 J_q'(k_0 a_k) \delta_{0l} Z_l + \mathcal{A}_{ql}^k k_l H_q^{(1)'}(k_l a_k) Z_l$$
$$+ \sum_{\substack{j=1 \\ j\neq k}}^{N} \sum_{m=-\infty}^{\infty} \left((-1)^q \mathcal{A}_{ml}^j H_{m-q}^{(1)}(k_l R_{kj}) e^{\mathrm{i}(m\alpha_{jk} - q\alpha_{kj})} k_l J_q'(k_l a_k) Z_l \right) = \sum_{n=0}^{\infty} \left(\mathcal{B}_{qn}^k \lambda_n I_q'(\lambda_n a_k) Y_{1nl} \right), \tag{A.6}$$

where

$$Z_l = \int_{\Omega_1+\Omega_2} f_l^2(z)\, \mathrm{d}z, \quad Y_{1nl} = \int_{\Omega_2} g_n(z) f_l(z)\, \mathrm{d}z. \tag{A.7}$$

Equations (A.4) and (A.6) together represent a system of infinite equations. This system involves an infinite number of unknown coefficients.

Appendix B: Derivation process to get a system of equations

By substituting the spatial velocity potential for the exterior region, given in Eq. (5.14), and for the interior regions, given in Eq. (5.15), into the matching condition for pressure

continuity (5.11) and the matching condition for velocity continuity (5.12), we obtain

$$\sum_{m=-\infty}^{\infty}\Bigg[\mathbf{I}_j \mathrm{i}^m e^{-\mathrm{i}m\beta} J_m(k_0 a_j) f_{10}(z) + \sum_{n=0}^{\infty} \mathcal{A}_{mn}^{j} H_m^{(1)}(k_n a_j) e^{\mathrm{i}m\theta_j} f_n(z) + \sum_{\substack{k=1\\k\neq j}}^{N}\sum_{n=0}^{\infty}\sum_{m_1=-\infty}^{\infty}\Big((-1)^{m_1}\mathcal{A}_{mn}^{k} H_{m-m_1}^{(1)}(k_n R_{kj}) e^{\mathrm{i}(m\alpha_{jk}-m_1\alpha_{kj})} J_{m_1}(k_n a_j) e^{\mathrm{i}m_1\theta_j} f_n(z)\Big)\Bigg] = \sum_{m=-\infty}^{\infty}\sum_{n=-2}^{\infty}\left(\mathcal{B}_{mn}^{k} J_m(\mu_n a_j) g_n(z)\right) e^{\mathrm{i}m\theta_j}, \tag{A.8}$$

$$\sum_{m=-\infty}^{\infty}\Bigg[\mathbf{I}_j \mathrm{i}^m e^{-\mathrm{i}m\beta} k_0 J_m'(k_0 a_j) f_{10}(z) + \sum_{n=0}^{\infty} \mathcal{A}_{mn}^{j} k_n H_m^{(1)'}(k_n a_j) e^{\mathrm{i}m\theta_j} f_n(z) + \sum_{\substack{k=1\\k\neq j}}^{N}\sum_{n=0}^{\infty}\sum_{m_1=-\infty}^{\infty}\Big((-1)^{m_1}\mathcal{A}_{mn}^{k} H_{m-m_1}^{(1)}(k_n R_{kj}) e^{\mathrm{i}(m\alpha_{jk}-m_1\alpha_{kj})} k_n J_{m_1}'(k_n a_j) e^{\mathrm{i}m_1\theta_j} f_n(z)\Big)\Bigg] = \sum_{m=-\infty}^{\infty}\sum_{n=-2}^{\infty}\left(\mathcal{B}_{mn}^{k} \mu_n J_m'(\mu_n a_j) g_n(z)\right) e^{\mathrm{i}m\theta_j}. \tag{A.9}$$

After multiplying Eqs. (A.8) and (A.9) by $f_l(z)e^{-\mathrm{i}s\theta_j}$ (for $l = 0, 1, 2, 3, \ldots$ and $s = \ldots, -3, -2, -1, 0, 1, 2, 3, \ldots$), and integrating over z within the appropriate domain specified by the boundary conditions (5.11) and (5.12), and over θ_j within the range of $[0, 2\pi]$, then by exploiting the orthogonality condition of the eigenfunctions, the resulting equations are obtained as

$$\mathbf{I}_j \mathrm{i}^s e^{-\mathrm{i}s\beta} J_s(k_0 a_j)\delta_{0,l} Z_l + \mathcal{A}_{sl}^{j} H_s^{(1)}(k_l a_j) Z_l + \sum_{\substack{k=1\\k\neq j}}^{N}\sum_{m=-\infty}^{\infty}\Big((-1)^{s}\mathcal{A}_{ml}^{k} H_{m-s}^{(1)}(k_l R_{kj}) e^{\mathrm{i}(m\alpha_{jk}-s\alpha_{kj})} J_s(k_l a_j) Z_l\Big) = \sum_{n=-2}^{\infty}\mathcal{B}_{sn}^{j} J_s(\mu_n a_j) Y_{nl}, \tag{A.10}$$

$$\mathbf{I}_j \mathrm{i}^s e^{-\mathrm{i}s\beta} k_0 J_s'(k_0 a_j)\delta_{0,l} Z_l + \mathcal{A}_{sl}^{j} k_l H_s^{(1)'}(k_l a_j) Z_l + \sum_{\substack{k=1\\k\neq j}}^{N}\sum_{m=-\infty}^{\infty}\Big((-1)^{s}\mathcal{A}_{ml}^{k} H_{m-s}^{(1)}(k_l R_{kj}) e^{\mathrm{i}(m\alpha_{jk}-s\alpha_{kj})} k_l J_s'(k_l a_j) Z_l\Big) = \sum_{n=-2}^{\infty}\mathcal{B}_{sn}^{j} \mu_n J_s'(\mu_n a_j) Y_{nl}, \tag{A.11}$$

where $\delta_{0,l}$ is the Kronecker delta function and

$$Z_l = \int_\Omega f_l^2(z)\mathrm{d}z, \quad Y_{nl} = \int_\Omega g_n(z) f_l(z)\mathrm{d}z. \tag{A.12}$$

Following a similar approach, if we multiply both sides in moored-edge conditions (5.10) by $e^{-\mathrm{i}s\theta_j}$, we obtain

$$\sum_{m=-\infty}^{\infty}\sum_{n=-2}^{\infty}\mathcal{B}_{mn}^{j}\left[a_j^2\mu_n^2 J_m^{''}(\mu_n a_j)+\nu\left\{a_j\mu_n J_m^{'}(\mu_n a_j)-m^2 J_m(\mu_n a_j)\right\}\right]\psi(\mu_n)e^{\mathrm{i}(m-s)\theta_j}=0, \tag{A.13}$$

$$\sum_{m=-\infty}^{\infty}\sum_{n=-2}^{\infty}\mathcal{B}_{mn}^{j}\Bigg[EI\Bigg\{a_j^3\mu_n^3 J_m^{'''}(\mu_n a_j)+a_j^2\mu_n^2 J_m^{''}(\mu_n a_j)-[1+(2-\nu)m^2]\mu_n J_m^{'}(\mu_n a_j)$$
$$+(3-\nu)m^2 J(\mu_n a_j)\Bigg\}+a_j^3\mathcal{N}\mu_n J_m^{'}(\mu_n a_j)-p_s\Bigg]\psi(\mu_n)e^{\mathrm{i}(m-s)\theta_j}=0, \tag{A.14}$$

where

$$\psi(\mu_n)=\frac{\mu_n^2\sinh(\mu_n h)+G\mu_n\cosh(\mu_n h)}{G\sinh(\mu_n h)-\mu_n\cosh(\mu_n h)}.$$

Again, integrating Eqs. (A.13) and (A.14) with respect to the θ_j over the region $[0,2\pi]$, the resultant equations are obtained as

$$\sum_{n=-2}^{\infty}\mathcal{B}_{sn}^{j}\left[a_j^2\mu_n^2 J_s^{''}(\mu_n a_j)+\nu\left\{a_j\mu_n J_s^{'}(\mu_n a_j)-s^2 J_s(\mu_n a_j)\right\}\right]\psi(\mu_n)=0, \tag{A.15}$$

$$\sum_{n=-2}^{\infty}\mathcal{B}_{sn}^{j}\Bigg[EI\Bigg\{a_j^3\mu_n^3 J_s^{'''}(\mu_n a_j)+a_j^2\mu_n^2 J_s^{''}(\mu_n a_j)-[1+(2-\nu)s^2]\mu_n J_s^{'}(\mu_n a_j)$$
$$+(3-\nu)s^2 J_s(\mu_n a_j)\Bigg\}+a_j^3\mathcal{N}\mu_n J_s^{'}(\mu_n a_j)-p_s\Bigg]\psi(\mu_n)=0. \tag{A.16}$$

When $p_s=0$, Eqs. (A.15) and (A.16) transform into the system of equations for free-edge conditions. Continuing with a similar approach, in the clamped-edge boundary conditions, multiplying both sides with $e^{-\mathrm{i}s\theta_j}$, the resultant equations are obtained as

$$\sum_{m=-\infty}^{\infty}\sum_{n=-2}^{\infty}\mathcal{B}_{mn}^{j}J_m(\mu_n a_j)\psi(\mu_n)e^{\mathrm{i}(m-s)\theta_j}=0, \tag{A.17}$$

$$\sum_{m=-\infty}^{\infty}\sum_{n=-2}^{\infty}\mathcal{B}_{mn}^{j}\mu_n J_m^{'}(\mu_n a_j)\psi(\mu_n)e^{\mathrm{i}(m-s)\theta_j}=0. \tag{A.18}$$

Again, integrating Eqs. (A.17) and (A.18) with respect to θ_j in the region $[0, 2\pi]$, yields

$$\sum_{n=-2}^{\infty} \mathcal{B}_{sn}^{j} J_s(\mu_n a_j)\psi(\mu_n) = 0, \tag{A.19}$$

$$\sum_{n=-2}^{\infty} \mathcal{B}_{sn}^{j} \mu_n J_s^{'}(\mu_n a_j)\psi(\mu_n) = 0. \tag{A.20}$$

Equations (A.10) and (A.11), (A.15) and (A.16), together with (A.19) and (A.20), collectively form a system of equations.

REFERENCES

[1] Abramowitz, M. & Stegun, I. A. 1965 *Handbook of mathematical functions: with formulas, graphs, and mathematical tables*. Dover Publications.

[2] Abul-Azm, A. 1994 Diffraction through wide submerged breakwaters under oblique waves. *Ocean Eng.* **21**, 683–706.

[3] Abul-Azm, A. & Gesraha, M. 2000 Approximation to the hydrodynamics of floating pontoons under oblique waves. *Ocean Eng.* **27**, 365–384.

[4] Akarni, H., El Aarabi, L., Mouakkir, L. & Mordane, S. 2021 Numerical modeling of the wave-plate-current interaction by the boundary element method. *Fluids* **6**, 435.

[5] Akarni, H., Mabchour, H., Aarabi, L. & Mordane, S. 2024 Wave reflection by rectangular breakwaters for coastal protection. *Fluid Dyn. Mater. Process.* **20**, 579.

[6] Ang, W. T. 2007 *A beginner's course in boundary element methods*. Universal Publishers.

[7] Ardhuin, F. & Magne, R. 2007 Scattering of surface gravity waves by bottom topography with a current. *J. Fluid Mech.* **576**, 235–264.

[8] Barman, K. K., Chanda, A. & Tsai, C. C. 2023 A mathematical study of a two-layer fluid flow system in the presence of a floating breakwater in front of vlfs. *Appl. Math. Model.* **122**, 706–730.

[9] Barman, K. K., Saha, S. & Zheng, S. 2025 Flexural wave interaction with compressive floating ice over undulating porous bed. *Proceedings of the Royal Society A* **481**, 20250067.

[10] Beavers, G. S. & Joseph, D. D. 1967 Boundary conditions at a naturally permeable wall. *J. Fluid Mech.* **30**, 197–207.

[11] Behera, H. 2015 Mathematical techniques for gravity wave interaction with porous and flexible structures. PhD thesis.

[12] Behera, H., Koley, S. & Sahoo, T. 2015 Wave transmission by partial porous

structures in two-layer fluid. *Eng. Anal. Bound. Elem.* **58**, 58–78.

[13] Behera, H. & Ng, C. O. 2018 Interaction between oblique waves and multiple bottom-standing flexible porous barriers near a rigid wall. *Meccanica* **53**, 871–885.

[14] Behera, H., Ng, C. O. & Sahoo, T. 2018 Oblique wave scattering by a floating elastic plate over a porous bed in single and two-layer fluid systems. *Ocean Eng.* **159**, 280–294.

[15] Behera, H. & Sahoo, T. 2015 Hydroelastic analysis of gravity wave interaction with submerged horizontal flexible porous plate. *J. Fluids Struct.* **54**, 643–660.

[16] Bhatta, D. D. 2011 Computations of hydrodynamic coefficients, displacement-amplitude ratios and forces for a floating cylinder due to wave diffraction and radiation. *Int. J. Nonlin. Mech.* **46**, 1027–1041.

[17] Bhatta, D. D., Rahman, M. & others 1995 Wave loadings on a vertical cylinder due to heave motion. *Int. J. Math. Math. Sci.* **18**, 151–170.

[18] Bi, C., Wu, M. S. & Law, A. W. K. 2022 Surface wave interaction with a vertical viscoelastic barrier. *Appl. Ocean Res.* **120**, 103073.

[19] Bora, S. N., Das, S., Meylan, M. H., Saha, S. & Zheng, S. 2023 Time-dependent water wave scattering by a marine structure consisting of an array of compound porous cylinders. *Phys. Fluids* **35**, 077103.

[20] Brebbia, C. A., Telles, J. C. F. & Wrobel, L. C. 2012 *Boundary element techniques: theory and applications in engineering*. Springer Science & Business Media.

[21] Cao, J., Wang, J., Wang, C., Wang, Z. & Yu, F. 2023 Wave diffraction and radiation studies of an array of coaxial double-layer porous cylindrical structures placed on a porous seabed. *Phys. Fluids* **35**, 127121.

[22] Chanda, A., Barman, S., Sahoo, T. & Meylan, M. 2024 Flexural-gravity wave scattering by an array of bottom-standing partial porous barriers in the framework of bragg resonance and blocking dynamics. *Phys. Fluids* **36**.

[23] Chanda, A. & Bora, S. N. 2020 Effect of a porous sea-bed on water wave scattering by two thin vertical submerged porous plates. *Eur. J. Mech. B/Fluids.* **84**, 250–261.

[24] Chanda, A. & Pramanik, S. 2023 Effects of a thin vertical porous barrier on the water wave scattering by a porous breakwater. *Phys. Fluids* **35**, 062120.

[25] Chanda, A., Sarkar, A. & Bora, S. N. 2022 An analytical study of scattering of water waves by a surface-piercing bottom-mounted compound porous cylinder placed on a porous sea-bed. *J. Fluids Struct.* **115**, 103764.

[26] Chen, H. B., Tsai, C. P. & Chiu, J. R. 2006 Wave reflection from vertical breakwater with porous structure. *Ocean Eng.* **33**, 1705–1717.

[27] Chen, J. T., Lin, Y., Lee, Y. T. & Wu, C. 2011 Water wave interaction with surface-piercing porous cylinders using the null-field integral equations. *Ocean Eng.* **38**, 409–418.

[28] Chen, Q., Li, T., Yang, Q., Law, S.-s., Cao, S. & Zhang, X. 2024 Effects of mass and damping ratios on the flow-induced vibration of two staggered circular cylinders. *Phys. Fluids* **36**, 077120.

[29] Cho, I. & Kim, M. 2008 Wave absorbing system using inclined perforated plates. *J. Fluid Mech.* **608**, 1–20.

[30] Cho, Y. S., Jeon, C. H., Lee, J. I. & Lee, B. H. 2006 Strong reflection of sinusoidal waves due to trapezoidal submerged porous breakwaters. *J. Coast. Res.* pp. 838–841.

[31] Chwang, A. T. 1983 A porous-wavemaker theory. *J. Fluid Mech.* **132**, 395–406.

[32] Corvaro, S., Mancinelli, A., Brocchini, M., Seta, E. & Lorenzoni, C. 2010 On the wave damping due to a permeable seabed. *Coast. Eng.* **57**, 1029–1041.

[33] Coudraye, F. d. L. d. l. 1796 Théories des vents et des ondes. *Kön. Ges. Wiss.* pp. 105–150.

[34] Craik, A. D. 2004 The origins of water wave theory. *Annu. Rev. Fluid Mech.* **36**, 1–28.

[35] Dalrymple, R. A., Losada, M. A. & Martin, P. 1991 Reflection and transmission from porous structures under oblique wave attack. *J. Fluid Mech.* **224**, 625–644.

[36] Das, S. 2025 Flexural-gravity wave dissipation under strong compression and ocean current near blocking point. *Waves Random Complex Media* **35**, 1571–1595.

[37] Das, S., Kar, P., Sahoo, T. & Meylan, M. H. 2018 Flexural-gravity wave motion in the presence of shear current: Wave blocking and negative energy waves. *Phys. Fluids* **30**, 106606.

[38] Das, S., Sahoo, T. & Meylan, M. 2018 Dynamics of flexural gravity waves:

from sea ice to hawking radiation and analogue gravity. *Proc. R. Soc. A* **474**, 20170223.

[39] Dash, S. K., Koley, S. & Zheng, S. 2024 Performance of an oscillating water column wave energy converter device under random ocean waves and ocean currents. *Phys. Fluids* **36**, 107165.

[40] Dean, R. G. & Dalrymple, R. A. 1991 *Water wave mechanics for engineers and scientists*, , vol. 2. World Scientific Publishing Company.

[41] Dean, W. R. 1945 On the reflexion of surface waves by a submerged plane barrier. *Math. Proc. Camb.* **41**, 231–238.

[42] Deng, Z., Wang, L., Zhao, X. & Huang, Z. 2019 Hydrodynamic performance of a t-shaped floating breakwater. *Appl. Ocean Res.* **82**, 325–336.

[43] Dhillon, H., Banerjea, S. & Mandal, B. 2014 Wave scattering by a thin vertical barrier in a two-layer fluid. *Int. J. Eng. Sci.* **78**, 73–88.

[44] Dick, T. M. & Brebner, A. 1968 Solid and permeable submerged breakwaters pp. 1141–1158.

[45] Dong, G., Zheng, Y., Li, Y., Teng, B., Guan, C. & Lin, D. 2008 Experiments on wave transmission coefficients of floating breakwaters. *Ocean Eng.* **35**, 931–938.

[46] Dora, R. R., Trivedi, K., Mohanty, S. K. & Koley, S. 2024 Oblique wave scattering by porous structures in the presence of current. *Eng. Anal. Bound. Elem.* **167**, 105885.

[47] Dorfmann, A. A. 1999 Water waves diffraction by a circular plate. *J. Comput. Appl. Math.* **110**, 287–304.

[48] Fehribach, J. D. 2024 *Multivariable and vector calculus*. Walter de Gruyter GmbH & Co KG.

[49] Flaugergues, M. 1793 Hollandsche maatschappye der weetenschappen te haarlem **xxix**.

[50] Garrett, C. J. R. 1971 Wave forces on a circular dock. *J. Fluid Mech.* **46**, 129–139.

[51] Gayen, R., Gupta, S. & Chakrabarti, A. 2016 Approximate solution of the problem of scattering of surface water waves by a partially immersed rigid plane vertical barrier. *Appl. Math. Lett.* **58**, 19–25.

[52] Gupta, S. & Gayen, R. 2018 Scattering of oblique water waves by two thin unequal barriers with non-uniform permeability. *J. Eng. Math.* **112**, 37–61.

[53] Hu, C. & Kashiwagi, M. 2009 Two-dimensional numerical simulation and experiment on strongly nonlinear wave–body interactions. *J. Mar. Sci. Technol.* **14**, 200–213.

[54] Huang, J. & Porter, R. 2023 Water wave propagation through arrays of closely spaced surface-piercing vertical barriers. *J. Fluid Mech.* **960**, A20.

[55] Isaacson, M., Baldwin, J., Allyn, N. & Cowdell, S. 2000 Wave interactions with perforated breakwater. *J. Waterw. Port Coast. Ocean Eng.* **126**, 229–235.

[56] Iwasaki, T. & Numata, A. 1970 Experimental studies on wave transmission of a permeable breakwater constructed by artificial blocks. *Coast. Eng. J.* **13**, 25–29.

[57] Jeffreys, H. 1944 Note on the offshore bar problem and reflection from a bar. *Grt. Brit. Ministry of Supply, Wave Report* .

[58] Jins, M. M., Vijay, K., Venkateswarlu, V. & Behera, H. 2025 Oblique wave interaction with a floating dock in the presence of inverted trapezoidal pile-rock breakwaters. *Eng. Anal. Bound. Elem.* **172**, 106111.

[59] Johnson, J. W., Fuchs, R. A. & Morison, J. 1951 The damping action of submerged breakwaters. *Eos, Transactions American Geophysical Union* **32**, 704–718.

[60] Jonsson, I. G. 1990 Wave-current interactions. *The sea* **9**, 65–120.

[61] Jonsson, I. G. & Wang, J. D. 1980 Current-depth refraction of water waves. *Ocean Eng.* **7**, 153–171.

[62] Kaligatla, R., Tabssum, S. & Sahoo, T. 2024 Surface gravity wave interaction with a partial porous breakwater in a two-layer ocean having bottom undulations. *Waves Random Complex Media* **34**, 3381–3412.

[63] Khan, M. B. & Behera, H. 2021 Impact of sloping porous seabed on the efficiency of an owc against oblique waves. *Renew. Energy* **173**, 1027–1039.

[64] Khan, M. B., Behera, H., Sahoo, T. & Neelamani, S. 2021 Boundary element method for wave trapping by a multi-layered trapezoidal breakwater near a sloping rigid wall. *Meccanica* **56**, 317–334.

[65] Koley, S., Sarkar, A. & Sahoo, T. 2015 Interaction of gravity waves with bottom-standing submerged structures having perforated outer-layer placed on a

sloping bed. *Appl. Ocean Res.* **52**, 245–260.

[66] Kriebel, D., Sollitt, C. & Gerken, W. 1999 Wave forces on a vertical wave barrier pp. 2069–2081.

[67] Li, A. & Liu, Y. 2019 New analytical solutions to water wave diffraction by vertical truncated cylinders. *Int. J. Nav. Archit.* **11**, 952–969.

[68] Li, A., Liu, Y. & Fang, H. 2023 Wave scattering by porous cylinders with inner columns near a vertical wall. *Phys. Fluids* **35**, 087111.

[69] Li, L., Yuan, Z., Ji, C. & Gao, Y. 2019 Resonant waves in the gap between two advancing barges. *Eur. J. Mech. B Fluids.* **77**, 108–117.

[70] Li, Y., Liu, Y. & Teng, B. 2006 Porous effect parameter of thin permeable plates. *Coast. Eng.* **48**, 309–336.

[71] Li, Y., Zhao, X., Geng, J., Mackay, E. & Johanning, L. 2022 Wave scattering by a vertical cylinder with a submerged porous plate: Further analysis. *Ocean Eng.* **259**, 111–117.

[72] Li, Z., Teng, B. & Gou, Y. 2024 Two-dimensional diffraction and radiation problems of a floating body in varying bathymetry. *Appl. Ocean Res.* **150**, 104103.

[73] Linton, C. M. & Evans, D. V. 1990 The interaction of waves with arrays of vertical circular cylinders. *J. Fluid Mech.* **215**, 549–569.

[74] Liu, P. L. F. & Abbaspour, M. 1982 Wave scattering by a rigid thin barrier. *J. Waterw. Port Coast. Ocean Div.* **108**, 479–491.

[75] Liu, P. L. F. & Albanaa, K. 2004 Solitary wave runup and force on a vertical barrier. *J. Fluid Mech.* **505**, 225–233.

[76] Liu, Y. & Li, H. J. 2013 Wave reflection and transmission by porous breakwaters: A new analytical solution. *Coast. Eng.* **78**, 46–52.

[77] Liu, Y. & Li, H. J. 2014 A new semi-analytical solution for gap resonance between twin rectangular boxes. *Proc. Inst. Mech. Eng. Pt. M* **228**, 3–16.

[78] Losada, I. J., Losada, M. A. & Roldán, A. J. 1992 Propagation of oblique incident waves past rigid vertical thin barriers. *Appl. Ocean Res.* **14**, 191–199.

[79] Love, A. E. H. 1888 The small free vibrations and deformation of a thin elastic shell. *Philos. Trans. R. Soc. A* **179**, 491–546.

[80] Mackay, E., Shi, W., Qiao, D., Gabl, R., Davey, T., Ning, D. & Johanning, L. 2021 Numerical and experimental modelling of wave interaction with fixed

and floating porous cylinders. *Ocean Eng.* **242**, 110118.

[81] Madsen, O. S. 1974 Wave transmission through porous structures. *J. Waterw. Port Coast. Ocean Eng.* **100**, 169–188.

[82] Maiti, P. & Mandal, B. 2014 Water wave scattering by an elastic plate floating in an ocean with a porous bed. *Appl. Ocean Res.* **47**, 73–84.

[83] Mandal, B. N. & Dolai, D. P. 1994 Oblique water wave diffraction by thin vertical barriers in water of uniform finite depth. *Appl. Ocean Res.* **16**, 195–203.

[84] Mandal, S., Datta, N. & Sahoo, T. 2013 Hydroelastic analysis of surface wave interaction with concentric porous and flexible cylinder systems. *J. Fluids Struct.* **42**, 437–455.

[85] Mandal, S. & Sahoo, T. 2014 Wave interaction with floating flexible circular cage system. *Proceedings of the 11th International Conference on Hydrodynamics, ICHD 2014* pp. 19–24.

[86] Martha, S., Bora, S. & Chakrabarti, A. 2007 Oblique water-wave scattering by small undulation on a porous sea-bed. *Appl. Ocean Res.* **29**, 86–90.

[87] Masoudi, E. 2019 Hydrodynamic characteristics of inverse T-type floating breakwaters. *Int. J. Marit. Technol.* **11**, 13–20.

[88] Masoudi, E. & Gan, L. 2020 Diffraction waves on large aspect ratio rectangular submerged breakwaters. *Ocean Eng.* **209**, 107474.

[89] Masoudi, E. & Marshall, A. 2024 Diffraction of waves by multi-pontoon rectangular floating breakwaters. *Ocean Eng.* **310**, 118789.

[90] Massel, S. & Mei, C. 1977 Transmission of random wind waves through perforated or porous breakwaters. *Coast. Eng.* **1**, 63–78.

[91] Mei, C. C. & Black, J. L. 1969 Scattering of surface waves by rectangular obstacles in waters of finite depth. *J. Fluid Mech.* **38**, 499–511.

[92] Meylan, M. H. 2019 The time-dependent vibration of forced floating elastic plates by eigenfunction matching in two and three dimensions. *Wave Motion* **88**, 21–33.

[93] Meylan, M. H. 2021 Time-dependent motion of a floating circular elastic plate. *Fluids* **6**, 29.

[94] Meylan, M. H., Bennetts, L. G. & Peter, M. A. 2017 Water-wave scattering and energy dissipation by a floating porous elastic plate in three dimensions. *Wave Motion* **70**, 240–250.

[95] Meylan, M. H. & Sturova, I. V. 2009 Time-dependent motion of a two-dimensional floating elastic plate. *J. Fluids Struct.* **25**, 445–460.

[96] Mi, Z., Pengzhen, L., Piguang, W., Chao, Z. & Xiuli, D. 2021 An analytical solution for the interaction of waves with arrays of circular cylinders. *Math. Probl. Eng.* **2021**, 1–12.

[97] Michele, S., Zheng, S., Buriani, F., Borthwick, A. G. & Greaves, D. M. 2023 Floating hydroelastic circular plate in regular and irregular waves. *Eur. J. Mech. B Fluids.* **99**, 148–162.

[98] Michele, S., Zheng, S. & Greaves, D. 2022 Wave energy extraction from a floating flexible circular plate. *Ocean Eng.* **245**, 110275.

[99] Miles, J. & Gilbert, F. 1968 Scattering of gravity waves by a circular dock. *J. Fluid Mech.* **34**, 783–793.

[100] Mohanty, S., Mondal, R. & Sahoo, T. 2014 Time dependent flexural gravity waves in the presence of current. *J. Fluids Struct.* **45**, 28–49.

[101] Mondal, T. K. & Manam, S. 2025 An analytical study on oblique wave scattering involving flexible porous structures in a two-layer fluid. *J. Fluid Mech.* **1008**, A49.

[102] Moreira, R. & Chacaltana, J. 2015 Vorticity effects on nonlinear wave–current interactions in deep water. *J. Fluid Mech.* **778**, 314–334.

[103] Nandi, K., Hossain, S., Sarkar, B. & De, S. 2025 Hydroelastic analysis of wave scattering by multiple bottom-standing flexible permeable barriers in uniform finite depth. *Sh. Offshore Struct.* pp. 1–15.

[104] Neelamani, S. & Rajendran, R. 2002 Wave interaction with T-type breakwaters. *Ocean Eng.* **29**, 151–175.

[105] Ning, D., He, Z., Gou, Y. & Göteman, M. 2019 Near trapping effect on wave-power extraction by linear periodic arrays. *Sustainability* **12**, 29.

[106] Ning, Z., Zhao, L., Teng, B. & Johanning, L. 2017 Wave diffraction from a truncated cylinder with an upper porous sidewall and an inner column. *Ocean Eng.* **130**, 471–481.

[107] Panduranga, K., Venkateswarlu, V., Koley, S. & Vijay, K. 2025 Analysis of wave trapping by a submerged viscoelastic plate near a partially reflecting vertical wall with uneven seabed. *Eng. Anal. Bound. Elem.* **179**, 106370.

[108] Park, M. S., Koo, W. & Choi, Y. 2010 Hydrodynamic interaction with an array of porous circular cylinders. *Int. J. Nav. Archit. Ocean Eng.* **2**, 146–154.

[109] Pascal, J. 1999 Linear stability of fluid flow down a porous inclined plane. *J. Phys. D: Appl. Phys.* **32**, 417.

[110] Peregrine, D. H. 1976 Interaction of water waves and currents. *Adv. Appl. Mech.* **16**, 9–117.

[111] Pete, M. A., Meylan, M. H. & Chung, H. 2004 Wave scattering by a circular elastic plate in water of finite depth: a closed form solution. *Int. J. Offshore Polar Eng.* **14**.

[112] Pham, D., Wang, C. M. & Utsunomiya, T. 2008 Hydroelastic analysis of pontoon-type circular vlfs with an attached submerged plate. *Appl. Ocean Res.* **30**, 287–296.

[113] Poisson, S. D. 1818 Mémoire sur la théorie des ondes. mem. acad. r. sci. inst. france. 1816, 2nd ser. pp. 70–186.

[114] Porter, R. & Evans, D. 1995 Complementary approximations to wave scattering by vertical barriers. *J. Fluid Mech.* **294**, 155–180.

[115] Porter, R., Zheng, S. & Liang, H. 2022 Scattering of surface waves by a vertical truncated structured cylinder. *Proc. R. Soc. A* **478**, 20210824.

[116] Reddy, M. & Neelamani, S. 1992 Wave transmission and reflection characteristics of a partially immersed rigid vertical barrier. *Ocean Eng.* **19**, 313–325.

[117] Ren, K., Wu, G. & Ji, C. 2018 Diffraction of hydroelastic waves by multiple vertical circular cylinders. *J. Eng. Math.* **113**, 45–64.

[118] Rostamiyan, Y., Fereidoon, A., Davoudabadi, M., Yaghoobi, H. & Ganji, D. 2010 Analytical approach to investigation of deflection of circular plate under uniform load by homotopy perturbation method. *Math. Comput. Appl.* **15**, 816–821.

[119] Roy, R., De, S. & Mandal, B. N. 2019 Water wave scattering by multiple thin vertical barriers. *Appl. Math. Comput.* **355**, 458–481.

[120] Russell, J. S. 1842 *Rep. Br. Assoc. Adv. Sci. Part ii* pp. 19–21.

[121] Russell, J. S. 1845 *Report on Waves: Made to the Meetings of the British Association in 1842-43*.

[122] Ryu, S., Kim, M. & Lynett, P. J. 2003 Fully nonlinear wave-current interactions and kinematics by a bem-based numerical wave tank. *Comput. Mech.* **32**, 336–346.

[123] Sabuncu, T. & Ömer Gören 1985 Second-order vertical and horizontal wave forces on a circular dock. *Ocean Eng.* **12**, 341–361.

[124] Sadiq, I. & Usha, R. 2008 Thin newtonian film flow down a porous inclined plane: Stability analysis. *Phys. Fluids* **20**, 022105.

[125] Saha, S., Bora, S. & Das, S. 2023 Time-dependent water wave scattering by a bottom-mounted porous compound cylinder fitted with an annular porous lid. *Waves Random Complex Media* pp. 1–22.

[126] Saha, S., Mohanty, S. K. & Bora, S. N. 2022 Flexural gravity wave resonance in the presence of current. *J. Waterw. Port Coast. Ocean Eng.* **148**, 04022003.

[127] Sahoo, T. 2012 *Mathematical techniques for wave interaction with flexible structures*. CRC Press.

[128] Sannasiraj, S., Sundaravadivelu, R. & Sundar, V. 2001 Diffraction–radiation of multiple floating structures in directional waves. *Ocean Eng.* **28**, 201–234.

[129] Sarkar, A. 2020 Diffraction and radiation of linear water waves by a vertical compound porous cylinder of various configurations in finite ocean depth. PhD thesis.

[130] Sarkar, A. & Chanda, A. 2022 Structural performance of a submerged bottom-mounted compound porous cylinder on the water wave interaction in the presence of a porous sea-bed. *Phys. Fluids* **34**, 092113.

[131] Selvan, S. A. & Behera, H. 2020 Wave energy dissipation by a floating circular flexible porous membrane in single and two-layer fluids. *Ocean Eng.* **206**, 107374.

[132] Selvan, S. A., Behera, H. & Sahoo, T. 2019 Reduction of hydroelastic response of a flexible floating structure by an annular flexible permeable membrane. *J. Eng. Math.* **118**, 73–99.

[133] Selvan, S. A., Gayathri, R. & Behera, H. 2021 Surface wave scattering by multiple flexible fishing cage system. *Phys. Fluids* **33**, 037119.

[134] Sharma, P., Sarkar, B. & De, S. 2024 Oblique wave scattering by single and double inverse T-type breakwaters. *Ocean Eng.* **303**, 117804.

[135] Siddorn, P. & Eatock Taylor, R. 2008 Diffraction and independent radiation by an array of floating cylinders. *Ocean Eng.* **35**, 1289–1303.

[136] Skvortsov, A. T., MacGillivray, I. R. & Godin, O. A. 2025 Acoustic waves in a perforated cylinder. *J. Acoust. Soc. Am.* **157**, 1880–1888.

[137] Sollitt, C. K. & Cross, R. H. 1972 Wave transmission through permeable breakwaters. *Coastal Eng.* pp. 1827–1846.

[138] Sulisz, W. 1985 Wave reflection and transmission at permeable breakwaters of arbitrary cross-section. *Coast. Eng.* **9**, 371–386.

[139] Swami, K. C., Koley, S. & Panduranga, K. 2024 Mathematical modeling of water waves interaction with trapezoidal-shaped breakwater in the presence of current. *Waves in Random and Complex Media* pp. 1–27.

[140] Syed, S. A. & Mani, J. 2004 Performance of rigidly interconnected multiple floating pontoons. *J. Nav. Archit. Mar. Eng.* **1**, 3–17.

[141] Taylor, G. I. 1955 The action of a surface current used as a breakwater. *Proc. R. Soc. Lond. A Math. Phys. Sci.* **231**, 466–478.

[142] Taylor, G. I. 1956 Fluid flow in regions bounded by porous surfaces. *Proc. R. Soc. A* **234**, 456–475.

[143] Timoshenko, S. & Woinowsky Krieger, S. 1959 *Theory of plates and shells*.

[144] Tkacheva, L. A. 2005 Action of a periodic load on an elastic floating plate. *Fluid Dynamics* **40**, 282–296.

[145] Torres Freyermuth, A., Brocchini, M., Corvaro, S. & Pintado Patiño, J. C. 2017 Wave attenuation over porous seabeds: A numerical study. *Ocean Model.* **117**, 28–40.

[146] Ursell, F. 1947 The effect of a fixed vertical barrier on surface waves in deep water. *Math. Proc. Camb.* **43**, 374–382.

[147] Vijay, K., Venkateswarlu, V. & Nishad, C. S. 2021 Wave scattering by inverted trapezoidal porous boxes using dual boundary element method. *Ocean Eng.* **219**, 108149.

[148] Wang, G., Huang, L., Ren, B. & Wang, Y. 2014 Theoretical analysis of the performance of wave dissipation of T-type open breakwater. *Adv. Sci. Technol. Water Resour.* **34**, 1–5.

[149] Wang, H., Bôas, A. B. V., Vanneste, J. & Young, W. R. 2025 Scattering of surface waves by ocean currents: the u2h map. *J. Fluid Mech.* **1005**, A12.

[150] Watanabe, E., Utsunomiya, T., Wang, C. & Hang, L. T. T. 2006 Benchmark hydroelastic responses of a circular vlfs under wave action. *Eng. Struct.* **28**, 423–430.

[151] Weber, W. 1825 *Wellenlehre auf Experimente gegründet*. Gerhardt Fleischer, Leipzig.

[152] Wiegel, R. L. 1960 Transmission of waves past a rigid vertical thin barrier. *J. Waterw. Harbors Div.* **86**, 1–12.

[153] Williams, A. N., Li, W. & Wang, K. H. 2000 Water wave interaction with a floating porous cylinder. *Ocean Eng.* **27**, 1–28.

[154] Yang, X. Y., Zhang, H. S. & Li, H. T. 2017 Wave radiation and diffraction by a floating rectangular structure with an opening at its bottom in oblique seas. *J. Hydrodyn.* **29**, 1054–1066.

[155] Yu, X. 1995 Diffraction of water waves by porous breakwaters. *J. Waterw. Port Coast. Ocean Eng.* **121**, 275–282.

[156] Yu, X. & Chwang, A. T. 1994 Wave-induced oscillation in harbor with porous breakwaters. *J. Waterw. Port Coast. Ocean Eng.* **120**, 125–144.

[157] Zeng, X. H. & Tang, S. Y. 2013 The hydrodynamic interactions of an array of truncated circular cylinders as each cylinder oscillates independently with different prescribed modes. *J. Hydrodyn. Ser. B.* **25**, 27–38.

[158] Zhan, J. m., Chen, X. b., Gong, Y. j. & Hu, W. q. 2017 Numerical investigation of the interaction between an inverse T-type fixed/floating breakwater and regular/irregular waves. *Ocean Eng.* **137**, 110–119.

[159] Zhao, H., Teng, B., Li, G. W. & Lin, Y. Z. 2003 An experimental study of first-harmonic wave force on vertical truncated cylinder. *China Offshore Platform* **4**, 4–18.

[160] Zhao, W., Molin, B., Wang, Y., Wolgamot, H. & Taylor, P. 2022 Nonlinear harmonics of gap fluid resonance with floating body motions. *J. Fluid Mech.* **951**, A23.

[161] Zhao, X., Ye, Z., Fu, Y. & Cao, F. 2014 A CIP-based numerical simulation of freak wave impact on a floating body. *Ocean Eng.* **87**, 50–63.

[162] Zhao, Y., Liu, Y., Li, H. J. & Chang, A. T. 2020 Iterative dual BEM solution for water wave scattering by breakwaters having perforated thin plates. *Eng. Anal.*

Bound. Elem. **120**, 95–106.

[163] Zheng, S., Antonini, A., Zhang, Y., Greaves, D., Miles, J. & Iglesias, G. 2019 Wave power extraction from multiple oscillating water columns along a straight coast. *J. Fluid Mech.* **878**, 445–480.

[164] Zheng, S., Antonini, A., Zhang, Y., Greaves, D., Miles, J. & Iglesias, G. 2019 Wave power extraction from multiple oscillating water columns along a straight coast. *J. Fluid Mech.* **878**, 445–480.

[165] Zheng, S., Liang, H. & Greaves, D. 2024 Wave scattering and radiation by a surface-piercing vertical truncated metamaterial cylinder. *J. Fluid Mech.* **983**, A7.

[166] Zheng, S., Liang, H., Michele, S. & Greaves, D. 2023 Water wave interaction with an array of submerged circular plates: Hankel transform approach. *Phys. Rev. Fluids* **8**, 014803.

[167] Zheng, S., Meylan, M., Greaves, D. & Iglesias, G. 2020 Water-wave interaction with submerged porous elastic disks. *Phys. Fluids* **32**, 047106.

[168] Zheng, S., Meylan, M. H., Zhu, G., Greaves, D. & Iglesias, G. 2020 Hydroelastic interaction between water waves and an array of circular floating porous elastic plates. *J. Fluid Mech.* **900**, A20.

[169] Zheng, S. & Zhang, Y. 2016 Wave diffraction and radiation by multiple rectangular floaters. *J. Hydraul. Res.* **54**, 102–115.

[170] Zheng, S. & Zhang, Y. 2018 Theoretical modelling of a new hybrid wave energy converter in regular waves. *Renew. Energ.* **128**, 125–141.

[171] Zheng, S., Zhang, Y. & Iglesias, G. 2018 Wave–structure interaction in hybrid wave farms. *J. Fluids Struct.* **83**, 386–412.

[172] Zheng, Y., Liu, P., Shen, Y., Wu, B. & Sheng, S. 2007 On the radiation and diffraction of linear water waves by an infinitely long rectangular structure submerged in oblique seas. *Ocean Eng.* **34**, 436–450.

[173] Zheng, Y., Shen, Y., You, Y., Wu, B. & Jie, D. 2006 Wave radiation by a floating rectangular structure in oblique seas. *Ocean Eng.* **33**, 59–81.

[174] Zilman, G. & Miloh, T. 2000 Hydroelastic buoyant circular plate in shallow water: a closed form solution. *Appl. Ocean Res.* **22**, 191–198.